SCIENCE & TECHNOLOGY

ARS JOURNAL

A PUBLICATION OF THE AMERICAN ROCKET SOCIETY

VOLUME 31 NUMBER 11 NOVEMBER 1961

LOS ANGELES PUBLIC LIBRARY

NOV 24 1961

BIND

SURVEY ARTICLE

Recent Developments in Rocket Nozzle Configurations. . . . . G. V. R. Rao 1486

CONTRIBUTED ARTICLES

Performance and Evaluation of Satellites Tiros I and Tiros II . . . . . S. Sternberg and A. Schnapf 1495

Gravitational Torque Impulse on a Stabilized Satellite. . . Paul F. Hultquist 1506

Gravity Gradient Determination of the Vertical . . . Robert E. Roberson 1509

Satellite Rendezvous Terminal Guidance System . . Kenneth F. Steffan 1516

Projected Path of the Longitudinal Axis of Earth-Stabilized Satellites . . . . . Avedis A. Aintablian 1522

Modified Chromium for Unprotected Structures. . . . . David M. Scruggs 1527

Pilot Performance Capabilities During Centrifuge Simulations of Boost and Re-Entry. . . . . Randall M. Chambers and John G. Nelson 1534

Sealed Cabin Experimentation . . . . . B. E. Welch, T. E. Morgan Jr., and F. Ulvedal 1541

Crew Physical Support and Restraint in Advanced Manned Flight Systems . . . . . H. A. Smedal, H. C. Vykukal, R. P. Gallant, and G. W. Stinnett 1544

Directional Solar Reflectances in the Space Vehicle Temperature Control Problem . . . . . D. K. Edwards 1548

Optimization of Multistage Orbit Transfer Processes by Dynamic Programming . . . . . F. T. Smith 1553

Method of Calculating Liquid Flow Fluctuations in Rocket Motor Supply Pipes . . . . . W. A. Woods 1560

TECHNICAL NOTES

Radiation Shielding of Space Vehicles by Means of Superconducting Coils. . Richard H. Levy 1568

Lunar Landing Vehicle Propulsion Requirements . . . . . J. Richard Wrobel and Robert R. Brashears 1570

Binder Crystallization in Polysulfide Propellant . . . . . W. E. Hunter, E. T. Foster, and G. F. Mangum 1573

Determination of Electron Density and Mobility in Slightly Ionized Cesium . . . . . George J. Mullaney and Norman R. Dibelius 1575

Comparison of the Exact and Approximate Methods for Predicting Free Molecule Aerodynamic Coefficients. . . . . Lee H. Sentman 1576

Suggested Method for Small Changes in Nodal Longitude for Polar Orbits . . . . . Paul D. Arthur and Reinhard Lahde 1579

Class of Minimum Altitude Variation Orbits About an Oblate Earth . . . . . L. Rider 1580

Measurement of Small Discharge Rate of an Intermittent Exhaust Jet. . William J. Guman 1583

Effect of Rapid Pressure Decay on Solid Propellant Combustion . . . Carl C. Clepluch 1584

Interaction of Centered Expansion Waves . . . . . George Rudinger 1587

Impulse Programming for Turbine Boost . . . . . J. J. Marcinek and R. E. Goldstein 1589

Analysis of Large Amplitude Re-Entry Oscillations . . . George S. Campbell 1590

Polar Hodograph for Ballistic Missile Trajectories . . . S. P. Altman and J. S. Pistiner 1592

Notes on Heat Sink Analysis . . . . . K. A. Adams and M. R. Soisew 1595

One-Dimensional Solid Propellant Oscillatory Burner . . . . . M. D. Horton 1596

Terminating the Iterative Solution of Kepler's Equation. . . . . Oliver K. Smith 1598

DEPARTMENTS

Technical Comments 1598

Patents. 1599

Book Notes 1600

Technical Literature Digest. 1601

RUSSIAN SUPPLEMENT...1613-1668

does

$$X^n + Y^n = Z^n$$

?

Pierre de Fermat's last theorem states that the above equation has no solutions in which x, y, and z are positive whole numbers if "n" is a whole number greater than two. Mathematicians have yet to prove him wrong.

But their attempts to prove the theorem (or conjecture, since it *hasn't* been proved) have produced some of the most revolutionary concepts in modern algebra and number theory!

Questions are what answers are made of. Questions about our universe, for example. What is the Moon made of? Is there life on other planets? The answers are coming from Cal Tech's Jet Propulsion Laboratory for the National Aeronautics and Space Administration.

JPL scientists and engineers are supervising the design of spacecraft and their instruments to be sent to the Moon and planets. Ranger, Surveyor, Mariner. Some day, they'll be remembered as our first steps into space.

Today, they're a job to do. And a fascinating job at that. If you'd like to put your experience to work on this kind of a job, maybe JPL is your kind of place. Write to us and find out. It never hurts to ask questions.

JET PROPULSION LABORATORY
4806 OAK GROVE DRIVE, PASADENA, CALIFORNIA
Operated by California Institute of Technology for the National Aeronautics & Space Administration

All qualified applicants will receive consideration for employment without regard to race, creed or national origin/U.S. citizenship or current security clearance required.

ARS JOURNAL

A PUBLICATION OF THE AMERICAN ROCKET SOCIETY

EDITOR — Martin Summerfield

ASSOCIATE TECHNICAL EDITOR — Irvin Glassman

MANAGING EDITOR — Margaret Sherman

STAFF EDITOR — Barbara Nowak

ART EDITOR — John Culin

ASSOCIATE EDITORS

Igor **Jurkevich**, *G. E. Space Sciences Laboratory, Russian Supplement;* George **F. McLaughlin**, *Patents;* **Charles J. Mundo, Jr.**, *Raytheon Co., Guidance;* **Bernard H. Paiewonsky**, *Aeronautical Research Associates of Princeton, Flight Mechanics;* **M. H. Smith**, *Princeton University, Technical Literature Digest*

ASSISTANT EDITORS

Carol Falcetti, Norma Herrin, Carol Rubenstein

DIRECTOR OF MARKETING

Owen A. Kean

ADVERTISING PRODUCTION MANAGER

Walter Brunke

ADVERTISING REPRESENTATIVES

New York
D. C. Emery and Thomas Harford
400 Madison Ave., New York, N. Y.
Telephone: Plaza 9-7460

Los Angeles
James C. Galloway and Co.
6335 Wilshire Blvd., Los Angeles, Calif.
Telephone: Olive 3-3223

Chicago
Thomas M. Bryne, Jr.
2316 Sherman Ave., Evanston, Ill.
Telephone: 869-1831

London
B. C. Nichols
151 Fleet St.
London E. C. 4, England

American Rocket Society

500 FIFTH AVE., NEW YORK 36, NEW YORK, AREA CODE 212 PE 6-5845

Founded 1930

OFFICERS

President	Harold W. Ritchey
Vice-President	William H. Pickering
Executive Secretary	James J. Harford
Treasurer	Robert M. Lawrence
General Counsel	Andrew G. Haley
Director of Publications	Irwin Hersey

BOARD OF DIRECTORS

(Terms expire on dates indicated)

Ali B. Cambel	1962	Samuel Herrick	1963
Richard B. Canright	1962	Arthur Kantrowitz	1963
William J. Cecka, Jr.	1963	A. K. Oppenheim	1961
James R. Dempsey	1961	Simon Ramo	1963
Herbert Friedman	1962	David G. Simons	1961
George Gerard	1961	John L. Sloop	1961
Robert A. Gross	1962	Martin Summerfield	1962
Abe M. Zarem	1963		

TECHNICAL COMMITTEES AND CHAIRMEN

Astrodynamics, Robert M. L. Baker, Jr.
Communications and Instrumentation, Frank W. Lehan
Electric Propulsion, Ernst Stuhlinger
Guidance and Control, James S. Farrior
Human Factors and Bioastronautics, Eugene B. Konecci
Hypersonics, William H. Dorrance
Liquid Rockets, Martin Goldsmith
Magnetohydrodynamics, Milton M. Slawsky
Missiles and Space Vehicles, William M. Duke
Nuclear Propulsion, Robert W. Bussard
Physics of the Atmosphere and Space, Herbert Friedman
Power Systems, John H. Huth
Propellants and Combustion, Peter L. Nichols, Jr.
Ramjets, William H. Avery
Solid Propellant Rockets, G. Daniel Brewer
Space Law and Sociology, Andrew G. Haley
Structures and Materials, George Gerard
Test, Operations, and Support, Bernhardt L. Dorman
Underwater Propulsion, Herman E. Sheets

Scope of ARS JOURNAL

This Journal is devoted to the advancement of astronautics through the dissemination of original papers disclosing new scientific knowledge and basic applications of such knowledge. The sciences of astronautics are understood here to embrace selected aspects of jet and rocket propulsion spaceflight mechanics, high speed aerodynamics, flight guidance, space communications, atmospheric and outer space physics, materials and structures, human engineering, overall system analysis and possibly certain other scientific areas. The selection of papers to be printed will be governed by the pertinence of the topic to the field of astronautics, by the current or probable future significance of the research, and by the importance of distributing the information to the members of the Society and to the profession at large.

Information for Authors

Manuscripts must be as brief as the proper presentation of the ideas will allow. Exclusion of dispensable material and conciseness of expression will influence the Editors' acceptance of a manuscript. In terms of standard-size double-spaced typed pages, a typical maximum length is 22 pages of text (including equations), 1 page of references, 1 page of abstract and 12 illustrations. Fewer illustrations permit more text, and vice versa. Greater length will be acceptable only in exceptional cases.

Short manuscripts, not more than one quarter of the maximum length stated for full articles, may qualify for publication as Technical Notes or Technical Comments. They may be devoted to new developments requiring prompt disclosure or to comments on previously published papers. Such manuscripts are published within a few months of the date of receipt.

Sponsored manuscripts are published occasionally as an ARS service to the industry. A manuscript that does not qualify for publication according to the above-stated requirements as to subject, scope or length, but which nevertheless deserves widespread distribution among jet propulsion engineers, may be printed as an extra part of the Journal or as a special supplement, if the author or his sponsor will reimburse the Society for actual publication costs. Estimates are available on request. Acknowledgment of such financial sponsorship appears as a footnote on the first page of the article. Publication is prompt, since such papers are not in the ordinary backlog.

Manuscripts must be double spaced on one side of paper only with wide margins to allow for instructions to printer. Include a 100 to 200 word abstract. State the authors' positions and affiliations in a footnote on the first page. Equations and symbols may be handwritten or typewritten; clarity for the printer is essential. Greek letters and unusual symbols should be identified in the margin. If handwritten, distinguish between capital and lower case letters, and indicate subscripts and superscripts. References are to be grouped at the end of the manuscript and are to be given as follows. For journal articles: Authors first, then title, journal, volume, year, page numbers; for books: Authors first, then title, publisher, city, edition and page or chapter numbers. Line drawings must be clear and sharp to make clear engravings. Use black ink on white paper or tracing cloth. Lettering should be large enough to be legible after reduction. Photographs should be glossy prints, not matte or semi-matte. Each illustration must have a legend; legends should be listed in order on a separate sheet.

Manuscripts must be accompanied by written assurance as to security clearance in the event the subject matter lies in a classified area or if the paper originates under government sponsorship. Full responsibility rests with the author.

Preprints of papers presented at ARS meetings are automatically considered for publication.

Submit manuscripts in duplicate (original plus first carbon, with two sets of illustrations) to the Managing Editor, ARS JOURNAL, 500 Fifth Avenue, New York 36, N.Y.

ARS JOURNAL is published monthly by the American Rocket Society Inc. and the American Interplanetary Society at 20th & Northampton Sts., Easton, Pa., U. S. A. Editorial offices: 500 Fifth Ave., New York 36, N. Y. Price: $18.00 per year, $3.00 per single copy. Second-class postage paid at Easton, Pa., with additional entry at New York, N. Y. This publication is authorized to be mailed at the special rates of postage prescribed by Section 132.122. Notice of change of address should be sent to the Secretary, ARS, at least 30 days prior to publication. Opinions expressed herein are the authors' and do not necessarily reflect the views of the editors or of the Society.

© Copyright 1961 by the American Rocket Society, Inc.

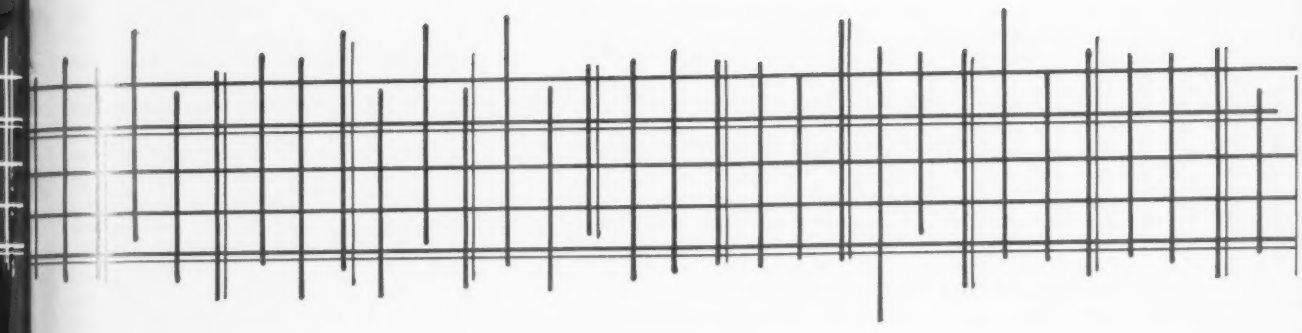

genus: homo · species: sapiens discipline: factors engineering

At the six major RCA Defense Electronic Products facilities, teams of psychologists and design engineers are deeply involved in the highly specialized, incredibly complex study of human factors engineering—man/machine interfaces, auto-instructional methods, decision processes, read-in/read-out optimization techniques, sensory perception, the entire spectrum of psychological-physiological-physical disciplines.

Whether your requirements involve human factors study of command and control functions for defense networks, or projected life support systems for space exploration, a total RCA capability stands ready to assist you . . . from feasibility study to project completion. Write Defense Electronic Products, Radio Corporation of America, Camden, N. J.

RCA®

The Most Trusted Name in Electronics

RADIO CORPORATION OF AMERICA

Recent Developments in Rocket Nozzle Configurations

G. V. R. RAO

National Engineering Science Co.
Pasadena, Calif.

THE THRUST of a rocket engine is primarily dependent upon the momentum imparted to the products of combustion by discharging them through an exhaust nozzle. During their passage through the nozzle, the exhaust gases are continuously accelerated from low subsonic velocities to high supersonic velocities at the nozzle exit. For the purpose of understanding the flow process, the nozzle can be divided into three portions: the convergent subsonic section, the throat section, and the divergent supersonic section. This division is appropriate because of the different effects each part has in determining the thrust developed by the rocket, and because different methods of analysis have to be used in determining the flow field in these three regions.

The mass flow rate through a rocket nozzle is determined by the area of the throat section and operating conditions of the combustion chamber. Design changes in the configuration of the convergent portion of the nozzle would influence the mass flow of the exhaust gases and also, to some extent, the combustion efficiency achieved in the chamber. The sonic velocity attained by the exhaust gases is fixed by the combustion chamber conditions and can be further increased by the expansion occurring in the divergent supersonic portion of the nozzle. This additional velocity, leading to thrust increment, is dependent only on the configuration of the diverging nozzle walls and the exit area. In recent years the design of the divergent supersonic portion of the rocket nozzle has received considerable attention. The scope of this review will be limited to this portion of the nozzle and improvement thereof.

Analysis of rocket nozzle flows in any real case should include radiative heat loss, chemical reactions due to incomplete combustion, and chemical properties of the exhaust gases. However, gross performance comparisons can be made by assuming that the exhaust gases expand adiabatically and behave like an ideal gas with a constant ratio of specific heat capacities.

The appropriate choice of nozzle configuration for a specific rocket engine may, to a great extent, depend on the fabrication methods of nozzle walls, cooling requirements, allowable limits on dimensions, influence of nozzle weight on overall rocket performance, etc. Detailed examination of all these features involves various special engineering fields aside from the knowledge of supersonic expansion process of the exhaust gases, and, as such, is not considered within the scope of this paper.

The thrust performance of uniform exit flow nozzles and conical nozzles serves as reference in comparing the performance of other types of nozzles and is briefly examined prior to the discussion of recent developments in nozzle configurations.

Received Sept. 12, 1961.

Uniform Exit Flow Nozzle

The thrust of a nozzle can be shown to reach a maximum when the nozzle is designed for parallel uniform exit flow, with exit plane pressure equal to ambient pressure. Such a nozzle is generally known as the *ideal nozzle* for expanding the gases from the chamber pressure P_c to ambient pressure p_a. The ratio of exit area to throat area of such a nozzle is given by

$$\frac{A_e}{A_t} = \left(\frac{\gamma-1}{2}\right)^{1/2}\left(\frac{2}{\gamma+1}\right)^{(\gamma+1)/2(\gamma-1)} \left(\frac{p_a}{P_c}\right)^{-(1/\gamma)}\left[1-\left(\frac{p_a}{P_c}\right)^{(\gamma-1)/\gamma}\right]^{-1/2} \quad [1]$$

where γ is the isentropic exponent governing the expansion process. For rocket engines operating at high altitudes, the ratio p_a/P_c will be very low, and large area ratios for the ideal nozzles would be required.

To obtain optimum performance from a rocket engine operating over a wide range of altitudes, variations in the nozzle exit area as indicated by Eq. 1 would be required. Mechanical variation of rocket nozzle area ratio is very difficult because of the extremely high temperatures involved and the attendant complexity. Thus taking into consideration the performance requirements over the entire trajectory of the rocket vehicle, an appropriate fixed exit area for the nozzle is chosen. The performance merit of the divergent supersonic portion of a nozzle can be measured in terms of its vacuum thrust coefficient C_{f_v}, defined as

$$C_{f_v} = \frac{\text{Thrust when discharging to vacuum}}{P_c A_t}$$

where P_c and A_t denote the chamber pressure and throat area

---

G. V. R. Rao is an Associate Director of National Engineering Science Co. Born in Rajahmundry, India, he attended the Madras Engineering College, and later New York University, where he received a D.Sc. in Aeronautical Engineering in 1949. Before joining NESCO, Dr. Rao was an aerodynamicist with General Electric's Aircraft Gas Turbine Division from 1952 to 1955, research scientist at Marquardt Aircraft from 1955 to 1958, and until recently, engineering specialist at Rocketdyne. Dr. Rao has made numerous contributions in the field of jet engines and rocket propulsion.

respectively. The vacuum thrust coefficient of an ideal nozzle is an explicit function of nozzle area ratio A_e/A_t and the isentropic exponent γ.

When the ideal nozzle is operated in the presence of an ambient pressure p_a, the thrust coefficient is written

$$C_f = C_{f_{videal}} - \frac{p_a}{P_c} \cdot \frac{A_e}{A_t} \qquad [2]$$

The above equation is often referred to as one-dimensional thrust coefficient equation. One-dimensional thrust coefficients for various values of isentropic exponent γ, area ratio A_e/A_t, and operating pressure ratio p_a/P_c can be evaluated from flow tables such as are given in (1),[1] or more exactly, from tabulations of thermodynamic data for the particular combustion gas.

The design of nozzle wall configuration to produce the desired uniform exit flow can be accomplished by the well-known method of characteristics (2). The computation for the wall contour generally requires high speed computing machines; several such contours are described in (3). Foelsch (4) developed an elegant approximation to obtain the nozzle contour by hand computations. The length of a uniform exit flow nozzle can be reduced to some extent by allowing all the expansion to occur immediately downstream of the throat, and then constructing the nozzle contour to turn the flow suitably so as to achieve uniform axial flow at the exit. Minimum lengths of nozzles required to obtain uniform exit flows for different values of exit to throat area ratio are computed for $\gamma = 1.23$ (see Fig. 1). In computing these nozzle lengths it was felt that a sharp corner downstream of the throat should be avoided, and thus a wall contour having a radius of curvature equal to 0.4 times the throat section radius was used.

As is evident from Fig. 1, the ideal nozzles that give maximum thrust performance are long and, consequently, heavy. The following sections will deal with methods of reducing nozzle length without appreciable loss in thrust performance.

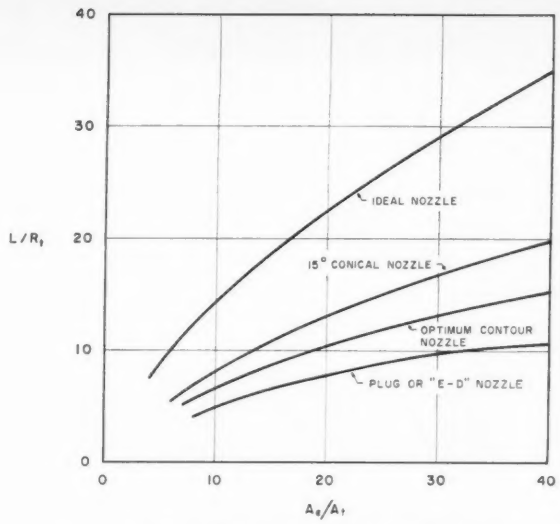

Fig. 1 Length comparison of various types of nozzles

Conical Nozzles

The vacuum thrust coefficient of any nozzle shorter than the uniform flow nozzle will naturally be less than the one-dimensional value. The thrust coefficient C_{f_v}, used in Eq. 2, will have to be adjusted accordingly. The simplest geometric shape for the divergent nozzle is a truncated cone, as shown in Fig. 2a. Even though the exit velocity of a conical nozzle is essentially equal to the one-dimensional value corresponding to the area ratio, the flow directions are not all axial, and hence there is a thrust decrement due to the flow divergence. Assuming a conical type flow at the nozzle exit, Malina (5) has shown that the exit momentum is equal to the value computed from one-dimensional theory multiplied by a factor

$$\lambda = (1 + \cos \alpha)/2 \qquad [3]$$

where α denotes the half angle of the cone. The thrust coefficient of a conical nozzle discharging into vacuum can be written

$$C_{f_{conical}} = \frac{p_e}{P_c} \cdot \frac{A_e}{A_t} + \left(\frac{1 + \cos \alpha}{2}\right) \frac{\rho_e V_e^2 A_e}{P_c A_t} \qquad [4]$$

where p_e, ρ_e, V_e are the one-dimensional pressure, density, and velocity computed at the exit of the nozzle. Experimental results (6) on conical nozzles of various cone half angles bear out the validity of the above relationship.

In using Eq. 4, the exit flow parameters based on the ratio of throat to exit areas measured in plane sections normal to the axis are usually computed. Landsbaum (7) suggested that, to be consistent with the concept of conical exit flow, the exit area preferably should be computed over a spherical surface. This spherical surface area will be slightly larger than the plane section area A_e. Strictly speaking, the exit flow parameters are functions of conical flow expanding from a critical section to the exit section, both measured along spherical surfaces normal to the conical flow field. The critical section area may differ from the geometrical throat area A_t due to the effect of nozzle configuration as well as the nonideal nature of the flowing medium. Even for inviscid flows, the nonuniformity of flow in the throat region caused by configuration geometry yields critical section area significantly less than the plane cross-sectional area A_t, as shown in (8).

In the case of small rocket engines fitted with small area ratio nozzles, simple fabrication methods are preferred, and it is a common practice to use conical nozzles. Usually a half cone angle of 15° is used for the divergent section and, as can be seen from Fig. 1, the length of 15° conical nozzle is considerably less than that of a uniform exit nozzle. The decrement in thrust coefficient of a 15° conical nozzle compared to one-dimensional is only about 1.7% and varies slightly with altitude conditions, as can be seen from Eq. 4. Thus, a 15° conical nozzle is often used as a reference in comparing lengths and thrust performance of new types of nozzles.

Contoured Nozzles

The loss in thrust of a conical nozzle due to flow divergence becomes large with increasing cone angles associated with reduction in nozzle length. By contouring the nozzle wall, as shown in Fig. 2b, the flow can be turned closer to axial direction, and the loss in thrust due to flow divergence can be reduced to some extent. Several methods have been suggested for contouring the nozzle walls. Sinyarev and Doborovolskii, in their textbook on liquid rocket engines (9), have suggested the use of a suitable circular arc for the nozzle contour. Dillaway (10) computed nozzle contours by a gradual reduction of the nozzle wall slope as one approaches the nozzle exit. Instead of summing up the flow divergence loss across the entire exit plane, Overall (11) incorrectly concluded that the loss in thrust depends only on the nozzle wall slope at the exit. The exit flow of a contoured nozzle is strongly affected by the nozzle contour, and no simple relation such as Eq. 4 can be

[1] Numbers in parentheses indicate References at end of paper.

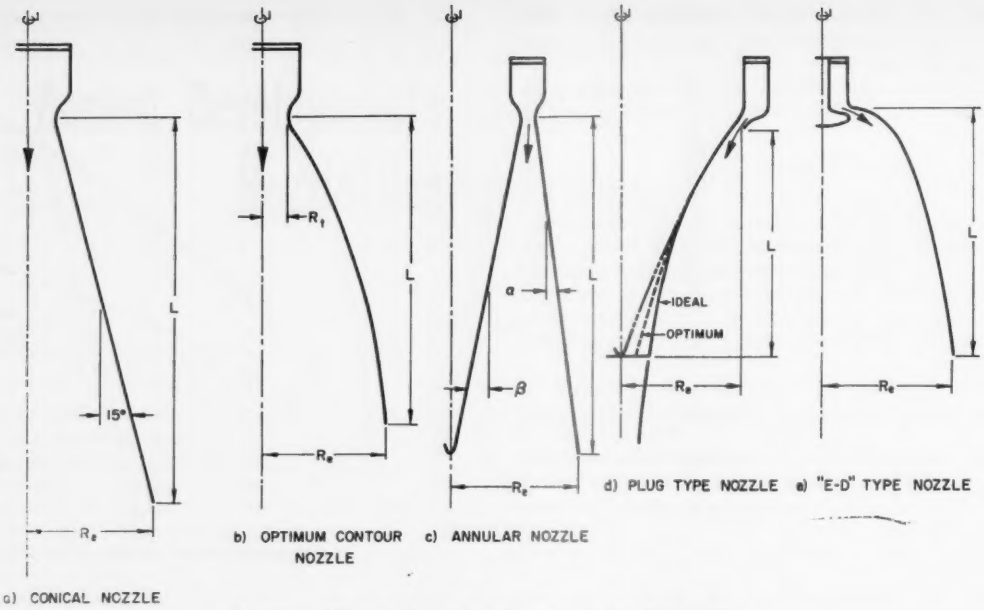

Fig. 2a–e Main features of various types of rocket nozzles

derived. The vacuum thrust coefficient of a contoured nozzle can be evaluated as

$$C_{f_v} = \int_{A_e} \frac{p}{P_c A_t} 2\pi r dr + \int_{A_e} \frac{\rho V^2 \cos\theta}{P_c A_t} 2\pi r dr \qquad [5]$$

where the integration is carried out across the entire area A_e of the exit plane normal to the nozzle axis. The pressure p, density ρ, velocity V, and its direction θ are evaluated in the exit plane at a distance r from the nozzle axis. Landsbaum (12) suggested that one can examine truncated portions of several uniform exit flow nozzles of different area ratios and choose the one contour that yields the best performance. A similar approach was suggested by Demuth and Ditore (13). Experimental evaluation of such cutoff portions of uniform exit flow nozzles was reported by Farley and Campbell (14) and showed close agreement with theoretical estimates. Recently Ahlberg, Hamilton, Migdal, and Nilson (15) made a study of nozzle optimization by considering truncated portions of uniform exit flow nozzles.

In contrast to all the forementioned semiempirical methods, a direct and very elegant approach to nozzle contour design was made by Guderley and Hantsch (16). They formulated the problem of finding exit area and nozzle contour to yield optimum thrust when the nozzle length and ambient pressure have prescribed values. Using the calculus of variations, they solved the problem for the exit flow field required to deliver optimum thrust under the prescribed restrictions. After the required exit flow is found, the method of characteristics in supersonic flow is used to develop the nozzle contour between the throat and the nozzle exit. The nozzle contour thus obtained can also be interpreted as the optimum thrust contour for the particular values of exit area and length.

Because of the complicated nature of the solution presented by Guderley and Hantsch, the optimum thrust contours for rocket nozzles were completely ignored until recent years. In reformulating the problem, Rao (17) found a simplified approach for the contour calculations. In a recent paper Guderley (18) discussed the difference between his and Rao's method of reaching the same solution. Several optimum thrust nozzles were computed for $\gamma = 1.23$, and a systematic study of their parameters was given in (19). The length of a contoured nozzle required to yield the same vacuum thrust coefficient as that of a 15° conical nozzle is shown in Fig. 1 plotted against nozzle area ratio.

Computing nozzle contours by the method of characteristics can also be extended to the case of variable value of γ, as shown in (20). The method of optimizing nozzle contours for the case of nonconstant γ was treated in (21). Examination of contour calculations at different values of γ, given in (19), has shown that when the exit area ratio and length are both prescribed, the differences in nozzle contours are negligible. However, it should be remembered that the flow process in a nozzle of a given configuration is strongly governed by the isentropic exponent γ, and hence the nozzle thrust coefficient would greatly depend upon the value of γ. It was also observed that the optimum thrust nozzle contour can be closely approximated by a parabola. The parabola has to fit the maximum wall inclination θ_m in the throat region and the wall inclination θ_e at the nozzle exit. Parameters θ_m and θ_e are implicit functions of the nozzle exit area and length. Charts showing the values of these parameters and a simple geometric construction of the parabolic arc are given in (22).

An optimum thrust nozzle contour (16, 17) designed for an ambient pressure p_a and prescribed length would require the flow conditions on the nozzle wall at the exit to satisfy the following relationship

$$\frac{p - p_a}{(1/2)\rho V^2} \sqrt{M^2 - 1} = \sin 2\theta \qquad [6]$$

where p, ρ, V, M and θ denote the pressure, density, velocity, Mach number, and flow direction, respectively. For the case of small divergence angles, Knuth (23) suggests that the flow conditions at any individual element of nozzle wall can be assumed to be independent of the rest of the wall contour. He shows that by applying Eq. 6 at each of the individual wall elements, a relationship between the local flow parameters is obtained. The nozzle contour is then constructed through stepwise integration.

In general, the rocket nozzle contours chosen for optimum thrust performance require wall angles of about 28° to 30°

downstream of the throat. The required wall inclination at the nozzle exit is about 10° to 14° depending upon the area ratio and length of the nozzle. Nozzle contours having such parameters are widely used for liquid rocket engines, and no specific difficulties attributable to the contour are experienced with hot exhaust gases. However, the exhaust products of solid rocket engines often contain particles of metal oxides. The dynamics of hot gases laden with small particles up to as much as 30% by weight has to be considered. Optimization of nozzle contours for such flows must then consider the velocity lag of particles and hence becomes very difficult. Kliegel (24) analyzed flows of such gas-particle mixtures through several contoured nozzles. He concluded that in the case of highly curved nozzle walls, the gas particles impinge on the wall at the exit, produce a decrement in thrust, and aggravate problems of erosion. Consequently, for solid rocket engine applications, he suggests nozzle contours with less amount of turning than the optimum thrust contours.

Annular Nozzles

In conventional nozzles we generally have the throat and exit areas formed by circular cross sections normal to the nozzle axis. There is another type of nozzle, widely used in jet engines, called an *annular nozzle*. The throat section is an annulus formed between a central plug and an outer tail pipe. Downstream of the throat section the exhaust gases are made to expand in a diverging annulus formed between the converging central plug and the diverging tailpipe, as shown in Fig. 2c. If the central plug vertex lies in the exit plane and the diverging walls are formed of conical surfaces, an expression for thrust lost due to flow divergence can be derived.

$$\lambda = \frac{(1/2)\,(\sin\alpha + \sin\beta)^2}{(\alpha + \beta)\sin\beta + \cos\beta - \cos\alpha} \qquad [7]$$

where α is the angle between the outer wall and the nozzle axis, and β is the angle between the inner plug wall and the nozzle axis. For the same exit to throat area ratio and nozzle length, the throat annulus can be located at different radial distance from the nozzle axis, leading to corresponding changes in the values of α and β. In the case of a divergent annular nozzle formed between a straight tailpipe and a conical central plug, the thrust decrement due to flow divergence can be obtained by substituting α equal to zero in Eq. 7. As β approaches zero the inner plug vanishes, and only the diverging outer wall remains. In this case Eq. 7 reduces to the flow divergence loss factor discussed in connection with the conical nozzle thrust performance.

The thrust loss due to flow divergence in an annular nozzle, as indicated by Eq. 7, would be less than that in a conical nozzle of the same area ratio and length. The flow divergence loss in an annular nozzle can be reduced further by contouring the nozzle walls. However, in this case the contour optimization becomes more complicated than in a conventional nozzle, since the inner wall and outer wall contours have to be optimized simultaneously.

Self-Adjusting Type Nozzles

In the several types of nozzles discussed above, the expansion of the exhaust gases is governed solely by the diverging walls of the nozzle; this expansion process can be optimized by suitably contouring the divergent walls. The ambient pressure has no influence on the expansion process occurring inside the nozzle, and the exhaust gases would continue to expand along the diverging nozzle walls to pressures considerably below the ambient pressure. This overexpansion of the gases would proceed until flow separates from nozzle walls (25, 26). The nozzle wall pressure would then rise abruptly to the ambient pressure across an oblique shock (27, 28). The occurrence of these subambient pressures on some portions of the nozzle walls reflects a loss in thrust performance in rocket engines operating below the design altitudes. In recent years, considerable attention has been given to the development of new types of nozzles in which the expansion process is directly or indirectly regulated by the ambient pressure. Since the exhaust flow in these types of nozzles adjusts itself to conform to the external conditions, this author prefers to denote them as *self-adjusting type*.

These self-adjusting type nozzles can be classified in two categories: 1) plug-type nozzles and 2) expansion-deflection type nozzles. The essential features of these nozzle types

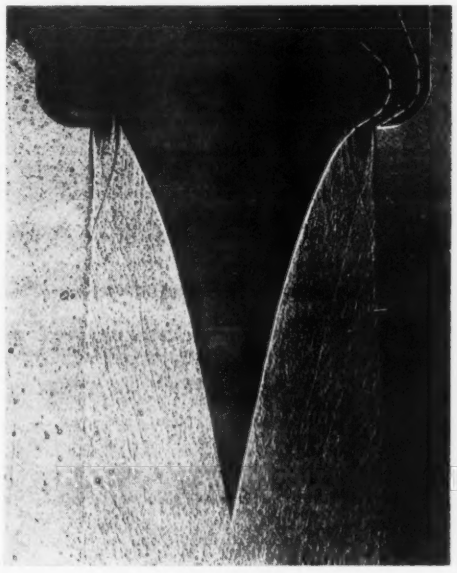

Fig. 3a Shadowgraph of flow around a plug nozzle at design pressure ratio

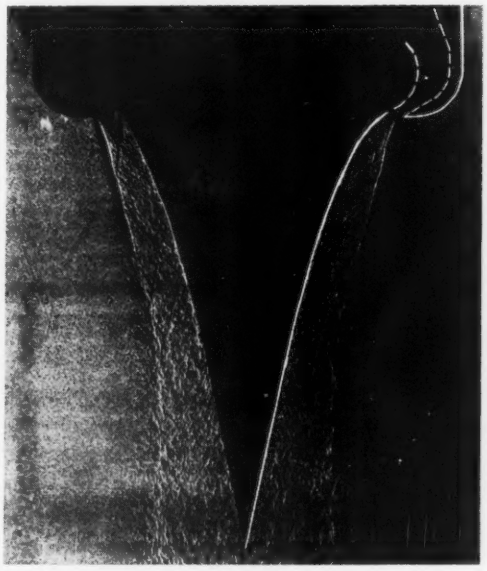

Fig. 3b Shadowgraph of flow around a plug nozzle at below design pressure ratio

will be briefly described here, and the reader is advised to refer to cited literature for detailed information.

Plug Type Nozzles

An all external expansion ideal plug nozzle is schematically shown in Fig. 2d. The nozzle throat is located as an annulus at the outer diameter, with the exhaust gases issuing in an inward direction. At the outer edge of the annulus, often denoted *cowl-lip*, following jet engine terminology, the exhaust gases expand abruptly to the ambient pressure. The flow of the exhaust gases is controlled by the expansion waves originating from the cowl-lip, and the flow turning is affected by the plug surface. One can design the plug surface so as to expand the gases from a chamber pressure P_c to an ambient pressure p_a, producing uniform exit flow parallel to the nozzle axis. The external diameter, i.e., cowl-lip diameter, of such an ideal plug would be the same as the exit diameter of a uniform flow convergent-divergent nozzle expanding the gases to the same ambient pressure p_a. However, the plug type nozzle is much shorter than the equivalent convergent-divergent nozzle as shown in Fig. 2d. Simple approximate methods suggested by Krase (29) or Greer (30) can be used to design ideal plug nozzle contours by hand calculations. Exact computations generally require high speed computing machines.

The thrust performance of the ideal plug nozzle shown in Fig. 2d at design and above design pressure ratios, i.e., P_c/p_e, would be identical to that of a convergent-divergent ideal nozzle. Any ballooning out of the exhaust gases that occurs at above design pressure ratios does not affect the flow along the wall in either type of nozzle. However, at below design pressure ratio, the flow in the plug nozzle is radically different from that in a conventional nozzle. The expansion occurring at the cowl-lip would proceed only up to the ambient pressure p_a and not all the way down to the design exit pressure p_e. Shadowgraphs of flow around a plug nozzle operating at two different pressure ratios are reproduced from (33) and shown in Figs. 3a and 3b. The self-adjusting nature of the flow at below design operating pressure ratio can be seen clearly in this shadowgraph. This terminated expansion wave would intersect with plug wall at a point where wall pressure p_w is nearly equal to p_a; the difference between p_w and p_a is only due to the axisymmetric nature of flow. If the expansion were to proceed uninterrupted, the wall pressures would continue to fall to reach p_c at plug vertex. Now, however, the expansion is interrupted at $p_w \simeq p_a$, and the convex surface of the plug downstream of this point causes a gradual compressive turning of the exhaust gases. Consequently, the wall pressure downstream of this location would rise to values higher than p_a. Beale and Povolny (31) measured wall pressure distribution on an external plug operating at below design condition, and their data shows this increase in wall pressures due to the compression. These increased pressures on the downstream portions of the plug wall give rise to a thrust increment over that of a convergent-divergent nozzle. This behavior, briefly discussed in (29), is also experimentally indicated by data given in (32). A comparison between the performance of a conventional nozzle and a plug type nozzle was given in a recent paper by Berman (33). Due to the self-adjusting nature of the flow, a plug nozzle operating at below design pressure ratio shows a thrust advantage over a conventional nozzle, as indicated in Fig. 4, which is reproduced from (33). It should be borne in mind that the amount of recompression occurring on the plug surface is intimately connected with the plug wall contour and consequently affects the off-design performance of the plug nozzle. Thus, general comparisons regarding the thrust advantage of plug nozzles cannot be made.

Plug nozzle concept applied to rocket engines presents a great advantage in the development of large engines. The annular combustion chamber can be built up from segments of nearly rectangular chambers; the consequent design advantages are discussed in (33).

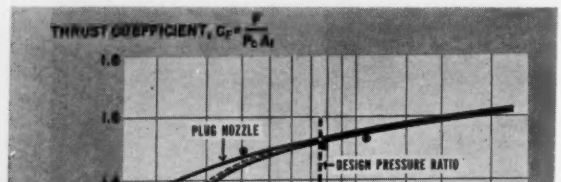

Fig. 4 Thrust performance of plug and conventional nozzles

Plug Contours

Just as in the case of conventional convergent-divergent nozzles, one may ask whether the plug length can be shortened without undue loss in thrust. The wall pressures on an ideal plug nozzle and their contribution to axial thrust fall off considerably as the vertex is approached. Hence, the plug end portion can be cut off to some extent without much sacrifice in thrust. The plug end may further be modified by using a large cone angle at the plug vertex so as to avoid a flattened base. Both these plug modifications are shown in Fig. 2d. Experimental data taken on low expansion ratio plug nozzles, reported in (34), indicate that cone half angles as large as 40° can be used without undue loss in thrust performance. Berman and Crimp (35) also indicated that experimental data on plug type rocket nozzles showed performance reduction of only 1% by using cone half angles even up to 30°.

Similar to the approach taken in optimizing the conventional nozzle contour, optimum plug contour for a given length may be sought. Rao discussed the solution of such problems and presented typical optimum plug contours in (36). The reduction in the nozzle length that can be achieved by the use of plug type nozzle is indicated in Fig. 1. For comparison, the equivalent area ratio of a plug nozzle is defined as $\pi R_e^2/A_t$, where R_e is the radius of the cowl-lip and A_t denotes the area of the throat annulus. The length required for a plug nozzle to yield 99.5% of vacuum thrust coefficient of ideal nozzle of the same area ratio is plotted in Fig. 1 against nozzle area ratio. The plug contour solution as given by Rao yields a blunt base diameter less than that of a truncated ideal plug contour as sketched in Fig. 2d. It should be noted that, due to the convergence of flow along the plug surface, boundary layer thickness increases rapidly towards the plug vertex. The plug contours (36) computed for inviscid flow can be further corrected to accommodate this increasing boundary layer thickness. Such corrections would reduce the size of the plug base, bringing it closer to a conical vertex. Thus, a conical plug vertex with optimized flow direction at the throat may be a suitable approach. The method indicated in (36) can be used to obtain the optimum flow direction at the throat applicable to the particular plug parameters.

In evaluating the thrust performance of a plug type nozzle, it should be remembered that the plug wall pressures are affected by the external pressure at the cowl and also by the flow behavior near the plug vertex. If the missile flight conditions are such that the pressure downstream of the cowl is different from ambient pressure, necessary corrections to the performance should be made. It is difficult to predict analytically the flow at the plug vertex at subdesign pressure

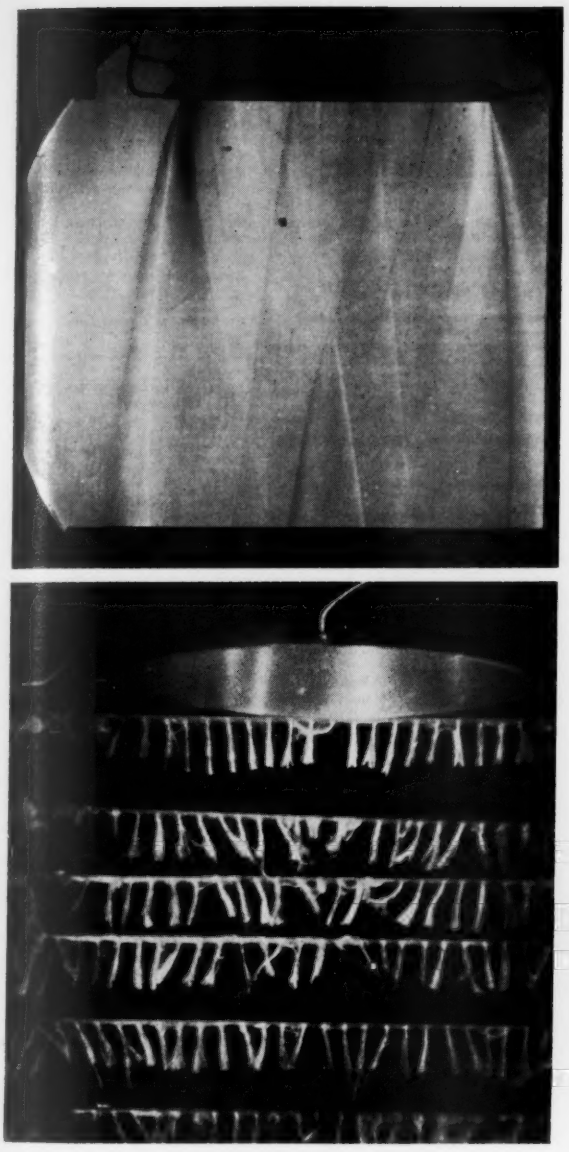

Fig. 5a Schlieren and tuft photographs of flow in an E-D nozzle at high pressure ratio

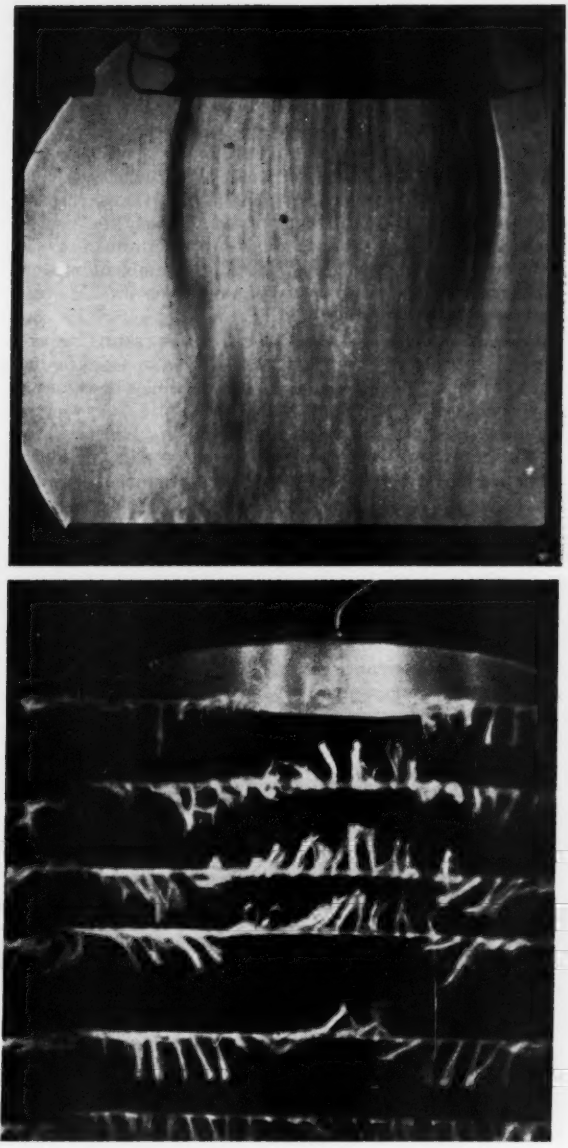

Fig. 5b Schlieren and tuft photograph of flow in an E-D nozzle at low pressure ratio

ratio operation, and the thrust performance can best be ascertained through tests simulating the rocket flight conditions.

In a recent paper, Berman and Neuffer (37) discussed modifications to the plug nozzle concept by incorporating a certain amount of internal expansion preceding the external plug. Since the effect of the external pressure on the flow is thus partly restricted, one would find that in this case the self-adjusting property of the flow is inhibited.

E-D Type Nozzle

Instead of locating the throat of the rocket motor at the outer diameter, as in the case of a plug nozzle, a compact combustion chamber with the throat section annulus located close to the nozzle centerline can be constructed. In this case, the exhaust gases issue forth from the throat in an outward direction as shown in Fig. 2e and expand around the shoulder of the central plug. The nozzle wall contour in the form of a shroud would turn the expanding exhaust gases into a nearly axial direction. This type of nozzle is denoted the *Expansion-Deflection* or *E-D* type, and its essential features are discussed in (38).

The self-adjustment of flow in an E–D type nozzle occurs because the pressure at the base of the central plug limits the amount of expansion of the exhaust gases around the shoulder at the throat. Hence a certain amount of compressive turning takes place along the nozzle wall in a manner similar to that occurring in a plug nozzle. Even though the pressure at the base of the central plug cannot be directly related to the ambient pressure, it was found to produce sufficient self-adjustment of the flow during low pressure ratio operation. Schlieren and tuft photographs of flow in an E-D nozzle are reproduced from (38) and presented here in Figs. 5a and 5b. The adjustment of flow at low pressure ratios in an E-D nozzle causes an annular flow attached to the nozzle walls. Hence, the nature of flow in the central region cannot be deciphered from the schlieren photograph. The accompanying tuft photograph shows the main flow

annulus near the wall and eddies, some even in the reverse direction, in the central region. The wall pressure distribution reported in (39) indicates that the flow along the wall of an E-D nozzle, operating at below design pressure ratio, undergoes a gradual compression just as in the case of the plug nozzle.

Considering an annular throat section with radially outward flow, the method of optimizing the wall contour of E-D type nozzle was presented in (39). It was observed that the length of an E-D type nozzle is nearly the same as that of a plug nozzle for equivalent thrust performance.

When the ratio of chamber pressure to ambient pressure is sufficiently high, the thrust performance of an E-D nozzle would be the same as that of a plug nozzle designed for comparable parameters. However, when this operating pressure ratio is low, i.e., at low altitudes, the flow in a plug nozzle adjusts itself to the pressure at the cowl-lip, whereas in an E-D nozzle the flow adjusts itself to the pressure occurring behind the central plug. If the secondary effects caused by flight velocity of the missile are ignored, it can be said that the plug nozzle flow adjusts itself to the ambient pressure. In the case of an E-D nozzle, however, the pressure at the base of the central plug can be lower than the ambient because of the ejector action of the surrounding supersonic stream. Since the flow in an E-D nozzle adjusts itself to a lower pressure, the compression on the nozzle wall would be retarded to some extent compared to a plug nozzle. Thus, under similar subdesign conditions, an E-D nozzle may show lower thrust performance than a plug type nozzle. It appears feasible that a certain amount of bleed could spoil the ejector action in an E-D nozzle so as to bring the pressure behind the central base up to the ambient. Only by such means can the performance of an E-D nozzle be brought up to that of an all external plug nozzle at the subdesign pressure ratios. Since the E-D type nozzle is built around a compact combustion chamber, it may present certain advantages regarding weight and cooling requirements, the consideration of which is beyond the scope of the present discussions. If nozzles of very high area ratios of the order of 100 and above are required for rocket engines operating in space, the E-D type nozzle may be chosen in view of the compact combustion chamber and reduced length.

Concluding Remarks

In retrospect, the subject of this review has been limited to different types of nozzles and nozzle contours with a view toward improving the nozzle thrust performance. The rocket nozzle, however, must always be considered as a part of the total system, which sometimes leads to a set of confining restrictions overweighing the problem of thrust optimization. In order to provide the system design engineer with a greater choice of nozzle parameters, a large variety of novel nozzle configurations, such as the toroidal, horizontal flow, and reverse flow, are currently being studied by several rocket engine manufacturers. A problem that in the writer's knowledge has not been approached is that of thrust optimization including irreversibility in the nozzle flow.

In addition to providing forward thrust, the propulsion nozzle may be called on to provide side forces for vehicle guidance. These side forces may come either from jet vanes, nozzle rotation, or secondary fluid injection. The gas dynamic design of such nozzles would depend upon a new set of performance parameters in addition to optimization of thrust. These additional features of nozzle performance might be the decisive factors in the choice of the type of nozzle and its contour.

References

1 Seifert, H. S. and Crum, J., "Thrust Coefficients and Expansion Ratio Tables," The Ramo-Wooldridge Corp., Los Angeles, Calif., February 1956.

2 Shapiro, A. H., *The Dynamics and Thermodynamics of Compressible Fluid Flow*, Vol. 1, The Ronald Press Co., New York, 1953.

3 Clippinger, R. F., "Supersonic Axially Symmetric Nozzles," *Ballistics Research Lab., Rep. No. 794*, Aberdeen Proving Grounds, Aberdeen, Md., December 1951.

4 Foelsch, K., "The Analytical Design of an Axially Symmetric de Laval Nozzle for a Parallel and Uniform Jet," *J. Aeronaut. Sci.*, vol. 16, March 1949, pp. 161–166, 188.

5 Malina, F. J., "Characteristics of the Rocket Motor Based on the Theory of Perfect Gases," *J. Franklin Inst.*, vol. 230, 1940, pp. 433–454.

6 Tsien, H. S. (ed.), *Jet Propulsion*, A reference text prepared by Staff of GALCIT and JPL, 1946.

7 Landsbaum, E. M., "Thrust of a Conical Nozzle," ARS JOURNAL, vol. 29, no. 3, March 1959, pp. 212–213.

8 Rao, G. V. R., "Evaluation of Conical Nozzle Thrust Coefficient," ARS JOURNAL, vol. 29, no. 8, August 1959, pp. 606–607.

9 Sinyarev, G. B. and Doborovolskii, M. V., *Zhidkostne Raketne Dvigateli*, Moscow, 1957.

10 Dillaway, R. B., "A Philosophy for Improved Rocket Nozzle Design," JET PROPULSION, vol. 27, no. 10, October 1957, pp. 1088–1093.

11 Overall, R. E., "An Experimental Conclusion of Contoured and Conical Nozzles," presented at ARS Solid Propellant Rocket Research Conf., Princeton, N. J., Jan. 28–29, 1960 (*ARS preprint no. 1044–60*).

12 Landsbaum, E. M., "Contour Nozzles," ARS JOURNAL, vol. 30, no. 3, March 1960, pp. 244–250.

13 Demuth, O. J. and Ditore, M. J., "Graphical Methods for Selection of Nozzle Contours," presented at ARS Solid Propellant Rocket Research Conf., Princeton, N. J., Jan. 28–29, 1960 (*ARS preprint no. 1046–60*).

14 Farley, J. M. and Campbell, C. E., "Performance of Several Method of Characteristics Exhaust Nozzles," *NASA TN-203*, October 1960.

15 Ahlberg, J. H., Hamilton, S., Migdal, D. and Nilson, E. N., "Truncated Perfect Nozzles in Optimum Nozzle Design," ARS JOURNAL, vol. 31, no. 5, May 1961, pp. 614–620.

16 Guderley, G. and Hantsch, E., "Beste Formen für Achsensymmetrische Uberschallschubdrisen," *Zeits. für Flugwissen-schaften*, vol. 3, September 1955.

17 Rao, G. V. R., "Exhaust Nozzle Contour for Optimum Thrust," JET PROPULSION, vol. 28, no. 6, June 1958.

18 Guderley, G., "On Rao's Method for the Computation of Exhaust Nozzles," *Zeits. für Flugwissenschaften*, December 1959.

19 Rao, G. V. R., "Optimum Performance of Contoured Nozzles," *Proc.* Liquid Propellant Information Agency, *JANAF*, vol. 1, 1959 (unclassified).

20 Guentert, E. C. and Neumann, H. E., "Design of Axisymmetric Exhaust Nozzles by Method of Characteristics Incorporating a Variable Isentropic Exponent," *NASA TR R-53*, 1959.

21 Rao, G. V. R., "Contoured Rocket Nozzles," *Proc.* 9th Internatl. Astro. Fed. Congress, Amsterdam, 1958.

22 Rao, G. V. R., "Approximation of Optimum Thrust Nozzle Contour," ARS JOURNAL, vol. 30, no. 6, June 1960, p. 561.

23 Knuth, E. L., "Optimum Contours for Propulsion Nozzles," ARS JOURNAL, vol. 30, no. 10, October 1960, pp. 983–984.

24 Kliegel, J. R. and Nickerson, G. R., "Flow of Gas-Particle Mixtures in Axially Symmetric Nozzles," presented at ARS Propellants, Combustion, and Liquid Rockets Conf., Palm Beach, Florida, April 26–28, 1961 (*ARS preprint no. 1713–61*).

25 Green, L., Jr., "Flow Separation in Rocket Nozzles," JARS, vol. 23, no. 1, Jan.-Feb. 1953, pp. 34–35.

26 Foster, C. R. and Cowles, F. B., "Experimental Study of Gas-Flow Separation in Overexpanded Exhaust Nozzles for Rocket Motors," *CIT-JPL Progress Rep. no. 4–103*, May 1949.

27 Summerfield, M., Foster, C. R. and Swan, W. C., "Flow Separation in Overexpanded Supersonic Exhaust Nozzles," JET PROPULSION vol. 24, no. 5, Sept.-Oct. 1954, pp. 319–321.

28 Mager, A., "On the Model of the Free, Shock-Separated Turbulent Boundary Layer," *J. Aeronaut. Sci.*, February 1956.

29 Krase, W. H., "Performance of Plug Nozzles for Turbojet and Rocket Exhausts," presented at ASME Gas Turbine Power Division Meeting, Cincinnati, Ohio, March 1959.

30 Greer, H., "Rapid Method for Plug Nozzle Design," ARS JOURNAL, vol. 31, no. 4, April 1961, pp. 560–561.

31 Beale, W. T. and Povolny, J. H., "Internal Performance of Two-Dimensional Wedge Exhaust Nozzles," *NACA RME56K29b*, Feb. 28, 1957.

32 Krull, H. G. and Beale, W. T., "Effect of Plug Design on Performance Characteristics of Convergent-Plug Exhaust Nozzles," *NACA RME54H05*, October 1954 (declassified September 1958).

33 Berman, K., "The Plug Nozzle—A New Approach to Engine Design," ASTRONAUTICS, vol. 5, no. 4, April 1960.

34 Krull, H. G., Beale, W. T. and Schmiedlin, R. F., "Effect of Several Design Variables on Internal Performance of Convergent-Plug Exhaust Nozzles," *NACA RME56G20*, October 1956 (declassified July 1958).

35 Berman, K. and Crimp, F. W., "The Performance of Plug-Type Rocket Exhaust Nozzles," presented at ARS Solid Propellant Rocket Research Conf., Princeton, N. J., Jan. 28–29, 1960 (*ARS preprint no. 1047–60*).

36 Rao, G. V. R., "Spike Nozzle Contour for Optimum Thrust," *Ballistic Missile and Space Technology*, Vol. 2, C. W. Morrow (ed.), Pergamon Press, New York, 1961.

37 Berman, K. and Neuffer, B., "Plug Nozzle Flexibility," ASTRONAUTICS, vol. 5, no. 9, September 1960.

38 Rao, G. V. R., "The E-D Nozzle," ASTRONAUTICS, September 1960.

39 Rao, G. V. R., "Analysis of a New Concept Rocket Nozzle," *Liquid Rockets and Propellants Progress in Astronautics and Rocketry*, Vol. 2, M. Summerfield (ed.), Academic Press, New York, 1960.

Performance and Evaluation of Satellites Tiros I and Tiros II

S. STERNBERG[1]
A. SCHNAPF[2]

Astro-Electronics Division
Radio Corporation of America
Princeton, N. J.

The design and instrumentation of the first two Tiros satellites and their associated ground-based data-acquisition stations, the performance of the systems after launch, and the subsequent performance evaluation are briefly described. Representative TV photographs of Earth and its cloud cover taken by Tiros are reproduced. The Tiros I system proved the feasibility of TV observation of meteorological phenomena from a satellite as a practical aid to weather research and forecasting. The evaluation program produced data providing the basis for instrumentation design improvements in Tiros II and revealed an unexpected torque due to the Earth's magnetic field, which caused a slow angular drift of the spin-axis vector. From the latter discovery, a magnetic attitude control arrangement used to neutralize the torque or to control it as a means of limited "steering" of the satellite was conceived for Tiros II. The performance of Tiros II corroborated the conclusions drawn from Tiros I and confirmed the operational feasibility of the new devices aboard. Further, both civilian and military weather agencies are making operational use of the Tiros II data.

TIROS I and II, experimental meteorological satellites, were successfully orbited on April 1, 1960, and Nov. 23, 1960, respectively.[3] Tiros I demonstrated the feasibility of using a satellite to observe the Earth's cloud cover by means of a television camera. During its 78 days of successful operation, it transmitted over 22,000 TV pictures to the two Tiros ground-based data acquisition stations and proved the overall design concepts of most of the 40 electronic and mechanical subsystems aboard the satellite. Tiros II, in addition to carrying the same TV subsystem as Tiros I, was instrumented with IR radiation detectors designed by NASA's GSFC to measure the Earth's heat budget and was equipped with a magnetic attitude control system. The TV subsystem, as of early June, has been operating over six and a half months, thus exceeding by far its design lifetime of three months. During this period, Tiros II transmitted 32,000 TV pictures from its two cameras.

Launching of Tiros I

The Tiros I satellite was launched into an almost circular direct orbit at an altitude of 400 n miles at an inclination of 48.3°. The orbit eccentricity has been calculated as 0.004214.

The satellite was spin stabilized, with the spin axis vector presumably fixed in space. Thus, as it orbited around the Earth, the cameras faced either toward or away from the Earth, depending on its location along the orbit. The time of launch was selected so that the sun was "behind" the satellite (within 60° of the optical axis), illuminating the Earth during those portions of the orbit when the cameras were facing it. Due to rotation of the Earth around the sun, this favorable relationship was expected to exist for only about four months out of twelve, and during these four months, due to orbital precession, the cameras were expected to encounter cycles of good, poor, and no-illumination. However, all portions of the global belt—scanned from 50° N to 50° S lat—were covered many times during the scheduled three months of active operation for the system, so that favorable illumination of all points over a succession of orbits was assured.

A successful separation of the satellite from the 248 ABL solid rocket was achieved after a 20-min coast period to overcome any residual burning effects of the third stage. Following separation, the satellite precession dampers performed exceptionally well by removing spin axis wobble and keeping the spin axis fluctuation within $\pm\frac{1}{2}°$. Seven minutes after third stage and payload separation, the Tiros "Yo-Yo" weights were successfully released to despin the payload in $\frac{1}{2}$ sec from the third stage (injection) rotation of 84 rpm to a spin rate of 10 rpm.

During the first orbital pass, 99 min after launch, cloud cover photos were transmitted to the Tiros ground stations at Fort Monmouth and the RCA (Astro-Electronics Div.) plant just east of Princeton. From that time, during the majority of the orbits, pictures and performance data were transmitted to the Kaena Point, Hawaii, Fort Monmouth, and AED ground stations. By the end of June, over 22,000 pictures and many chart-rolls of telemetry data indicating the performance of the many subsystems had been received for study.

Eight weeks after launch, a pair of spin-up rockets was fired to increase the payload spin rate from 9.4 to 12.85 rpm. Five months after launch, the second pair of spin-up rockets was fired successfully to increase the satellite's spin rate from 11.7 to 13.5 rpm.

Design of the Tiros I System

A top view of the Tiros I satellite, with its "top hat" removed to show the components within, is shown in Fig. 1.

Presented at the ARS 15th Annual Meeting, Washington, D. C., Dec. 5–8, 1960; revision received Sept. 25, 1961.

[1] Chief Engineer. Fellow Member ARS.

[2] Manager, Project Tiros. Member ARS.

[3] The Tiros I project was performed under the sponsorship originally of ARPA and later of NASA and under the technical direction of the U. S. Army Signal Research and Development Laboratory. (The Tiros I satellite and the ground-based Command and Data Acquisition System were reviewed in great detail at the ARS west coast meeting in May 1960, and in articles published in ASTRONAUTICS in the June 1960 issue.) The Tiros II project was under the sponsorship and technical direction of NASA.

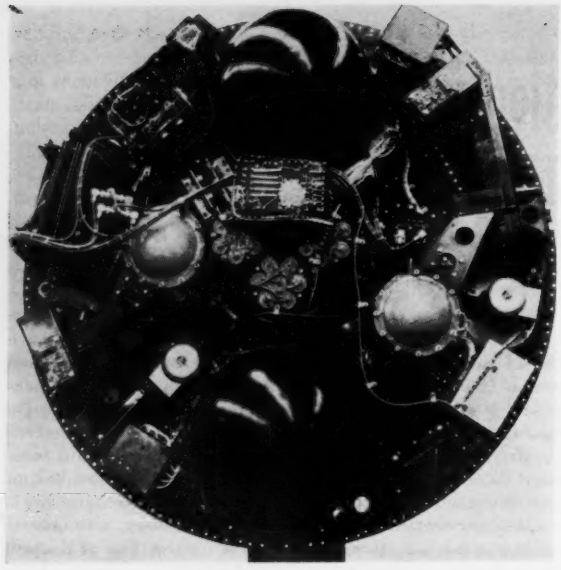

Fig. 1 The satellite baseplate of Tiros I, showing major components

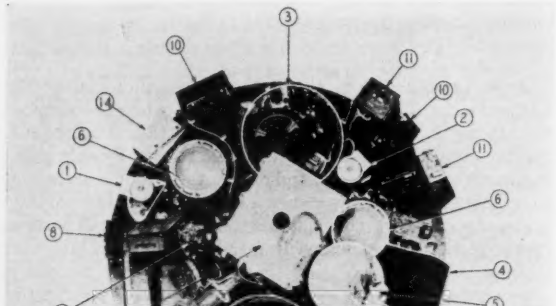

Fig. 2 The satellite baseplate of Tiros II

1. Wide-Angle TV camera
2. Narrow-Angle TV camera
3. Television tape recorders
4. Infrared system, 5-channel radiometer
5. Infrared system, electronics
6. Electronic clocks for timing sequence of operations
7. Relays for magnetic stabilization system controlling satellite's attitude
8. Control box for electronic systems
9. Infrared horizon scanner
10. Electronic circuits for cameras
11. Electronic circuits for TV tape recorders
12. Telemetry switches
13. Antenna diplexer (covering storage batteries)
14. Automatic signal generator
15. Fuse board and current regulator

For comparison, a similar view of the newer Tiros II satellite is shown in Fig. 2. The satellite is approximately 42-in. diam and $22\frac{1}{2}$ in. high. More than 9200 solar cells for the power supply are mounted over most of the top surface and well down the sides on 18 panels that offer a flat structural mounting. A receiving antenna projects from the top, and the four elements of the transmitting antenna extend from the bottom surface. The wide-angle camera lens may be seen projecting below the baseplate.

The satellite contained two independent TV camera chains identical except for their optical systems. One is known as the wide-angle camera chain, which takes a picture covering about 700 miles on a side when the satellite is looking straight down; the other is the narrow-angle camera chain, which covers an area of about 70 miles on a side. The output of each camera chain could be transmitted directly to an Earth-based ground station as it is taken, or the camera video output could be stored on tape when the satellite was out of range of a ground station for later transmission to the ground. Operation of the camera chains was commanded from the ground for functioning either under the direct control of the ground station or at a remote location by the satellite contained function-control equipment.

The major satellite components, as they were arranged on the baseplate, are shown in Fig. 3. Each TV camera chain has its own TV camera, video tape recorder, TV transmitter, command receiver, and function-control equipment. A common power supply includes the solar cells, the storage batteries, and various voltage regulators and converters.

Some forty parameters relating to the satellite's well-being and operation were telemetered through two redundant communication channels, slightly displaced in frequency at 108mc. This data was sent periodically through the satellite's beacon transmitters, which were used at other times to radiate a tracking signal.

A horizon detector, using an infrared sensor, was designed to develop data on the attitude of the satellite's spin axis, which also was transmitted over the beacon transmitters (see Fig. 4). A set of nine solar cell, "sun-angle" sensors equally spaced around the periphery was included to indicate the angle on the satellite baseplate between the TV camera radius vector and that of the sun direction for each picture taken. This information was sent over the TV transmitters. From this data, the intersection of the optical axis with the Earth and its geographical orientation could be determined for each picture. Neither of these subsystems operated completely successfully.

Three devices for control of the satellite dynamics were carried in the payload. The first is a precession damper which damped out "wobble" due to precession or nutation within 60 sec after separation of the satellite from the third stage of the launching rocket. The second is a momentum type despin mechanism called a *Yo-Yo*. Despin was required because the combination of the third-stage rocket and the satellite was spun up to approximately 84 rpm to stabilize the trajectory during the final coast period. However, to avoid smearing the pictures taken by the satellite, its spin stabilization rate had been set at 9 to 12 rpm. A set of weights at the ends of cables, wound around the satellite during the launch phase, was released, unwound, and jettisoned shortly after separation; the resulting energy loss reduced the spin rate to its proper orbital value. The third mechanism was built around spinup rocket motors, which were installed at the baseplate periphery to provide a means of increasing the spin rate after magnetic drag had slowed it below the value for proper stabilization. These rockets were controlled from the ground.

The basic Tiros ground station, as distinguished from other stations in the Tiros ground complex, is called a Command and Data Acquisition Station. The CDA station performs two primary functions: it commands or programs the satellite picture taking, and it receives and processes the picture-taking data from the satellite. By locating one such station in Hawaii, and another at Fort Monmouth, N. J. (for the Tiros I system), radiocommunication contact of 6 to 14 min for all but three or four orbits each day was provided. The backup and evaluation CDA station, located at the

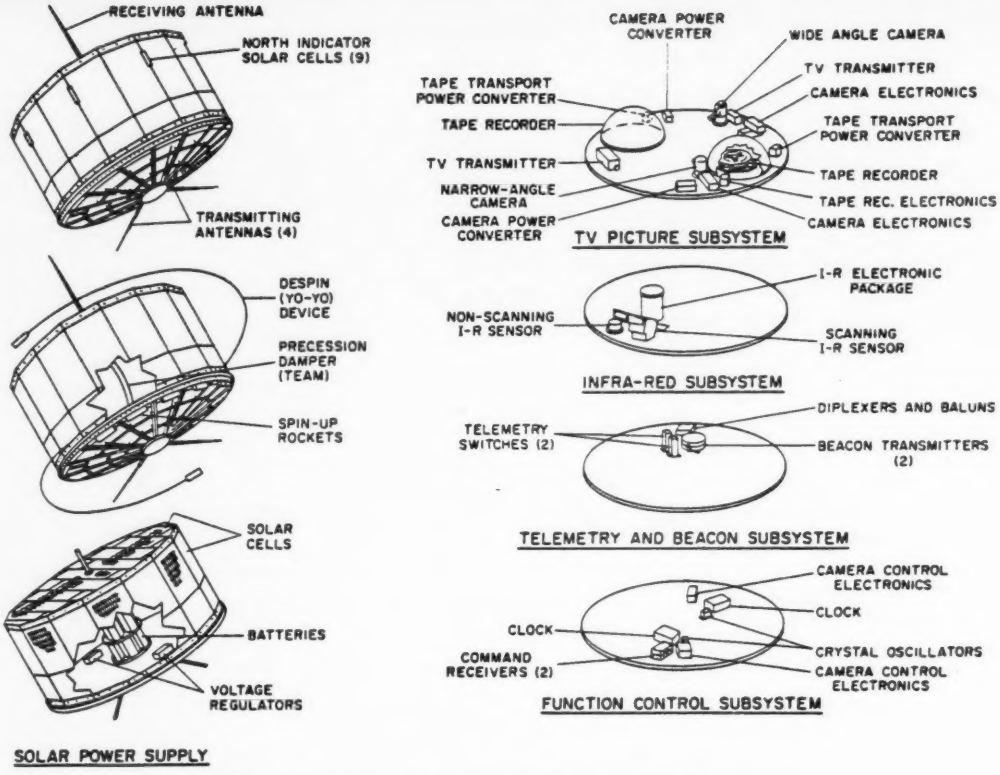

Fig. 3 Arrangement of components on the satellite baseplate

Astro-Electronics Division of RCA, was in operation for two weeks after launch.

These stations also have provisions for receiving and processing both the sun angle, or North indication, information and the telemetry data. Video data is recorded on tape and presented as a display on a TV monitor, from which it is photographed. The satellite is tracked by stations of the U. S. Minitrack Network, which also receive and process the attitude data imposed on the beacon transmitter carrier.

Programming for the satellite is determined by the NASA Goddard Space Flight Center in Washington, D. C. The pertinent information is sent to the cognizant CDA station, where it is set up on the station programming equipment prior to satellite contact. This includes instructions for the area to be photographed, the cameras to be used and the order of their use, and setting of the satellite clocks that time its remote operation. When the satellite comes within communications range, the program is sent automatically at high speed to allow time for receiving stored picture data as well as direct pictures when desired.

Post-Launch Operation of the Tiros I Data Acquisition System

The Tiros I satellite system required an extensive ground complex for satellite control, data recovery, and data analysis. The satellite was tracked by the Minitrack system, a network of radio-interferometer stations originally established for the IGY Vanguard program and located principally on the American continents. The network was expanded and improved (and is now operated by NASA) for tracking and data recovery on all of the scientific space projects of the United States. Tracking data was fed by teletype (both radio links and hard lines) to the Space Computing Center in Washington, via the NASA Space Operations Control Center. The Computing Center established or revised orbit parameters, based on Minitrack data and checked by independent observations from the Smithsonian Astrophysical Laboratory and various military tracking facilities. The Computing Center also analyzed attitude data from the horizon scanner and from the photo interpretation groups to permit predictions of the areas where photography would be possible. It incorporated both types of data in weekly predictions of satellite acquisition data for ground stations and of favorable photographic intervals. This information was transmitted to the Meteorological Satellite Section of the U. S. Weather Bureau and to the Tiros I Technical Control Center at the

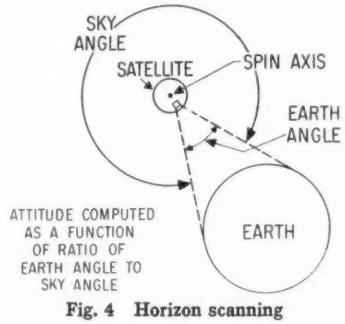

Fig. 4 Horizon scanning

NASA Goddard Space Flight Center. Meteorologists reviewed the data for selection of the intervals where pictures should actually be taken and prepared recommended operating programs. The Technical Control Center reviewed the satellite power supply condition and ground station opera-

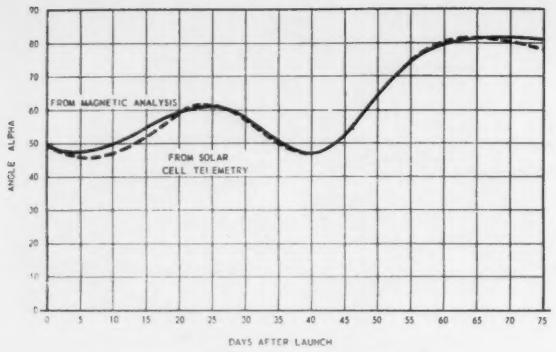

Fig. 5 Angle alpha vs. days after launch

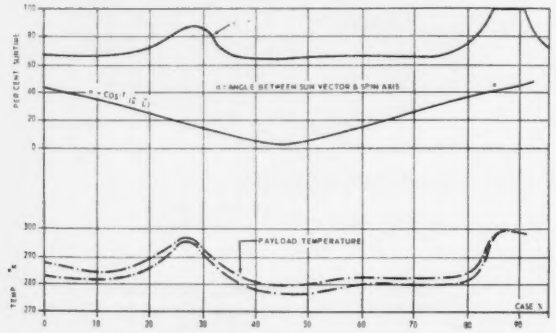

Fig. 6 Predicted satellite temperatures for an unperturbed orbit as a function of time after launch

tional readiness and prepared final operating instructions for the principal ground stations. The instructions were transmitted by teletype to Space Operations Control, where they were routed by teletype to the various stations concerned. The Computing Center simultaneously prepared individual acquisition messages for all ground stations and condensed data for picture orientation in the time intervals actually selected.

The CDA stations, on instructions from Tiros I Technical Control, transmitted the operating commands to the satellite and received and recorded the pictures, telemetry data, and attitude information from the satellite. Pictures were recorded directly on film and simultaneously on magnetic tape. The directly recorded film was mailed to the U. S. Naval Photo Interpretation Center at Suitland, Md., for development and subsequent processing. The magnetic tapes were played back immediately after the pass to provide pictures for local interpretation. Two tape recordings were made, and, after verification that good pictures had been obtained and that both tapes contained good data, the secondary tape was erased for reuse, and the primary tape was used for the production of enhanced quality pictures. The tape finally went to the Naval Photo Interpretation Center along with the enhanced pictures for experimentation with photo interpretation techniques.

Meteorologists stationed at the local CDA stations performed rapid meteorological analyses of the secondary pictures and transmitted weather reports based on these analyses to the U. S. Weather Bureau's National Meteorological Center at Suitland, Md. They also made crude measurements on the pictures to assist in the rapid determination of attitude and transmitted these data to the Computing Center.

Meanwhile, the ground station personnel read telemetry records, transmitted reports to Tiros I Technical Control and horizon scanner attitude data to the Computing Center, and issued a "pass success" report, noting any anomalies in satellite or ground station performance.

In addition to the CDA stations, four stations were equipped to record additional horizon scanner attitude data—three of the Minitrack stations and the Atlantic Missile Range station on Ascension Island.

Tiros I Performance

Tiros I was intended to be an exploratory meteorological satellite. It was expected to determine the feasibility of using TV sensors from satellites to photograph the Earth's cloud cover for use in weather analysis as well as to test its design concepts. From the very first picture acquired on April 1 (orbit no. 1) the Tiros satellite system demonstrated the capability of television picture taking techniques that can be used as a means of presenting a very large amount of weather data over a large part of the Earth in a very short time—particularly the observation of cloud patterns that are not readily observed by conventional weather stations. Over 22,000 pictures were acquired from Tiros I between April and June of 1960; only a portion have yet been given a comprehensive research analysis.

TV Cameras

The quality of the pictures from the TV cameras was excellent, exceeding that obtained during evaluation tests. These cameras were optimized for photographing cloud cover rather than land areas, e.g., the dynamic range, spectral response, filters. Change in electrical or optical focus was not noticed on any of the pictures evaluated. From measurements of the aspect ratio it was seen that, during the first several hundred orbits, the total aspect ratio remained completely within the design specifications. A comparison of the results and the earlier estimates of the TV signal levels shows good correlation between measured Tiros radiation pattern and the received signal levels.

Telemetry

The Tiros I telemetry subsystem was designed to be simple and reliable and to give an overall accuracy of ±5% of full scale on each side of the center of a direct writing pen recorder chart. Transmission of a series of telemetered data was triggered automatically each time the satellite was interrogated. The 39 telemetered parameters were transmitted and recorded in about 30 sec. As each telemetry cycle was recorded, a transparent "standard curve" overlay chart was laid over the recorder strip chart to determine any extreme or unusual deviations. These quantitative values, plus information on any unusual operating conditions, were teletyped to the NASA Technical Control Center.

The Tiros I telemetry records show an accuracy close to ±5% for most data. In general the communications system performed very well.

Electrical Power Subsystem

Prior to the Tiros I launching, the energy available to the instrumentation was calculated for each day of the initial three months of satellite life. The equations employed to perform these calculations required use of the time variation of the angle alpha (angle between the sun vector and the satellite spin axis) and the solar cell temperatures throughout the period of interest. These quantities had been calculated for a specific launch time of April 1 and were based on the spin axis remaining fixed in inertial space upon achieving orbit.

A one-hour delay that occurred in launch time invalidated these calculations. Furthermore, revised calculations could not be initiated because of the lack of accurate attitude data. A permissible programming load range was determined on the basis of early telemetered solar cell temperatures and esti-

mates of the angle alpha. It restricted the total load requirements to the range between 23,000 and 30,000 w-min/day or 16.0 to 20.8 average watts.

About two months after launch, calculations were carried out which derived the alpha angle variation with time, based on the interaction of the Earth's magnetic field and the magnetic dipole characterizing the Tiros satellite. The alpha angle derived from solar cell telemetry compared closely with these calculations.

Because there was a lack of data concerning variations of the angle alpha, the solar cell telemetered voltage and temperature were employed to determine alpha. Thus, alpha was not used as a means to find a result but was calculated from the telemetered data. Fig. 5 is a plot of the angle alpha for the first 75 days after launch—the greater part of the operational life of Tiros I. The alpha values shown are average values of 6 to 16 telemetered data points each day. Throughout the 75-day period, the alpha variation calculated from solar cell telemetry differs by no more than 3 to 5° from that predicted by the magnetic-dipole analysis.

In general, the total battery voltages remained in a region of 26 to 31 v, which was the design range. A maximum measurement error of 1.3 v could have occurred, but this was masked by the tolerance in battery voltage.

Horizon Scanner

The attitude indicator subsystem of the Tiros I satellite was built around an infrared horizon scanner unit, and it delivered a pair of spaced pulses indicating the duration of the scan from horizon to horizon of the Earth. Some of the characteristics of this subsystem proved to be unsuitable for its intended operation, and it was not possible to use its returned data for satellite attitude measurements. Analysis of the performance of the subsystem showed that: 1) the actual field of the horizon scanner (nominally one degree square) was too large, with insufficiently sharp boundaries, to permit reliable triggering at grazing incidence with the horizon; and 2) the spectral response was such as to permit transitions from Earth to clouds to trigger the sensor. Since the recovery time of the associated electronics ranged between 300 and 500 millisec, some spurious triggers blocked transmission of succeeding valid pulses.

The wide spectral response caused the sensor to be vulnerable to spurious triggers from reflected solar radiation and changes in radiation intensity as the sensor swept the Earth. The sensor field of view was too large and too "fuzzy" to cause a rapid enough change in energy to trigger the electronics for angles of attack of less than 30°.

Thermal Design

The approach to the temperature control problem for Tiros I comprised three main areas: 1) analysis of the heat flow problem; 2) development of suitable surfaces and surface coatings for application to the satellite; and 3) experimental verification of the thermal design.

When the constraints on the thermal design were established, the only significant parameters available for thermal control were: 1) the surface radiative properties; 2) the hour of launch; and 3) the degree of thermal communication among the mass elements of the satellite.

The temperature time distributions for Tiros I in orbit as obtained from the telemetry data indicated excellent agreement with the predicted thermal responses of the eight temperature sensors (thermistors), four of which were located on the baseplate and two each on the interior surfaces of the top and side skins. Compensation for the known temperature gradient between the baseplate and the average component temperature was required to obtain an exact fit between the telemetered data and the temperature prediction curves, since they referred to different thermal elements.

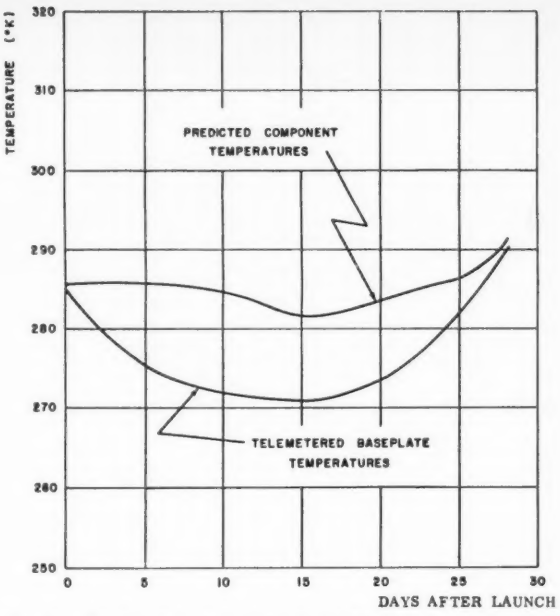

Fig. 7a Predicted and measured satellite temperatures as a function of time after launch

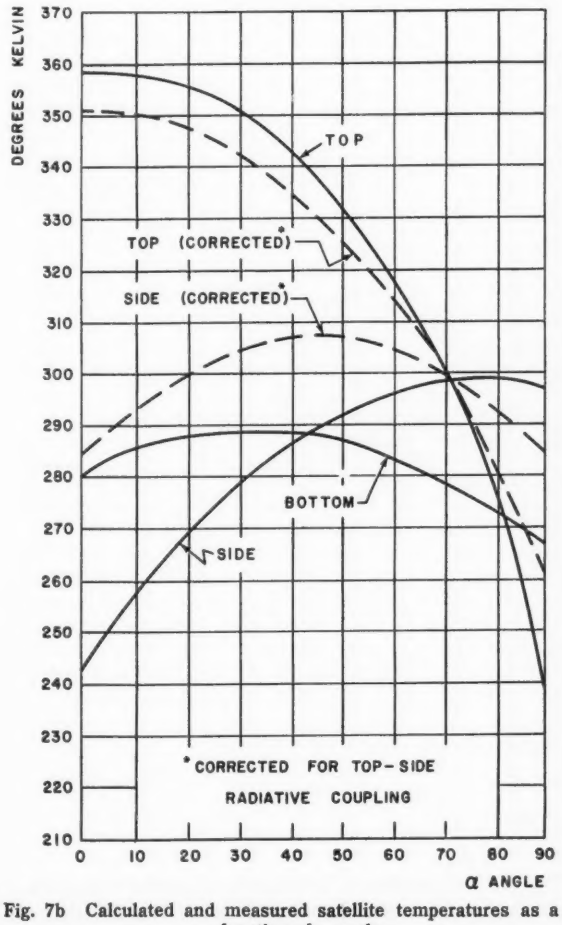

Fig. 7b Calculated and measured satellite temperatures as a function of α angle

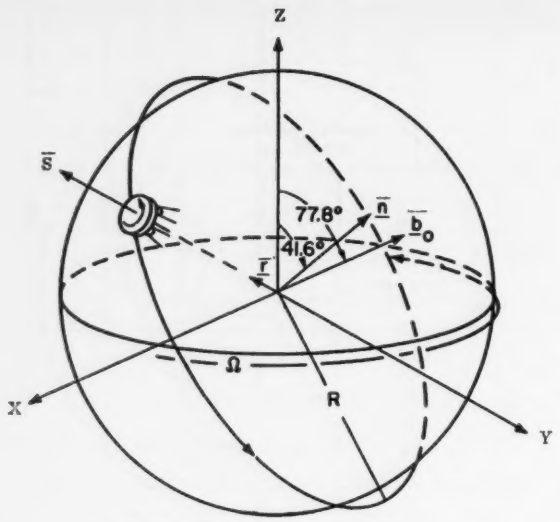

Fig. 8 Tiros I space coordinates

It was noted with some consternation in the first few days after launch that the satellite temperatures were not following the predicted pattern (shown in the lower curves of Fig. 6). This prediction was based on the evolution of alpha angle for the case of an unperturbed orbit. A plot of the alpha angle vs. time curve (shown in Fig. 5), using the temperatures obtained from Tiros I telemetry data (shown in Fig. 7b), was compared with the pattern of Fig. 6; this indicated that the spin axis was far from remaining stationary in inertial space. The situation soon was confirmed from reduced pictorial data obtained from the TV subsystem. The temperature data, however, first indicated the precessing spin axis and its resultant angle with the solar flux vector, which was in excellent agreement with that obtained from pictorial data. It thus afforded a basis for predicting the wanderings of the spin axis for the remaining life of Tiros I. Fig. 7a shows the calculated time history of the component temperature, based on the actual spin axis orientation and the telemetered baseplate temperature as received from Tiros I in orbit. Since only average values of the telemetered temperatures need be employed in this comparison, the random errors in the telemetry system and readout are necessarily removed by the averaging process. For the date of launch, the two curves differ by 1°C, whereas the component to baseplate temperature gradient does not reach its maximum 12°C until the tenth day after launch. The influence of initial temperature and thermal inertia would reasonably explain the lack of a temperature gradient on the date of launch. The reduction of the component to baseplate gradient during the 25th to 28th day is also understandable in terms of both the large α angle and Ψ that existed at this time. From the thermal test it was ascertained that a 9°C gradient existed between component and baseplate temperature for the α = zero, Ψ = 1.0 conditions.[4]

Tiros I Performance Evaluation

The performance of the major satellite functional equipments, in general, was excellent. For one period of about 10 hours coincident with a temperature peak, excessive noise in the horizon scanner system caused it to be inoperative. Other than that, variations in performance were either negligible or were previously accounted for by temperature calibrations. No indication of bearing wear or interference by material deposition was noticed in the electromechanical components.

The first significant satellite malfunction observed was in the electronic clock that controlled the remote operation of the narrow-angle camera. This component stopped operating after 22 orbits but started functioning again during the second month (during orbit 573) of the satellite's life and continued to be operative through the third month in orbit. An analysis of this problem led to the hypothesis that a defective wiring connection, rather than a part failure, was the cause. However, the difficulty in pinpointing what happened emphasizes the problem of analysis of the satellite's performance from a remote position.

The performance anomaly relating to the satellite's attitude was both a major annoyance and a potential dividend. The attitude of the satellite changed in a fashion much different and to a greater extent than was anticipated. Great care had been taken to insure that all sources of external torques had been considered before approving a satellite design with no attitude correction system. Five major external torques that could affect the satellite were known. These are differential gravity, magnetic field interaction with eddy current moments, magnetic field interaction with ferromagnetic materials, drag due to air and/or microscopic dust, and solar radiation pressure. The first two and the last could be handled passively in the satellite design with the knowledge available. The magnetic materials problem was more difficult because of the nonlinearity of the system, and the air dust drag problem was almost impossible to combat because of the lack of information about the distribution at the altitudes in question.

The analysis of this problem was hampered by two other factors in component design. One is that the spectral response of the infrared horizon scanner was not optimum, so that the data transmitted was extremely noisy, and the computer program written beforehand was unable to produce consistent determinations of the axis orientation. The second factor is that the lens of the wide-angle camera was chosen primarily to meet a 104° coverage-angle requirement, and some of its distortion characteristics made attitude determination by photo interpretation cumbersome and not too precise. (Methods were later developed for optimum use of both the horizon scanner data and the pictures in making rapid and reasonably good attitude determinations on a day to day basis.)

However, using the information available at the time, a study and analysis of the spin-axis motion led to the discovery of its major causes. The investigation was pursued along the following lines:

The time of injection and the trajectory of the launch vehicle determined that the coordinates of the satellite spin vector on the celestial sphere should have been the following: declination +19.8°, right ascension (RA) + 58.6° (Fig. 8).

After several days of picture taking, it became apparent from analyses of photographs showing the horizon or identifiable landmarks that the direction of the spin vector (and, hence, the camera axes) was not fixed but was moving southward by as much as 3 to 5° per day (Fig. 9). On April 23, an analysis of photographs indicated that the spin axis had reached its southernmost declination, namely, −30°. At this time its RA had increased to +69.0°. Several days later it was determined from photographs that the spin vector was moving northward again and its RA increasing eastward at a greater rate than previously.

Due to a torque exerted on the orbit by the Earth's bulge, the orbit regressed westward around the Equator 4.547° per day (Fig. 8). It is apparent that if the spin vector were to remain fixed in space, the westward motion of the orbit would cause an angle to develop between the orbital plane and the spin axis. Since Tiros I had the shape of a short

[4] Ψ is the fraction of the total orbit time that the satellite is illuminated by the sun.

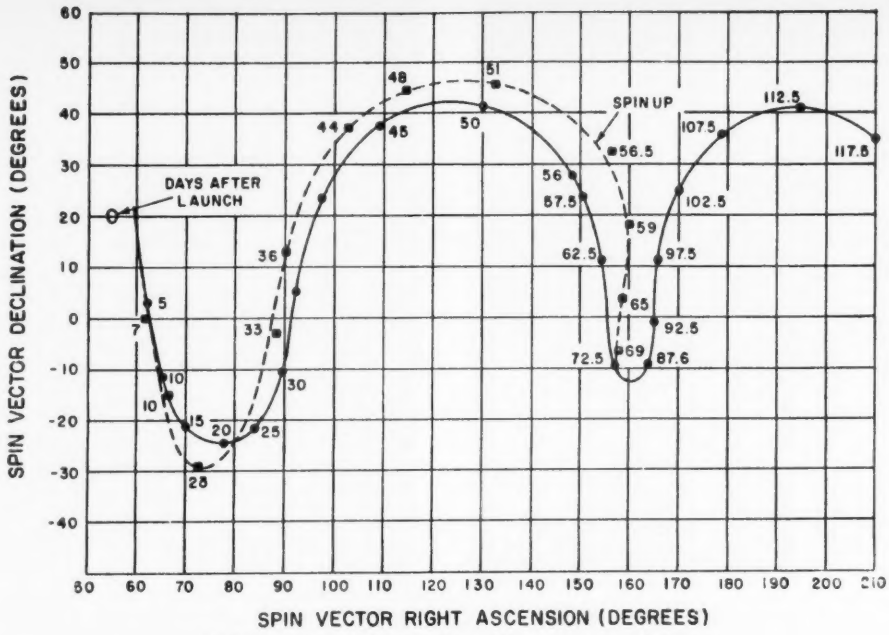
SPIN VECTOR DECLINATION (DEGREES)
SPIN VECTOR RIGHT ASCENSION (DEGREES)
DAYS AFTER LAUNCH
SPIN UP
Solid line: theoretical data. Dotted line: experimental data

Fig. 9 Plot of the angular motion of the Tiros I Spin axis. Observed motion of the Tiros I spin vector based on an analysis of photographs (dashed line) compared with the theoretical motion based on the effects of a magnetic dipole moment along the spin axis and differential gravity (solid line). Declination is +north and −south of the celestial equator; right ascension is + east of the vernal equinox along the celestial equator. Increased stability of both the theoretical and observed motion is seen after spin-up on May 27 (56 days after launch). The last picture with clearly identifiable landmarks was received on June 9 (69 days after launch)

cylinder ($22\frac{1}{2}$-in. high and 42-in. diam), the moment of inertia about its spin axis was larger than the other principal moments of inertia. Hence, when the angle between the orbital plane and the spin axis was greater than zero and less than 90°, a torque due to a differential gravity (similar to that exerted by the sun and moon on the Earth causing its precession) was exerted on the satellite. The nature of this torque was investigated but was rejected as the primary torque causing the observed forced precession, because it would have caused the spin vector to move northward instead of in the observed southerly direction.

The minimum spin vector declination of −30° was reached about April 23. At this time the orbit had regressed 100°, and the unit vector $\bar{n}$, normal to the orbital plane, lay in the same meridional plane as the unit vector $\bar{s}$ along the satellite spin axis. Shortly thereafter, when $\bar{n}$ developed a westerly component with respect to $\bar{s}$ and the satellite spin-axis declination was observed moving northward, the possibility of a magnetic couple being the primary force became apparent, and it became the focal point of investigation.

A computer program was undertaken using the initial injection conditions of Tiros I on April 1, 1152 GMT. The results are plotted together with the observed motion of the spin axis in Fig. 9 and show excellent agreement. In this computer run, a time function for the spin rate was introduced reflecting its observed decrement from 10.0 rpm on April 1 to 9.4 rpm on May 27. (The decay in spin is due to a very small torque caused by eddy currents generated in the spinning satellite by the Earth's magnetic field.) On May 27, a pair of spin-up rockets was fired at 2133 GMT, increasing the spin rate to 12.875 rpm. Greater stability was effected at higher values of the spin rate, and this increased stability can be seen in the plot after spin-up (Fig. 9).

The outcome of this investigation has indicated that the angular motion of the spin axis of Tiros I can be explained quite well by considering two torques: 1) a primary torque caused by the interaction of a magnetic dipole along the satellite spin axis (caused by residual permanent magnetism of ferromagnetic materials or by closed current loops in the instrumentation or by a combination of the two) with the Earth's magnetic field; and 2) a secondary torque caused by differential gravity in the Earth's gravitational field.

About the middle of June 1960, there were intermittent indications that one TV camera chain was remaining in operation beyond the time of its normal shutdown; within several days a loss of power supply capacity became evident.

Symptoms pointed to an inoperative relay in the wide-angle camera system as the probable cause of Tiros' difficulty. The malfunction made it impossible to turn off the transmitter. This apparently drained the batteries and eventually caused the transmitter to burn out. This damage seems to have affected the entire satellite system.

There appeared to be some limited operational capability remaining in the narrow-angle camera system. However, it would be extremely difficult, perhaps frequently impossible, for meteorologists to identify and orient the narrow-angle camera pictures. The satellite's attitude sensors were not working, and there were no longer wide-angle photos, which frequently picked up identifiable geographic landmarks, to assist scientists in orienting narrow-angle cloud cover photos.

The decision to discontinue attempts at interrogating Tiros I was made after orbit 1302 over Fort Monmouth about midnight Wednesday, June 29. The wide-angle camera system and all telemetry had ceased to function. (The 108.00 mc tracking beacon continued to operate.)

Of the 22,952 frames transmitted by Tiros, 17,449 were received at Fort Monmouth, N. J.; 4698 from the narrow-angle camera, and 12,751 from the wide-angle camera. Kaena Point, Hawaii (this station was time shared with the Discoverer Program) received 5503 frames; 1117 from the narrow-angle, and 4386 from the wide-angle camera. Of the total frames received, it is estimated that over 60%

Fig. 10 Tiros cloud-cover photograph no. 1. High background contrast and small nadir angle permitted detection of cirrus clouds (high altitude, ice crystal clouds) and the cirrus bands related to the jet streams, as shown here. It is known that these bands occur about 50 to 75 miles to the warm side of the jet. It is also possible to recognize whether a deck of clouds is stratiform or cumuliform, and thus whether the air in which they occur is stable (smooth) or unstable (turbulent), respectively

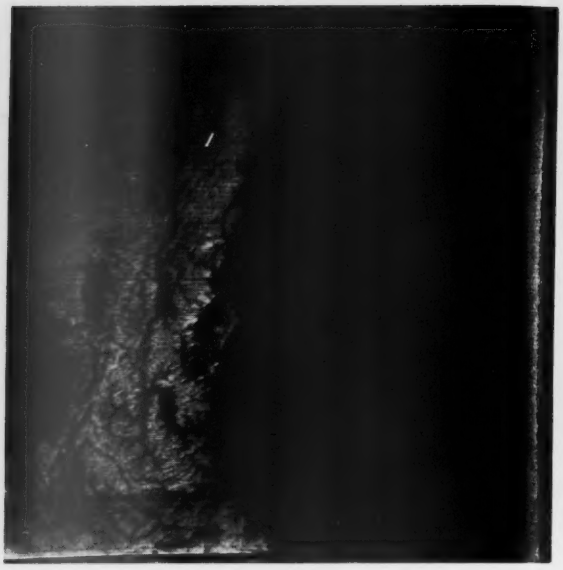

Fig. 11. Tiros cloud-cover photograph no. 2. A view of a deck of stratocumulus clouds west of lower California. The feathery white area is due, at least in part, to snow fields on the U. S. western mountains

Fig. 12 Tiros cloud-cover photograph no. 3. Storm systems, tropical and extratropical (occurring outside of the tropics), are easily recognizable and could, therefore, be located with fair precision. An extensive storm over the mid-Pacific is shown in this photograph

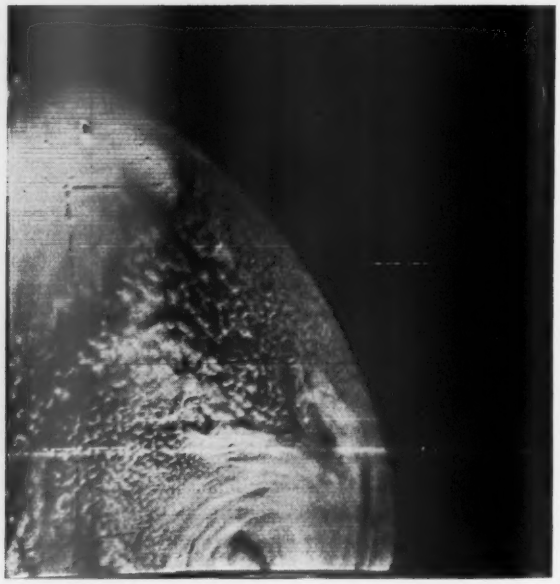

Fig. 13 Tiros cloud-cover photograph no. 4. A storm in the Gulf of Alaska can be seen here, with a cold front emanating from the storm at the lower left, extending westward across the Pacific. The fronts associated with these extratropical cyclones are easily visible on the satellite-produced pictures

represent good quality cloud cover photographs useful to meterological research.

Design of the Tiros II Satellite

Shortly after the successful launch of the Tiros I satellite, RCA was awarded a contract by NASA to modify the duplicate test and backup models built for Tiros I so that they could accommodate an infrared experiment, for which the equipment was supplied by NASA. In addition to the integration of the NASA "scanning" and "non-scanning" infrared devices into the original satellite design, some of the existing hardware was modified so that even better performance would be realized with cloud pictures from Tiros II.

As a result of the observations made on Tiros I spin-axis motion, and analysis and tests in a magnetic test fixture, one of the major additions to Tiros II was the inclusion of an attitude-control device that would control the satellite's spin-axis orientation in the manner to obtain optimum performance from the infrared subsystem, cameras, and power supply.

The attitude control is achieved by developing within the

Fig. 14 Tiros cloud-cover photograph no. 5. This image shows large cumulus clouds over Somaliland. The NE tip of Somaliland is strikingly seen at the bottom center. The Arabian Peninsula is visible to the right across the Red Sea

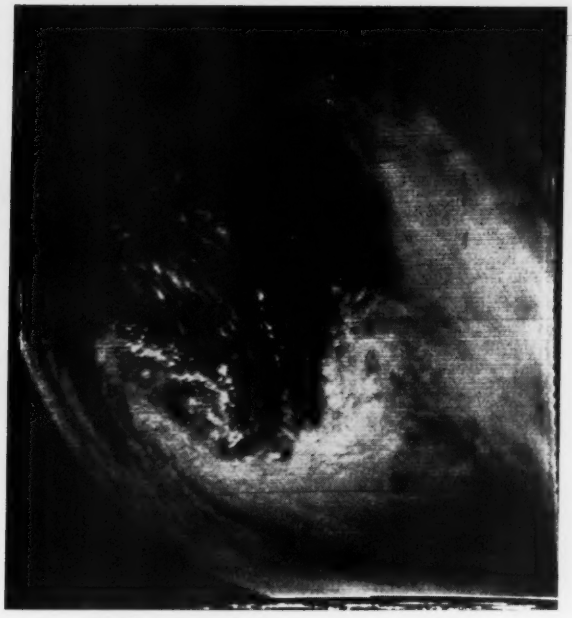

Fig. 15 Tiros cloud-cover photograph no. 6. A storm in the South Indian Ocean is shown here. The fine structure characteristic of storms over ocean areas and the clockwise circulation of South Hemisphere storms are easily seen

satellite by electromagnetic means a torque, or torques, which can be related to the noncontrolled torque in a way to alter the spin-axis motion in the direction desired. This is accomplished by programming (from the ground) various steady currents in a coil that is wrapped around the periphery of the satellite. The magnetic dipole, which is really equivalent to a small bar magnet in the satellite, interacts with the Earth's magnetic field as the satellite orbits, the net result being a torque acting on the spinning body. This torque precesses the spin axis of the satellite.

Five pairs of spin rockets were mounted on the Tiros II base to maintain effective spin rate control.

The NASA infrared experiment incorporated in Tiros II consists basically of two radiometers, a tape recorder, and a transmitter. One scanning radiometer measures five spectral ranges (listed in Table 1). These sensors view a narrow field at a 45° angle to the satellite spin axis. A reference level is obtained by having them alternately look up at 45° to the axis into space.

Table 1 Scanning IR Sensors

IR Channel	Band, μ	Data
1	5.9– 7.0	Radiation from atmospheric water vapor
2	8.0–12.0	Cloud cover
3	0.2– 5.0	Earth's albedo
4	7.5–30.0	Earth's total emission
5	0.6– 0.8	Visible spectrum; for reference

The second radiometer is a non-scanning IR detector that looks over a wide field through the satellite base parallel to the spin axis.
Its two detectors cover the following range:

Black cone	0.2–50 μ	Earth's total reflective and thermal radiation
White cone	5–30 μ	Earth's thermal radiation

The measured energy data is stored on the IR tape recorder, and a composite signal is placed back to the Tiros ground station complex at a 30 to 1 accelerated rate. Since the IR is scanning continuously, only the last 100 min of observation are played back.

The Tiros II program had considerable influence in the modification of the existing CDA ground stations so that they were capable of programming and acquiring the data from the newly added experiments and satellite improved functions.

The Tiros I Kaena Point station was retrofitted by RCA and was then relocated at San Nicolas Island on the Pacific Missile Range. The stations at Ft. Monmouth, N. J., and the backup station at RCA, Astro-Electronics Division at Princeton, N. J., remained part of the Tiros II ground complex.

Tiros II Performance Evaluation

Tiros II overall system performance is currently under evaluation. However, a summary of the satellite's performance can be presented at this time. A detailed report is to be prepared shortly after the Tiros II payload ceases to perform a useful function.

At 6:13 a.m. on Nov. 23, 1960, the satellite was placed into an orbit with an apogee of 453 statute miles and a perigee of 387 statute miles. The orbit eccentricity was calculated as 0.007.

The first cloud pictures returned revealed that the wide-angle camera resolution was lower than that of the equivalent Tiros I camera. Studies to date suggest that the optical system was contaminated with foreign residue. More than 21,000 pictures have been transmitted by this camera, and, even with reduced detail, over 78% have been useful to the meteorologists.

The narrow-angle camera has produced about 11,000 pictures. The quality of these has been better than those of Tiros I.

The passive thermal control design has again proved effective for this longtime operation. The electronic systems

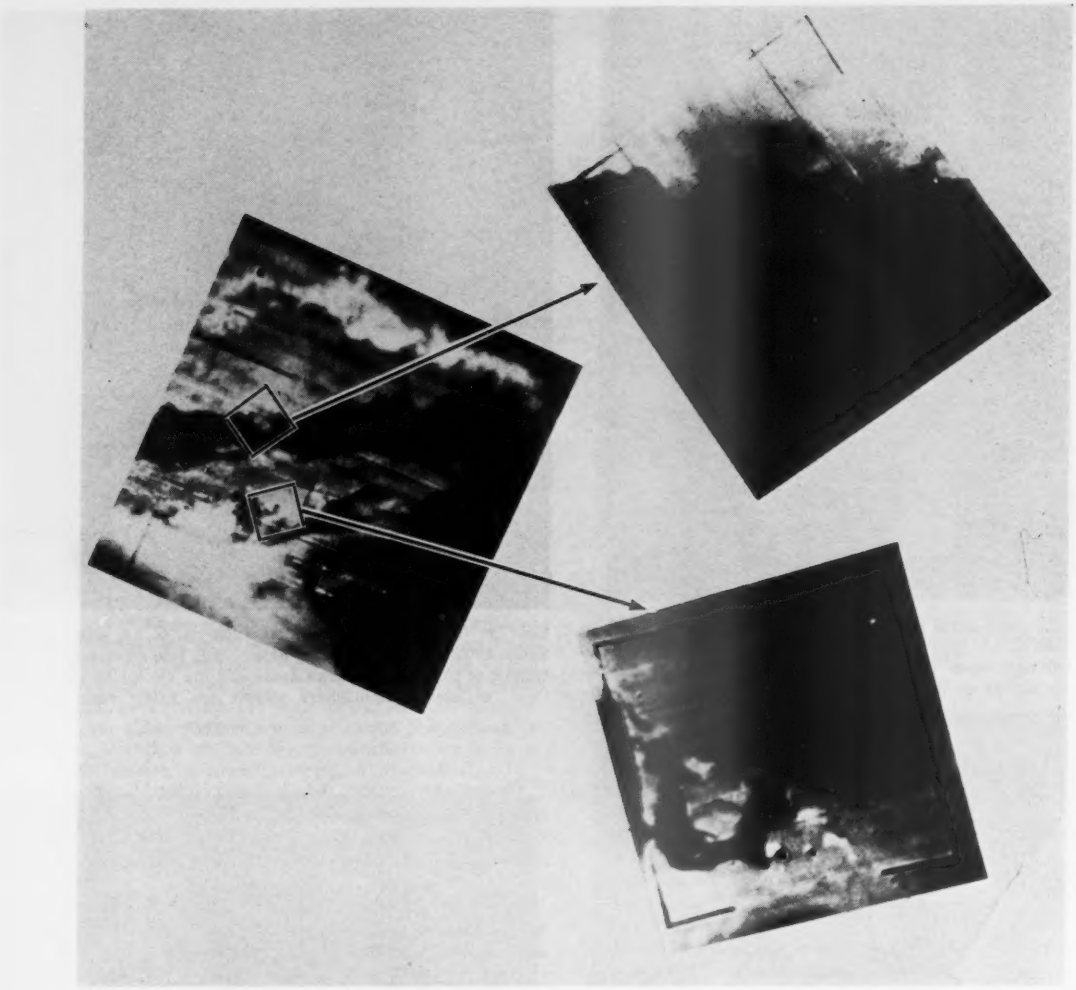

Fig. 16 Tiros cloud-cover photograph no. 7. A wide-angle view in (a) shows the lower California Peninsula. In (b) an inlet of the Bay of Sebastian, Vizcaino, is seen close-up. The view in (c) is of the Island of Tiburon and San Esteban in the Gulf of California

have experienced low rate temperature variations between +8° to 20°C over 190 days (2850 orbits).

The solar cell (and nickel-cadmium battery) power supply has been extremely stable and has provided adequate power and power regulation.

The magnetic attitude control coil has been effectively applied throughout this period to torque the spin axis. The results have been very satisfactory.

In general, all of the electronic subsystems have exhibited good performance. Erratic performance was observed in one remote picture taking electronic clock in January 1961. Remote programming of the wide-angle camera was, therefore, discontinued at that time. However, in April, remote programming was reinstated, and the wide-angle camera chain has worked satisfactorily in all modes since then.

The Tiros II satellite orbit-injection spin rate was 120 rpm. The activation of the Yo-Yo despin system reduced this to 8 rpm. On Nov. 25, 1960, two pairs of spin-up rockets were fired successfully by command from the ground station at RCA, increasing the spin from 8 to 11 rpm and then from 11 to 14 rpm. After six and a half months, the spin decay has caused the satellite to go from 14 to 10 rpm.

From the meteorological standpoint, the continuous cloud cover observations have been of significant operational use to both civilian and military weather services. Over 408 nephanalyses have been made.

The Meteorological Significance of the Tiros Satellites

Early pictures returned from the Tiros I satellite demonstrated that significant weather systems could be recognized and located from weather satellite observations. However, the sheer magnitude of the avalanche of data returned by Tiros has prevented the completion of meteorological research analysis. The task of simply keeping track of the data has overburdened the facilities of all the meteorological agencies involved in the program.

Some time before the Tiros I vehicle was launched, meteorologists decided that the largest initial effort with any pictures received should be the operational use of satellite weather information for synoptic, i.e., overall, weather analysis on any experimental basis. This dictated that attention should be restricted almost exclusively to the images received from the wide-angle camera. The temporary technical difficulties with the narrow-angle cameras that occurred after the launch of Tiros I, did not, therefore, have a significant effect on meteorological evaluation.

The meteorological data provided by means of Tiros confirmed the high degree of organization of cloud patterns of all scales that occurs in the atmosphere (see Figs. 10–17). The limited view of clouds and their distribution prior to Tiros only suggested that this might be true. The fact that such a high degree of organization does exist only increases the usefulness of weather satellites, for distinctive, recognizable patterns naturally allow more information to be more rapidly culled from imagery data.

Large scale cloud and weather systems have been easily recognized. A fascinating discovery by Tiros was that many extratropical as well as tropical cyclones are characterized by a very distinct vortex or spiral-cloud pattern about their centers. An interesting observation is that, in addition to the fact that cyclones can be recognized, each individual storm seems to have some distinctive characteristics in its associated cloud pattern that may mark it apart from other existing cyclones, so that a specific storm can perhaps be recognized even before confirmation of its identity is received from its actual location. This would simplify even more the task of tracking the weather observed on the pictures. A storm was observed off the coast of Madagascar and was easily tracked on the Tiros images for five consecutive days. It has also been found that the weather fronts associated with such midlatitude storms are striking and obvious on the images.

Another milestone in the early life of Tiros I was the observation of a typhoon north of New Zealand. Also of great significance was the inference, on occasion, of the locations of the jet streams over the eastern Mediterranean and other areas from cloud bands observed on the satellite images. As an aid in the analysis of synoptic weather charts, Tiros has proved itself.

The degree to which cloud identification is possible with the wide-angle camera images is a function of the variables in the Tiros images, such as the angle of view, angle of illumination, and cloud-ground contrasts. It is sometimes possible to differentiate between stratiform and cumuliform clouds on the Tiros pictures, although it is usually impossible to deduce the height of the clouds in question. It appears that the very high clouds, the cirrus clouds, normally composed of ice crystals, are not recognized at all unless viewed at small nadir angles and with very sharp cloud-ground contrasts.

It has been found that clouds are not usually seen at all, unless the cloud cover is at least somewhere between scattered and broken. The line that appears to be the edge of a cloud band or deck is actually where the cloud cover decreases to scattered. Some exceptions to this conclusion have been found, again, in regions where a high cloud-ground contrast is viewed at small nadir angles. Incidentally, ice cover in the Gulf of St. Lawrence was seen and mapped from Tiros I images.

The variations in brightness of the cloud images over an area, or the relative brightness of the clouds, appear to be attributable to the variation in the thickness of the clouds. However, the absolute brightness of the cloud images depends on many factors in addition to cloud thickness. It is not unreasonable to assume that these other factors remain constant within limited areas, thus lending credance to the above conclusion.

The narrow-angle pictures have shown that specific cloud types are recognizable, and, like the wide-angle picture, also have shown detail of certain cloud patterns that cannot be synthesized from conventional ground reporting, including some too small for adequate analysis on the wide-angle pictures. In one case, an extensive grayish area on a wide-angle image, thought simply to be ground of higher reflectivity, was very clearly shown on the narrow-angle view to be an area of fair weather cumulus cloud streets.

Fig. 17 Tiros cloud-cover photograph no. 8. This picture was taken by the narrow-angle camera of the Tiros II satellite. The ground detail shown in this view was caused by clear winter skies and melting snow conditions which left forest, river and lake areas clear while the ground remained ice covered. Section lines, rivers and lakes are clearly discernible as white lines or areas. The geographic area covered in this photograph includes the town of Cochrane, Ontario, Canada

The Tiros satellites have contributed meteorological data from areas of the world where conventional weather data is most sparse, such as the oceans. With Tiros II, because of its controllable spin-axis altitude, the value of the information has been enhanced because of the ability to select to some degree the areas of coverage. Operational experience with Tiros I and II and the successful orbiting of Tiros III on July 12, 1961, have now established the great desirability of of weather satellites as a permanent addition to weather observational networks.

Tiros II included a major effort in international cooperation. Analyses of Tiros II cloud picture data have been used by other nations. The outstanding performance of the overall Tiros system in meeting its objectives has placed in the hands of the meteorologist a new and powerful tool for weather observation. The full impact of the Tiros satellites on meteorology cannot yet be evaluated However, the Tiros I, II, and III experimental satellites have established a firm foundation for the future weather satellite that will become part of the national and international meteorological programs.

Acknowledgments

Some of the material in this paper relating to the analysis of the magnetic dipole on the satellite's spin axis first appeared in a paper by W. R. Bandeen and W. P. Manger (Ref. 1). The authors would like to express their thanks for these contributions and for the assistance of L. Krawitz, J. Strother, and J. Owens of the Astro-Electronics Division of RCA.

Reference

1 Bandeen, W. R. and Manger, W. P., "Angular Motion of the Spin Axis of the Tiros I Meteorological Satellite Due to Magnetic and Gravitational Torques," *NASA Tech. Note*, 1960.

Gravitational Torque Impulse on a Stabilized Satellite

PAUL F. HULTQUIST[1]

Ball Brothers Research Corp.
Boulder, Colo.

The angular impulse in pitch and roll imparted to a totally stabilized, solar oriented satellite by gravitational torque over a year's time is computed for a jet controlled satellite with one axis normal to the ecliptic and a transverse axis along the solar vector. Both circular and elliptical orbit cases are considered.

TO ESTIMATE the gas requirements of a gas jet stabilization system for an orbiting solar observatory, it was necessary to calculate the angular impulse imparted to the satellite by various perturbing torques. Although gravitational torques have been investigated previously (1–5),[2] none of these studies gave directly applicable results. The derivation through Eq. 7 follows closely the treatment of Nidey (4).

The particular satellite in question has a lower wheel-like portion spinning at about $^1/_2$ rps to give gyroscopic stability. The upper portion consists of a solar cell panel and instrument housing driven by a servo against the wheel to keep the panel and instruments pointed toward the sun in azimuth. A second servo provides fine control of the instruments over a limited range of angle in elevation. Both servos are controlled by photoelectric sun sensors mounted on the instrument package. Gas jet systems are used to maintain wheel spinrate and to control the attitude of the satellite about the pitch axis (transverse axis normal to the solar vector) to within the limits of the elevation servo range of travel. In an advanced model it is proposed to control the satellite also about the roll axis (solar vector) to within a small angle. The dead zone in the jet system prevents dissipation of gas in correcting for small cyclic perturbations. Thus in calculating the long term angular impulse, it is possible to average the gravitational torque over one orbit but not over longer periods.

The analysis should also apply to a conventional satellite oriented in a fixed configuration with respect to the ecliptic by means of inertia wheels. The dead zone in the gas system in this case corresponds not to the limits of axis misalignment but rather to the limits of wheel speed which require gas jet dumping to rid the system of accumulated angular impulse. The angular impulse imparted to the yaw axis in this case would also be of interest and could be calculated by the same procedure.

The calculations were made assuming a spherical Earth. However, oblateness was accounted for in the motion of the orbital plane. This approximation should be sufficiently accurate for preliminary design purposes.

Fig. 1 shows the coordinate system. Axes x, y, z form a geocentric ecliptic system with the sun always along the x-axis. Unit vectors in this system are **i**, **j**, **k**. The u, v, w system is a geocentric equatorial system with the u-axis along the equatorial-orbital line of nodes. The x', y', z' system is a rotating geocentric orbital system with the satellite always on the x'-axis. The unit vectors here are **I**, **J**, **K**. Because of stabilization, the principal axes of the satellite coincide closely with the geocentric ecliptic axes. The definitions of Ω, λ, η, i, and e can be determined by referring to Fig. 1.

The torque on the satellite is given by

$$\mathbf{L} = -\int \mathbf{r} \times \left[\frac{gR_e^2\mathbf{R}}{R^3}\right]\rho dV \qquad [1]$$

where

$\mathbf{L}$ = vector torque on the satellite
$\mathbf{r}$ = vector from satellite CM to dV
$\mathbf{R}$ = vector from Earth's center to dV
ρ = density of volume element dV
R_e = radius of Earth
g = acceleration of gravity at Earth's surface

The integration is performed over the volume occupied by the satellite. Now let $\mathbf{R} = \mathbf{R}_c + \mathbf{r}$, where $\mathbf{R}_c$ is the vector from Earth's center to CM. Then

$$\mathbf{L} = -gR_e^2\int R^{-3}(\mathbf{r} \times \mathbf{R}_c)\rho dV \qquad [2]$$

since $\mathbf{r} \times \mathbf{r} = 0$. For a satellite of small size $|\mathbf{r}| \ll |\mathbf{R}| = R$, and

$$R^{-3} = (\mathbf{R}\cdot\mathbf{R})^{-3/2} = R_c^{-3}\left[1 + 2\frac{\mathbf{r}\cdot\mathbf{R}_c}{R_c^2} + \left(\frac{r}{R_c}\right)^2\right]^{-3/2}$$

$$\cong R_c^{-3}\left[1 + \frac{2\mathbf{r}\cdot\mathbf{R}_c}{R_c^2}\right]^{-3/2} \cong R_c^{-3}\left[1 - 3\frac{\mathbf{r}\cdot\mathbf{R}_c}{R_c^2}\right] \qquad [3]$$

Then

$$\mathbf{L} = -\frac{gR_e^2}{R_c^3}\int(\mathbf{r} \times \mathbf{R}_c)\left[1 - 3\frac{\mathbf{r}\cdot\mathbf{R}_c}{R_c^2}\right]\rho\, dV$$

$$= -\frac{gR_e^2}{R_c^3}\mathbf{R}_c \times \int \mathbf{r}\left[1 - \frac{3\mathbf{r}\cdot\mathbf{R}_c}{R_c^2}\right]\rho\, dV$$

$$= -\frac{3gR_e^2}{R_c^5}\mathbf{R}_c \times \int \mathbf{r}(\mathbf{r}\cdot\mathbf{R}_c)\rho\, dV \qquad [4]$$

since $\int \mathbf{r}\,\rho dV = 0$ by definition.
Now $\mathbf{R}_c/R_c$ is a unit vector, namely, **I**. Thus

$$\mathbf{L} = -\frac{3gR_e^2}{R_c^3}\int(\mathbf{I} \times \mathbf{r})(\mathbf{r}\cdot\mathbf{I})\rho\, dV \qquad [5]$$

Received Jan. 23, 1961.

[1] Staff Scientist, Advanced Systems Dept., and Associate Professor (on leave), Department of Applied Mathematics, University of Colorado, Boulder.

[2] Numbers in parentheses indicate References at end of paper.

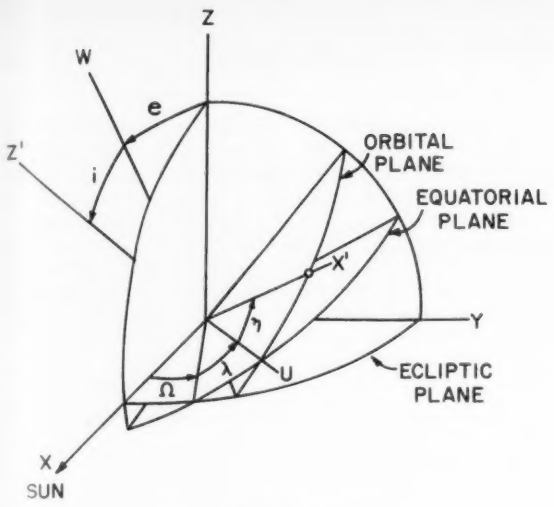

Fig. 1 Coordinate system

Since

$$\mathbf{I} = (\mathbf{I}\cdot\mathbf{i})\,\mathbf{i} + (\mathbf{I}\cdot\mathbf{j})\mathbf{j} + (\mathbf{I}\cdot\mathbf{k})\mathbf{k}$$

and

$$\mathbf{r} = \mathbf{i}x + \mathbf{j}y + \mathbf{k}z$$

the expression $(\mathbf{I}\times\mathbf{r})(\mathbf{r}\cdot\mathbf{I})$ under the integral sign becomes

$$\begin{aligned}&\mathbf{i}\{(\mathbf{I}\cdot\mathbf{j})[(\mathbf{I}\cdot\mathbf{i})xz + (\mathbf{I}\cdot\mathbf{j})yz + (\mathbf{I}\cdot\mathbf{k})z^2] - (\mathbf{I}\cdot\mathbf{k})[(\mathbf{I}\cdot\mathbf{i})xy + (\mathbf{I}\cdot\mathbf{j})y^2 + (\mathbf{I}\cdot\mathbf{k})yz]\} +\\ &\mathbf{j}\{(\mathbf{I}\cdot\mathbf{k})[(\mathbf{I}\cdot\mathbf{i})x^2 + (\mathbf{I}\cdot\mathbf{j})xy + (\mathbf{I}\cdot\mathbf{k})xz] - (\mathbf{I}\cdot\mathbf{i})[(\mathbf{I}\cdot\mathbf{i})xz + (\mathbf{I}\cdot\mathbf{j})yz + (\mathbf{I}\cdot\mathbf{k})z^2]\}\\ &\mathbf{k}\{(\mathbf{I}\cdot\mathbf{i})[(\mathbf{I}\cdot\mathbf{i})xy + (\mathbf{I}\cdot\mathbf{j})y^2 + (\mathbf{I}\cdot\mathbf{k})yz] - (\mathbf{I}\cdot\mathbf{j})[(\mathbf{I}\cdot\mathbf{i})x^2 + (\mathbf{I}\cdot\mathbf{j})xy + (\mathbf{I}\cdot\mathbf{k})xz]\}\end{aligned} \quad [6]$$

Because of the choice of axes, $\mathbf{L}$ simplifies on integration to

$$\mathbf{L} = \frac{3gR_e^2}{R_c^3}\{\mathbf{i}(\mathbf{I}\cdot\mathbf{j})(\mathbf{I}\cdot\mathbf{k})[I_y - I_z] + \mathbf{j}(\mathbf{I}\cdot\mathbf{k})(\mathbf{I}\cdot\mathbf{i})[I_z - I_x] + \mathbf{k}(\mathbf{I}\cdot\mathbf{i})(\mathbf{I}\cdot\mathbf{j})[I_x - I_y]\} \quad [7]$$

where I_x, I_y and I_z are the principal moments of inertia of the satellite.

It is now possible to evaluate the dot products with the aid of the transformation matrix from the x, y, z axes to the x', y', z' axes. The transformation from the x, y, z set to the u, v, w set is given by the matrix $\mathbf{A}$

$$\mathbf{A} = (a_{ij}) \quad [8]$$

where

$$\begin{aligned}a_{11} &= \cos\Omega\cos\lambda - \cos e\sin\Omega\sin\lambda\\ a_{12} &= \sin\Omega\cos\lambda + \cos e\cos\Omega\sin\lambda\\ a_{13} &= \sin e\sin\lambda\\ a_{21} &= -\cos\Omega\sin\lambda - \cos e\sin\Omega\cos\lambda\\ a_{22} &= -\sin\Omega\sin\lambda + \cos e\cos\Omega\cos\lambda\\ a_{23} &= \sin e\cos\lambda\\ a_{31} &= \sin e\sin\Omega\\ a_{32} &= -\sin e\cos\Omega\\ a_{33} &= \cos e\end{aligned}$$

and the transformation from the u, v, w set to the x', y', z' set by the matrix $\mathbf{B}$

$$\mathbf{B} = (b_{ij}) \quad [9]$$

where

$$\begin{aligned}b_{11} &= \cos\eta\\ b_{12} &= \cos i\sin\eta\\ b_{13} &= \sin i\sin\eta\\ b_{21} &= -\sin\eta\\ b_{22} &= \cos i\cos\eta\\ b_{23} &= \sin i\cos\eta\\ b_{31} &= 0\\ b_{32} &= -\sin i\\ b_{33} &= \cos i\end{aligned}$$

Then the entire transformation is given by

$$\mathbf{T} = \mathbf{BA} = \left(\sum_k b_{ik}a_{kj}\right) \quad [10]$$

Finally

$$(\mathbf{I}\cdot\mathbf{j})(\mathbf{I}\cdot\mathbf{k}) = B_1C_1\cos^2\eta + (B_1C_2 + B_2C_1)\sin\eta\cos\eta + B_2C_2\sin^2\eta \quad [11a]$$

$$(\mathbf{I}\cdot\mathbf{k})(\mathbf{I}\cdot\mathbf{i}) = A_1C_1\cos^2\eta + (A_1C_2 + A_2C_1)\sin\eta\cos\eta + A_2C_2\sin^2\eta \quad [11b]$$

$$(\mathbf{I}\cdot\mathbf{i})(\mathbf{I}\cdot\mathbf{j}) = A_1B_1\cos^2\eta + (A_1B_2 + A_2B_1)\sin\eta\cos\eta + A_2B_2\sin^2\eta \quad [11c]$$

where

$$\begin{aligned}A_1 &= \cos\lambda\cos\Omega - \sin\lambda\sin\Omega\cos e\\ A_2 &= \sin\Omega\sin e\sin i - \sin\lambda\cos\Omega\cos i - \cos\lambda\sin\Omega\cos e\cos i\\ B_1 &= \cos\lambda\sin\Omega + \sin\lambda\cos\Omega\cos e\\ B_2 &= -\cos\Omega\sin e\sin i - \sin\lambda\sin\Omega\cos i + \cos\lambda\cos\Omega\cos e\cos i\\ C_1 &= \sin\lambda\sin e\\ C_2 &= \cos e\sin i + \cos\lambda\sin e\cos i\end{aligned}$$

At this point, it is possible to average over one orbit, assuming that the gas jet system does not operate oftener than once in several orbits. Thus, it is reasonably safe to permit cyclic terms to average out. Two cases now arise, one for circular orbits and one for elliptical orbits.

Circular Orbits

In this case, R_c is constant and gR_e^2/R_c^3 may be replaced by ω^2, the square of the orbital angular velocity. The averages of the trigonometric functions are

$$\frac{1}{2\pi}\int_0^{2\pi}\cos^2\eta\,d\eta = \frac{1}{2\pi}\int_0^{2\pi}\sin^2\eta\,d\eta = \frac{1}{2}$$

and

$$\frac{1}{2\pi}\int_0^{2\pi}\sin\eta\cos\eta\,d\eta = 0$$

Thus the average torque over one orbit is

$$\bar{\mathbf{L}} = (3/2)\omega^2[\mathbf{i}(B_1C_1 + B_2C_2)(I_y - I_z) + \mathbf{j}(A_1C_1 + A_2C_2)(I_z - I_x) + \mathbf{k}(A_1B_1 + A_2B_2)(I_x - I_y)] \quad [12]$$

To find the annual angular impulse, it is now necessary to integrate the components of $\bar{\mathbf{L}}$ with respect to the time. Here, however, the cyclic components may not be permitted to average out over the periods of λ and Ω, since the gas jet system will be required to counteract the accumulated angular impulse relatively often per year. Hence, it seems reasonable to integrate the absolute value of each component. Because a certain amount of angular impulse may have been accumulated just before a particular torque component changes sign, the estimates derived from this process will tend to be conservative, i.e., to overestimate the gas requirement.

A numerical calculation for the **i** and **j** components was carried out using $e = 23.45°$, $i = 33.333°$, $\Omega_0 = 0°$ and $\lambda_0 = 0°$. Integration steps of two-day length were used, which was sufficiently accurate for the purpose. $\Delta\Omega$ was taken as twice (360/365.25) deg and $\Delta\lambda$ was calculated to be 12.474 deg per two days by the use of King-Hele's formula (6) for the nodal regression rate

$$\frac{d\lambda}{R_e} = -10.00\left(\frac{R_e}{R_c}\right)^{7/2}\cos i \quad \text{deg/day} \quad [13]$$

The integrals of $|B_1C_1 + B_2C_2|$ and $|A_1C_1 + A_2C_2|$ are about the same, i.e., about 8.4×10^6 sec. Graphs of $B_1C_1 + B_2C_2$ and $A_1C_1 + A_2C_2$ are given in Figs. 2 and 3. The appearance of the graphs suggests that some sensitivity to the starting values of Ω and λ might be expected in the integrals of the absolute values. The graphs also show why numerical integration was chosen: A detailed examination of the integrands to determine the changes in sign for an analytical treatment appeared to be more troublesome than a straight numerical treatment.

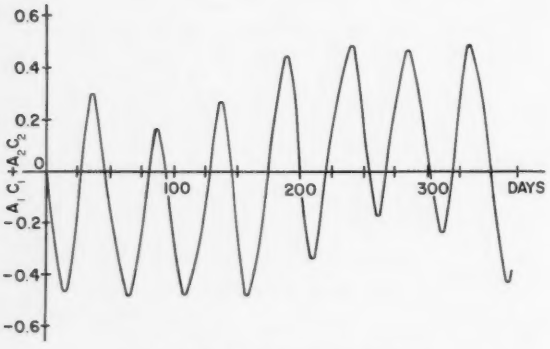

Fig. 2 $A_1C_1 + A_2C_2$ vs. time in days

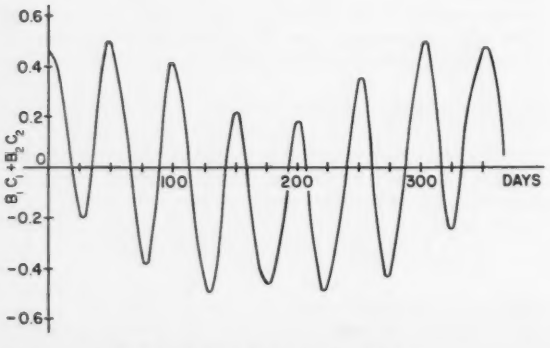

Fig. 3 $B_1C_1 + B_2C_2$ vs. time in days

Elliptical Orbits

Averaging over one elliptical orbit is somewhat more difficult since η does not vary linearly with t as in the circular case. The time average can be written for the **i** component as

$$\frac{1}{T}\int_0^T \frac{(\mathbf{I}\cdot\mathbf{j})(\mathbf{I}\cdot\mathbf{k})}{R_c^3}\,dt = \frac{1}{T}\int_0^{2\pi} \frac{(\mathbf{I}\cdot\mathbf{j})(\mathbf{I}\cdot\mathbf{k})}{R_c^3}\left(\frac{dt}{d\eta}\right)d\eta \quad [14]$$

where T is the period. Now

$$R_c^3 = \frac{a^3(1-\epsilon^2)^3}{[1 + \epsilon\cos(\eta - \eta_p)]^3} \quad [15]$$

where

η_p = angular position of perigee
a = major semiaxis length
ϵ = eccentricity of the orbit

Furthermore, $dt/d\eta$ can be found from conservation of (orbital) angular momentum

$$R_c^2\,\dot{\eta} = \text{const} = C \quad [16]$$

or

$$\dot{\eta} = \frac{C}{R_c^2} \quad [17]$$

Thus

$$\left(\frac{1}{R_c^3}\right)\frac{dt}{d\eta} = \frac{1 + \epsilon\cos(\eta - \eta_p)}{aC(1-\epsilon^2)} \quad [18]$$

and

$$\frac{1}{T}\int_0^T \frac{(\mathbf{I}\cdot\mathbf{j})(\mathbf{I}\cdot\mathbf{k})}{R_c^3}\,dt = \frac{1}{aTC(1-\epsilon^2)}\int_0^{2\pi}(\mathbf{I}\cdot\mathbf{j})(\mathbf{I}\cdot\mathbf{k})[1 + \epsilon\cos(\eta - \eta_p)]d\eta \quad [19]$$

It is not difficult to show that

$$\int_0^{2\pi}\cos^2\eta\cos(\eta - \eta_p)\,d\eta = \int_0^{2\pi}\sin^2\eta\cos(\eta - \eta_p)d\eta = \int_0^{2\pi}\sin\eta\cos\eta\cos(\eta - \eta_p)d\eta = 0$$

since η_p can be considered as a constant over one orbit.

Hence the **i** component average reduces to

$$\bar{L}_x = \frac{3gR_e^2\pi}{aTC(1-\epsilon^2)}(B_1C_1 + B_2C_2) \quad [20]$$

with similar results for the other components. Since

$$C = 2\pi a^2T^{-1}(1-\epsilon^2)^{1/2} \quad [21]$$

Eq. 20 reduces to

$$\bar{L}_x = \frac{3}{2}\frac{gR_e^2}{a^3}(1-\epsilon^2)^{-3/2} \quad [22]$$

Note that as $\epsilon \to 0$, $a \to R_c$, and this expression approaches that of the circular case. Finally

$$\bar{\mathbf{L}} = \frac{3}{2}\frac{gR_e^2}{a^3}(1-\epsilon^2)^{-3/2}\{\mathbf{i}(B_1C_1 + B_2C_2)(I_y - I_z) + \mathbf{j}(A_1C_1 + A_2C_2)(I_z - I_x) + \mathbf{k}(A_1B_1 + A_2B_2)(I_x - I_y)\} \quad [23]$$

To find the total angular impulse counteracted by the gas jet system, it is necessary to integrate the absolute values of the components numerically. In this case, however, η_p varies as well as Ω and λ. Upon selection of the appropriate Δt, the corresponding $\Delta\eta_p$ for the numerical integration can be found from King-Hele's expression (6) for the rate of rotation of the line of apsides

$$\frac{d\eta_p}{dt} = 5.00\left(\frac{R_e}{\bar{R}_c}\right)^{7/2}(5\cos^2 i - 1) \quad \text{deg/day} \quad [24]$$

where $\bar{R}_c$ is the mean R_c. (This mean must also be used in the calculation of $d\Omega/dt$ in Eq. 13 for the elliptical case.)

References

1 Schindler, G. M., "On Satellite Librations," ARS JOURNAL, vol. 29, no. 5, May 1959, pp. 368–370.

2 Sohn, R. L., "Attitude Stabilization by Means of Solar Radiation Pressure," ARS JOURNAL, vol. 29, no. 5, May 1959, pp. 371–373.

3 Roberson, R. E., "Gravitational Torque on a Satellite Vehicle," *J. Franklin Inst.*, vol. 265, January 1958, pp. 13–22.

4 Nidey, R. A., "Gravitational Torque on a Satellite of Arbitrary Shape," ARS JOURNAL, vol. 30, no. 2, February 1960, pp. 203–204.

5 Sonnabend, D., "The Dumbbell Effect ad Rigorum," *Lockheed MSD Publ. 445247*, Sunnyvale, Calif., Feb. 3, 1960.

6 King-Hele, D. G., "The Effect of the Earth's Oblateness on the Orbit of a Near Satellite," *Proc. Royal Society A*, vol. 247, Sept. 9, 1958, pp. 49–72.

Gravity Gradient Determination of the Vertical[1]

ROBERT E. ROBERSON[2]

Consultant in Astronautics
Fullerton, Calif.

The foundations of methods for determining the vertical by differential gravity measurements are examined. Expressions are derived for the output of a differential accelerometer pair, and the use of the output of a triad of such devices is considered. It is shown how the vertical is indicated thereby, and the error behavior of the indication is discussed for pitch and roll orientation modes. An elementary error analysis is included based on the explicit derivation of error terms in the outputs of the accelerometer pairs, from which it is concluded that bias and scale factor errors of 10^{-4} for each pair at the level of 10^{-7} g/m are needed if the attitude indication error is to be of the order of 1 min of arc.

IT IS now well-known that the gradient of any gravitational field within which a space vehicle finds itself exerts a torque on the vehicle tending to align its long axis with the field gradient. But the true role of the effect is as an attitude sensor, since restoring terms thereby appear in the equations of attitude motion which have the same form as those which normally would have been introduced for stability by an independent control system operating on explicitly sensed orientation. When "equivalent sensing" is done in this way by the entire vehicle, orientation is not available as an explicit sensing output that might be desired for various reasons. However, it is possible to construct instruments that are individually sensitive to the gravity gradient effect in the same way. Placed within a vehicle, their outputs may be used for control of the vertical and for obtaining a record of vehicle deviations from the vertical. Both pendulum devices and accelerometer pairs have been suggested for this purpose.

The existing literature on gravity gradient sensing is reviewed in (1)[3] and updated in (2). It is shown there that several schemes for using differential accelerometers should work in principle, and it is implied that these appear more attractive in general than pendulum methods. It is concluded, though, that existing error studies are not adequate for a fair assessment of expected performance and that certain generalizations of existing studies, e.g., to studies of compensation methods, are desirable if one is to consider this class of sensors seriously.

The purpose of this paper is to formulate the analytical principles of differential accelerometer gravity gradient sensors in detail, to discuss alternative mechanization possibilities and describe previous proposals within this unified analytical framework, and to study the nature and magnitudes of the errors that are inherent to this type of instrument. It is

Presented at the ARS 15th Annual Meeting, Washington, D. C., Dec. 5–8, 1960.

[1] This work was supported by the Flight Control Laboratory of Wright Air Development Div. under Contract AF33(616)-6674.

[2] Member ARS.

[3] Numbers in parentheses indicate References at end of paper.

recommended that the reader review pp. 407–413 of (1) as a preliminary to the following presentation.

Analytical Preliminaries

Force on a Proof Mass

Refer to Fig. 1 in which $\mathfrak{X}_i$ is an inertial frame of reference, X_i is a frame fixed in the body of a space vehicle, $\mathbf{R}$ is the vector location of the origin of the latter relative to the origin of the former. Let m be a proof mass within the body, located relative to X_i by the vector $\mathbf{a}$. Analogously, Δm_i is a mass element of the body located at $\boldsymbol{\rho}_i$ relative to X_i. Denote the external gravitational field by $\mathbf{F}(\mathbf{r})$, a point function of position $\mathbf{r}$ relative to the origin of $\mathfrak{X}_i$. Finally, define $\mathbf{F}_c$ as the force of constraint exerted on the proof mass by the vehicle.

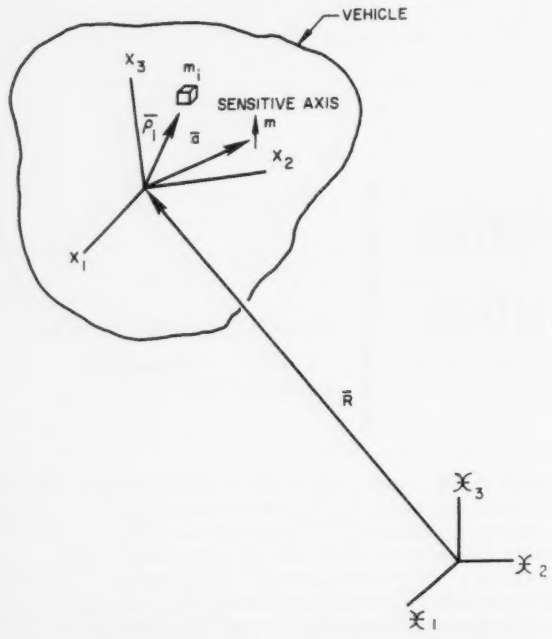

Fig. 1 Basic reference frames and vector relationships

It is desired to find the value of $\mathbf{F}_c$ such that the location of the proof mass remains fixed within the vehicle; i.e., such that $\mathbf{a}$ is constant or undergoes a prescribed motion as seen within the X-system. An accelerometer, specifically a single axis accelerometer, placed at the location of m will be sensitive to the component of $\mathbf{F}_c$ in the direction of the accelerometer sensitive axis, the latter described by a unit vector at the proof mass location.

There is no loss in generality if it is assumed that the origin of X_i coincides with the center of mass of the body (not including the proof mass).[4] In this case it is simple to write the equations for the translatory motion of the main body as

$$\sum_i \Delta m_i(\ddot{\mathbf{R}} + \ddot{\boldsymbol{\rho}}_i) = \sum_i \Delta m_i \mathbf{F}(\mathbf{R} + \boldsymbol{\rho}_i) + \sum_i m \Delta m_i \mathbf{F}_i - \mathbf{F}_c \qquad [1]$$

in which $\mathbf{F}_i$ is the specific force of gravitational attraction of a unit proof mass on a unit mass at the location of Δm_i, and the summation is carried over all particles of the main body. There is a continuous analog of this, of course, in which the sums are replaced by integrals over volume elements of the body, but it is more convenient in the sequel to retain the discrete form. At the same time, the equations of motion of the proof mass itself are encompassed by

$$m(\ddot{\mathbf{R}} + \ddot{\mathbf{a}}) = m\mathbf{F}(\mathbf{R} + \mathbf{a}) - \sum_i m \Delta m_i \mathbf{F}_i + \mathbf{F}_c \qquad [2]$$

One can eliminate $\mathbf{R}$ between Eqs. 1 and 2 to find the constraint force in terms of the motion of the X-system and of the proof mass relative to it, namely

$$\mathbf{F}_c = \mu\ddot{\mathbf{a}} + \mu\left[\sum_i (\Delta m_i/M)\mathbf{F}(\mathbf{R} + \boldsymbol{\rho}_i) - \mathbf{F}(\mathbf{R} + \mathbf{a})\right] + \sum_i m \Delta m_i \mathbf{F}_i \qquad [3]$$

in which $M = \sum_i \Delta m_i$ and $\mu = mM/(m + M)$ is the reduced mass, closely equal to m since $M \gg m$. The terms in Eq. 3 may be considered separately and simplified.

Proof Mass Acceleration

The term $\ddot{\mathbf{a}}$ is the second time derivative of $\mathbf{a}$ as seen from inertial space. For our purposes here, it is necessary to formulate it in terms of quantities seen from the X-reference frame. Let $\boldsymbol{\omega}$ be the angular velocity of this frame relative to inertial space. Denote by $\mathbf{A}$ and $\mathbf{V}$ respectively the apparent acceleration and velocity of the proof mass as seen by an observer fixed in the X-system. This apparent motion may arise either because the proof mass is constrained to remain fixed in the vehicle frame while the center of mass wanders, or because the proof mass is deliberately made to undergo some motion relative to the frame—for example, in order to compensate certain error terms. Then $\ddot{\mathbf{a}}$ can be written in the well-known form

$$\ddot{\mathbf{a}} = \mathbf{A} + 2\boldsymbol{\omega} \times \mathbf{V} + \dot{\boldsymbol{\omega}} \times \mathbf{a} + \boldsymbol{\omega} \times (\boldsymbol{\omega} \times \mathbf{a}) \qquad [4]$$

Gravitational Interaction With Vehicle

The term $\bar{\mathfrak{F}} = -\sum_i m \Delta m_i \mathbf{F}_i$ is the net gravitational force of the parts of the vehicle on the proof mass. Although it can be computed when the details of the mass distribution of the vehicle are given, not much can be said about its form in a general way. The force is simply related to an arbitrary $\mathbf{a}$ only for continuous bodies with spherical symmetry about the center of mass. Fortunately, in practice the structure of the body normally does not change much during the period of interest, so that $\bar{\mathfrak{F}}$ is composed of a constant plus a smaller variable part. The effect of the constant part can be imagined to be biased out of an instrument located at the proof mass, and it is only the changes in $\bar{\mathfrak{F}}$ which ultimately are of concern. We may write $\bar{\mathfrak{F}}(\mathbf{a})$ to show explicitly that this force is a function of the location of the proof mass as well as the mass distribution of the vehicle.

Gravity Gradient

Since the magnitudes of $\boldsymbol{\rho}_i$ and $\mathbf{a}$ may be assumed far less than the magnitude of $\mathbf{R}$ for realistic space vehicles, one can use the usual vector expansion formulas to write

$$\mathbf{F}(\mathbf{R} + \mathbf{a}) = \mathbf{F}(\mathbf{R}) + \mathbf{a}\cdot\text{grad}\,\mathbf{F}\,|_{\mathbf{R}} + (1/2)(\mathbf{a}\cdot\text{grad})^2\mathbf{F}\,|_{\mathbf{R}} + \cdots$$

and analogously for $\mathbf{F}(\mathbf{R} + \boldsymbol{\rho}_i)$. From these it follows that

$$\sum_i \frac{\Delta m_i}{M}\mathbf{F}(\mathbf{R} + \boldsymbol{\rho}_i) - \mathbf{F}(\mathbf{R} + \mathbf{a}) \approx -\mathbf{a}\cdot\text{grad}\,\mathbf{F} + \text{grad}\cdot\boldsymbol{\vartheta}\cdot\text{grad}\,\mathbf{F} \qquad [5]$$

[4] It must not be forgotten that the center of mass generally is not fixed within the physical structure of the vehicle.

in which $\mathcal{I}$ is the dyadic

$$\mathcal{I} = \frac{1}{2}\left(\frac{1}{M}\sum_i \Delta m_i \boldsymbol{\rho}_i\boldsymbol{\rho}_i - \mathbf{aa}\right) \qquad [6]$$

and it is understood that the gradients are formed in rectangular coordinates and evaluated at the point **R**. The second term on the right-hand side of Eq. 5 is extremely small relative to the first—down at least by a factor of 10^{-6} for realistic space vehicles. Therefore, attention will be concentrated on the detailed form of the dyadic term $\mathbf{a}\cdot\text{grad}\,\mathbf{F}$.

Its dyadic nature was clearly described by Crowley, Kolodkin, and Schneider, but the explicit form is given there only for an inverse-square field. For the present, it is merely supported that the force field **F** is derived from a potential function U.

It is convenient to develop the subsequent expressions by considering vector components in a local triad of unit vectors $\mathbf{e}_1$, $\mathbf{e}_2$, $\mathbf{e}_3$ at the proof mass. This is not essential, but it will be natural to consider these axes as the nominal sensitive axes of an accelerometer triad. The local system can be defined by any set of three angles φ_1, φ_2, φ_3 that describes a linear orthogonal transformation of X-axes into $\mathbf{e}_1$, $\mathbf{e}_2$, $\mathbf{e}_3$.[5] A typical case is shown in Fig. 2, but many other possibilities exist. In some instrument concepts $\mathbf{e}_1$, $\mathbf{e}_2$, $\mathbf{e}_3$ may be made to coincide with X_1, in others the angles φ_1, φ_2, φ_3 may be arbitrary but constant. In still others, these angles may be functions of time as the accelerometer triad is rotated around within the vehicle. In this case, in order to give a complete dynamical description of the instrument, the angular velocity $\boldsymbol{\omega}$ of the X-frame must be replaced in Eq. 4 by $\boldsymbol{\omega} + \boldsymbol{\Omega}$, where $\boldsymbol{\Omega}$ is the angular velocity of the $\mathbf{e}_1$, $\mathbf{e}_2$, $\mathbf{e}_3$ system with respect to the X-system. For the particular transformation shown in Fig. 2 one would have

$$\boldsymbol{\Omega} = \dot{\varphi}_1\mathbf{e}_X + \dot{\varphi}_2(\mathbf{e}_Y\cos\varphi_1 + \mathbf{e}_Z\sin\varphi_1) + \dot{\varphi}_3\mathbf{e}_3 \qquad [7]$$

$$= (\dot{\varphi}_1\cos\varphi_2\cos\varphi_3 + \dot{\varphi}_2\sin\varphi_3)\mathbf{e}_1 + (-\dot{\varphi}_1\cos\varphi_2\sin\varphi_3 + \dot{\varphi}_2\cos\varphi_3)\mathbf{e}_2 + (\dot{\varphi}_1\sin\varphi_2 + \dot{\varphi}_3)\mathbf{e}_3 \qquad [8]$$

Now let a_j, $R_j (j = 1, 2, 3)$ be components of **a** and **R** relative to the base vectors $\mathbf{e}_1$, $\mathbf{e}_2$, $\mathbf{e}_3$ and assume analogous notation for other vectors. Denote the second partial derivatives of U with respect to the R_j by $\Phi_{jk} = \partial^2 U/\partial R_j\partial R_k$ and third partials correspondingly by Φ_{ijk}. In these terms

$$-\mathbf{a}\cdot\text{grad}\,\mathbf{F} = (a_j\Phi_{jk})\mathbf{e}_k$$

$$\text{grad}\cdot\mathcal{I}\cdot\text{grad}\,\mathbf{F} = -(I_{jl}\Phi_{jlk})\mathbf{e}_k \qquad [9]$$

in which repeated indices denote summation over 1, 2, 3.

For the special case of an inverse-square field where

$$U = -K/|\mathbf{R}|$$

the origin of $\mathfrak{X}_i$ being at the center of attraction, the matrix of Φ_{jk} is $\Phi_{jk}{}^*$ given by

$$\Phi_{jk}{}^* = \begin{bmatrix} -\frac{K}{R^5}(R_2^2 + R_3^2 - 2R_1^2) & \frac{3K}{R^5}R_1R_2 & \frac{3K}{R^5}R_1R_3 \\ \frac{3K}{R^5}R_2R_1 & -\frac{K}{R^5}(R_1^2 + R_3^2 - 2R_2^2) & \frac{3K}{R^5}R_2R_3 \\ \frac{3K}{R^5}R_3R_1 & \frac{3K}{R^5}R_3R_2 & -\frac{K}{R^5}(R_1^2 + R_2^2 - 2R_3^2) \end{bmatrix} \qquad [10]$$

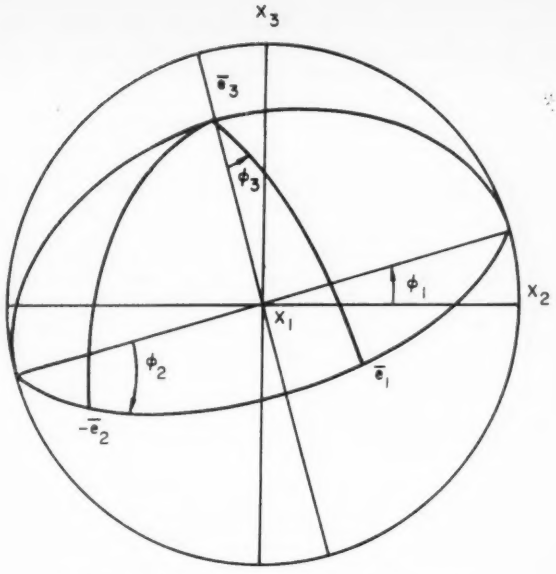

Fig. 2 Typical transformation of X_i into $\mathbf{e}_1,\mathbf{e}_2,\mathbf{e}_3$

However, we do not yet need to use this form. The point of importance is that the Φ_{jk} are symmetric (in j and k) point functions of position, and therefore of the three components R_1, R_2, R_3.

Accelerometer Reading

An accelerometer is essentially a device which measures one component in the direction of its sensitive axis of a force on a proof mass. It does this by measuring the input to a calibration transducer, probably in electrical form, just necessary to provide the proper component of constraint force needed to keep the proof mass in a fixed location or to cause it to undergo a prescribed motion relative to the body. Thus, except for errors, one may presume that the basic instrument output is a signal proportional to one component of $\mathbf{F}_e$ and having different units. It is more conventional to speak of the output as simply *measured value* of that component, with the implication that the proper scale and unit change have been made.

Three common types of errors are scale factor errors, bias errors, and axis misalignment errors. Consider an accelerometer whose sensitive axis is nominally along the base vector $\mathbf{e}_k$ (where k may be 1, 2, or 3), so that it nominally measures the component $(\mathbf{F}_e)_k$. A scale factor error causes the measured value to be increased by a multiplicative factor $(1 + \epsilon_k)$, where ϵ_k is a numerical factor that is small relative to unity and not necessarily constant for all levels of $|\mathbf{F}_e|$. A bias consists of an extra additive term δ_k which may be

[5] There should be no confusion in using axis labels and labels for unit vectors along axes interchangeably in the discussion. Only the unit vectors actually are used in equations.

constant or may vary with time in a systematic or random fashion. Finally, suppose that the true sensitive axis, though nominally along $\mathbf{e}_k$, actually is along a unit vector which has very small projections along the other two axes of the triad as well. For example, if $k = 3$ the sensitive axis might be along

$$\cos \zeta_{32} \sin \zeta_{31}\mathbf{e}_1 + \sin \zeta_{32}\mathbf{e}_2 + \cos \zeta_{31} \cos \zeta_{32}\mathbf{e}_3 \approx \mathbf{e}_3 + \zeta_{31}\mathbf{e}_1 + \zeta_{32}\mathbf{e}_2$$

when ζ_{31} and ζ_{32} are very small angles. In short, for sensitive axes nominally along $\mathbf{e}_k$ there generally are misalignment angles ζ_{ik}, ζ_{jk} $(i \neq j \neq k)$, a total of six in all for a triad of accelerometers. Thus, the projection of $\mathbf{F}_c$ on the sensitive axis nominally along $\mathbf{e}_k$ actually is closely[6]

$$(\mathbf{F}_c)_k + \zeta_{ik}(\mathbf{F}_c)_i \qquad i \text{ summed, } i \neq k$$

From these remarks it follows that the measured value f_k of $(\mathbf{F}_c)_k$, or accelerometer output, is

$$f_k = (1 + \epsilon_k)(\mathbf{F}_c)_k + \delta_k + \zeta_{ik}(\mathbf{F}_c)_i \qquad [11]$$

Here products of ϵ_k by the ζ_{ik} have been dropped as giving relative errors of the order of 10^{-9} under normal circumstances. Note that neither this approximation nor the previous one that $\zeta_{ik} \ll 1$ is really essential—it merely simplifies the writing of the misalignment angles or larger scale factor errors, this being done quite straightforwardly.

The final form of the accelerometer output now is found explicitly by expressing $(\mathbf{F}_c)_k$ according to Eqs. 3–5 and 9, first resolving vectors into the $\mathbf{e}_1$, $\mathbf{e}_2$, $\mathbf{e}_3$ system and not forgetting to replace $\boldsymbol{\omega}$ by $\boldsymbol{\omega} + \boldsymbol{\Omega}$ in Eq. 4. The result is

$$f_k = \mu(1 + \epsilon_k)\{A_k + [2(\omega_i + \Omega_i)V_j + (\dot{\omega}_i + \dot{\Omega}_i)a_j]\epsilon_{ijk} + (\omega_i + \dot{\Omega}_i)[a_i(\omega_i + \Omega_k) - a_k(\omega_i + \Omega_i)] + a_j\Phi_{jk} - I_{jl}\Phi_{jlk}\} - (1 + \epsilon_k)\bar{\mathfrak{F}}_k + \delta_k \sum_{i \neq k} \zeta_{ik}(F_c)_i \qquad [12]$$

This is the equation basic to the discussion which follows, the f_k being the fundamental sensed quantity and the orientation implicit in Φ_{jk} to be inferred. Here ϵ_{ijk} is the usual "ϵ-symbol" equal to $+1$ when (i, j, k) is a cyclic permutation of $(1, 2, 3)$, equal to -1 when a cyclic permutation of $(1, 3, 2)$ and zero otherwise. The $(\mathbf{F}_c)_i$ in the last term of Eq. 12 can be expanded using Eq. 3 of course, but since the ζ_{ik} are assumed to be very small quantities the explicit form of the force is not fundamental to the development of the principles that follow, and it is more convenient just to represent the force components by single symbols. Note that the terms of Eq. 12 are not summed over k, although other repeated indices denote summation.

Instrument Concepts

General Principles

The orientation of the X-system may be described by any three angles $\bar{\theta}_1$, $\bar{\theta}_2$, $\bar{\theta}_3$ that define a linear orthogonal transformation from $\mathfrak{X}_1$, $\mathfrak{X}_2$, $\mathfrak{X}_3$ to X_1, X_2, X_3. In particular, if certain orbit parameters are added to the characterization, these may be identical with the angles θ_i introduced in (1) to describe satellite attitude deviations. All that is known of vehicle position is the projection of $\mathbf{R}$ on the vehicle axes, which can be expressed in terms of R and $\bar{\theta}_i$. Thus self-contained sensing methods such as this do not determine position in space uniquely.

[6] For ζ_{ik} of a few seconds of arc, which is typical, the relative error of the approximation is of the order of 10^{-9} to 10^{-10}.

The $\boldsymbol{\omega}$ and $\dot{\boldsymbol{\omega}}$ components in Eq. 12 can be replaced by combinations of the $\bar{\theta}_i$ and their first and second derivatives, while if desired the Ω_i and $\dot{\Omega}_i$ can be replaced correspondingly by expressions involving φ_j and their derivatives. In effect, Eq. 12 is a single relationship among R, $\bar{\theta}_i$ and the parameters φ_i, a_i, A_i and $\bar{\mathfrak{F}}_i$ describing the state of the internal accelerometer. Actually R enters implicitly through Φ_{jk} and its spatial derivatives, $\bar{\theta}_i$ through the same functions and the ω_i.

It follows that Eq. 12 is a single scalar relationship among four unknown variables and a set of instrument parameters, some of which like the a_i may not be easily measurable, or may not be constant. So an alternative point of view is that there really are seven or more unknowns. The problem of determining position and orientation by gravitational measurements is simply one of adding enough additional constraints or measurements to effectively augment this equation by three or more other independent relationships, thereby making the solution determinant.

There are literally dozens of ways to design instruments on the basis of these principles, but the methods involve two major techniques. First, one uses multiple accelerometers located in various parts of the vehicle and having various sensitive axis orientations. Each such accelerometer adds another scalar equation of the form of Eq. 12. It might appear that this merely causes one to fall behind on the number of unknowns relative to the number of equations, for each new accelerometer also adds three new a_i components. However, if it is supposed that the relative locations of a number of proof masses are quantities that can be measured accurately by some calibration procedure, then no additional unknown location parameters arise in the new equation.

Second, one augments the equations (or reduces the number of variables) by direct independent measurement or control of certain quantities. For example, the φ_i ordinarily should be considered known (measurable) quantities rather than unknowns to be determined along with the more fundamental unknowns R, $\bar{\theta}_i$. It is possible that the a_i also can be inferred by some kind of calibration technique, together with a knowledge of center of mass shifts from moving parts. A definite possibility of this class is to measure a yaw angle in the case of a satellite by an independent means and to use the gravity gradient method only to infer the angles characterizing the departure of body axes from the nominal "vertical." (In fact, if the field gradient is radially symmetric in a plane normal to $\mathbf{R}$, a degenerate case occurs, and one cannot hope to infer anything concerning rotation about $\mathbf{R}$ by purely gravitational methods.)

After having sufficient information in principle to solve the problem, there remains the actual operation of obtaining the solution. Here, too, there is considerable latitude for ingenuity in the instrument concept, since there are at least three ways to go about it. First, one may control some of the variables so that certain complicating terms disappear from the equations to be solved. For example, one may cause (by means of a closed loop system) the angles φ_i to assume values such that the output of one or more accelerometer is nulled. (This seems to be a procedure common to all methods proposed in the existing literature.) Second, one may make direct independent measurements of certain quantities and use these measurements to take terms out of the equations. An example is the measurement of $\boldsymbol{\omega}$ by rate gyros and the biasing out of all ω-terms in Eq. 12. Third,

one has the option of a "brute force" numerical solution of the equations. Probably the best procedure in this case is to solve Eq. 12 explicitly for the Φ_{jk} or the linear combination $a_j\Phi_{jk}$. These terms are the major ones containing the position and attitude unknowns, so the solution is equivalent to solving for these. Other terms contain the same components, but these are small and can be ignored in the first approximation. Then the solution so obtained is substituted into the small terms previously ignored in order to get an improved solution. In short, the solution is by iteration, but in practice one improved approximation should suffice.

Triad of Accelerometer Pairs

Although the foregoing remarks show that information from a single body-mounted accelerometer can be considered as an entity and combined with other information only in the data processing, they also state that in order to avoid adding new unknowns with each new accelerometer one must be able to measure their difference distances. For this reason, and because the values of a_i generally change whenever there is translational movement of internal parts, even though the accelerometer remains fixed in the body, it is convenient to turn directly to accelerometer pairs as fundamental devices.

Let the outputs of two accelerometers both be described by Eq. 12, using primes on the symbols to denote the second accelerometer, and consider the difference output $\Delta f_k = f_k' - f_k$. Define $\Delta\mu = \mu' - \mu$, $\Delta\epsilon_k = \epsilon_k' - \epsilon_k$ (a quantity of the order of ϵ_k or ϵ_k'), $d_i = a_i' - a_i$, $\Delta\mathfrak{F}_k = \mathfrak{F}_k' - \mathfrak{F}_k$, $\Delta\delta_k = \delta_k' - \delta_k$ (a quantity of the order of δ_k' or δ_k), $\Delta I_{jl} = I_{jl}' - I_{jl}$. Note that since Φ_{jk} and Φ_{jlk} are evaluated at the center of mass, they are the same for both accelerometers, as are the ω_i. Finally, assume that if the accelerometers are rotated within the vehicle they are rotated as a rigid unit, so that Ω_i also is the same for each. It can be shown that in this case the difference $\ddot{\mathbf{s}}' - \ddot{\mathbf{s}} = (\dot{\boldsymbol{\omega}} + \dot{\boldsymbol{\Omega}}) \times \mathbf{d} + (\boldsymbol{\omega} + \boldsymbol{\Omega}) \times [(\boldsymbol{\omega} + \boldsymbol{\Omega}) \times \mathbf{d}]$ regardless of the location of the center of rotation of the accelerometer pair.

Finally, define $\sum f_k = f_k' + f_k$ (a measurable quantity), denote by $\Phi_{ki}{}^*$ the part of Φ_{ki} attributable to the locally strongest inverse-square field and by $\Delta\Phi_{ki}$ the difference $\Phi_{ki} - \Phi_{ki}{}^*$, and introduce

$$\Psi_{ki} = \Phi_{ki}{}^* - (\omega_j + \Omega_j)\epsilon_{jki} + [(\omega_k + \Omega_k)(\omega_i + \Omega_i) - (\omega_j + \Omega_j)(\omega_j + \Omega_j)\delta_{ik}] \quad [13]$$

$$\Delta_k = \mu\Delta\Phi_{ki}d_i - \mu\Delta I_{jl}\Phi_{jlk} - \epsilon_k'\mathfrak{F}_k' + \Delta\delta_k + (1/2)[2\Delta\mu + \mu(\epsilon_k' + \epsilon_k) + \sum_{i \neq k} (\zeta_{ik}' + \zeta_{ik})] \sum f_k \quad [14]$$

(remembering that repeated index k is not summed, but others are). Then to within second-order terms in small quantities

$$\Delta f_k = \mu\Psi_{ki}d_i + \Delta_k \quad [15]$$

The term involving Ψ_{ki} is to be considered the major term in Eq. 15, since it is from this that the basic inferences about position and orientation are to be made. The Δ_k is in the nature of an error, the terms of which are considered in detail later.

There are two arrangements of accelerometer axes of primary interest. In Type 1, the separation of the accelerometers is parallel to their sensitive axes ($d_k = d$, $d_i = 0$ for $i \neq k$). In Type 2, it is perpendicular to their sensitive axes ($d_k = 0$, $d_i = d$ for $i = k + 1$ or $k + 2$). For the moment not including the Δ_k-terms, Eq. 15 takes the form

$$\Delta f^{(k)}{}_k = \mu d[\Phi_{kk}{}^* + (\omega_k + \Omega_k)^2 - |\boldsymbol{\omega} + \boldsymbol{\Omega}|^2] \quad [16]$$

for Type 1, and for Type 2 either

$$\Delta f_k{}^{(k+1)} = \mu d[\Phi_{kk+1}{}^* - (\dot{\omega}_{k+2} + \dot{\Omega}_{k+2}) + (\omega_k + \Omega_k)(\omega_{k+1} + \Omega_{k+1})] \quad [17]$$

or

$$\Delta f_k{}^{(k+2)} = \mu d[\Phi_{kk+2}{}^* + (\dot{\omega}_{k+1} + \dot{\Omega}_{k+1}) + (\omega_k + \Omega_k)(\omega_{k+2} + \Omega_{k+2})] \quad [18]$$

Note that subscripts are to be interpreted modulo 3. Thus ω_4 is to be interpreted as ω_1, etc. All of the instrument arrangements considered by (3, 5, 6) are embraced by these cases, although not so for those of (4). For the latter one must return to Eq. 12, but this special arrangement will be treated elsewhere.

Consider first the case in which the accelerometers are quiescent within the vehicle, so $\boldsymbol{\Omega} \equiv 0$. If Eq. 16 is written out in full for the three possible values of k, using Eq. 10 one obtains

$$\begin{aligned}
\Delta f^{(1)}{}_1 &= -\mu d[(K/R^5)(R_2{}^2 + R_3{}^2 - 2R_1{}^2) + (\omega_2{}^2 + \omega_3{}^2)] \\
\Delta f^{(2)}{}_2 &= -\mu d[(K/R^5)(R_1{}^2 + R_3{}^2 - 2R_2{}^2) + (\omega_1{}^2 + \omega_3{}^2)] \\
\Delta f^{(3)}{}_3 &= -\mu d[(K/R^5)(R_2{}^2 + R_1{}^2 - 2R_3{}^2) + (\omega_1{}^2 + \omega_2{}^2)]
\end{aligned} \quad [19]$$

It is clear that these three expressions are not linearly independent, so there is no option of using three Type 1 accelerometer pairs to infer orientation and position error. Moreover, none of the three involves θ_i to first order, so they are useful primarily to infer R. For this, assuming something can be done about the ω-terms (see later), a single Type 1 pair suffices.

Similarly from Eqs. 17 and 18

$$\begin{aligned}
\Delta f^{(2)}{}_1 &= \mu d[3KR_1R_2/R^5 - \dot{\omega}_3 + \omega_1\omega_2] \\
\Delta f^{(3)}{}_2 &= \mu d[3KR_2R_3/R^5 - \dot{\omega}_1 + \omega_2\omega_3] \\
\Delta f^{(1)}{}_3 &= \mu d[3KR_3R_1/R^5 - \dot{\omega}_2 + \omega_3\omega_1] \\
\Delta f^{(3)}{}_1 &= \mu d[3KR_1R_3/R^5 + \dot{\omega}_2 + \omega_3\omega_1] \\
\Delta f^{(1)}{}_2 &= \mu d[3KR_2R_1/R^5 + \dot{\omega}_3 + \omega_1\omega_2] \\
\Delta f^{(2)}{}_3 &= \mu d[3KR_3R_2/R^5 + \dot{\omega}_1 + \omega_2\omega_3]
\end{aligned} \quad [20]$$

Two of these may be adjoined to a single Type 1 pair to make a triad from which (again assuming the ω-terms can be handled) R_1, R_2, R_3 can all be determined. As such a triad, for definiteness take those whose outputs are designated $\Delta f^{(3)}{}_3$, $\Delta f^{(1)}{}_3$, $\Delta f^{(2)}{}_3$. Note that the triad can be realized physically by just four individual accelerometers, all their axes parallel to X_3, whose outputs are examined by pairs. (See Fig. 3b.) Recall also that the components R_i and ω_i are resolved in triad axes.

Aside from errors and dynamic effects from internal motion of the triad, the triad conceptually contains all the information about R and θ_i that potentially can be extracted by gravitational means alone. But it remains now to look deeper into the extraction process and then to consider the errors in the procedure and their reduction.

Preferential Internal Alignment

It has been stated previously that one method of inference depends on the control of certain variables. A possibility of this kind is to control the internal alignment of the triad so that it comes into coincidence with the natural vertical reference frame relative to the gravitating center. For example, the reference frame might be precisely the normal to the local gravitational equipotential surface. In this case $R_1 = R_2 = 0$ and $R_3 = R$, while the ω_i are just the ω_{ri} defined by Eq. 1.8 of (2). With the triad in such an orientation, the orientation

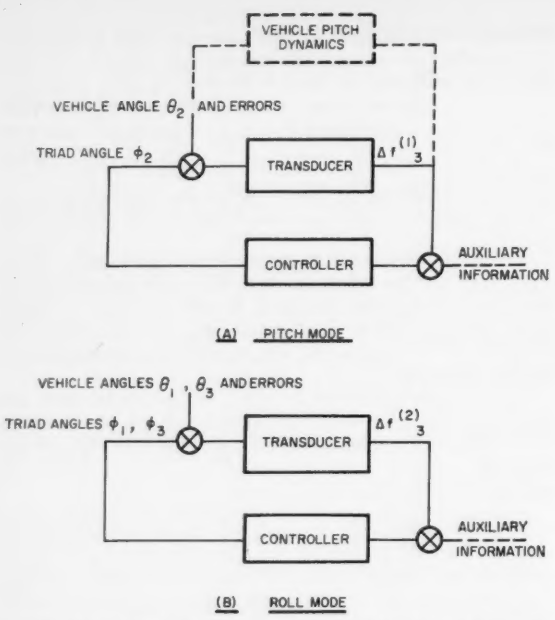

Fig. 3 Orientation control of gravity gradient accelerometer triad

error of the vehicle frame itself is inferred simply by the triad orientation angles φ_i relative to the vehicle frame.

Consider the case of the triad close to the vehicle axes so the φ_i are small and the vehicle axes close to the reference frame so the θ_i are small. (See definitions in Ref. 1.) We may write $\mathbf{R} = R\xi_3$ to first order in these angles (neglecting cross products of φ_i and θ_i by other small quantities, which would have to be reconsidered in a detailed error analysis) as

$$\mathbf{R} = R\mathbf{e}_1\left[-(\theta_2 + \varphi_2) - \nu_1 \frac{\sin i \cos \beta}{\cos \lambda}\right] + R\mathbf{e}_2\left[(\theta_1 + \varphi_1) - \nu_1 \frac{\cos i}{\cos \lambda}\right] + R\mathbf{e}_3 \quad [21]$$

where ν_1 is an oblateness parameter as discussed in Chapter I of (2). At the same time

$$\begin{aligned} \omega_1 &= \dot\theta_1 + \omega_0(\theta_3 + \varphi_3) + \omega_{r1} \\ \omega_2 &= \dot\theta_2 + \omega_{r2} \\ \omega_3 &= \dot\theta_3 - \omega_0(\theta_1 + \varphi_1) + \omega_{r3} \end{aligned} \quad \ldots\ldots\ldots\ldots\ldots\ldots\ldots\ldots\ldots\ldots\ldots\ldots\ldots\ldots\ldots\ldots [22]$$

where ω_{r1}, ω_{r2}, ω_{r3} are the components of angular velocity of the attitude reference frame. Also, $\Omega_i = \dot\varphi_i$ to this order of approximation.

The instrument outputs are

$$\Delta f^{(1)}_3 = -\mu d\left[(\ddot\theta_2 + \ddot\varphi_2) + 3\omega_0^2(\theta_2 + \varphi_2) - 2e\omega_0^2 \sin \omega_0 t + \ddot\nu_1 \frac{\sin i \cos \beta^*}{\cos \lambda} + 3\omega_0^2 \nu_1 \frac{\sin i \cos \beta}{\cos \lambda} - \dot i_1 \omega_0 \frac{\sin i \sin \beta}{\cos \lambda} + \dot\nu_1 \dot\lambda \frac{\sin i \cos \beta^* \sin \lambda}{\cos^2 \lambda}\right] \quad [23]$$

$$\Delta f^{(2)}_3 = \mu d\left[(\ddot\theta_1 + \ddot\varphi_1) + 2\omega_0^2(\theta_1 + \varphi_1) + 2\omega_0(\dot\theta_3 + \dot\varphi_3) + \dot\nu_2 \omega_0 - \dot\Omega \omega_0 \sin i \sin \omega_0(t - t_0) - \ddot\nu_1 \frac{\cos i}{\cos \lambda} - \dot\nu_1 \dot\lambda_1 \frac{\cos i \sin \lambda}{\cos^2 \lambda} - 3\nu_1 \omega_0^2 \frac{\cos i}{\cos \lambda}\right] \quad [24]$$

$$\Delta f^{(3)}_3 = \mu d\left[\omega_0^2(1 - 10e \cos \omega_0 t) - 2\omega_0(\dot\theta_2 + \dot\varphi_2) - 2\omega_0\left(\dot\Omega \cos i + \dot\nu_1 \frac{\sin i \cos \beta^*}{\cos \lambda}\right)\right] \quad [25]$$

These are interpreted easily if there is quiescence of the triad relative to the field ($\dot\theta_1 + \dot\varphi_1 \equiv 0$) and if one ignores the small effects from eccentricity and oblateness. One sees that $\Delta f^{(1)}_3$ is simply a measure of $\theta_2 + \varphi_2$, $\Delta f^{(2)}_3$ of $\theta_1 + \varphi_1$, and $\Delta f^{(3)}_3$ of ω_0 and therefore of major semi-axis. In fact, though, the situation is not this simple.

If one attempts to drive $\Delta f^{(1)}_3$ and $\Delta f^{(2)}_3$ to zero to obtain alignment of the third pair with the gravitational field, one must contend with both dynamic effects and the presence of error terms. One has a control situation of the type shown in Fig. 3 where the instrument outputs $\Delta f^{(1)}_3$ and $\Delta f^{(2)}_3$ are used as inputs to controllers whose outputs are used to adjust the triad angles φ_i. One would use $\Delta f^{(1)}_3$ to control φ_2 and $\Delta f^{(2)}_3$ to control φ_1, in each case possibly coupled with auxiliary information. The object in each case is to obtain a stable system such that the actual φ-angles are a measure of the θ-angles, i.e., such that the quantities $\epsilon_i = \theta_i + \varphi_i$ go to zero.

This control problem has not been studied here, but see Gordon (6) for a development of this approach. Purely for illustration, one might imagine a linear controller for the pitch mode for which $\mu d K(s)\varphi_2 = -\Delta f^{(1)}_3$. Using Eq. 23, this gives

$$\ddot\epsilon_2 + 3\omega_0^2 \epsilon_2 + K(s)\varphi_2 = \text{error terms} \quad [26]$$

in which the error terms form a trigonometric series with base frequency ω_0 and coefficients which involve e and ν_1, numerically of the order of $10^{-3}\,\omega_0^2$ except for the effect of eccentricity, which may be larger. But the latter is merely the driving term that gives the geometric libration error that one should expect with any such sensing method when used on an eccentric orbit. One may rewrite Eq. 26 in terms of a new transfer function $K'(s) = s^2 + 3\omega_0^2 + K(s)$ as

$$\epsilon_2 = \frac{K(s)}{K'(s)}\,\theta_2 + \frac{1}{K'(s)}\,(\text{error terms}) \quad [27]$$

from which it is seen that ϵ_2 can never be driven to zero and held there in the presence of θ_2 motions. However, the function K/K' can be chosen to minimize the effects of θ_2 motions of the type expected.

The comments above refer to the use of the device purely as a sensor. If it is coupled back into the control loop, the effect is to add a second loop in the diagram of Fig. 3a, this time between $\Delta f^{(1)}_3$ and vehicle angle θ_2 by way of a block representing the vehicle pitch dynamics. Clearly this is a much more sophisticated situation which deserves extended study.

Similar considerations for the roll mode, following the scheme of Fig. 3b, also give rise to complications because of the yaw rate terms arising in Eq. 24. The result is that the error ϵ_1 takes the form

$$\epsilon_1 = \frac{K_1(s)}{K'(s)}\,\theta_1 + \frac{K_2(s)}{K'(s)}\,\theta_3 + \frac{1}{K'(s)}\,(\text{error terms}) \quad [28]$$

One has the option of trying to choose $K_1(s)$ so as to minimize the response to both θ_1 and θ_3; but a better procedure in this case might be to introduce θ_3 information from a yaw rate gyro into the loop and essentially remove the θ_3-term from Eq. 28.

This whole problem area needs more searching examination, with special attention to the choice of $K(s)$ and the effect of errors, if the gravity gradient device is to be considered seriously.

Preferential alignments other than the one discussed above are possible, and may be indicated if different combinations of accelerometers into pairs are used, e.g., as in (4). However, exactly the same logical problems are involved as in the present case and it does not seem profitable to explore the many alternatives here.

Other examples also could be given of the use of auxiliary information. If rate measurements are available from rate gyros, for example, these could be introduced directly as biasing terms to cancel the ω-components appearing in Eqs. 19 and 20, since their natural outputs are precisely the components in question. Whether the resulting simplification in mechanization more than makes up for the practical disadvantages of having the gyros is a question which would have to be investigated, but the answer may well be affirmative, especially for the case of large angular motions.

In the "brute force" methods, one returns to Eq. 16 with an arbitrary alignment of accelerometer axes and treats the instrument outputs as differential equations to be solved numerically for the attitude variables. The process certainly can be alleviated by such a simplifying choice as $\varphi_i = 0$, which involves no loss in generality. But this method creates a significant on-board computation burden, and it would appear better to make further simplifications of the relationships by varying orientation and/or using rate gyro output data.

Elementary Error Considerations

Beginning with Eq. 16, the error terms encompassed by Δ_k in Eq. 15 were ignored. It is evident, however, that they will appear in the measured values of Δf_k whenever the latter are used as indicators of attitude deviation, e.g., by the technique described above, and will contribute errors to the attitude inference. Therefore, it is important to examine the individual terms of Eq. 14 more closely to get some idea of their magnitudes.

The error from the noninverse-square character of the gravitational field has been considered in (7) and other reports of the same series. The major error, of course, is from oblateness, its peak value being about 6 min of arc relative to the geocentric vertical. However, this may be removed as an error term by redefining the reference system effectively by introducing ν_1 of just the right magnitude to compensate the effect. One is left with the gravitational effects of sun and moon and of the Earth's gravity anomalies. The sun's field gives an attitude deviation error in the worst configuration of only a few hundredths of a second of arc out to one Earth radius, but increases with distance from the Earth. The moon's effect is of the order of 1 sec, and the gravity anomalies have an rms value that should drop to $^1/_2$ sec or less at one Earth radius.

It already has been commented that the term in $I_{jl}\Phi_{jlk}$ is down by about 10^{-6} relative to the dominant term in the gravitational attraction, so the difference term $I_{jl}\Phi_{jlk}$ could not contribute more than about $^1/_2$ sec.

The vehicle attraction $\mathfrak{F}_k'$ is difficult to calculate because of its dependence on vehicle mass distribution. However, it appears only as a product with an accelerometer scale factor error. Reasonable values for this product would seem to be at least two orders of magnitude below 1 sec.

The bias error of a terrestrial accelerometer might lie in the range 10^{-4} to 10^{-5} g, which obviously would be intolerable in measuring 10^{-10} g. However, it may be assumed that $\Delta\delta_k$ is the bias error that remains when the accelerometer pair is carefully calibrated in situ. It probably would not be safe to assume it is any better than 10^{-4} of the peak output, corresponding to about 20 sec, but it may be worse than this. In general, it might be expected that this would be a major source of error together with vehicle motion and compensation errors.

The remaining terms in Eq. 15 represent a scale factor error. Again, in the absence of definite low level accelerometer data it would not be safe to assume this was better than one part in 10^4 (20 sec error at full scale), and this may not be a sufficiently conservative assumption.

Assuming that suitable accelerometers can be developed, that the "natural" output (including the oblateness effect) is taken as the vertical reference, and that vehicle attitude errors can be compensated to within about 1%, it is conjectured that the errors from vehicle attitude motions are dominant in using the gravity gradient method purely for sensing, and that these can be perhaps 0.1° for attitude oscillations of 10°. If such oscillations can be kept smaller and compensation can be improved, an ultimate accuracy of perhaps 1 min relative to the gravitational vertical seems possible from a consideration of the natural error producing effects. This error analysis has been a very crude first approximation, but a more elaborate one probably is not justified without further accelerometer development aimed at this application.

References

1 Roberson, R. E., "Attitude Control of Satellites and Space Vehicles," *Advances in Space Science*, Vol. 2, Academic Press, New York, 1960, pp. 351–436.

2 Roberson, R. E. (ed.), "Sensing and Actuating Methods," *Methods for the Control of Satellites and Space Vehicles*, Vol. 1, Systems Corp. of America Final Tech. Rep. on Contract AF33(616)-6674 with the Flight Control Laboratory of Wright Air Development Div. USAF, dated July 31, 1960 (see Chap. IIIa).

3 Crowley, J. C., Kolodkin, S. S. and Schneider, A. M., "Some Properties of the Gravitational Field and Their Possible Application to Space Navigation," *IRE Trans. on Space Electronics and Telemetry*, Set-5 no. 1, March 1959, pp. 47–54.

4 Streicher, M., Zehr, R. and Arthur, R., "An Inertial Guidance Technique Useable in Free Fall," *Proc.* National Aeronautical Electronics Conf., Dayton, Ohio, May 1959, pp. 768–772.

5 Carroll, J. J. and Savet, P. H., "Space Navigation and Exploration by Gravity Difference Detection," presented at the IAS National Summer Meeting, Los Angeles, Calif., June 1959 (*IAS paper no. 59–91*).

6 Gordon, R., "A Pure Inertial Attitude Reference System for Orbital Vehicles," presented at the Sixth Annual East Coast Conf. on Aeronaut. and Navigational Electronics, Baltimore, Md., October 1959.

7 Davidson, J. J. et al., "Research on Instrumentation of Satellites and Other Hypersonic Vehicles for Precise Surveying, Mapping, and Target Location," New York University College of Engineering Research Div., *First Quar. Rep. 639*, I on Contract DA 44-009-ENG 3768, December 1958–February 1959.

Satellite Rendezvous Terminal Guidance System

KENNETH F. STEFFAN[1]

Aerospace Corp.
Los Angeles, Calif.

The terminal guidance system concept presented here is suitable for a variety of space rendezvous missions, such as the interrogation and possible negation of enemy satellites, maintenance and supply of space stations, and performance of space rescue. A distinguishing feature of this system is the intermittent instrumentation of the interceptor trajectory corrections. The velocity corrections that are made to the interceptor vehicle to achieve rendezvous are divided into two orthogonal channels. Each channel commands velocity corrections by intermittent operation of the constant thrust engine associated with that channel. The orthogonality of the channels is maintained by the attitude control system. The interceptor closing rate is controlled by the longitudinal channel and the lateral velocity of the interceptor by the normal velocity channel. A complete treatment of the interchannel coupling effects is given, since these effects determine the parameters of the longitudinal channel. The optimization procedures employed in the design concept to achieve rendezvous in the minimum time consistent with a small fuel requirement are also discussed in detail. The logic employed in the terminal guidance system is relatively simple and easily mechanized.

THE PRIMARY function of a satellite rendezvous terminal guidance system is to place the interceptor in the immediate vicinity of the target satellite with a small component of relative velocity. This function is somewhat more stringent than that of a satellite interceptor guidance system in which the relative velocity is not controlled.

The terminal guidance system concept to be presented is suitable for a variety of space rendezvous missions, such as the in-space assembly of a number of large subsystems, the maintenance and supply of space stations, and the performance of space rescue missions. A distinguishing feature of this system is the intermittent instrumentation of the interceptor trajectory corrections. This instrumentation offers several advantages: 1) it permits the use of constant thrust rocket engines, thus eliminating the development risks and costs of variable thrust engines; 2) it considerably simplifies interceptor attitude control and sensor gimbaling requirements; and 3) it permits the use of small relative closing velocities, thus allowing the employment of more optimum boost trajectories and greatly relaxing the requirements placed upon the acquisition sensor.

Discussions of alternate terminal guidance systems for satellite rendezvous may be found in (1–4).[2]

System Description

The terminal guidance system is required to compensate for various errors accumulated in the launch phase of the interceptor and the tracking of the target satellite. These errors are removed by a series of discrete velocity corrections that are computed by the terminal guidance system and implemented by the propulsion system of the interceptor. The velocity corrections, determined from position and velocity data, such as the range, range rate, and angular rate of the line of sight (LOS), are supplied by the terminal sensor. Range and range rate information can readily be obtained from a radar terminal sensor, and angular rate data from sensitive rate gyros affixed to the tracking head. Two gyros with sensitive axes aligned along the vehicle pitch and yaw axes may be employed to supply the terminal guidance system with the required LOS angular rate information (see Fig. 1).

The velocity corrections made to the interceptor vehicle to achieve rendezvous are divided into two orthogonal channels. Each channel commands velocity corrections by intermittent operation of the constant thrust engine associated with that channel. The first channel is defined by the velocity component normal to the LOS and hence is termed the *normal velocity channel;* the second is defined by the velocity component along the LOS and is termed the *longitudinal channel.* Control of the velocity components present in each channel is accomplished by the normal velocity and range rate control systems, respectively. Channel orthogonality is maintained by the attitude control system of the interceptor, which nulls the radar dish gimbal angle and hence drives the longitudinal axis of the interceptor to coincide with the radar dish axis (see Fig 2).

The velocity corrections in the plane normal to the LOS are implemented by a single nozzle with thrust axis pointed through the center of gravity of the rendezvous vehicle. The required orientation of the thrust vector in the normal plane is attained by vehicle roll commands. Permission to fire a normal correction is issued by a lockout feature that examines the error present in the roll channel of the body attitude servo system.

The normal velocity control system establishes the interceptor on a collision course with the target. This objective is accomplished by stabilizing the LOS between the vehicles in inertial space. LOS stabilization is achieved by discrete normal velocity corrections that null the LOS angular rate when it exceeds a threshold value.

The interceptor relative velocity normal to the LOS is obtained by the product of the smoothed range r^* and the

Presented at the ARS 15th Annual Meeting, Washington, D.C., Dec. 5–8, 1960; revision received Sept. 14, 1961.

[1] Head, Radio Guidance and Tracking Section.

[2] Numbers in parentheses indicate References at end of paper.

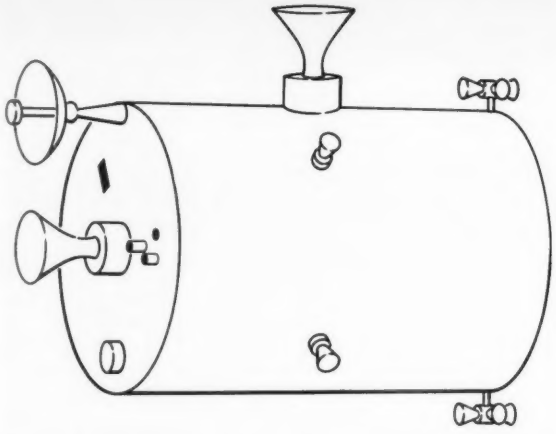

Fig. 1 Simple schematic of the rendezvous vehicle configuration

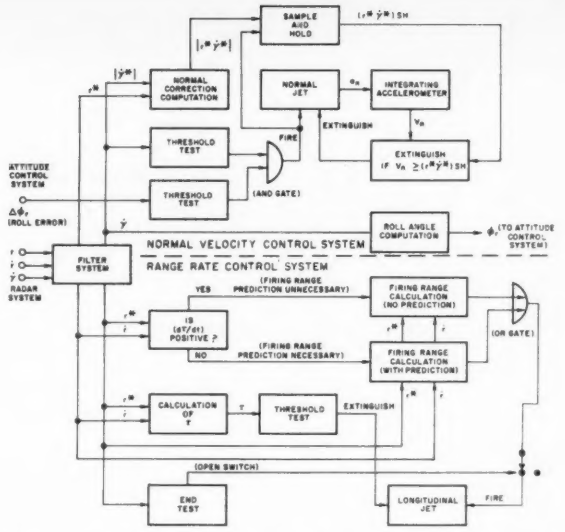

Fig. 2 Terminal guidance system block diagram (functional)

smoothed angular rate of the LOS, $\dot{\gamma}^*$. The modified proportional navigation system herein described intermittently nulls $\dot{\gamma}^*$ when it exceeds a correction threshold. When $\dot{\gamma}^*$ exceeds the threshold, a measure of the interceptor normal velocity is calculated as the product of the current values of r^* and $\dot{\gamma}^*$. This value, which is the magnitude of the velocity correction to be made to the vehicle in the normal plane, is then metered against the signal supplied by the body mounted integrating accelerometers. These accelerometers begin integrating upon initiation of the normal correction.

Determination of an optimum correction threshold depends on several factors, which include: minimization of required propellant, radar noise, range rate coupling, frequency of normal velocity corrections, allowable change in rendezvous attitude during terminal guidance, and terminal guidance system simplicity. Upon consideration of these factors, a constant threshold in the angular rate of the LOS was found to be very satisfactory. In essence, the system described above may be visualized as erecting a *normal velocity funnel* about the target vehicle. The normal velocity of the interceptor relative to the target is thus constrained to lie within the confines of the funnel. Owing to the choice of a constant threshold in $\dot{\gamma}$, the confines of the funnel are straight lines. The described system allows a major portion of the normal velocity error to be removed at ranges where the angular rate data is most accurate. Furthermore, the use of a constant angular rate threshold involves only a very simple logical computation that is readily instrumented in an airborne digital computer.

In addition to the establishment and maintenance of a collision course, control of the closing rate of the interceptor vehicle is necessary in order to achieve rendezvous. It will be assumed that the interceptor has been established in an orbit that approximately intersects that of the target satellite. As the satellites near the intersection volume, the interceptor will lead the target, and a relative closing velocity of approximately 500 fps will exist between them. The preceding conditions have been established by the interceptor launch system. This nominal initial closing rate is determined primarily by considerations of the acquisition radar and the maximum bound on the duration of the homing phase. Since an initial relative closing rate has been previously established, the longitudinal corrections made during terminal guidance simply reduce this closing rate as the interceptor nears the target. The longitudinal corrections, which are made approximately along the LOS, are implemented by a single nozzle oriented along the roll axis of the rendezvous vehicle.

It is desired to achieve rendezvous in the shortest time consistent with a minimum fuel usage and the available vehicle acceleration. In addition, it is necessary to stipulate that the longitudinal velocity corrections be unilateral, due to vehicle design considerations. In view of the above considerations, it would appear optimum to achieve rendezvous by applying only one longitudinal velocity correction occurring at the very end of the terminal guidance phase. However, the use of a single longitudinal correction is not feasible due to normal velocity loop coupling, radar noise, etc. Indeed, the strong coupling from the range rate control system into the normal corrections makes the distasteful problem of frequent normal corrections a distinct possibility. Frequent normal corrections must be avoided, since adequate time must be allotted between corrections for filtering of the angular rate data and rolling the rendezvous vehicle.

The buildup of the angular rate may be limited by control of the initial time to closest approach τ. This, in turn, is readily accomplished by control of the interceptor closing rate. Thus it is quite possible to design a range rate control system to maintain a certain minimum time interval between normal corrections. The system to be presented maintains a minimum value of 20 sec between normal corrections. This is accomplished by constraining the time to closest approach to lie between 30 and 50 sec. The control of the time to closest approach τ is achieved by means of an on-off control system which employs a simple prediction process to prevent τ from dropping below the desired minimum value of 30 sec.

The longitudinal velocity corrections may be metered through the basic sensing element, i.e., the radar system. Switching decisions in the range rate system are made entirely on the basis of the values of τ calculated from the filtered range data and the direct range rate data supplied by the radar system. (This calculation is constantly in process in the digital computer.) The above constraint on τ forces the range to decrease approximately exponentially as a function of time. The variation is only approximately exponential, since the true curve is composed of linear and parabolic segments due to the alternation of free flight and longitudinal thrusting periods, respectively. During the initial portion of the terminal guidance phase, the initial time to closest approach greatly exceeds 30 sec and the range rate control loop is inoperative.

As the range becomes sufficiently small at the end of the

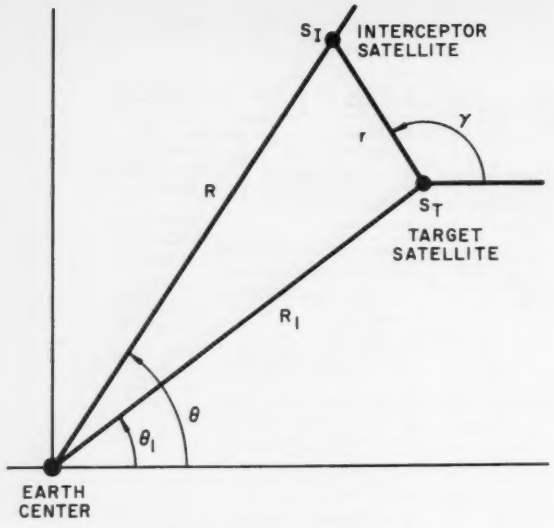

Fig. 3 Coordinate system

terminal phase, the range rate control loop is opened to permit vehicle control by a rendezvous maintenance or docking system. This range is chosen to afford the most desirable velocity and position entry conditions into the maintenance mode. If an initial closing velocity of 500 fps is assumed, the system achieves rendezvous from a range of 120,000 ft in approximately 400 sec. Rendezvous is assumed to be complete when the range becomes less than 200 ft.

System Analysis

Equations of Motion

The geometry of the problem of the relative motion of two nearby satellites is shown in Fig. 3.

The desired equations of motion may be written by Lagrange's method as

$$\ddot{r} - r\dot{\gamma}^2 = -\Omega^2 r[1 - 3\cos^2(\gamma - \theta_1)] + a_r \qquad [1]$$

$$r\ddot{\gamma} + 2\dot{r}\dot{\gamma} = -3\Omega^2 r \sin(\gamma - \theta_1)\cos(\gamma - \theta_1) + a_n \qquad [2]$$

These equations are valid in an inertial coordinate system centered in the target. To an observer in the interceptor, unaware that the interceptor is an Earth satellite, the terms involving Ω^2 in Eqs. 1 and 2 appear as small disturbing accelerations. However, these terms can have a large effect if the interception time becomes long. Also, if the satellites are very far from the Earth, the $\Omega \to 0$ and Eqs. 1 and 2 reduce to the simple form below

$$\ddot{r} - r\dot{\gamma}^2 = a_r \qquad [3a]$$

$$r\ddot{\gamma} + 2\dot{r}\dot{\gamma} = a_n \qquad [3b]$$

In the analysis that follows, Eqs. 3 are used. The complete equations were simulated on an analog computer; results agree very favorably with results obtained from the simplified set.

Normal Velocity Control

The analysis of the normal velocity control system must begin with a determination of the functional form of the angular rate of the LOS. The derivation of this behavior for the conditions applicable during a zero-thrust period is shown below. If the initial conditions upon entry into a zero-thrust period are denoted by the zero subscripts, one has by conservation of angular momentum

$$\frac{\dot{\gamma}}{\dot{\gamma}_0} = \frac{1}{(r/r_0)^2} \qquad [4]$$

If the normal velocity control system is operative, the interceptor is approximately on a collision course, and the range may be approximated by a linear function as

$$r \cong r_0 + \dot{r}t \qquad \dot{r} < 0 \qquad [5]$$

Thus

$$\left(\frac{r}{r_0}\right)^2 = \left(1 + \frac{\dot{r}}{r_0}t\right)^2 \qquad [6]$$

$$= (1 - t/\tau)^2 = (1 - t')^2 \qquad [7]$$

where

τ = initial time to closest approach $= r_0/-\dot{r}$
t' = normalized time $= t/\tau$

Hence

$$\frac{\dot{\gamma}}{\dot{\gamma}_0} \cong \frac{1}{(1 - t/\tau)^2} = \frac{1}{(1 - t')^2} \qquad [8]$$

The above expression indicates the behavior of the angular rate of the LOS during zero-thrust periods.

The behavior of $\dot{\gamma}$ during periods of normal thrusting is also of interest. Since each normal velocity correction removes only the sampled value of $r^*\dot{\gamma}^*$ present at the beginning of the correction, it is obvious that a residual amount of normal velocity will remain at the conclusion of the normal correction, unless the normal velocity correction could be performed instantaneously. This residual normal velocity supplies one of the components of the residual LOS angular rate which makes possible the induced limit cycle in the normal channel. This limit cycle, in turn, removes the necessity of rolling the rendezvous vehicle between corrections.

The equations of motion for the free space model during the normal velocity correction are

$$\ddot{r} - r\dot{\gamma}^2 = 0 \qquad [9]$$

$$r\ddot{\gamma} + 2\dot{r}\dot{\gamma} = a_n \qquad [10]$$

where a_n is interceptor normal acceleration. From Eqs. 5 and 10

$$\ddot{\gamma} + \left(\frac{2\dot{r}}{r_1 + \dot{r}t}\right)\dot{\gamma} = \frac{a_n}{r_1 + \dot{r}t} \qquad [11]$$

where the subscript 1 denotes conditions at beginning of normal correction, subscript 2 denotes conditions at end of normal correction. The above differential equation is linear in $\dot{\gamma}$ if $\ddot{r} \cong 0$ and the general solution may be written as

$$\dot{\gamma} = \frac{1}{(r_1 + \dot{r}t)^2}\left[a_n t\left(r_1 + \frac{\dot{r}}{2}t\right) + r_1^2\dot{\gamma}_1\right] \qquad [12]$$

The time required to remove the initial normal velocity is given by

$$t_n = r_1\dot{\gamma}_1/-a_n \qquad [13]$$

where a_n is negative to provide the correct guidance sense.

The residual angular rate may then be determined from Eq. 12 as

$$\dot{\gamma}_2 = \frac{a_n\dot{r}\dot{\gamma}_1^2}{2(a_n - \dot{r}\dot{\gamma}_1)^2} \qquad [14]$$

Since

$$|\dot{r}\,\dot{\gamma}_1| \ll |a_n|$$

$$\dot{\gamma}_2 \cong \frac{a_n \dot{r}\,\gamma_1^2}{2a_n^2} = \frac{\dot{r}}{2a_n}\dot{\gamma}_1^2 \qquad [15]$$

This residual angular rate $\dot{\gamma}_2$ is one of the two components that comprise the initial angular rate condition for entry into the next normal velocity cycle. The other contribution is the lag error of the filter in the angular rate channel. During the initial portion of the terminal guidance phase, the time to closest approach is quite large. This large value of τ results in relatively slow growth of the angular rate of the LOS $\dot{\gamma}$. This slow growth of $\dot{\gamma}$, in turn, results in a very small filter lag error. Thus, in the initial phase of terminal guidance, the primary contribution to the initial angular rate of the LOS results from the non-impulsive thrusting term derived above.

Hence, by combining the results of Eqs. 8 and 15, it is possible to completely formulate the behavior of the resultant limit cycle in the normal loop during the initial portion of the terminal guidance phase. Thus

$$\frac{\dot{\gamma}}{(\dot{r}/2a_n)\dot{\gamma}_1^2} = \frac{1}{(1-t')^2} \qquad [16]$$

Therefore, when $\dot{\gamma} = \dot{\gamma}_1$, in the above expression $t' = t'_c$, the normalized time of zero normal thrust, i.e., normalized time between normal velocity corrections.

The system behavior during this period is illustrated in Fig. 4. Rearranging Eq. 16 and solving for t'_c

$$t'_c = 1 - \sqrt{(\dot{r}/2a_n)\dot{\gamma}_1} \qquad [17]$$

The elapsed real time between normal corrections is given by

$$t_c = \tau t'_c \qquad [18]$$

where τ is computed at the beginning of the zero-thrust period.

The above expressions enable one to calculate quickly the time between normal velocity corrections under the assumption that the angular rate filter has no lag error. If it is desired to maintain a certain minimum time interval between normal corrections, an equivalent initial time to closest approach τ may be determined readily, since t'_c will be approximately constant during the period of interest. This equivalent minimum value of τ must be exceeded at all times if the minimum time between corrections is to be guaranteed. Control of τ is achieved by controlling the closing rate of the interceptor vehicle.

The variation of the normalized time between normal corrections as a function of the angular LOS rate threshold is presented in Fig. 5. The example values of initial closing rate $\dot{r}$ and the vehicle normal acceleration a_n are

$$\begin{aligned} \dot{r} &= -500 \text{ fps} \\ a_n &= -10 \text{ ft/sec}^2 \\ \dot{\gamma}_1 &= 2 \text{ milliradians/sec} \end{aligned} \qquad [19]$$

If the example values shown above are employed, the time between normal corrections t_c may be shown as a function of interceptor range at the beginning of the normal velocity cycle. This presentation is shown in Fig. 6.

If a threshold of 2 milleradians/sec is chosen, it is seen that the resultant normalized time between corrections is 0.7764. Hence, if it is desired to maintain at least 20 sec between normal corrections for purposes of filtering the angular rate data and rolling the rendezvous vehicle, it is seen that

$$\tau \geq \frac{20}{t'_c} = \frac{20}{0.7764} = 25.8 \text{ sec} \qquad [20]$$

This result is slightly in error due to neglect of the second

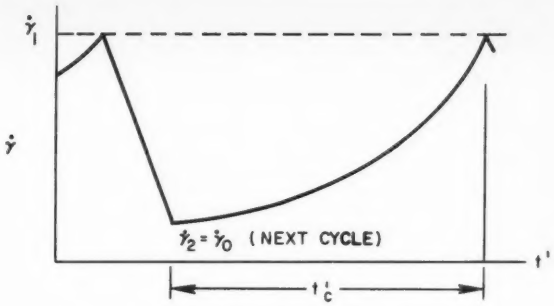

Fig. 4 Approximate behavior of LOS angular rate

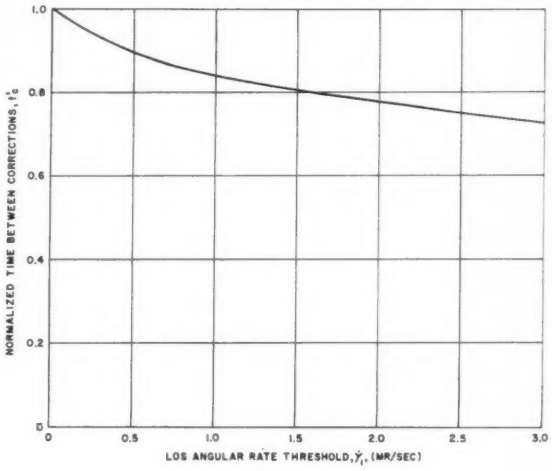

Fig. 5 t_c' variation with $\dot{\gamma}_1$

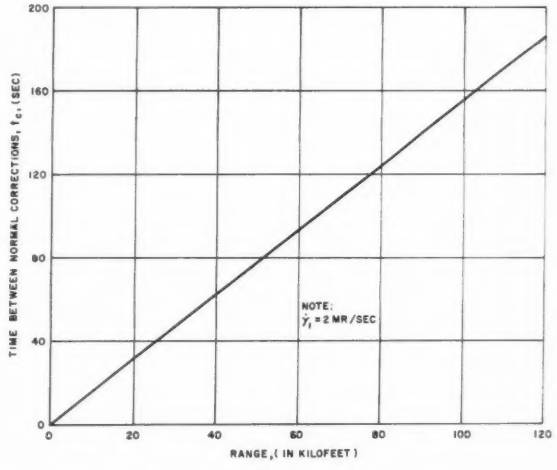

Fig. 6 t_c variation with range

contribution to the initial LOS angular rate, i.e., the filter lag error. This contribution is present, since the triggering of normal correction is dictated by an examination of the *filtered* values of $\dot{\gamma}$. Upon initiation of a normal correction, the normal velocity control system removes a normal velocity that is equivalent to the threshold value of $\dot{\gamma}$. Since the actual magnitude of $\dot{\gamma}$ will exceed that present at the output

of the filter, a residual $\dot{\gamma}$ will remain at the conclusion of the correction which is equal to the lag error of the filter. This residual amount contributes directly to the initial condition for the next normal velocity cycle.

As is the case with the residual due to non-impulsive normal thrusting, it is quite possible to remove a major portion of this residual by prediction techniques. However, this procedure is unnecessary, even unwise, since the residuals allow the establishment of a normal velocity limit cycle. This limit cycle eliminates the necessity for rolling the interceptor between normal corrections, since the direction of the normal corrections is now invariant in the normal plane.

In order to reduce the filter lag to a reasonable amount and yet maintain adequate noise rejection capability, a zero ramp-error filter was chosen with transfer function given by

$$F_{\dot{\gamma}}(s) = \frac{\frac{2\zeta}{\omega_1}s + 1}{\frac{s^2}{\omega_1^2} + \frac{2\zeta}{\omega_1}s + 1} \qquad [21]$$

where

$\zeta = 0.7$
$\omega_1 = 1$ rad/sec

A detailed analysis of the characteristics of this filter (which is not presented here) revealed that due to the additional filter lag contribution to the initial LOS angular rate, the range rate control system must maintain a minimum τ of 30 sec as contrasted with the 25.8 sec suggested in Eq. 20.

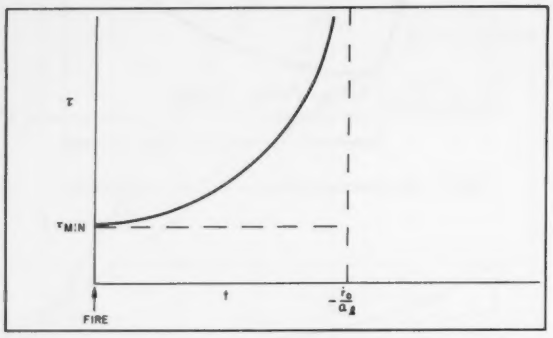

Fig. 7 τ variation, initial positive slope

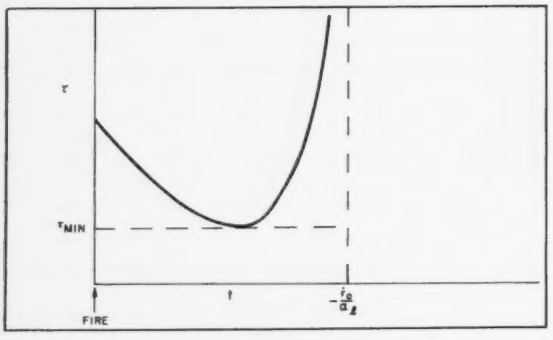

Fig. 8 τ variation, initial negative slope

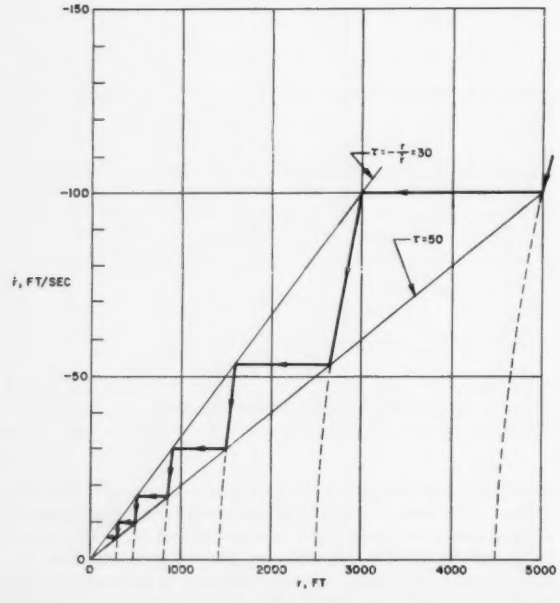

Fig. 9 τ funnel

Range Rate Control System

Since the range rate control system must maintain a time to closest approach of at least 30 sec, it appears feasible to construct an on-off control system that would constrain the time to closest approach to lie between specified limits. The lower limit of 30 sec is specified by the considerations of the normal velocity control system previously derived. The upper limit is set by consideration of the total rendezvous time, the interface with rendezvous maintenance mode, the time required to allow the range filter to settle after an acceleration input period, and the total number of longitudinal corrections. Upon consideration of the above criteria, the upper τ limit was chosen as 50 sec.

In order to implement the above system, one might examine the behavior of τ during a period of longitudinal thrusting.

$$\dot{r} = \dot{r}_0 + a_l t \qquad \dot{r}_0 < 0 \qquad [22]$$

$$r = r_0 + \dot{r}_0 t + (a_l/2)t^2 \qquad [23]$$

$$\tau = \frac{\dot{r}}{-\dot{r}} = \frac{r_0 + \dot{r}_0 t + (a_l/2)t^2}{-(\dot{r}_0 + a_l t)} \qquad [24]$$

$$\frac{d\tau}{dt} = -\left[1 - a_l \frac{(r_0 + \dot{r}_0 t + (a_l/2)t^2)}{(\dot{r}_0 + a_l t)^2}\right] \qquad [25]$$

It is noted that the initial slope of the τ curve may be positive or negative, depending upon the initial conditions. This situation is represented pictorially in Figs. 7 and 8.

If the initial slope $d\tau/dt$ is positive, the longitudinal correction is initiated on the basis of the expression

$$r \leq \tau_{\min}(-\dot{r})$$
$$\leq 30(-\dot{r}) \qquad [26]$$

The initial slope is positive if

$$r_0 \geq (-\dot{r}_0)^2/a_l \qquad [27]$$

This follows immediately from Eq. 25.

As may readily be seen from Fig. 8, prediction will be necessary to initiate a longitudinal correction in order to prevent τ

from dropping below 30 sec if the initial slope $d\tau/dt$ is negative. Thus, if

$$r < (-\dot{r})^2/a_t \qquad [28]$$

then $d\tau/dt = 0$ when

$$a_t \frac{[r_0 + \dot{r}_0 t + (a_t/2)t^2]}{(\dot{r}_0 + a_t t)^2} = 1 \qquad [29]$$

Solving for t

$$t = (1/a_t)[-\dot{r}_0 - \sqrt{2a_t r_0 - \dot{r}_0^2}\,] \qquad [30]$$

This is then the time at which τ attains a minimum value. The negative sign is employed in the quadratic solution, since this sign results in the minimum value solution. The positive sign gives the undesired maximum value. Substituting into Eq. 24

$$\tau_{\min} = \frac{2r_0 - (\dot{r}_0^2/a_t)}{\sqrt{2a_t r_0 - \dot{r}_0^2}} \qquad [31]$$

Solving for r_0

$$r_0 = \frac{\dot{r}_0^2}{2a_t} + \frac{a_t}{2}\tau_{\min}^2 \qquad [32]$$

In summary, if

$$r \geq (-\dot{r})^2/a_t \qquad [27]$$

fire when

$$r \leqq \tau_{\min}(-\dot{r}) \leqq 30(-\dot{r}) \qquad [26]$$

If

$$r < (-\dot{r})^2/a_t \qquad [28]$$

fire when

$$r = \frac{\dot{r}^2}{2a_t} + \frac{a_t}{2}\tau_{\min}^2 \qquad [32]$$

Longitudinal corrections are terminated when

$$\tau \geq 50 \quad \text{sec} \qquad [33]$$

This system assures that the time to closest approach will lie between 30 and 50 sec after range rate control is initiated.

The behavior of the range rate control system is visualized quite readily in the phase plane, as shown in Fig. 9. The phase plane makes it possible to estimate quickly the number of longitudinal corrections and the required rendezvous time for any given initial conditions. Since the response is constrained to lie between the radial lines in the phase plane, it is seen that the resultant range response is approximately that of an exponential in time as was previously mentioned.

Normal Velocity and Range Rate Loop Coupling

An examination of the coupling from the normal loop into the range rate loop will now be undertaken. This coupling takes the form of a centripetal acceleration due to the angular rotation of the LOS. This acceleration reduces the closing velocity of the interceptor.

From previous work

$$\ddot{r} - r\dot{\gamma}^2 = 0 \qquad [9]$$

$$r \cong r_0 + \dot{r}t \qquad \text{if } \ddot{r} \cong 0 \qquad [5]$$

$$\frac{\dot{\gamma}}{\dot{\gamma}_0} \cong \frac{1}{(1 - t')^2} = \frac{1}{(1 - t/\tau)^2} \qquad [8]$$

Thus

$$\dot{\gamma}^2 = \dot{\gamma}_0^2/(1 - t/\tau)^4 \qquad [34]$$

Integrating Eq 9

$$\Delta\dot{r} = \dot{\gamma}_0^2 \int_0^{t_c'\tau} \frac{(r_0 + \dot{r}t)dt}{(1 - t/\tau)^4} \qquad [35]$$

$$= \frac{\dot{\gamma}_0^2 \tau r_0}{2}\left[\frac{1}{(1 - t_c')^2} - 1\right] \qquad [36]$$

An examination of the above expression shows that the primary reduction in closing rate occurs at the large ranges when τ and r_0 are large. Indeed, the major reduction occurs during the first normal velocity cycle. If typical values are inserted in Eq. 36, it is found that the reduction in closing rate is less than 10 fps, a negligible amount.

It should not be inferred from the above result that the closing rate of the interceptor remains invariant during terminal guidance until disturbed by the range rate system. Indeed, this is quite incorrect. The above derivation assumed a free space model of the homing situation. An exact solution of the problem with the gravitational acceleration of Earth indicates the possibility of an appreciable reduction (40 fps or so) in closing rate for certain initial conditions. However, this reduction is unaffected by a change in the parameters of the normal velocity control loop. Hence, a more stringent stabilization of the LOS will not reduce the effects due to disturbing accelerations caused by the presence of Earth.

References

1 Duke, W. M., Goldberg, E. A. and Pfeffer, I., "Error Analysis Considerations for a Satellite Rendezvous," presented at the ARS Semi-Annual Meeting, Los Angeles, Calif., May 9–12, 1960 (*ARS preprint no. 1198-60*).

2 Sears, N. E., Jr. and Felleman, P. G., "Terminal Guidance for a Satellite Rendezvous," presented at the ARS Controllable Satellites Conference, M.I.T., April 30–May 1, 1959 (*ARS preprint no. 778-59*).

3 Clohessy, W. H. and Wiltshire, R. S., "Terminal Guidance System for Satellite Rendezvous," presented at the IAS National Summer Meeting, Los Angeles, Calif., June 16–19, 1959 (*IAS paper no. 59-93*).

4 Swanson, R. S., Petersen, N. V. and Hoover, L. R., "An Astro Vehicle Rendezvous—Guidance Concept," *Western Aviation*, vol. 40, no. 2, February 1960, pp. 12–15, 31–32.

Projected Path of the Longitudinal Axis of Earth-Stabilized Satellites

AVEDIS A. AINTABLIAN[1]

Lockheed Missiles and Space Co.
Sunnyvale, Calif.

A mathematical model that describes the motion of a point as seen by an orbiting satellite is presented. The model describes the resultant velocity vector on the surface of Earth as a function of satellite velocity and attitude, inclination of the orbital plane, latitude, longitude, altitude, and the rotation of Earth. The satellite is assumed to be oriented with its longitudinal axis perpendicular to the Earth's radius. Equations presented are limited to sensors whose axis is stabilized along the local vertical.

A MATHEMATICAL model is presented which describes the motion of a point as seen by an orbiting satellite, or, if transposed to Earth, it will describe the apparent projected velocity of the satellite. This projected velocity will be a function of the inclination angle of the orbit plane i, latitude ϕ, longitude β, altitude H, rotation of Earth ω, and the attitude of the satellite (pitch, roll and yaw rates). Mathematically, the above may be represented as

$$V = f\left(i, \phi, \beta, H, \omega, V_{sg}, \theta, \rho, \psi, \frac{d\theta}{dt}, \frac{d\rho}{dt}, \frac{d\psi}{dt}\right)$$

The equation of the various velocity vectors is derived for a circular orbit and spherical Earth. This assumption is justified, since apogee and perigee velocities vary by about 2% for near-circular orbits at nominal speed of 25,000 fps.

The equations of the velocities presented are derived in two directions: one along the vehicle path V_P, and the other perpendicular to it, V_Q. The equations for V_P and V_Q are in the form to permit their evaluation for zero and nonzero rates of pitch, roll, and yaw, and total velocity is obtained by the following equation:

$$V_T = \sqrt{(V_P)^2 + (V_Q)^2}$$

Relative Velocities

The equations of the velocities presented in this section are obtained by considering 1) circular orbit velocity of the satellite and the projected satellite velocity V_{sg}; 2) velocity vectors due to the rotation of Earth; 3) velocity vectors due to pitch, roll, and yaw rates; and 4) the total resultant velocity vector due to the combined effects mentioned above.

Circular Orbit and Projected Velocities

The circular orbit velocity V_s of the satellite is obtained by using Kepler's law of orbital motion

$$V_c = \sqrt{\mu/a} = V_s$$

where, from the Inverse-Square Law the constant $\mu = GM_e$, and the projected satellite velocity V_{sg} is obtained from similar triangle relationship, as shown in Fig. 1. Then

$$V_{sg} = V_s \frac{R_0}{r} = \frac{R_0}{r}\sqrt{\frac{\mu}{a}}$$

for a circular orbit of $a = r = R_0 + H$. The projected velocity of the satellite on the ground is then

$$V_{sg} = R_0(GM_e)^{1/2}/r^{3/2}$$

$$V_{sg} = R_0(GM_e)^{1/2}/(R_0 + H)^{3/2}$$

Projected Vehicle Path

The projection of the vehicle point P_{sg} on the surface of Earth will be in a plane through the center of Earth at a radius R_0 with an inclination angle i and for simplicity will be placed through the x-axis. Point P_{sg} can be represented vectorially as

$$\mathbf{P}_{sg} = R_0[\mathbf{i}\cos(\beta_v - \omega_v t) + \mathbf{j}\sin(\beta_v - \omega_v t)\cos i + \mathbf{k}\sin(\beta_v - \omega_v t)\sin i]$$

where

$\mathbf{i}, \mathbf{j}, \mathbf{k}$ = unit vectors along x, y, z (vectors are in boldface)
β_v = initial point of the projected vehicle point on the ground
ω_v = angular velocity of vehicle

Looking from the positive z-axis (North Pole) toward the origin, the Earth rotates counterclockwise, whereas the vehicle travels in a clockwise direction. The velocity vector $\mathbf{V}_{sg}$ can be obtained by differentiating the vector $\mathbf{P}_{sg}$ with respect to time

$$\mathbf{V}_{sg} = \frac{d}{dt}(\mathbf{P}_{sg})$$

Since the magnitude of V_{sg} has been obtained in a previous section, the present concern is its direction. The direction of V_{sg} is obtained by dividing the velocity vector $\mathbf{V}_{sg}$ by the absolute value of V_{sg} such that $\mathbf{V}_{sg}/|V_{sg}|$ is equal to the unit vector along V_{sg} (direction of the projected vehicle path). Then

$$\frac{\mathbf{V}_{sg}}{|V_{sg}|} = \frac{1}{\omega_v R_0}\frac{d}{dt}[\mathbf{P}_{sg}]$$

$$\therefore \mathbf{V}_{sg}/|V_{sg}| = \mathbf{i}\sin(\beta_v - \omega_v t) - \mathbf{j}\cos(\beta_v - \omega_v t)\cos i - \mathbf{k}\cos(\beta_v - \omega_v t)\sin i$$

which expresses the direction of projected vehicle path.

Velocity Due to Earth's Rotation

The velocity of a point P_e on the surface of the ground due to Earth's angular speed is presented in this section. The relationship of the orbit plane and projected velocity vector path is shown in Fig. 2.

Received Dec. 30, 1960.

[1] Senior Research Engineer, Space Systems Div.

Point P_e on the surface of Earth may be defined in terms of the longitude β, the latitude ϕ, and the angular velocity of Earth ω_e in terms of a fixed x, y, z coordinate system with reference to the center of Earth.

Using vectorial notation, point P_e can be represented as

$$\mathbf{P}_e = R_0\{[\mathbf{i}\cos(\omega_e t - \beta_0) + \mathbf{j}\sin(\omega_e t - \beta_0)]\cos\phi + \mathbf{k}\sin\phi\}$$

and its velocity vector is obtained by differentiation

$$\mathbf{V}_e = \frac{d}{dt}(\mathbf{P}_e)$$

$$\mathbf{V}_e = \omega_e R_0 \cos\phi[-\mathbf{i}\sin(\omega_e t - \beta_0) + \mathbf{j}\cos(\omega_e t - \beta_0)]$$

where $\mathbf{i}$, $\mathbf{j}$, $\mathbf{k}$ are unit vectors along x, y, z.

It is desirable to express the velocity vector V_e in terms of the apparent ground vehicle velocity V_{sg} to aid the manipulation of the equations. It is useful to express components of V_e to be parallel and perpendicular to the direction of V_{sg}. Thus, a common point P is of interest, defining P_e and P_{sg}, such that

$$\mathbf{P}_e = \mathbf{P}_{sg}$$

The relationship between V_{sg}, V_e with its components is

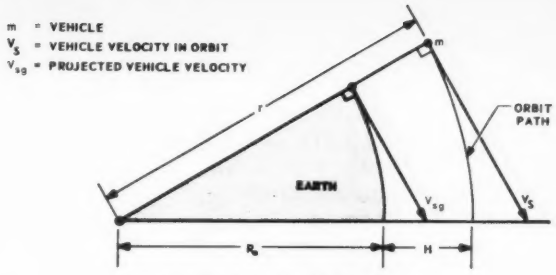

Fig. 1 Projected vehicle velocity

shown in Fig. 3, where

α = $90° + \delta$
V_e = velocity of a point at the surface of Earth due to Earth's rotation
V_{ep} = velocity component of V_e parallel to V_{sg}
V_{eq} = velocity component of V_e perpendicular to V_{sg}
$\cos\alpha$ = $-\cos i/\cos\phi$

Parallel component of V_e (V_{ep})

The component of V_e parallel to V_{sg} can be obtained by

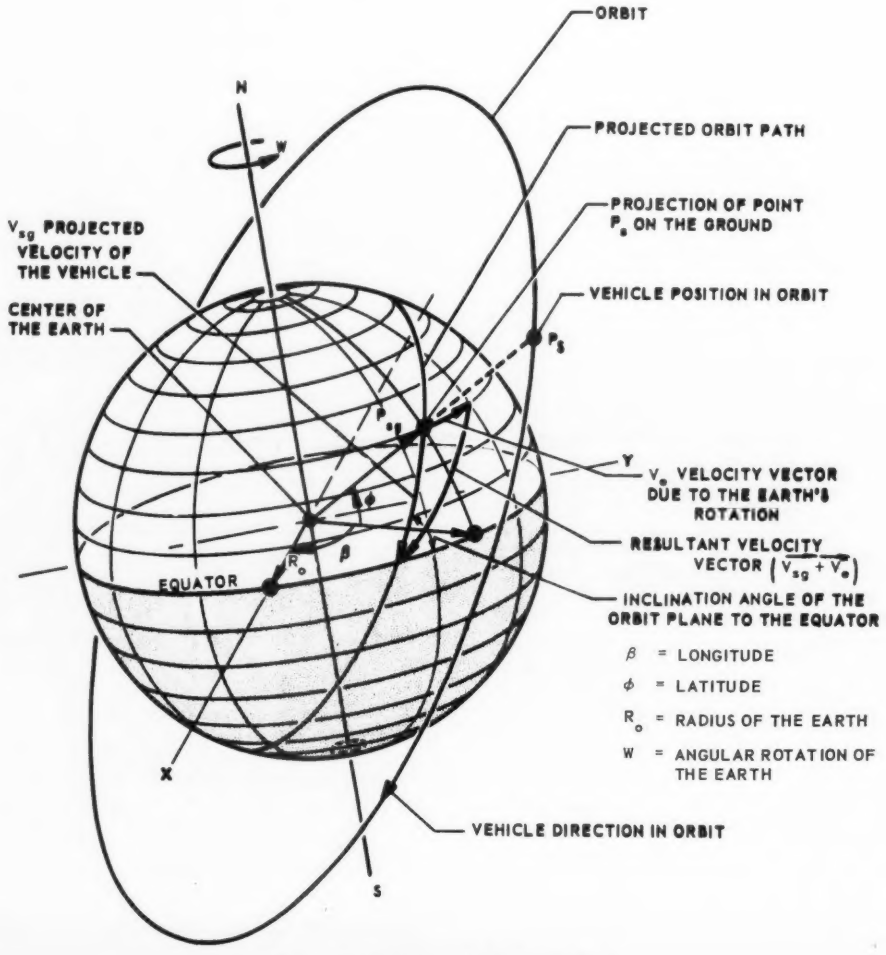

Fig. 2 Orbit plane and relative motion

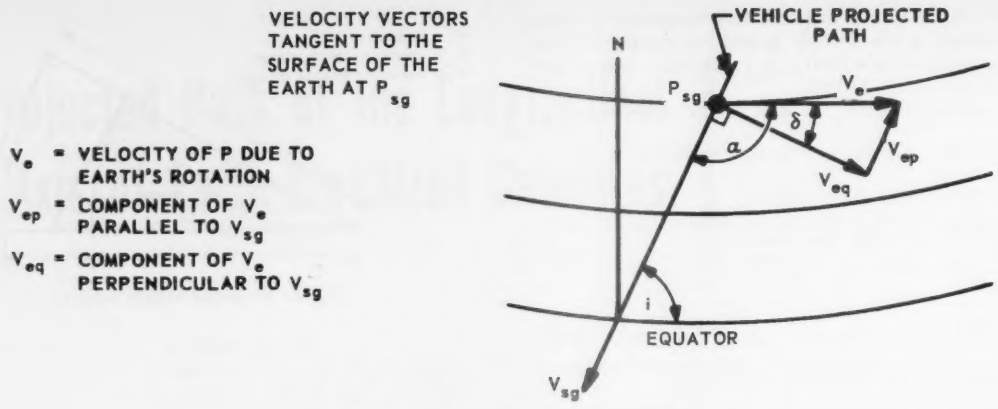
VELOCITY VECTORS TANGENT TO THE SURFACE OF THE EARTH AT P sg
V e = VELOCITY OF P DUE TO EARTH'S ROTATION
V ep = COMPONENT OF V e PARALLEL TO V sg
V eq = COMPONENT OF V e PERPENDICULAR TO V sg
VEHICLE PROJECTED PATH
N
P sg
V e
δ
α
V ep
V eq
i
EQUATOR
V sg

Fig. 3 Velocity vector due to Earth's rotation

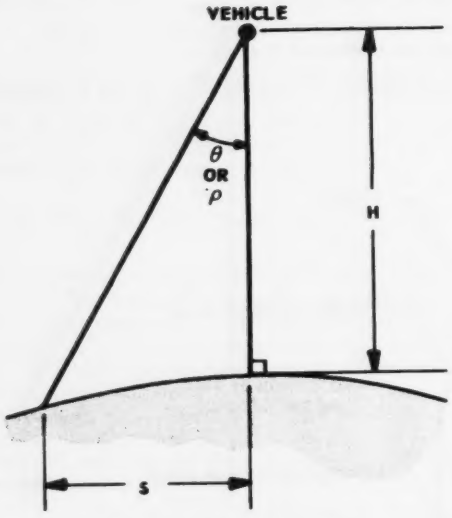

Fig. 4a Pitch roll, condition

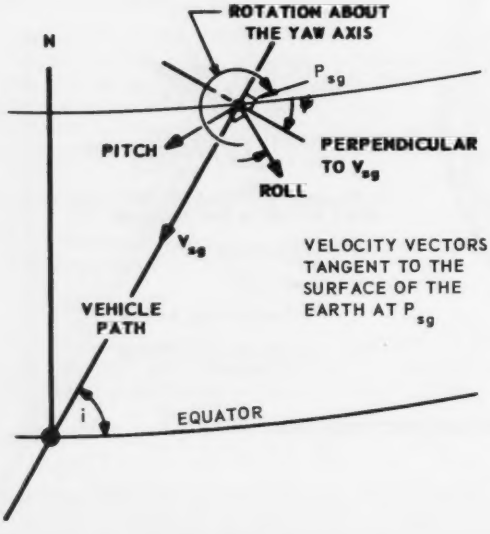

Fig. 4b Yaw conditions

taking the dot product of the vector V_e and the unit vector along V_{sg}. Mathematically, this can be expressed as

$$V_{ep} = \mathbf{V}_e \cdot \frac{\mathbf{V}_{sg}}{|V_{sg}|}$$

Substituting values of V_e and $\mathbf{V}_{sg}/|V_{sg}|$ and performing the operation while taking into account that $\mathbf{P}_e = \mathbf{P}_{sg}$ gives

$$\mathbf{V}_e \cdot \frac{\mathbf{V}_{sg}}{|V_{sg}|} = |V_e| \cos \alpha =$$

$$\omega_e R_0 \cos \phi \left(-\frac{\cos i}{\cos (\phi)} \right) = -\omega_e R_0 \cos i$$

The significance of this relationship is that the component of V_e parallel to the orbit plane remains constant, and its magnitude is equal to Earth's equatorial velocity mutliplied by the cosine of the inclination angle. In addition, the apparent projected vehicle velocity, altitude, latitude, and longitude do not contribute in any way to the value of V_{ep}.

Perpendicular component of V_e (V_{eq})

The component of V_e perpendicular to V_{sg} is obtained as follows:

$$V_{eq} = |V_e| \sin \alpha$$

$$V_{eq} = \omega_e R_0 \cos \phi \sin \alpha$$

$$V_{eq} = \omega_e R_0 \cos \phi (1 - \cos^2 \alpha)^{1/2}$$

$$V_{eq} = \omega_e R_0 (\cos^2 \phi - \cos^2 i)^{1/2}$$

The latitude of the subsatellite point is obtained from

$$\cos \phi = (\cos^2 \sigma_1 + \sin^2 \sigma_1 \cos^2 i)^{1/2}$$

Substituting for $\cos^2 \phi$ gives the desired result

$$V_{eq} = \omega_e R_0 [\cos^2 \sigma_1 + \sin^2 \sigma_1 \cos^2 i - \cos^2 i]^{1/2}$$

$$\therefore V_{eq} = \omega_e R_0 \sin i \cos \sigma_1$$

The component of V_e perpendicular to the orbit plane is equal to a constant times the cosine function of the vehicle longitudinal angle. It is a maximum at the Equator at crossing of the orbit plane. The above equation is a general case whereby the assumption made previously for the orbit plane passing through the x-axis is not necessary.

Pitch, Roll, and Yaw Equations

The velocity vectors resulting from pitch, roll, and yaw

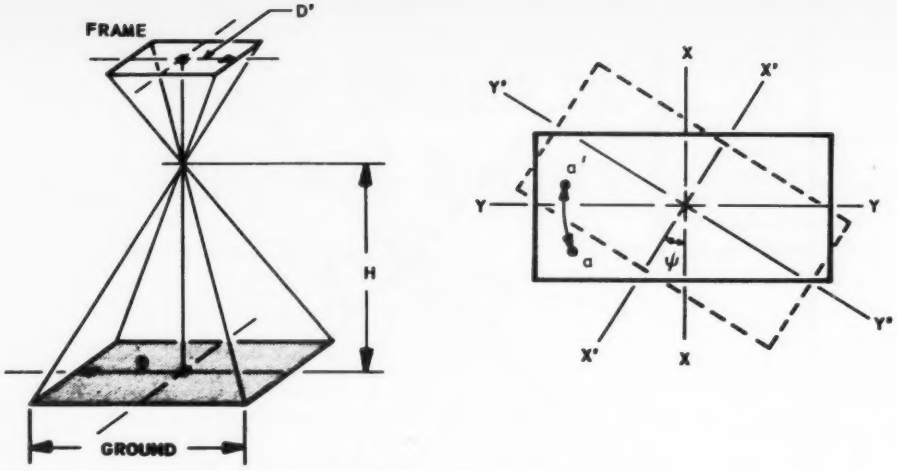

Fig. 5 Displacement due to yaw

motions are described and presented in this section. The contribution of each (pitch, roll, or yaw) has been studied and expressions derived; their combined effect will be presented in the following section.

Pitch rate

Consider a vehicle at an altitude H above the ground. A pitch angle θ will sweep an arc (distance) s as shown in Figs. 4a and 4b. Limiting θ for small angles gives

$$S_\theta \approx H \tan \theta$$

$$V_\theta = \frac{dS_\theta}{dt} = H \frac{d}{dt} (\tan \theta)$$

where

H = altitude, constant
S_θ = arc distance subtended by pitch angle
V_θ = apparent ground velocity due to pitch rate

Then

$$V_\theta = (H/\cos^2 \theta)\dot{\theta}$$

Roll rate

A roll angle ρ will sweep an arc S_ρ as shown in Figs. 4. Using the procedure described in the section on pitch rate, the roll distance and velocity are obtained and can be expressed as

$$S_\rho \approx H \tan \rho$$

$$V_\rho = (H/\cos^2 \rho)\dot{\rho}$$

Yaw rate

Consider an area on the surface of Earth being transposed to an image frame at an altitude H (see Fig. 5). When pitch and roll are equal to zero for a yaw angle displacement of ψ degrees, point a will appear at a'. Then, the velocity of an arbitrary point within this area due to yaw can be expressed as

$$V_\psi = D\psi$$

When pitch and roll are equal to zero for a yaw angle ψ, the velocity V_ψ of a point due to yaw rate will have components perpendicular and parallel to the vehicle path. The components of V_ψ may be expressed as

$$V_{\psi p} = V_\psi \cos \psi$$

where the velocity is parallel to V_{sg} and

$$V_{\psi q} = V_\psi \sin \psi$$

where it is perpendicular to V_{sg}.

Total Relative Velocities

Previous sections presented individual velocity vectors due to vehicle velocity, rotation of Earth and velocities due to pitch, roll, and yaw rates. This section will present the combined effects of various velocities parallel and perpendicular to the projected vehicle path on the ground (see Fig. 6).

Velocities parallel to vehicle path

The contribution of the velocities parallel to the projected vehicle path are as follows:

V_{sg} = apparent ground velocity of vehicle
V_{ep} = parallel component of V_e, due to Earth's rotation
$V_{\theta p}$ = pitch velocity parallel to V_{sg}
$V_{\rho p}$ = roll velocity parallel to V_{sg}
$V_{\psi p}$ = yaw velocity parallel to V_{sg}

Then the total parallel component V_p is obtained as

$$V_P = V_{sg} + V_{ep} + V_{\theta p} + V_{\rho p} + V_{\psi p}$$

where the sign in actual evaluation could be positive or negative.

$$V_{sg} = R_0(GM_e)^{1/2}/(R_0 + H)^{3/2}$$

$$V_{ep} = -\omega_e R_0 \cos i$$

$$V_{\theta p} = V_\theta \cos \psi = \frac{H}{\cos^2 \theta} \dot{\theta} \cos \psi$$

$$V_{\rho p} = V_p \sin \psi = \left(\frac{H}{\cos^2 \rho} \dot{\rho}\right) \sin \psi$$

$$V_{\psi p} = V_\psi \cos \psi = D\psi \cos \psi$$

Replacing the individual terms in the general equation, we

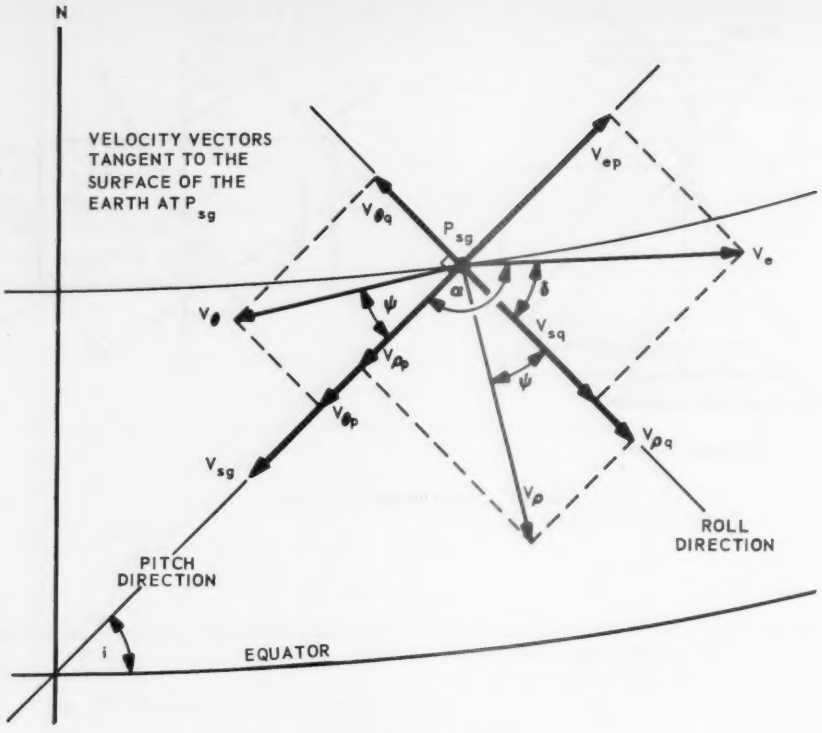

Fig. 6 Total velocities

V_{eq} = projected vehicle velocity
V_e = velocity of P due to Earth's rotation
$V\theta$ = velocity due to pitch angle θ
V_ρ = velocity due to roll angle θ
ψ = yaw angle
i = inclination angle of orbit plane to the Equator

Subscripts

p = component of V parallel to V_{sq}
q = component of V perpendicular to V_{sq}

obtain

$$V_P = \frac{R_0(GM_e)^{1/2}}{(R_0 + H)^{3/2}} - \omega_e R_0 \cos i + \left(\frac{H}{\cos^2\theta}\dot{\theta} + D\dot{\psi}\right)\cos\psi + \left(\frac{H}{\cos^2\rho}\dot{\rho}\right)\sin\psi$$

Velocities perpendicular to vehicle path

The contribution of the velocities perpendicular to the projected vehicle path are

V_{eq} = perpendicular component of V_e due to Earth's rotation
$V_{\dot{\theta}q}$ = pitch velocity perpendicular to V_{sq}
$V_{\dot{\rho}q}$ = roll velocity perpendicular to V_{sq}
$V_{\dot{\psi}q}$ = yaw velocity perpendicular to V_{sq}

Then the total perpendicular component V_Q is obtained as

$$V_Q = V_{eq} + V_{\dot{\theta}q} + V_{\dot{\rho}q} + V_{\dot{\psi}q}$$

$$V_{eq} = \omega_e R_0 \sin i \cos\sigma_1$$

$$V_{\dot{\theta}q} = \frac{H}{\cos^2\theta}\dot{\theta}\sin\psi$$

$$V_{\dot{\rho}q} = \frac{H}{\cos^2\rho}\dot{\rho}\cos\psi$$

$$V_{\dot{\psi}q} = D\dot{\psi}\sin\psi$$

therefore

$$V_Q = \omega_e R_0 \sin i \cos\sigma_1 + \left(\frac{H}{\cos^2\theta}\dot{\theta} + D\dot{\psi}\right)\sin\psi + \frac{H}{\cos^2\rho}\dot{\rho}\cos\psi$$

Total velocity vector

The total velocity vector is obtained from the resultant parallel and perpendicular components of velocities as follows:

$$V_T = \sqrt{(V_P)^2 + (V_Q)^2}$$

Thus, total resultant relative velocity can be obtained with ease for zero and nonzero values of each case or for the combined effects of pitch, roll, and yaw rates.

Nomenclature

a = semimajor axis of the ellipse
b = semiminor axis of the ellipse
G = gravity force
M = mass
t = time
δ = angle between V_e and V_{eq}, perpendicular to V_{sq}
σ_1 = $(\beta_v - \omega_v t)$, satellite anomaly

Modified Chromium for Unprotected Structures

David M. Scruggs[1]

The Bendix Corp.
South Bend, Ind.

Ceramic additions to chromium have produced a material with the ability to withstand a heat flux of 400 Btu/sq ft/sec in air without erosion or structural failure. This material is a mixture of electrolytic chromium and an oxide of a Group 2 metal. Exposure in air forms a complex oxide coating of high refractoriness and will not lower the chromium melt point. It was found that chromium could be made to withstand oxidizing environments to 3800°F, whereas pure chromium will withstand 3200°F in supersonic air for a matter of seconds. Modified chromium can be extruded, hot formed, and easily machined. Extruded material has exhibited room temperature ductility in the order of 15% elongation in tensile testing. Strength oxidation resistance and ductility have been improved over those of arc melted chromium.

AN APPLIED research study was initiated to investigate material systems that were to be immune to glide re-entry environment withstanding oxidation and erosion of hypersonic gas. Systems were investigated with the goal of achieving a material that would withstand conditions without secondary protection methods and without cooling except by radiation. A series of properties were chosen and ranked to facilitate the compromise solution to the inherent problems of re-entry, in particular oxidation resistance, strength, reliability, and light weight. The principal criterion selected was the ability to withstand an arbitrary heat flux of 400 Btu/sq ft/sec in air.

The first step in defining the material system was to investigate a number of materials that were available in their commercial form, such as ceramics, refractory metals, and graphite. A kerosene-oxygen small scale rocket was used for screening materials at a heat flux of 400 Btu/ sq ft/sec. This apparatus operates at 50 psi chamber pressure and the gases at exit are at Mach 1.8 and 4800°F. A fuller discussion of the apparatus and the heat flux calorimetry can be found in (1).[2] No material was found to withstand the defined conditions without excessive ablation, erosion, or cracking. Surface temperature generated in this test ranged from 3000° to 3500°F, according to the material.

Upon deriving a list of primary attributes that would be necessary for structural material in glide re-entry, certainly resistance to rapidly moving gas, or erosion, was the most important, followed by oxidation resistance, tensile strength, elongation, density, and elastic modulus. Certain other service qualities such as machineability, forgeability, and emissivity are important. Table 1 presents a brief list of different properties and attributes as they vary from metal through cermets to ceramic structures. In particular, where formability or ability to be cast is used, a metal is necessary. The ceramic materials, of course, rank high in rigidity and oxidation resistance. Unfortunately, the usual cermet concept, i.e., a mixture of metal and ceramic, although designed particularly to gain the attributes of each system, has proved to represent the poorer aspects of both the metal and the ceramic system. Metallic properties are inherently more suited to structures that must be fabricated in large size and number and that must withstand multiaxial stress. A number of avenues of approach, none clear cut, are possible using refractory metals. Principally because of its excellent oxidation resistance, chromium was chosen for modification with the aim of producing structures that would withstand glide re-entry.

As can be seen from Fig. 1, chromium is the best of the refractory metals for resistance to oxidation at 2000°F and higher (2). A number of investigators (3) have found, however, that chromium forms an oxide scale that crumbles and flakes off at temperatures above 2000° F. A photograph of a pure chromium disk that has been subjected to 400 Btu heat flux is shown in Fig. 2. At 3200° to 3250°F, by total radiation pyrometer measurement, the surface melts or fluxes, resulting in failure. It can be seen in Fig. 3 from the chromium-oxygen system equilibrium diagram (4) that an addition of a small amount of oxygen greatly lowers the refractoriness of chromium in the Cr_2O_3 rich portion of the diagram. The eutectic is quite low, 3020°F. The actual reactions take place with other lower oxide forms of chromium in a nonequilibrium ternary or quaternary fashion, but the binary diagram serves to point out the direct cause of failure. Thus, where temperatures are high and heating is rapid in the presence of oxygen, chromium cannot be expected to react as a refractory to its melt point, but only to be useful to 3200°F or less in air.

There has been a variety of work on different alloy combinations using chromium as a base material. Probably some of the best of these are described in (2). In alloy work with chromium, it is unfortunate that solid solutioning does not occur with some useful metal to keep the liquidus near the chromium melt point, since the usual alloy addition succeeds only in lowering the refractoriness of the resulting alloy due to eutectic formation. In short, there is no alpha-phase chromium alloy available for use in a glide re-entry structure. The answer must then lie in altering the refractory ability of the chromium itself. This report covers the work of this nature that was done at Bendix Products Division.

Chromium

The general properties of chromium are not particularly promising when viewed for use at high temperature. While the oxidation rate at 2000°F is quite acceptable, this rate gains considerably as the temperatures increase. Fig. 4, showing tensile strength of chromium, has been reproduced from (2). At 2000°F the tensile strength is only 8500 psi and falling rapidly, and it all but disappears at 2600°F. Ductility is

Presented at the ARS Meeting, Palm Springs, Calif., April 4–6, 1961; revision received Sept. 25, 1961.

[1] Materials Engineer, Bendix Products Div.

[2] Numbers in parentheses indicate References at end of paper.

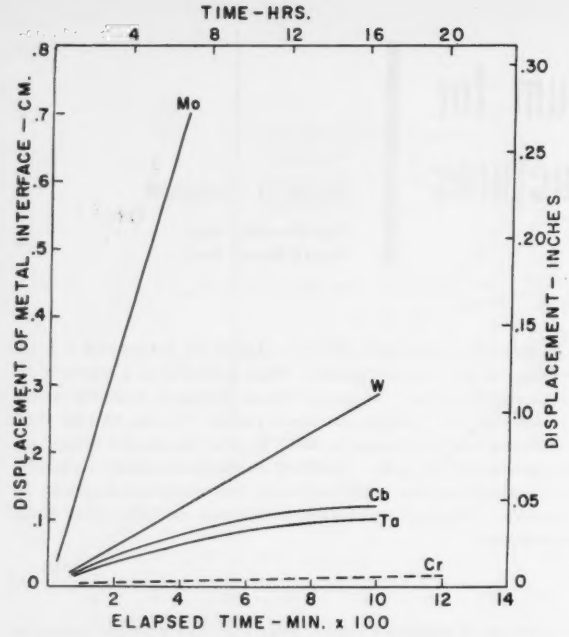

Fig. 1 Oxidation rates of the refractory metals in terms of surface displacement at 2010° F

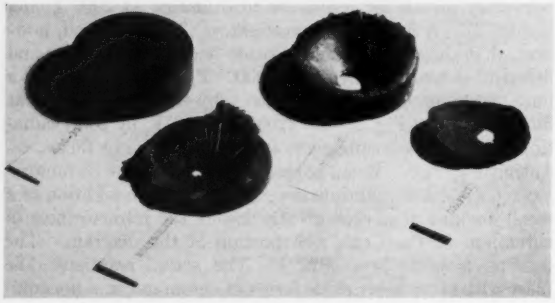

Fig. 2 Heat flux samples after test at 400 Btu/sq ft/sec

absent at room temperature, and chromium is very notch sensitive. It is beyond the scope of this paper to review the nitrogen embrittling of chromium (5); however, if ultra pure chromium that is ductile at room temperature is exposed to air at red heat, it quickly absorbs nitrogen and embrittles, nullifying the effect of high purity. More specifically, to resort to ultra high purity is in direct opposition to the engineering techniques of alloying, high production, and low cost quality. Erosion resistance is not satisfactory near 3200°F. Chromium itself then is not completely acceptable for oxidation resistance, has nothing to promise in erosion resistance, is a material that is extremely difficult to form, and has very low strength at 2600°F.

Attention will first be turned toward the most stringent problem, that of erosion resistance and the chromium oxide reactions. Some means of modifying the chromium had to be found so that the chromic oxide and lower oxides would not flux with the chromium substrate. A stable oxide film that would protect the underlying chromium without reaction was needed. It is the oxide formation that gives chromium its oxidation resistance, so if the oxide scale is removed, the chromium rapidly oxidizes and is very active in forming a new film of oxide. Chromium is similar in this case to aluminum and its coating of aluminum oxide. Chromium has an affinity for oxygen (6), illustrated by the fact that to protect it from oxygen in a hydrogen atmosphere, the hydrogen must have a dew point of about −50°F at 2300°F. The addition of hydrides, silicides, borides, and other intermetallics was expected to form a ternary composition because of the activity of the chromium and its affinity for silicon, nitrogen, or any high valence elements. A set of rules that will help to clarify the problem and the solution involved can be delineated for alloy selection.

Rule 1: Helpful metallic alloy additions can be designed only for solid solution or to form nonsensitive inclusions as oxides or nitrides of the alloy addition.

Rule 2: A second phase, if used, must not react to form a eutectic with the stable oxide or suboxides of the base metal. If possible, the second phase would react with and change the nature of the oxide of the base metal to 1) hold the oxide scale; 2) reduce oxygen diffusion; and 3) prevent fluxing with the base metal.

Rule 3: The method of formation of the hard phase or the second phase is immaterial.

Rule 4: The micromorphology of the second phase has an extreme importance, usually eclipsing compositional considerations.

Modified Chrome

Following the set of guide rules, the first definite step in modifying chrome for use in glide re-entry conditions would be to add some nonsensitive material that will not flux with the chromium-chromium oxide system. This system will form some stable oxygen diffusion barrier, which will remain intact throughout the service life of the material. The most logical approach was to add a spinel forming ceramic, such as MgO, to form an $MgO \cdot Cr_2O_3$ spinel because of its high melt point and stability. It would still be questionable that the spinel would be stable in the exposure during re-entry at high temperature. Before any testing need be carried out, it could also be assumed from theory that an oxide addition such as a very small, hard particle would increase the strength of the basic chromium material. It follows that the addition of the light oxide would lower the density and change the modulus of the material.

It was found that the addition of the Group 2 oxides,[3] in particular magnesium and calcium oxides, did form an oxide system that adequately protected the chromium to a degree that was not anticipated. The successful addition of ceramic corresponded to a 2 : 1 mole ratio of Cr_2O_3 to MgO in the surface oxide expressed in chemical notation $MgO \cdot 2Cr_2O_3$. The melt point of this complex is taken to be the liquidus at its lowest point between $MgO \cdot Cr_2O_3$ spinel and Cr_2O_3, this point corresponding to 3900°F. This equilibrium diagram is not

[3] Patent applied for.

Table 1 Selection criteria

Metal	Cermet	Ceramic
Ductility, good	poor	very poor
Castable	...	difficult to form
Malleable	no	no
Machineable	fair to poor	poor
Oxidation, good to very poor	poor	no problem
Conductivity, high	medium	low

Table 2 Erosion data for various materials in kerosene plus oxygen gases, Mach 1.8 4800°F, 400 Btu/sq ft/sec heat flux

Material	Exposure time, min	Surface temp. by optical pyrom-eter	Erosion, mils/sec	Estimated thickness eroded, 30 min
Modified chrome-30	10.0	3480	0	0
Chromium	2.1	...	2.3	4.1 in.
Tungsten	4.2	3200	1.0	1.8 in.
Graphite, ATJ	4.0	3330	0.97	1.7 in.
Molybdenum	0.7	...	2.84	5.1 in.
Trevarno glass phenolic F-122	0.4	...	19.3	34.7 in.

completely explored (7) but is sufficient, as data presented later will illustrate. The liquidus point for the $CaO \cdot Cr_2O_3$ system at $CaO \cdot 2Cr_2O_3$ is at 3800°F.

A photograph of the sample disk of modified chromium using MgO addition is shown in Fig. 2. This photograph also illustrates molybdenum and graphite. These particular samples are listed in Table 2, which summarizes selected materials screened at 400 Btu heat flux. The excellent results, particularly as the surface temperature was above the melting point of the chromium itself, were rather surprising.

Other results were obtained in a plasma jet at the University of Dayton operated at the various energy levels listed. Apparent surface temperature was obtained by correcting an optical thermopile reading using a calculated emittance. In order to correlate the two sets of data, the kerosene-oxygen torch was used at increased heat fluxes until surface melting occurred. Melting was detected at 500 Btu/sq ft/sec heat flux and 3750°F by optical pyrometer. The pyrometer was calibrated and at that temperature read ±20°F. Correcting for an emittance of 0.9 by applying the ratios of the fourth powers, the actual temperature is then 3850°F. This temperature agrees with the liquidus point of the pure oxide complex and also with the data of (8, 9), since the heat flux at failure is nearly equivalent, if it is considered that the apparent surface temperatures are arrived at using a lower emittance.

The modification of chromium employing magnesia has been coded as Chrome Cerametalix-30 and will be referred to as *Chrome 30*. Using the modification rules as outlined, chromium has thus been enhanced in its ability to withstand re-entry conditions even beyond its melt point at the surface, thus providing operation in environments beyond which the pure material could operate. The results obtained demonstrate the applicability of the rules listed above.

Given an erosion resistance that permits operation at 2600°F and higher as a possible structural material in re-entry, practical questions involving structural feasibility must be answered. Fortunately, there are some useful metallic properties present in modified chromium. There are also a number of other attributes gained through the addition of ceramic to chromium. It can be seen in Fig. 4 that oxidation rate at the lower temperatures (2000°F and above) were reduced by a significant factor. At 2200°F the rate for Chrome 30 is only slightly higher than at 2000°F. Flaking of oxide scale occurs on cooling from 2400°F. Samples were removed from the furnace for weighing resulting in a recorded loss at 2400°F for Chrome 30. Weight is thus lost at this temperature and above. The data plotted from (10) were obtained by continuous weighing on a microbalance. Points on the curve in Fig. 4 marked with diamonds are from data released by WADD (9). A slightly different modification of chromium

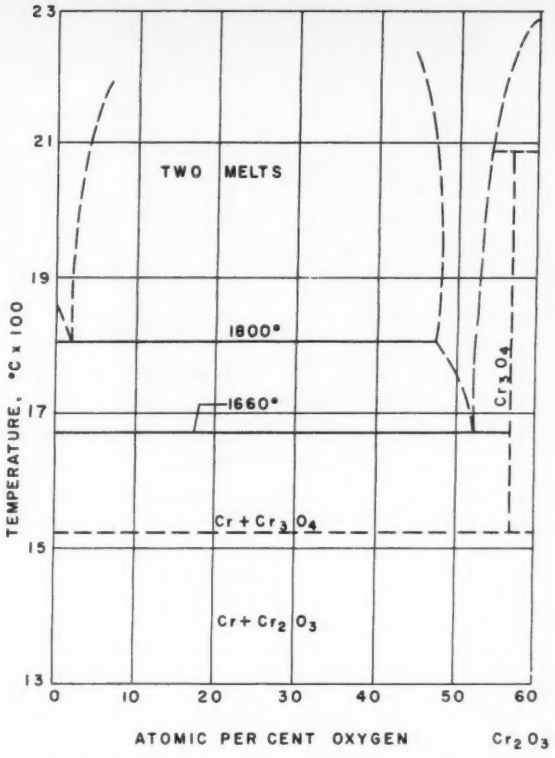

Fig. 3 Equilibrium diagram chromium-oxygen system

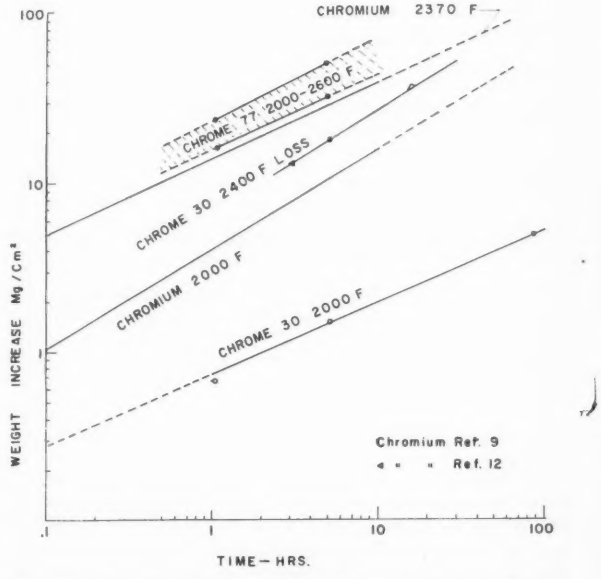

Fig. 4 Oxidation rates of chromium and modified chromium at various temperatures

employing calcia is shown in the oxidation chart coded Chrome 77. This modification does not flake except for *polka dotting*, which uncovers only a small area of the metal. Another aspect of long term stability at high temperature in terms of stress rupture data remains to be investigated.

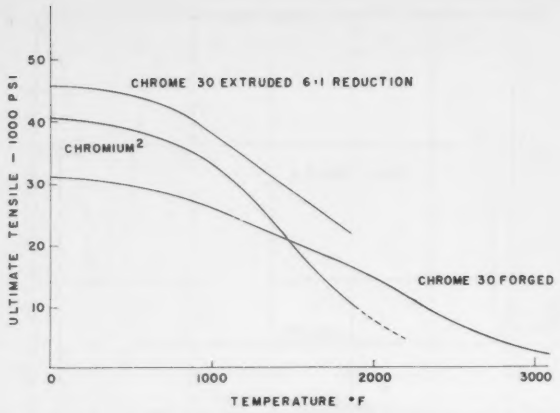

Fig. 5 Ultimate tensile strengths of chromium and Chrome 30 at various temperatures

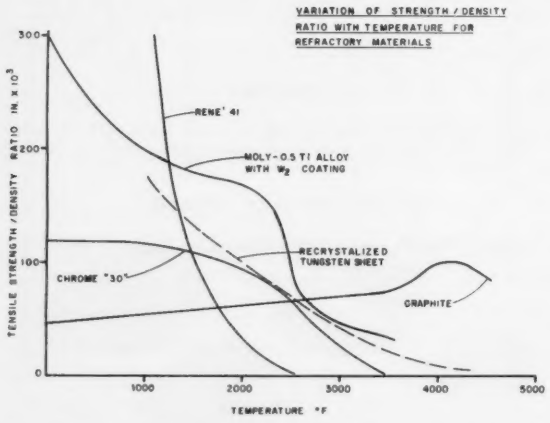

Fig. 6 Strength-density ratio at various temperatures for selected refractory materials

Table 3 Cold working and retention of strength after recrystallization—Chrome 30

Condition	Transverse strength
Before work	30,000 psi
Cold work 50%	77,000 psi
Soak 1 hr 2200°F	59,000 psi

The addition of ceramic definitely increases the strength at higher temperatures of the chromium. Tensile strength of chromium and Chrome 30 are plotted in Fig. 5. In considering certain nonmetallic materials, it is illuminating to note that beryllium oxide has a tensile strength of only 600 psi at 2600° F (11). Modified chromium is not only oxidation and erosion resistant, but also compares favorably on a strength weight basis with recrystallized molybdenum at 2600° F. Semchyshen and Barr (12) report yield strengths of molybdenum-0.5 titanium sheet ranging from 5900 psi to 11,100 psi at 2400° F. A generalized plot of the ultimate tensile strength to density ratio in in. $\times 10^3$ is presented in Fig. 6. Values for Chrome 30 are based on as-forged material. The operating limit of nickel base alloys is exceeded by roughly 800° F at the present state of the art. Extruded material strength included in the curve would correspondingly raise the Chrome 30 ordinate values.

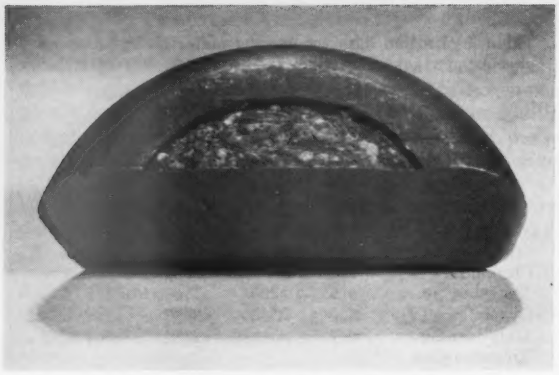

Fig. 7 As-forged section of Chrome 30 reduced 75%

Modified chromium surpasses the base metal in refractory ability and strength and also closely parallels the metallic nature of the matrix. Chrome 30 can be cold worked over 50% and hot worked at higher values by forging and extruding. Fig. 7 illustrates a single 75% reduction by hot forging. Cold working can be accomplished by press forging at room temperature, keeping the material generally under compression. Working to a 50% reduction has been accomplished without cracking of the part. Internal cracks sometimes form and cause failure at low work percentages. Increase of strength by cold working at room temperature is considered impractical at this time. Nitrogen level in chromium has been shown to be of extreme importance in determining the ductility and transformation temperature (5). Commercially pure materials are used in Chrome 30, and no attempts have been made to lower the nitrogen content or to measure it at this time. The ceramic addition is also a gross source of contamination. The unworked microstructure of modified Chrome 30 is shown in the photomicrographs of Fig. 8. Fig. 9 is a cold worked structure deformed over 50%. In this case the outside fibers are deformed by the working. This is a promising sign in the state of the art with chromium. Since this example is contaminated chromium material with over 10% by volume of ceramic added, it is even more significant. Cold working of the modified chromium produces strain effects and increases the strength of the matrix. The ceramic at the grain boundaries enables the material to hold a considerable amount of the strain even through recrystallization. Chrome 30 was cold worked 50% at room temperature and recrystallized at 2200°F for 1 hr. Table 3 summarizes the changes in transverse strength. The material had completely recrystallized at 2200°F, but no grain growth had occurred.

Modified chromium has the mechanical working characteristics of a metal at elevated temperatures. This is extremely important since forged structures, extruded rods and tubes, and rolled plates are made possible. Not only are these processes capable of producing large shapes in quantity, but hot working has the effect of producing built-in quality. Hidden defects in the material will generally cause failure during fabrication. Ceramics and certain metal alloys cannot be worked and are therfore difficult to control in so far as mechanical properties are concerned. Chromium as a pure metal has been handled principally in laboratory amounts and worked as an ultra pure product, and working has been accomplished using protective sheaths to prevent contamination. Spachner and Rostocker (13) report forging arc melted chromium using $^1/_{16}$ in. reductions on 3-in. diam $\times$ 6-in. high ingot progressing to higher and higher reductions. Forging modified chromium, as shown in Fig. 7, is done at

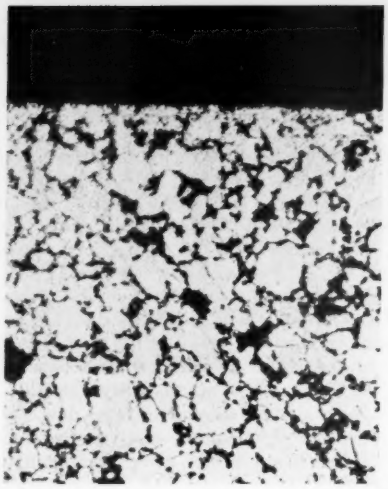

Fig. 8 Surface photomicrograph of unworked Chrome 30 (100X)

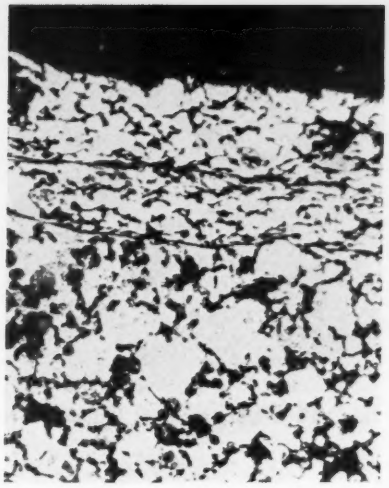

Fig. 9 Surface photomicrograph of Chrome 30 worked 50% in compression at room temperature (100X)

2600°F at reductions of 30 to 50% in one pass and results in increased strength of the finished material. The material, while ductile at 2600°F, has no tensile elongation at 2200°F and below.

Extrusion has been performed using a 6:1 reduction. A further increase in strength results (see Fig. 5), and it is very important to note that considerable ductility is achieved at 1800°F and below. Spachner and Rostocker report finding an increase in the ductility of arc melted chromium by plastically prestraining the material at a high temperature below the recrystallization temperature. This effect is termed rheotropic recovery. Extruded modified chromium exhibits greater ductility at 1800°F than the forged material at 3100°F. A portion of this change in plastic behavior can be attributed to decrease in porosity in extruded material (about 4%). Extrusion was accomplished at 2200°F. Since this temperature is above the recrystallization temperature, it must also be true that the ceramic particles serve to lock in the stresses in much the same manner as they prevent grain growth. It would be beneficial, of course, if further working at lower temperatures would provide ductility at room temperature. Certainly this commercial grade material is sufficiently ductile to operate well in unprotected structures at 2600°F.

Table 4 Properties of modified Chromium 30

Tensile strength	Red. in area	Ultimate psi
Test Temperature		
Forged		
72°F	0	30,000
1800°F	0	18,000
2600°F	6%	6,300
3100°F[a]	10%	1,800
Extruded 10:1		
72°F	12	56,000
1800°F	30	23,000
2500°F	...	4,800
Compressive strength, 0.2% offset yield, psi		
72°F		35,000
1800°F		18,000
Density, lb/cu in.		0.23
Hardness R_b		60
Expansion 0–1000°F in./in. °F × 10^{-6}		3.0
0–1800°F in./in. °F × 10^{-6}		3.0
Emissivity in air, 1200°F and above		0.9
Electrical resistivity; ohm-cm × 10^{-5}		4.8

[a] Constant load induction heated apparatus. Tensile test loading 300 lb/min

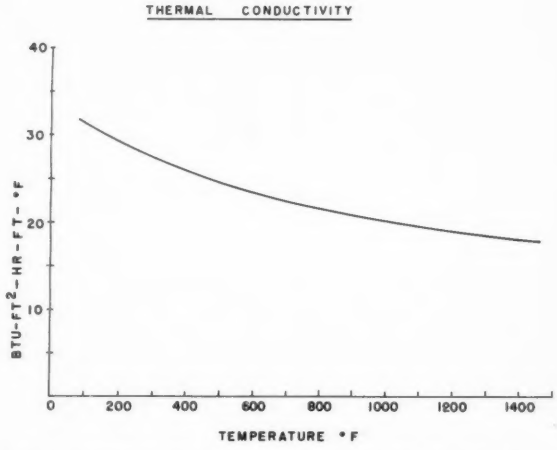

Fig. 10 Thermal conductivity for modified chromium (Chrome 30)

Machineability of Chrome 30 is similar to cast iron. Depths of cut can be as large as 0.150 in. with no lubrication or cooling, using high speed steel tools. Surface finish is excellent, and results are probably traceable to the ceramic particles that tend to break up the material. Long coils of machined material are common. Spachner and Rostocker report difficulty machining forged chromium using cuts 0.015 in. or less and lubricant to prevent galling. These observations agree with those of the author.

The materials in question were developed in April 1960 and have been produced in quantity since that time. A list of properties is given in Table 4. A plot of thermal conductivity for Chrome 30 is given in Fig. 10 (14).

Testing of a similar nature on the modified chromium was conducted under the direction of Materials Central, WADD (8, 9). The information is listed in Table 5.

Generally the properties are equivalent or better than arc melted chromium, and in many cases they approach the properties of pure molybdenum and tungsten, as they are now available. Larger structures are being tested for re-entry conditions. Fig. 11 shows a photograph of a thin wall re-entry type structure for testing in plasma jet. This part has been exposed to 2000°F to form an oxide film which is more

Fig. 11 Thin wall re-entry shape of Chrome 30 for subscale testing

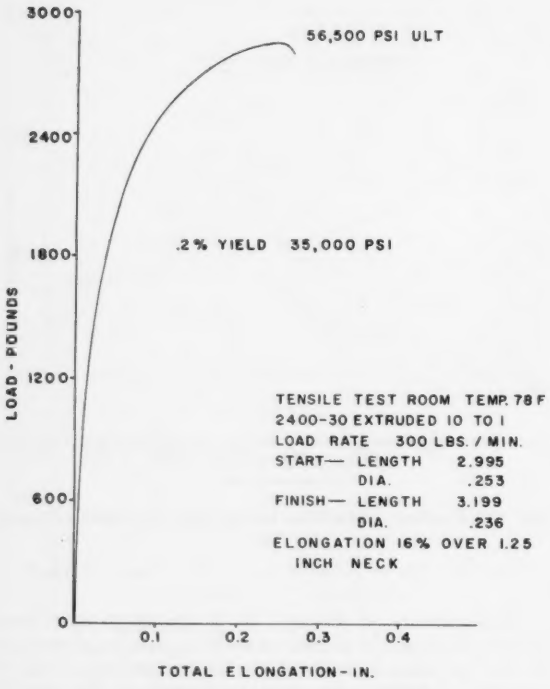

Fig. 12 Room temperature tensile stress-strain curve

Table 5 Plasma jet testing of Chrome 30

Heat flux at sample Btu/sq ft/sec	Apparent surface temperature	Exposure time, sec	Gas temperature, °F	Erosion, mils/sec
103	...	780	3470	none
200	2415	360	4950	none
300	2720	300	5420	none
403	3500	300	6650	none
448	3800	300	6740	none
500	3950	300	...	none
537	...	70	7210	2.3

stable than one formed at higher temperature. At high flux, the film remains completely intact through heating and at temperature but flakes off in cooling.

Ductility in Modified Chromium

Further research in extruded material at extrusion ratios of 10:1 and higher have produced chromium that is ductile in tension and bending at room temperature. An actual stress strain curve of extruded modified chromium is reproduced in Fig. 12. The tensile bar is the same diameter along its gage length, and the 16% elongation takes place along the entire length. Fig. 13 shows an untested bar, a room temperature test, and a 600°F test (19% elongation). The same material when loaded in bending is also plastic at room temperature. In some of the latest work on extruded pure chromium, Brandes and Stone (15) report that they were able to prepare chromium with a small amount of bend ductility but were unable to produce chromium with any elongation in tension at room temperature. In fact, elongation of only 3½% was reported at 200°C.

Exposure of pure chromium at high temperature in air causes a complete loss of room temperature ductility even after electropolishing. Extruded modified chromium has been exposed for several hours at different temperatures above 1800°F in air. This exposure does not affect room temperature ductility or strength even when the surface is left undisturbed.

Tensile testing at room temperature of a bar held for one hour at 1800°F yields the same strength and ductility as a bar of the same material tested in the as-extruded condition. The metals molybdenum and tungsten recrystallize when held at temperature above their recrystallization point and suffer loss of room temperature ductility. In the case of modified chromium, however, long time exposure at high temperature, as explained previously, does not alter room temperature ductility. Load and deflection curves for different samples of modified chromium are plotted in Fig. 14. A photograph of a bend sample is shown in Fig. 15. The sample had been held for an hour at 2300°F before being bent at room temperature. Modified chromium embrittles during exposure to air at 1000°F. The stress-deflection curve is plotted as curve 3 in Fig. 14. However, if the material is first exposed to high temperature soaking, 1800°F or higher, further exposure at 1000°F does not affect room temperature ductility for the investigated exposure times of 1 and 2 hr, or conversely, high temperature exposure, after holding at 1000°F, restores room temperature ductility.

Surface notch effects have been known to drastically affect the ductility of pure chromium. Many researchers have electrolytically polished all bend and tensile samples before testing. No such precaution has been taken with the modified chromium in this report. In certain room temperature bending tests, surface cracks have developed on the tension side of the bend sample, but deflection continued, and the cracks would not propagate. Very thin sheets (8 mil) of modified chromium have been notched and bent up to 90° without crack propagation. This illustrates considerable ability to distribute load in a ductile manner. The very encouraging results which have been obtained thus far demonstrate that the future of chromium as an engineering material of construction depends on the abilities of the chromium ceramic composite material that has been described. Modified chromium differs physically from pure chromium in several categories, which are listed in Table 6.

Summary

A set of target criteria was established for glide re-entry structure. In general, the most attractive solution would involve a nonoxidizing lightweight metal with high surface emissivity.

Fig. 13 Tensile bars of modified chromium

Fig. 15 Bend test sample of modified chromium

Table 6 Physical differences between modified chromium and pure chromium

	Chromium	Modified chromium
Strength	low	higher
Oxidation	good—scales	better—resists scaling
Weight	0.26#/cu in.	0.238#/cu in.
Machineability	poor—surface galls	good—smooth surface
Room temperature ductility	only in ultra pure chomium	present in extruded material
Ductility after high temperatures	disappears	retains ductility
Workability	requires cladding special technique	forged, extruded and rolled unprotected

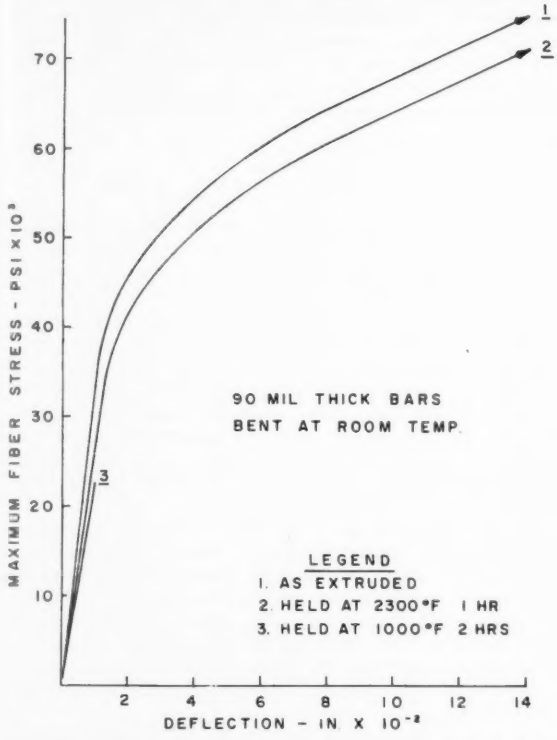

Fig. 14 Stress-deflection curves of modified chromium in bending

A modification of chromium employing a ceramic addition succeeds in providing sufficient erosion resistance to chromium to enable it to withstand surface temperatures above the melting point of the chromium for periods of 10 min and longer. The ideal structure is further approached with modified chromium through its light weight, thermal shock resistance, and high emittance of its oxide film. Sufficient strength is available to enable modified chromium to operate as a lightly stressed structure at temperatures that melt nickel and cobalt base superalloys, that is, 2600°F and higher.

Metallic properties are maintained in modified chromium to the extent that this material can be hot worked and formed into structures with the inherent benefits of a mill product. The ductility and strength of modified chromium under 2600°F can be used to advantage in sustaining higher stress loading where temperature gradients exist. This is particularly true in a re-entrant structure designed to provide radiation cooling from the unexposed surface. Its ability to withstand oxidizing gases to nearly 4000°F may be used in the near future by employing modified chromium for cladding or shielding high strength alloyed tungsten or molybdenum.

Chromium, as modified, can be used in glide re-entry without fear of catastrophic oxidation and with a surface that can tolerate temperatures in excess of the melting point of the structure, thus providing two encouraging safety factors.

References

1 Vogan, J. W., "Thermal Protective Surface for Structural Plastics," *WADD 60-110*, Part I, January 1960, pp. 7–10.

2 Tietz, T. E., Wilcox, B. A. and Wilson, J. W., "Mechanical Properties & Oxidation Resistance of Certain Refractory Metals," Stanford Research Inst., Menlo Park, Calif., Department of Navy, Jan. 30, 1959, pp. 15, 19–76.

3 Wilson, J. W., "Chromium & Rhenium," *Space Aeronautics*, vol. 31, no. 3, March 1960, pp. 45-49.

4 Hansen, Max, *Constitution of Binary Alloys*, McGraw-Hill Book Co., New York, 1958, p. 547.

5 "Ductile Chromium," Amer. Soc. for Metals, Cleveland, Ohio, 1957.

6 "Brazing Manual," *AWS*, 1955, Reinhold Publishing Co., New York, p. 45.

7 Levin, E. M., McMurdie, H. F. and Hall, F. P., "Phase Diagrams for Ceramists," *Amer. Ceramic Soc.*, vols. 1 & 2, 1956 and 1959, pp. 81, 1109.

8 Rosenbury, J. W., "Progress Report in Arc-Plasma Material Evaluation Studies," Univ. of Dayton Research Inst., July 1960.

9 Unpublished Progress Reports, Univ. of Dayton.

10 Phalnikar, C. A., Evans, E. B. and Baldwin, W. M., Jr., "High Temperature Scaling of Cobalt-Chromium Alloys," *J. Electrochemical Soc.*, vol. 103, no. 8, 1956, p. 433.

11 Campbell, I. E., *High Temperature Technology*, John Wiley & Sons, New York, 1956, p. 46.

12 Barr, R. Q. and Semchyshen, M., "Mechanical Properties of Molybdenum & Molybdenum-Base Alloy Sheet," Symposium on Newer Metals, ASTM, *STP #272*, 1959.

13 Spachner, S. A. and Rostocker, W., "Properties of Forged Chromium," *Trans.*, Amer. Soc. for Metals 50, 1958, p. 842.

14 Allen, A. W. and Bickelhaupt, R. E., "Thermal Conductivity & Thermal Diffusivity of Ceramic-Metal Combinations," *Progress Rep.*, Dept. of Ceramic Engng., Univ. of Illinois, August 1960.

15 Brandes, E. I. and Stone, H. E. N., "The Properties of Extruded Chromium," *J. Inst. of Metals*, vol. 87, 1958–59, p. 42.

Pilot Performance Capabilities During Centrifuge Simulations of Boost and Re-Entry[1]

RANDALL M. CHAMBERS[2]
JOHN G. NELSON[3]

U. S. Naval Air Development Center
Aviation Medical Acceleration Laboratory
Johnsville, Pa.

This report presents nine principles concerning the effects of acceleration on human performance. These principles are derived from centrifuge experiments in which human subjects were exposed to acceleration environments which were designed to simulate three basic types of proposed space vehicles. These principles deal with the areas of: 1) performance tolerance; 2) practice effects; 3) restraint system; 4) individual differences; 5) control system; 6) control feedback; 7) task difficulty level; 8) display characteristics; and 9) higher mental processes. The need for research on the effects of acceleration variables other than peak gravity and direction of gravity is noted, as is the problem of interaction between variables.

THE GENERAL trend in the development of certain space vehicle designs suggests the desirability of having the occupant control the capsule attitude and monitor other systems during certain acceleration phases. However, there is a lack of data concerning the accelerations that man can endure and still be able to perform control functions reliably. Since the allocation of man-machine functions for any proposed space vehicle is dependent largely upon the acquisition of basic information pertaining to the capabilities and the reliabilities of human performance components within any proposed system, current aerospace concern over the problem of performance capabilities of an astronaut immersed in certain acceleration environments is well founded (1–4).[4]

Acceleration distorts, restricts, and modifies human physiology and behavior. As gravity increases, the human subject approaches blackout or unconsciousness, experiences pain and discomfort, and his eyes, heart, and musculature show somewhat specific symptoms in response to the acceleration stress. These and other symptoms may be differentially induced by several different characteristics of the acceleration, such as magnitude, rate of onset and decline, direction with respect to the human body, duration of peak, and the total number of g-seconds to which the person is exposed.

Fig. 1 illustrates three basic types of proposed vehicles which have been the basis of much of the effort of the human factors research at this laboratory. At the bottom left of the figure is shown a high drag, variable lift winged vehicle (Type I). In this vehicle, the pilot performs while sitting in a normal flying position and receives acceleration forces which are primarily head to foot with respect to his body ($+G_z$). At the top of the figure is shown the high drag capsule (Type II), in which the pilot performs while sitting facing backwards with respect to his velocity, and in which he receives acceleration forces which are primarily chest to back ($+G_x$). To the right is shown a sketch of a glide capsule (Type III), in which the pilot performs while facing forward in his vehicle, and in which he receives gravity forces which are resultants of back to chest ($-G_x$) and head to foot components ($+G_z$). During re-entry, the pilot in the high drag, variable lift winged vehicle is pressed down into his seat; the pilot in the high drag capsule is pressed against the back of his seat; and in the glide vehicle, the pilot is pressed against his shoulder straps. The above nomenclature may be clarified by Fig. 2.

In the Navy's Aviation Medical Acceleration Laboratory (AMAL), these accelerations are produced by a centrifuge with a 50-ft arm. A gondola is located at the end of the arm and is positioned by means of a remotely controlled double gimbal system. In the closed loop simulations, the pilot "flies" the centrifuge by means of his cockpit controls and so receives the appropriate linear acceleration components. In open loop, the centrifuge is programmed, and the pilot "flies" his instruments only.

Sensations reported by subjects in centrifuge simulations of the first vehicle type are: increased pressure of the buttocks on the seat; heaviness of the head, body and limbs; downward pull of the diaphragm; congestion in the lower segments of the body; greyout or blackout. There may be pain in the lower legs and in the toes and feelings of fullness in the lower extremities. Breathing is difficult and very tiring.

Sensations reported by subjects in centrifuge simulations of the second vehicle are: pressure on the chest and possible substernum pain; difficulty in seeing the instruments on the panel; loss of peripheral vision; blurring; difficulty in keeping the eyes open; fatigue; and difficulty in breathing.

Sensations reported by subjects in centrifuge simulations of the third vehicle are: fullness and possible pain in the face, arms, and legs; pressure points along the chest and face supports; blurring of vision; congestion in the nose; and abnormal ease of breathing.

Closed loop centrifuge simulations of each of the three types of vehicles have been completed in situations in which a wide variety of piloting problems have been presented to test pilots.

Presented at the ARS 15th Annual Meeting, Washington, D. C., Dec. 5–8, 1960.

[1] This manuscript is based primarily on recent work done at the Aviation Medical Acceleration Laboratory, some of which was in conjunction with NASA Langley Research Center, the NASA High Speed Flight Center, the NASA Ames Research Center, and the NASA Space Task Group.

[2] Head, Human Factors Branch, Aviation Medical Acceleration Laboratory. Member ARS.

[3] Research Psychologist, Aviation Medical Acceleration Laboratory.

[4] Numbers in parentheses indicate References at end of paper.

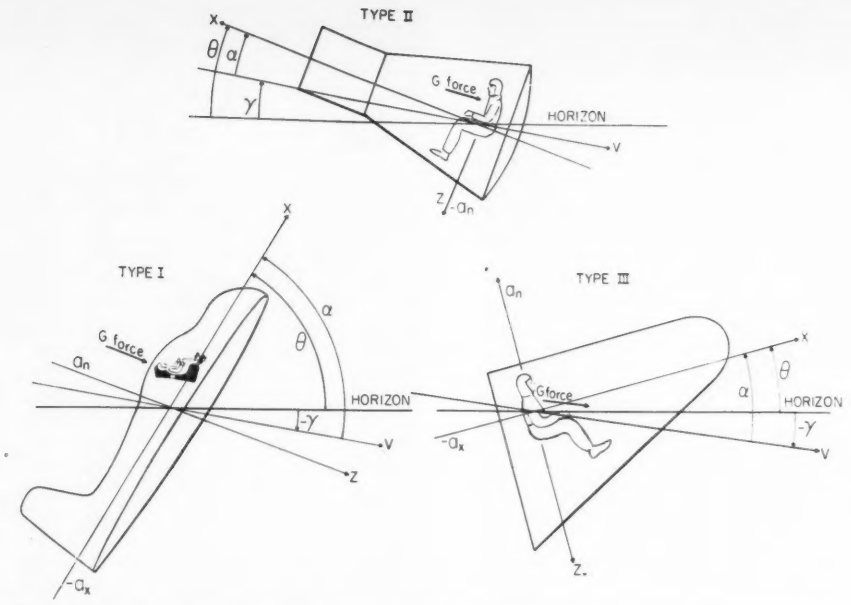

Fig. 1 Three basic types of proposed space vehicle configurations within which human factor problems have been studied at the AMAL

PHYSIOLOGICAL DESCRIPTION OF ACCELERATION

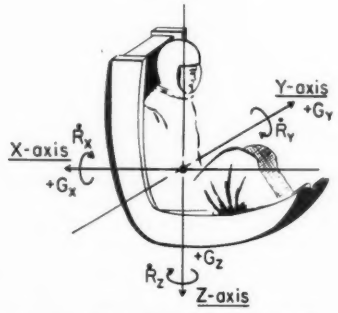

(Body Fluids, Heart Displacement, With Respect to Skeleton)

Linear Acceleration Modes

Description of Heart Motion

Actual	Other Descriptions			Symbol	Unit
Towards spine	Eye-balls-in	Chest-to-back	Backward facing	$+G_x$	g
Towards sternum	Eye-balls-out	Back-to-chest	Forward facing	$-G_x$	g
Towards feet	Eye-balls-down	Head-to-foot	Headward	$+G_z$	g
Towards head	Eye-balls-up	Foot-to-head	Footward	$-G_z$	g
Towards left	Eye-balls-left	———	Rightward	$+G_y$	g
Towards right	Eye-balls-right	———	Leftward	$-G_y$	g

$$NG = \frac{a}{g} = N_1 G_x + N_2 G_y + N_3 G_z$$

$$N^2 = N_1^2 + N_2^2 + N_3^2$$

Angular Acceleration Modes

Acceleration about X-axis (roll axis)	$\dot{R}_x$	rad/sec²
Acceleration about Y-axis (pitch axis)	$\dot{R}_y$	rad/sec²
Acceleration about Z-axis (yaw axis)	$\dot{R}_z$	rad/sec²

(Angular acceleration is positive or negative by right hand rule)

Fig. 2 Physiological nomenclature for human factors research on the effects of acceleration

The capabilities of the human pilot for performing launches and re-entries when he is given certain flight control quantities, certain types of piloting equipment and controls, and restraint equipment have been studied. In addition, there have been extensive experiments to determine the degree to which the human pilot may perform secondary monitoring, trouble-shooting, and communication tasks which were incidental to the primary flight mission. The attempt in these centrifuge simulations has been to determine the *performance tolerance limits* within the *physiological tolerance limits* which a human pilot may endure. It is these performance tolerance limits which are of the most use to engineers in making design decisions concerning the kinds of functions which may be best performed by an automatic system. Thus, in many of these studies on our acceleration facility, we have used the physiological tolerance limits as a range within which the performance tolerance limits were measured.

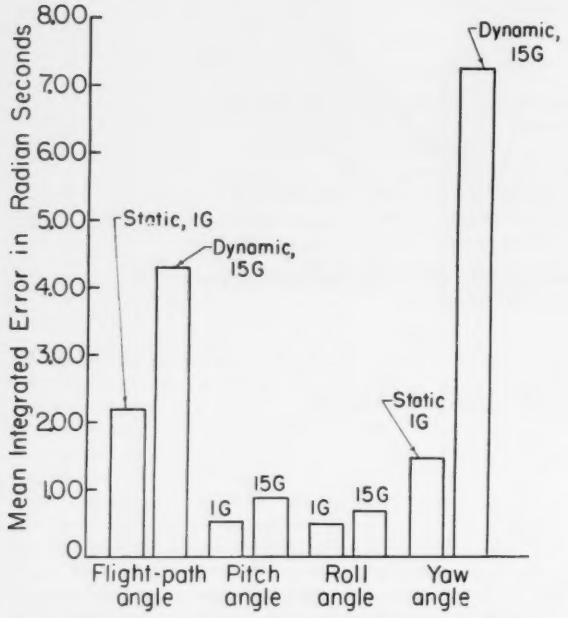

Fig. 3 Comparison of error scores for pilots performing a two-stage rocket launch simulation at + 1 G_z and + 15 G_z in the AMAL human centrifuge. The deterioration of performance at high gravity is demonstrated

There are several ways in which gravity may affect human performance. Performance change may be a direct result of the effects of the acceleration forces on receptors; it may be a result of effects on the central or autonomic nervous system, so that the control and coordination of component activities of different parts of the body are influenced; it may be a result of physical forces acting upon the body members themselves, without involvement of neural and sensory systems at all; or it may be interactions among these systems. The effects of gravity on mechanical and electronic apparatus pose serious measurement problems, and the subject's difficulty in moving and sometimes speaking or breathing makes test administration, as generally conducted, impossible. By necessity, performance measurements can be made only within ranges which are below the human physiological tolerance to gravity. In most experimental work, this is unknown for any given subject, and for safety reasons, extensive biomedical instrumentation is required simultaneously with the performance instrumentation.

The present paper summarizes one part of a human factors research effort which, during the past two years, has been concerned with the human performance capabilities of pilots during simulated boost, orbit, and re-entry rocket flight trajectories. Subjects were 38 men who collectively have received over 2600 closed loop centrifuge exposures to simulations of several basic types of proposed space vehicle designs. In view of space limitations, this paper will present only a few selected portions of the research.

Some of the conclusions which have been reached in the various experiments are formulated in this paper as general principles concerning the effects of acceleration stress on human performance.

Principle 1: Performance Tolerance

In addition to the physiological tolerance limits which define the end points for reliable functioning of any particular physiological system during exposure to acceleration stress,

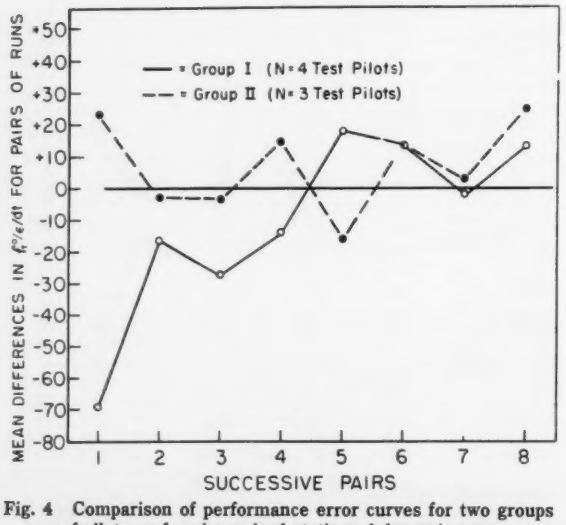

Fig. 4 Comparison of performance error curves for two groups of pilots performing paired static and dynamic runs

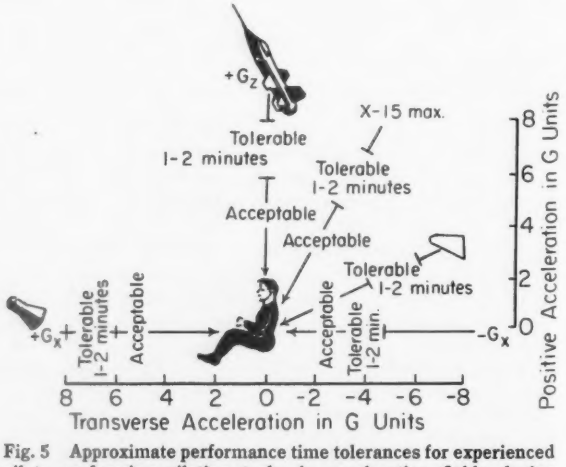

Fig. 5 Approximate performance time tolerances for experienced pilots performing piloting tasks in acceleration fields during centrifuge re-entry simulations of space vehicles. Based on data obtained at AMAL prior to utilization of contour couch and associated restraint components

Fig. 6 Early research restraint system developed by NASA Langley Research Center, North American Aviation and AMAL (3) (4)

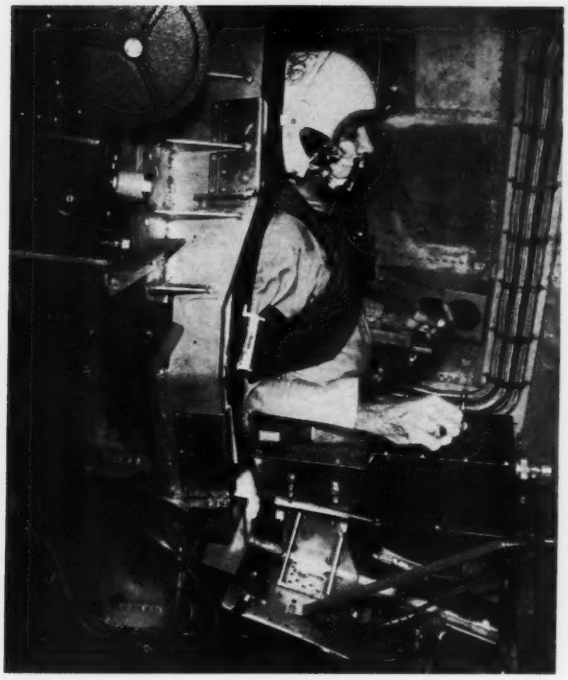

Fig. 7 Advanced restraint system developed for increasing human gravity tolerance and piloting performance capabilities in $+G_x$, $-G_x$, $+G_z$ environments. Developed by NASA Ames Research Center, NASA High Speed Flight Test Center and AMAL (5), (6), (7)

there are also performance tolerance limits which define the end points for reliable functioning of any particular performance ability system under these same conditions of acceleration. The physiological and performance tolerances may be functionally related but need not be the same, since both are dependent upon the criteria which are accepted. It is these performance tolerance limits which are of major importance in the allocation of man-machine functions.

Under conditions of moderate acceleration, experienced pilots use the motion and acceleration cues in performing their tasks, and these cues, along with reasonably high concentration and motivation, enable the pilot to do better under moderately high acceleration than under static conditions.

At high gravity, performance proficiency deteriorates markedly. This deterioration generally reflects impairment of vision and an inability to breathe, strain, or resist physiologically the effects of the acceleration. Fig. 3 summarizes the mean performance scores for test pilots who performed a simulated two-stage rocket launch both statically and during a centrifuge run which took them through a peak acceleration of $+15$ G_x. The same task was performed under both conditions. Performance scores are reported in terms of mean error in radian seconds for flight quantities designated as pitch, flight path error, roll error, and yaw error. When G_x was changed from $+1$ to $+15$, yaw angle error increased fivefold, while flight path angle doubled. Other levels were tested, and the results supported the principle that moderate gravity may improve performance.

Under high gravity, the main difficulty experienced by the pilots was an almost complete inability to see the panel instruments. Physiological recordings of electrocardiograph, breathing, and galvanic skin response indicated that the subjects were undergoing major physiological stress. For this particular type of task, it was concluded that the performance boundary was between $+13$ and $+15$ G_x.

Principle 2: Practice Effects

Major increments in performance proficiency in high gravity environments occur as a function of practice.

Practice results in physiological adaptation and conditioning, as well as learning to make performance compensations for the acceleration disturbances. The pilot improves his performance by: 1) accommodating the sensations induced by gravity; 2) learning to resist the effects of gravity through the use of the proper straining and breathing techniques; 3) learning or relearning the task in the context of changed muscular and sensory capacities induced by the acceleration; and 4) learning to execute the physiological and performance aspects of the task simultaneously. As an example of such learning, see Fig. 4. Group I had no prior centrifuge experience on the Johnsville centrifuge; Group II had prior centrifuge experience on other programs. Successive pairs indicate the first through eighth static-dynamic pair of runs which each pilot experienced. Each point is the mean difference between static and dynamic runs. Positive scores indicate that the pilot made more errors on the static runs; negative scores indicate that the pilot made more errors on the dynamic runs. The figure suggests that it required several trials for Group I to do as well on its dynamic runs as on its static runs, whereas Group II performance shows no change with practice.

Principle 3: Restraint System

The type of restraint system which is used for gravity protection has a very important influence on ability to perform within high acceleration fields.

Fig. 8 Advanced head restraint system augmenting system shown in Fig. 7

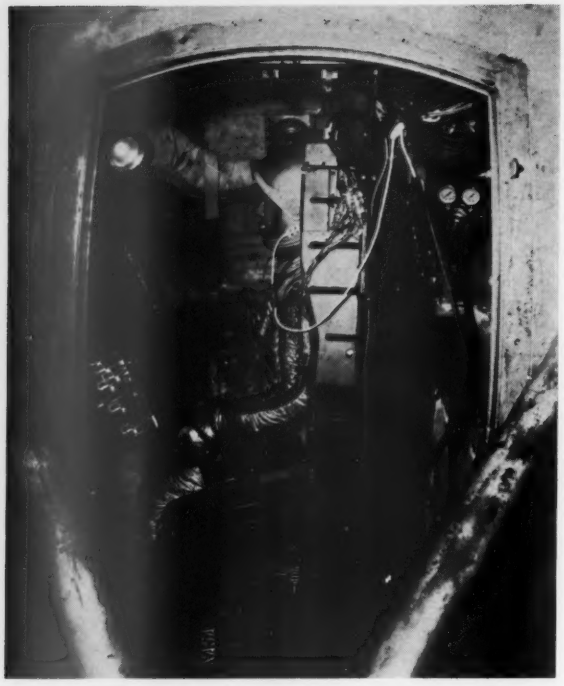

Fig. 9 Advanced restraint system designed to increase piloting capabilities for subject in a pressure suit undergoing high gravity. System developed by NASA Space Task Group and AMAL

As far as the human subject is concerned, high gravity may become low gravity if the appropriate restraint system is used. For example, we found in one study involving a number of test pilots that accelerations of -3.5 or $+6\,G_x$ made it difficult, if not impossible, for pilots to meet the performance criterion satisfactorily. However, using a different type of restraint system, it was found that pilots could perform the same piloting tasks satisfactorily at $-6\,G_x$ or at $+12\,G_x$. The different type of restraint system nearly doubled the acceleration limits within which pilots could perform satisfactorily.

Fig. 5 has been prepared to show the approximate performance time tolerances for experienced pilots for performing piloting tasks satisfactorily when immersed in acceleration fields during centrifuge simulations of several types of space vehicles. This figure shows only the tolerable times and gravity levels beyond which performance would be unsatisfactory. This data is based on work done at AMAL prior to the use of contour couches and associated restraint components. Fig. 6 shows the typical restraint system which was used for most of the above data. It will be noted that the head, hands, legs, trunk, and neck were not well restrained from the gravity forces.

Within $-3.5\,G_x$ to $-4.5\,G_x$, the pilots could perform satisfactorily for only one to two minutes. They had major difficulty in focusing their eyes, controlling their arms and legs, holding the head in position, and withstanding pain.

Figs. 7, 8 and 9 show advanced restraint systems, developed in cooperation with NASA, which have enabled pilots to perform better at higher acceleration levels. Examples shown include individually molded form-fitted contour couches, extensive chest, leg, arm, and helmet supports, and face supports (5). Results of several experiments are summarized in Fig. 10. (This figure is to be contrasted with Fig. 5.) It is noted that in the $+G_x$, $-G_x$, and $+G_z$ accelerated fields, the approximate amounts of time during which a pilot can perform piloting tasks satisfactorily have been greatly increased.

Principle 4: Individual Differences

Major individual differences exist among pilots in their ability to tolerate high gravity.

These differences are due to variations in piloting techniques, methods of fighting gravity, breathing and straining techniques, and ability to tolerate pain and to accommodate to any particular type of restraint system. Interest in the problem and susceptibility to motion sickness are additional variables which contribute to the pilot's ability to perform satisfactorily under high gravity.

Principle 5: Control System

In certain types of acceleration fields, pilot performance proficiency varies as a function of the characteristics of the control device which the pilot uses in performing his flight task.

In attempts to investigate the effect of acceleration forces on the ability of the pilot in high gravity environments, several different types of side arm controllers have been used. The controller to a large extent determines the extent to which the pilot may be able to perform a task satisfactorily. In the X-15 studies on the AMAL centrifuge, it was found that for high gravity profiles, a pilot's performance capabilities could be extended by using a side-arm controller rather than a center stick. In early versions of proposed space vehicles, various types of right-hand side-arm controllers have been tested: three-axis controllers, two-axis controllers with toe pedals; two-axis digital controllers with toe pedals, and force-stick controllers. Fig. 11 presents a diagram of four types of right-hand side-arm controllers: a three-axis, balanced controller, having all three axes intersecting at a point; a three-axis controller, unbalanced, having none of the three axes intersecting at a point; a two-axis finger tip controller, having two axes intersecting at a point, with yaw operated via toe pedals; and a two-axis controller whose axes do not intersect.

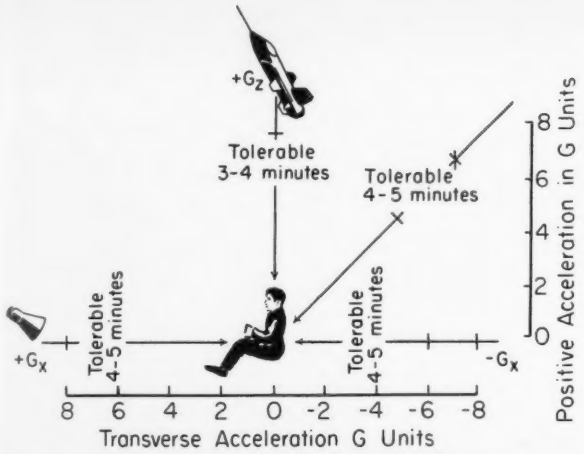

Fig. 10 Approximate performance time tolerances for pilots in advanced restraint system including individually molded contour couches and associated chest, leg, arm, and head restraints. This figure shows only approximate tolerable limits for the times and gravities indicated, beyond which satisfactory performances of the tasks involved would be impossible. These approximations are based on data obtained at AMAL during centrifuge simulations of proposed space vehicles

at a point, and which is accompanied by toe pedals for yaw control.

Fig. 12 illustrates the effect of two specific acceleration fields on the error performance in the pitch and roll of a tracking task for each of the four types of controllers. When the pilots performed in the $+6\ G_z$ by $0\ G_z$ field, pitch error performance on all four controllers was essentially the same; however, when these same pilots flew the same problem in the $-2\ G_z$ by $+4\ G_z$ field, pitch error performance on Type II controller greatly increased, whereas performance on the other three controllers remained essentially unchanged. For roll error, a change in gravity fields resulted in an increment in error for Types II and III controllers and a reduction in error for Types I and IV, resulting in a shift in the rank order of the controllers.

Principle 6: Control Feedback

Acceleration impairs the ability of the subject to sense changes in control characteristics which may occur as a function of specific acceleration vectors.

Control sensitivity dead band, breakout force, control friction, damping characteristics, control throw, control response time, stick force gradients, dynamic and static balance, and centering characteristics are subtle characteristics of controllers which subjectively change under gravity.

Principle 7: Task Difficulty Level

Changes in task characteristics which have little effect upon static performance may seriously impair performance under high gravity. Aerodynamic stability and damping, frequency, and other vehicle response characteristics may make the performance of the piloting task at high gravity more or less difficult. If the simulated vehicle is stable, well damped, and within desirable frequency ranges, the pilot may find performance at high gravity to be relatively easy. However, this same piloting task may be entirely impossible at the same gravity level if the simulated vehicle has unacceptable aerodynamic characteristics (6).

By varying the damping ratio conditions, the ease with

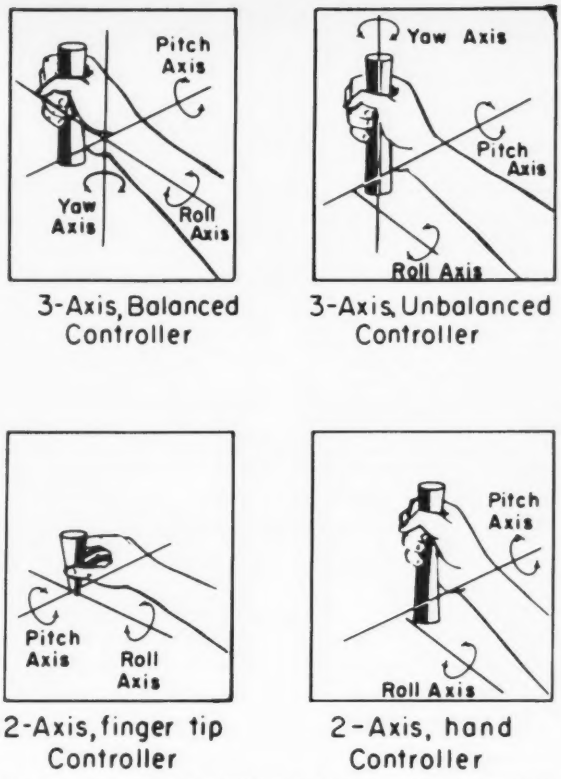

Fig. 11 Four types of right-hand side-arm controllers used in high gravity studies on AMAL centrifuge

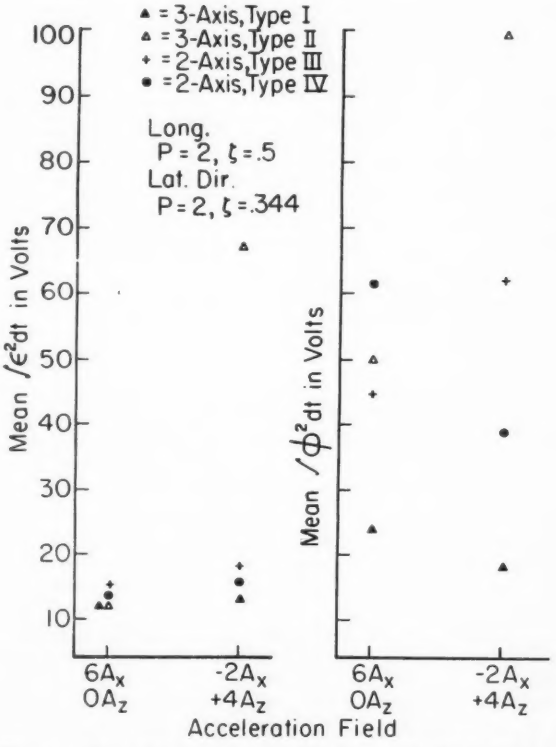

Fig. 12 Mean error scores for pitch error and for roll error components of a tracking task in which the same pilots flew the same problem in each of 2 g-fields using each of four side-arm controllers

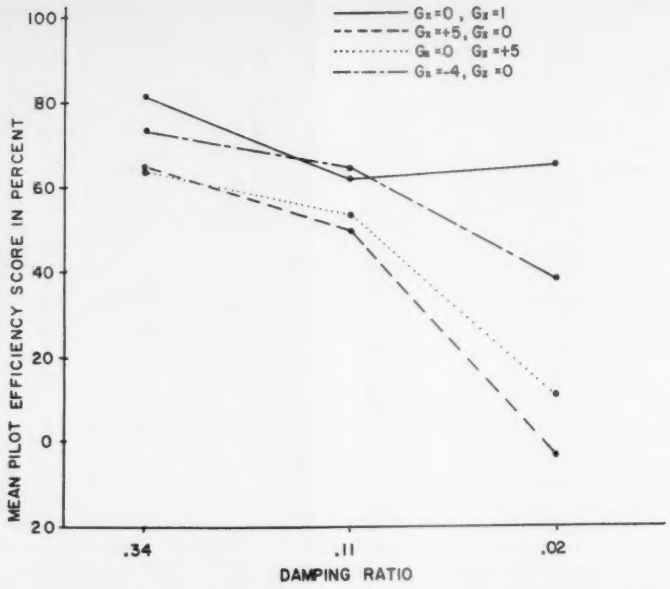

Fig. 13 Effects of damping ratio on mean efficiency score for tracking task performed in each of four acceleration environments

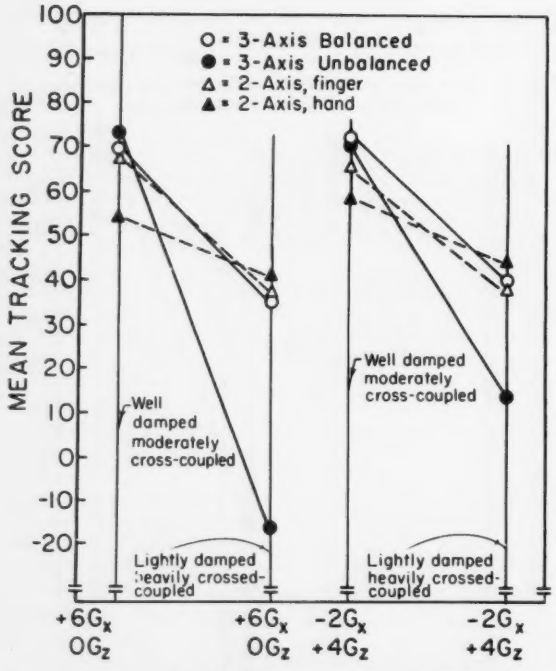

Fig. 14 Mean tracking efficiency scores for test pilots who performed the same tracking task with each of four different types of side-arm controllers within given acceleration fields

which a task may be performed may be made progressively more difficult. An illustration of this is Fig. 13, which shows the mean pilot efficiency scores for five test pilots who flew the same task at three different damping ratio levels within gravity fields which were as follows: $0\,G_x$ by $1\,G_z$ (static); $+5$ G_x by $0\,G_z$; $0\,G_x$ by $+5\,G_z$; and $-4\,G_x$ by $0\,G_z$. Each pilot performed the task at these gravity levels for 1 min. The figure shows a significant drop in piloting efficiency in all three acceleration fields as the damping ratio is reduced from 0.11 to 0.02. However, this drop is not shown for the static 1-g field. The graph also suggests that a differential effect is shown for the different gravity fields. There is a need for more research on the interaction effects between damping ratio, piloting efficiency, and acceleration (7).

Principle 8: Display Characteristics

The display characteristics of the task influence performance capabilities at high gravity.

The following variables are of major importance: the position of the display instrument with reference to the subject's visual field; the degree of interpretation which is required of the pilot; the accuracy of the instrument itself when exposed to high gravity; the illumination; the physical form in which the display information is presented; and the amount of instrument scanning that is required at high gravity.

During the occurrence of all types of high acceleration, the human subject experiences visual disturbances. Vision is one of the primary limiting factors for performance at high gravity. These disturbances result from shifts in the availability of arterial blood to the retina; mechanical pressure on the eyes, such as in "eyeballs in," "eyeballs out," "eyeballs up," and "eyeballs down"; mechanical forces acting on the eye musculature, eyelids, and associated structures; distortions of eye anatomy; and miscellaneous effects, such as the accumulation of tears in $-G_z$.

Principle 9: Higher Mental Processes

The ability to make time judgments and to estimate short intervals of time is impaired by moderate acceleration. It is hypothesized that intellectual skills, decision making, judgment, prediction, memory, and problem solving may be influenced temporarily. However, much more research is needed to determine these effects.

Conclusion

This paper has presented a summary of principles pertaining to human capabilities for performing in centrifuge simulated launch and re-entry profiles. It should be noted that the

foregoing principles are based upon research where the primary variables were peak gravity and direction of gravity with respect to the subject's body. Further research is needed to generate principles concerning the effects of rate of onset and decline, duration of peak gravity, angular acceleration, lateral gravity, and most particularly the interactions which may occur among the relevant variables. (See Fig. 14 for an illustration of this interaction effect.) While it is felt that these principles may be expanded by investigation of the above variables, it is postulated that they will, in general, hold for these cases. Work is now in progress or is planned to obtain empirical evidence to further test these principles and to generate specific theorems to cover specific conditions.

Nomenclature

V = velocity
θ = vehicle pitch angle
Φ = vehicle roll angle
α = angle of attack (angle between longitudinal axis and velocity vector)
ϵ = angle of attack error
x = longitudinal body axis of vehicle
z = axis perpendicular to the longitudinal axis in the plane of symmetry
γ = flight path angle
a_x = acceleration along the x-axis of the vehicle
a_n = acceleration along the z-axis of the vehicle
G_x = physiological gravity as measured along an axis perpendicular to the spinal column of the human body
G_z = physiological gravity as measured along the spinal column of the human body

References

1 Chambers, R. M. and Smith, B. J. (eds.), "What Needs Doing About Man in Space?" General Electric Co., Philadelphia, Pa., December 1959.

2 Creer, B. Y., Heinle, D. C. and Wingrove, R. C., "Study of Stability and Control Characteristics of Atmosphere Entry Type Aircraft Through a Piloted Flight Simulator," presented at the meeting of the Inst. of Aeronaut. Sci., New York, October 1959 (*IAS paper no. 59-129*).

3 Eggleston, J. M. and Cheatham, D. C., "Piloted Entries into Earth's Atmosphere," presented at the Inst. of Aeronaut. Sci., Los Angeles, Calif., June 1959.

4 Chambers, R. M. and Doerfel, H. V., "Closed-Loop Centrifuge Simulation of Space Vehicle Performance," presented at the ARS Semi-Annual Meeting, San Diego, Calif., June 8–12, 1959 (*ARS preprint no. 807-59*).

5 Smedal, H. A., Stinnett, G. W. and Innis, R. C., "A Restraint System Enabling Pilot Control Under Moderately High Acceleration in a Varied Acceleration Field," *NASA TN D-91*, NASA, Washington, D. C., May 1960.

6 Holleman, E. C., Armstrong, N. A. and Andrews, W. H., "Utilization of the Pilot in the Launch and Injection of a Multistage Orbital Vehicle," presented at the 28th Annual Meeting of the Inst. of Aeronaut. Sci., January 1960.

7 Chambers, R. M., "Effects of G Environments on Psychomotor Abilities," *Aerospace Medicine*, vol. 31, no. 4, 1960 (Abstract), p. 300.

Sealed Cabin Experimentation

B. E. WELCH[1]
T. E. MORGAN Jr.[2]
F. ULVEDAL[3]

School of Aerospace Medicine
USAF Aerospace Medical Center
Brooks AFB, Texas

IN THE design and development of a manned space vehicle, the answers to logistic problems are perhaps as important as the answer to the basic question of the type of life support system to be used. Certainly the two are inseparable, since the rate of use or production influences ultimate design. Many theoretical papers have been written about the logistic aspects of manned space flight (1–3).[4] To date, however, the experimental data that has been accumulated has been obtained either in a normal environment (4) or in small simulators for relatively short periods of time (5).

It seemed desirable, therefore, to obtain as much logistic data, and other pertinent information, as possible during the course of prolonged experiments in the two-man space cabin simulator. Four experiments were conducted. Three were carried out at a simulated altitude of 18,000 ft (40% oxygen atmosphere) for 14, 30, and 30 days. One was conducted at an altitude of 33,500 ft (96+% oxygen) for 17 days.

Presented at the National ARS-IAS Joint Meeting, Los Angeles, Calif., June 13–16, 1961.

[1] Chief, Space Ecology Branch.
[2] Chief, Sealed Environment Section, Space Ecology Branch.
[3] Sealed Environment Section, Space Ecology Branch.
[4] Numbers in parentheses indicate References at end of paper.

Methods

The space cabin simulator used in this series of experiments was designed to accommodate two people for periods up to 30 days. It is a hermetically sealed chamber containing all the necessary environmental controls and life support equipment with the exception of the heat exchanger and power supply. A detailed description of the cabin and its components has been presented elsewhere (6). A description of the controls and cabin furnishings as well as the psychomotor performance console also has been published (7,8). The simulator (Fig. 1) is an elliptically shaped steel cylinder 12-ft long, 8-ft high and 5-ft wide with a bound volume of 380 cu ft. At a 10 psi pressure differential (28,500 ft altitude) the leak rate of ambient gases into the simulator produces a pressure change of 2.4 mm per 24-hr period. In terms of volume, this leak is equivalent to 0.85 to 1.1 cu ft per day.

The performance of the crew members inside the simulator and the environmental conditions present at any given time are monitored by means of a console located outside the cabin (Fig. 2). Pressure, partial pressure of oxygen, and partial

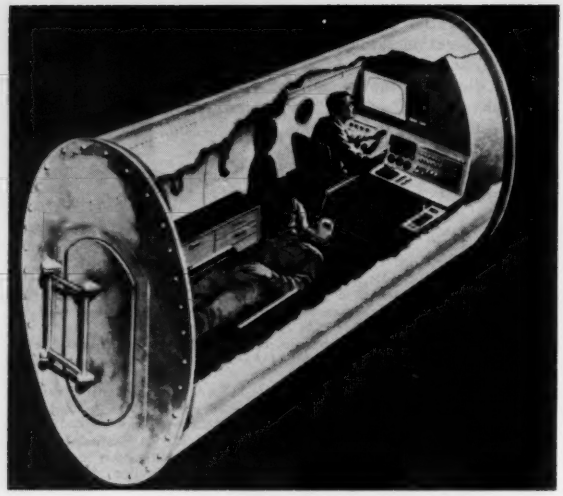

Fig. 1 Artist's conception of two-man simulator

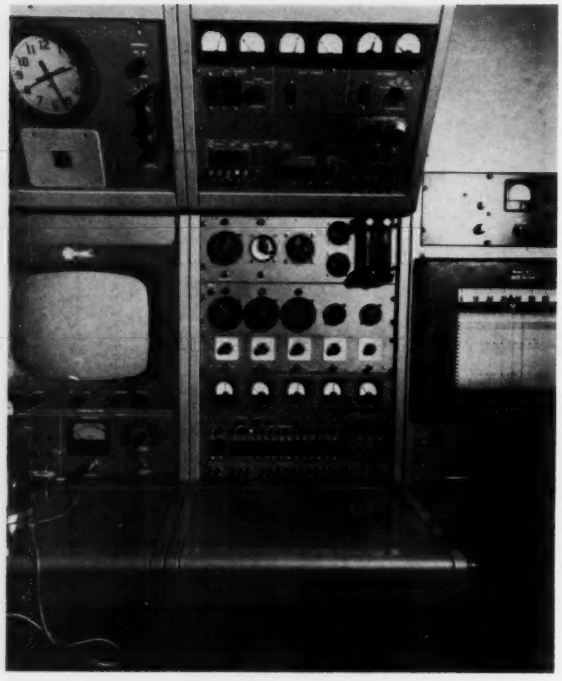

Fig. 2 Outside monitor console of two-man simulator

Table 1 Summary of environmental conditions

	14-day	30-day	17-day	30-day
Pressure, mm Hg	380	383	189	383
P_{O_2}, mm Hg	150	150	176	150
P_{CO_2}, mm Hg	2.5	6.4	3.0	1.5
Temperature, °C	22.8	22.6	21	23.1
Relative humidity, %	50	...	50	56

pressure of carbon dioxide are read and recorded in millimeters of mercury, permitting a rapid assessment of the conditions in the simulator at various altitudes.

A total of four experiments have been completed. A summary of the environmental conditions present during each of these experiments as well as other data pertinent to each flight is presented in Table 1. In every case, the individuals participating as simulator crew members were given a physical and psychological examination before and after the flight. In addition, in-flight measurements were made to ascertain cardiovascular, respiratory, and metabolic function.

Dehydrated, precooked food obtained from the Quartermaster Food and Container Institute was used on all flights (Table 2). Reconstitution of these foods requires only the addition of hot or cold water, depending on the food item, and takes from 15 sec to 15 min.

Caloric intake was determined by providing food packages of known weight and caloric composition. The men were allowed to consume the food ad lib with the requirement that they consume all the food in the package once it had been opened. Food consumed was then reported on a daily basis.

Water consumed during the experiment was obtained both from stored water supplies (14-day flight) and by a combination of stored and recycled water (17- and 30-day flights). All water was measured before using, and the amount and purpose recorded. In addition, the volume of all urine produced was recorded. Waste water was purified by a vacuum distillation process described previously (7).

Oxygen was supplied by means of three liquid oxygen converters[5] in the 14- and 30-day flights. Gaseous oxygen was used during the 17-day flight. Oxygen requirements were estimated from food intake and from metabolic rate data obtained during the 17-day flight and 30-day flight no. 2.

All data are shown as the average for two men for each of the flights discussed unless otherwise indicated.

Results and Discussion

The use of precooked, dehydrated foods appears to offer a logical solution to the problem of nutrition in space flight. It is true that there might be difficulties in rehydration in a weightless environment, but this problem seems small compared with the problem of the weight of canned foods (5) or with the problem of refrigeration of frozen foods. In the four flights, the weight of food and package required for 1 man/day averaged slightly more than 1 lb (range 1.32 to 0.68 lb/man/day). Previous experience in the one-man space cabin simulator (5) indicated that 7 lb/man/day of food and container were required when canned food items were used.

The average caloric intake from each flight is shown in Table 3. The measured average values range from a low of 1160 kcal/man/day in the 30-day no. 2 flight to a high of 1915 kcal/man/day in the 17-day flight. Individual measurements ranged from 1002 to 1940 kcal/man/day. If these average intake data are expressed on a body weight basis, the range is from 13 kcal/kg body weight to 29 kcal/kg body weight in the 30-day no. 2 and 14-day flights, respectively. The data obtained in the 14-day flight and the 17-day flight represent fairly accurate caloric requirements for man in the environmental and physical boundaries of the space cabin simulator. The weight loss experienced during the 14-day flight was minimal and of unknown composition. The weight loss during the 17-day flight was somewhat greater, but nitrogen-balance data and body-water data indicated that the weight loss was predominately water. Body composition

[5] Linde Co. Each converter has a 25-liter capacity and a boil-off rate of 0.8 liter/day.

data available on 30-day flights no. 1 and no. 2 were not adequate to permit good definition of the weight loss. It would appear, however, that a caloric requirement of 30 kcal/kg body weight is a realistic value to use in planning the nutritional aspects of space flight. This represents approximately a 50% increment over the basal metabolic rate.

A summary of water-intake and water-output data is presented in Table 4. The source of water in the 14-day flight was 100% stored supplies. During the 30-day no. 1, 17-day, and 30-day no. 2 flights, the source of water was from both stored supplies and recycled waste water, the latter comprising approximately 50, 68, and 70%, respectively, of the total used.

The water intake values shown in Table 4 include the water used to reconstitute food, as well as that consumed in liquid form as water or in beverages. Also shown is water derived from preformed water in the foods and from an estimate of the water of oxidation.

The average daily liquid water requirement for food, drink, and personal hygiene varied from 1254 to 2075 ml/man/day. Individual measurements ranged from 1208 to 2084 ml/man/day. These data indicate, therefore, that a water purification system, when used in conjunction with dehydrated foods, must be capable of producing in excess of 2.0 liter of potable water per man per day.

The average amount of urine produced daily per man ranged from 756 ml to 1158 ml, with individuals ranging from a flight low of 560 to a flight high of 1304 ml/man/day. The average daily insensible water loss could not be determined due to poorly defined changes in body composition with concomitant losses in body water. If one uses the 900 ml/man/day ground level insensible loss estimate of Kuno (9), it is evident that approximately 50% of the water excreted from the body is via this route. If it is planned to purify and reuse water in space, it will be essential to recover the insensible water also. In addition to being a source of water for purification, this particular supply might well constitute an excellent emergency supply or be used for personal hygiene without any processing other than condensation.

The oxygen requirement for individuals in the space cabin simulator can be estimated from caloric intake in food. In those instances where caloric intake does not meet caloric requirement, this calculation is not valid. Using 30 kcal/kg body weight as a starting point and the conversion value of 4.825 kcal/liter O_2, one can estimate oxygen requirements of 6.2 liter O_2/kg body weight. This relationship yields approximate oxygen requirements ranging from 400 liter/man/day in the 14-day flight up to 550 liter/man/day in 30-day flight no. 2.

As a further check on the calculation of the energy requirement and the validity of the 30 kcal/kg body weight conversion factor, the actual daily composition of oxygen was determined during the latter phase of 30-day flight no. 2. This was done by observing the oxygen removed or evaporated from the converters and subtracting from this figure the oxygen volume boiled-off and/or removed from the simulator in maintaining altitudes. Both of the latter values were obtained by collecting the gas in a spirometer and measuring its volume. This technique indicated that each man was using 575 liter O_2/day or 2890 kcal/day, based on the relationship of 4.825 kcal/liter O_2. Expressed on a body weight basis, the energy requirement is thus 33 kcal/kg body weight, which closely approximates the 30 kcal/kg body weight value cited above.

Table 2 Typical dehydrated food items

Pork chops	Peas
Chicken and rice	Carrots and peas
Cubed steak	Green beans
Swiss steak	Grapefruit-orange juice
Sliced roast beef and gravy	Peaches
Fish patties	Fruit cocktail
Roast pork	Pineapple
Oatmeal	Chocolate pudding
Mashed potatoes	Chicken and rice soup
Buttered rice	Cocoa
Carrots	Milk

Table 3 Average energy intake data

	Intake, kcal/man/day	Initial body wt., kg	Wt. change, kg	Intake, kcal/kg body wt./man/day
14-day	1855	64.75	−1.10	29
30-day no. 1	1537	70.28	−3.02	22
17-day	1915	69.83	−1.99	27
30 day no. 2	1160	87.99	−7.42	13

Table 4 Summary of water data, ml/man/day[a]

	14-day	30-day no. 1	17-day	30 day no. 2
Liquid water required	1732[b]	1738	2075	1254
Fluid intake	1182	1053	1473	1021
Food rehydration	550	545	470	203
Personal hygiene	...	140	132	30
Water in food and of oxidation	295	245	286	200
Liquid waste water produced				
Urine	832	1042	1158	756
Insensible water loss[c]	?	?	?	?
Personal hygiene	...	140	132	30
Water in feces[d]	50	62	70	48

[a] Each value is the average obtained from two men.
[b] Does not include water for personal hygiene.
[c] Kuno (9) has estimated this at 900 ml/man/day.
[d] Based on 80% of fecal weight.

mately 1 lb of food and container was required/man/day to supply from 1160 to 1915 kcal. This level of intake was not always adequate, as indicated by weight loss in both 30-day flights. The energy level was determined to be approximately 30 kcal/kg body weight. Water requirements were met by stored supplies in the 14-day flight and by both stored supplies and recycled water in the other flights. Water requirements in these experiments were found to be about 2.0 liter/man/day. Urine produced approximated 1.0 liter/man/day.

Summary

Data are presented from four separate experiments in the two-man space cabin simulator. These experiments lasted for 14 days, 17 days, 30 days, and 30 days at altitudes of 18,000, 33,500, 18,000, and 18,000 ft, respectively. Food was supplied in a precooked, dehydrated form. Approxi-

References

1 Lambertson, C. J., "From Submarines to Satellites," *Circulation Research*, vol. 6, July 1958, p. 405.

2 Konecci, E. B. and Wood, N. E., "Design of an Operational Ecological System," *Douglas Aircraft Paper 861*, 1959.

3 Bowman, N. J., "The Food and Atmosphere Control Problem on Space Vessels. Part I. Chemical Purification of Air," *J. British Interplanetary Soc.*, vol. 12, 1953, p. 118.

4 Clamann, H. G., "Some Metabolic Problems of Space Flight," *Federation Proc.*, vol. 18, no. 4, December 1959, p. 1249.
5 Steinkamp, G. R., Hawkins, W. R., Hauty, G. T., Burwell, R. R. and Ward, J. E., "Human Experimentation in the Space Cabin Simulator. Development of Life Support Systems and Results of Initial Seven-Day Flights," *School of Aerospace Medicine Rep. No. 59–101*, August 1959.
6 Nelson, J., "Closed Ecology Problems in a Space Cabin Simulator," Fourth Symposium, The Ballistic Missile and Its Space Technology, UCLA, August 24–27, 1959.
7 Welch, B. E., Morgan, T. E. and Ulvedal, F., "Observations in the SAM Two-Man Space Cabin Simulator. I. Logistic Aspects," *J. Aerosp. Med.*, vol. 32, no. 7, July 1961, pp. 583–590.
8 Hartman, B. O., "Experimental Approaches to the Psychophysiological Problems of Manned Spaced Vehicles," Lectures in Aerospace Medicine, *School of Aerospace Medicine Special Rep.*, Jan. 11–15, 1961.
9 Kuno, Y., *Human Perspiration*, Charles C. Thomas, Springfield, Ill., 1956.

Crew Physical Support and Restraint in Advanced Manned Flight Systems

H. A. SMEDAL[1]
H. C. VYKUKAL[2]
R. P. GALLANT[3]
G. W. STINNETT[4]

NASA Ames Research Center
Moffett Field, Calif.

A new concept in physical support and restraint for pilots and crews of motion flight simulators or advanced manned flight vehicles is described. The principle of a wear-in restraint that is easily secured to or released from the support structure, which is part of the vehicle, is the basic concept in this support and restraint system. Its capability as a functional support and restraint for vehicle control studies during sustained accelerations has been established by its use in three human centrifuge programs, but its capability for tolerance to impact accelerations is unproved. Further improvement and testing is contemplated in order to qualify it as an omnidirectional support and restraint system adequate for sustained and impact accelerations of high magnitude.

ADVANCED manned flight vehicles will require the development of physical support and restraint for the crew that permit maximum mobility, comfort, and function. The primary design requirement will be that it afford protection against moderately high level sustained accelerations during the launching of the vehicle and its subsequent re-entry into the Earth's atmosphere. It must also provide support for required activity during the weightlessness of orbital or extra-orbital periods. Finally, it must be capable of providing protection in the event of impact on landing, in which case very high omnidirectional accelerations of rapid onset but brief duration might result.

Presented at the National ARS-IAS Joint Meeting, Los Angeles, Calif., June 13–16, 1961.
[1] Captain, (MC) USN.
[2] Aeronautical Research Scientist.
[3] Equipment Specialist.
[4] Aeronautical Research Scientist and Pilot.

In the design of manned orbital or space vehicles a choice first must be made as to the position of the pilot relative to the vehicle direction of motion. Numerous investigations have been made in the past concerning tolerance to acceleration for various body positions and are described in (1–8).[5] As a result of these studies, it has been pointed out that man can withstand sustained accelerations of moderately high magnitude if the acceleration vector is applied in a direction transverse to the spinal axis of the body. In most of the investigations the subject has been positioned so that he sustains the inertial forces resulting from such acceleration transverse to the spinal axis but from chest to back (1–8). Fewer studies have been made of these tolerance levels when the inertial forces of acceleration are applied from back to chest (2–8), perhaps because chest to back forces are much easier to support than the back to chest variety. Contouring a support for

[5] Numbers in parentheses indicate References at end of paper.

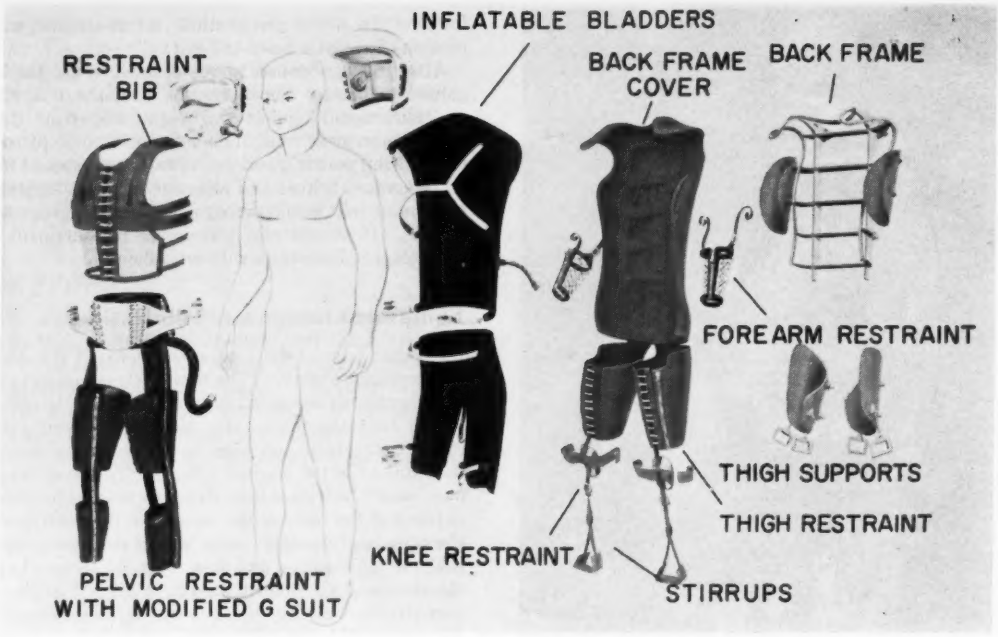

Fig. 1 Schematic of pilot's mobile restraint suit

the posterior half of the body is much less difficult than doing the same for the more mobile anterior half.

The aerodynamic heating and the deceleration problems associated with re-entry are less severe if the vehicle can develop lift. Furthermore, a lifting vehicle might be maneuvered to a landing point so that it would be desirable to place the pilot in a forward-facing seated position. In such a position the pilot during re-entry would be subject to acceleration forces applied along the spinal axis of the body, transversely to the spinal axis of the body, and along any intermediate vector.

As previously stated, most of our knowledge concerning tolerance to acceleration has come from studies in which the acceleration vector has been applied in a direction transverse to the spinal axis but resulting in the forces being applied in a chest to back direction. The restraint systems used in these past investigations have met the requirement for the particular study and have usually been designed to support the individual for accelerations applied in only one direction.

The NASA Ames Research Center made a study at the Naval Air Development Center, Aviation Medical Acceleration Laboratory, Johnsville, Pa. in the fall of 1959 that was designed to investigate the effects of acceleration on pilot performance as well as to obtain some meaningful data for use in establishing tolerance to acceleration levels. This study is reported in (7, 8). In this investigation the pilot was required to perform a control task in various sustained acceleration fields typical of those that might be encountered by a pilot flying an entry vehicle in which he is seated in a forward-facing position. The directions of acceleration studied were A_N, $+A_X$, $-A_X$, and a combination of A_N and $-A_X$. In the vernacular of the test pilot these are also known as eyeballs-down, eyeballs-in, eyeballs-out, and eyeballs-down-and-out accelerations. These studies required the development of the special restraint system that is described in (9).

As a result of the experience gained during this program, it was obvious that a number of changes would have to be made in the basic concept of such a multidirectional restraint system. The NASA posterior mold or couch that had been modified to hold the pilot in a sitting position appeared to afford adequate support in the eyballs-in and eyeballs-down directions of acceleration. However, the pilots complained of considerable discomfort in the chest and neck and a lack of mobility of the helmet. During the eyeballs-in acceleration the head tends to ride upward, and when this is not permitted discomfort in the neck results. Similarly, during eyeballs-down acceleration the body tends to settle downward, and the head must be permitted to follow. It was also found that the upper arm molds were too far back. This, together with the erectness of the posture of the pilot in the couch, forced the pilot to assume a somewhat unnatural attitude or position. The couches were individually molded and fabricated of styrofoam; they are light in weight but unwieldy to handle when pilots are to be alternated during tests in the motion flight simulator.

The anterior restraint was unsatisfactory from a psychological point of view. After each eyeballs-in run the anterior straps had to be manually tightened again. Even then a certain amount of slack had to be taken up during the onset of acceleration, and this was disturbing to the pilot. Once confidence was gained in the anterior support, apprehension was lessened but never entirely eliminated. All components of a restraint system must be able to create an unfailing sense of security, without which it cannot fulfill its function properly. The distribution of the stress for the anterior restraint over the shoulders and chest down to the level of the fourth or fifth rib anteriorly seemed ideal and interfered very little with respiration. The pelvic restraint was also satisfactory, except when the abdominal bladder of the *g*-suit was being used. The lack of integration at this point resulted in discomfort over the lower abdomen and interference with respiration due to combined pressures of the *g*-suit abdominal bladder and the pelvic restraint.

A troublesome problem was the pooling of tissue fluids and blood in the extremities, both upper and lower, on all accelerations except eyeballs in. Some protection was obtained from the use of elastic bandages, but these were not a satisfactory solution.

The restraint of the right arm and hand made it difficult to operate a side-arm controller. Excessive movement was permitted during acceleration in the eyeballs-out direction which interfered with the use of the controller. It was found difficult to provide adequate restraint without restricting arm movement.

In spite of the difficulties, some interesting data on tolerance to acceleration were obtained, generally at the level of 6 g

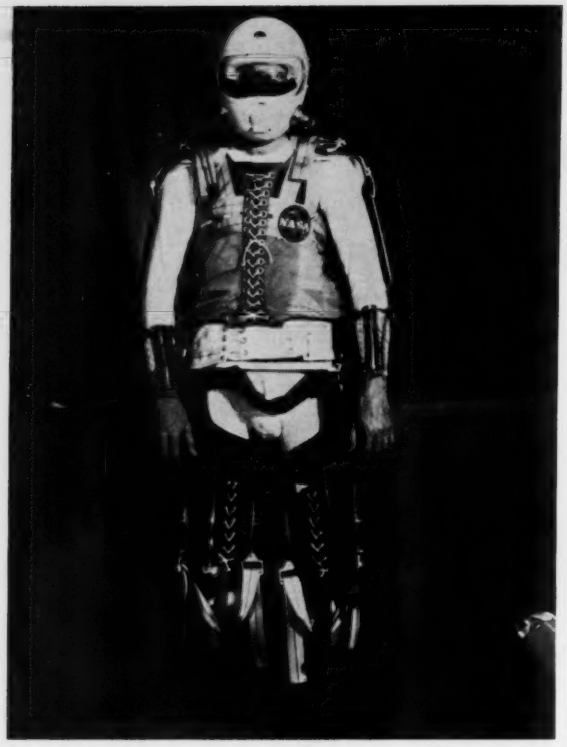

Fig. 2 Front view of pilot wearing mobile support and restraint system

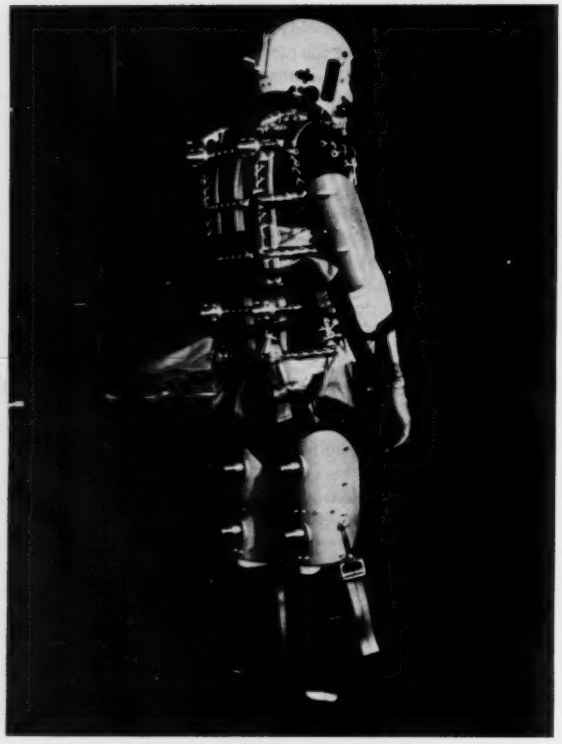

Fig. 3 Three quarter rear view of pilot wearing mobile support and restraint system

for 6 min in all the acceleration vectors studied, with the exception of eyeballs-down-and-out.

After this experience, it was decided to use the knowledge gained to design, construct, and evaluate new concepts in multidirectional support and restraint systems. Again, the basic requirement would be for the pilot to be placed in a forward-facing seated position. The system should incorporate an integrated helmet and restraint suit on a lightweight support frame that would permit easy ingress and egress from the vehicle. It should also permit the measurement of certain physiological quantities without difficulty.

Equipment Design and Fabrication

Two basic concepts were considered in the design of the new restraint system. The first of these concepts was somewhat similar to the initial system previously described. It required that the pilot enter the vehicle, seat himself in a support structure, and then be secured in the restraint much the same as in the original system. The basic support, however, would be a glass fiber structure molded to conform to the outlines of the body of the pilot from the head down through the torso and the legs. The second design concept required that the pilot put on and then wear the restraint system into the vehicle. He could then attach himself to the basic support structure already in place through a system of quick disconnects. This second system consisted of a lightweight torso and leg support frame, which would be constructed of aluminum for the torso framework and glass fiber for the thigh rests. Both systems were to make use of a similar anterior restraint fabricated of nylon cloth and webbing. In both systems, inflatable air bladders would be placed over the posterior torso framework and thigh rests and be positioned between the pilot and the support. The bladders would make the basic support adjustable to more than one pilot and would also cushion the forces over the back and thighs during eyeballs-in and eyeballs-down acceleration. The bladder also would make possible an adjustment of the fit of the anterior restraint during eyeballs-out acceleration.

A prototype of each system was fabricated and tested on the University of Southern California human centrifuge. As a result of these tests, it was decided that the wear-in restraint concept would be followed in further development work. The wear-in restraint is similar in concept to an item of pilot personal gear. Figs. 1–3 illustrate the complete suit. The weight of the system at present is approximately 30 lb.

A description of the various components of the restraint follows.

Head

A modified protective helmet is used to restrain the head, as shown in Fig. 4. A crushable material facemold insert permits an even distribution of the weight of the head over the brow and cheek bone areas with very little force being distributed to the chin during eyeballs-out acceleration. An adjustable pad in the back of the helmet permits adjustment for size and tightness of the face fit.

Upper Torso

The posterior portion of the torso restraint consists of a contoured welded aluminum frame covered with a high tensile strength nylon cloth.

A rubberized nylon bladder is between the nylon fabric of the combined posterior torso-seat support and the pilot's body. When inflated with air, this bladder contours to the body of the pilot, giving him a cushion for his back as well as his seat. This bladder arrangement also serves the dual purpose of permitting adjustment of the fit of the anterior chest and thigh restraints (Fig. 1). The anterior portion of the upper torso is supported by a nylon fabric bib secured to the aluminum

frame by straps extended around the back of the frame (Figs. 1–3). The upper part of the bib, which is the weight supporting area, extends from the region of the collarbone and shoulder down over the upper chest to the level of the nipple line (Fig. 2). The lower portion, made of nylon netting, extends from the lower border of the nylon fabric of the chest plate down to the upper portion of the pelvic restraint. This nylon netting serves only to maintain the usual contour of the abdomen and prevent major displacement of abdominal viscera.

Buttocks and thighs

The nylon cloth from the back support extends down under the buttocks and is secured to the glass fiber thigh supports. Fastened to this cloth area are straps that are adjusted for variations in sitting height of the pilots. The thigh supports are contoured glass fiber plates into which are fitted nylon bibs, which are brought over the anterior portion of the thigh and secured by adjustable lacings and zippers (Figs. 1 and 3).

Pelvis

The anterior portion of the lower abdomen and pelvis is restrained by a nylon fabric belt, which is secured at the back of the frame in the same manner as the nylon fabric bib for the upper chest (Figs. 1 and 3).

Knees

Padded aluminum cups, which are attached to the glass fiber thigh supports by nylon straps, restrain and support the knees (Figs. 1–3).

Arms

Coarsely woven or knotted tubular shaped fabrics consitute the forearm restraint (Figs. 1, 2, 5). This system incorporates the use of counterweights to balance the mass forces on the arm and permit easy fore and aft movement when using the side-arm controller (Fig. 5).

When the pilot enters the vehicle, the eight tapered pins mounted on the torso and thigh portions of the wear-in suit are inserted into female receptacles equipped with spring loaded plugs that are a part of the support structure in the vehicle. A similar male plug is mounted on the back of the helmet in a slotted metal plate; this plug also fits into a female receptacle with spring loaded plugs. The slotted plate on the helmet permits upward and downward excursion of the head. An air actuator with a manual override secures and releases the pins that hold the restraint suit and helmet in the support structure.

Discussion

The new Ames Research Center support and restraint system has had two additional evaluations since the initial trials at the University of Southern California. The first of these took place during a two-week period at the Naval Air Development Center, Aviation Medical Acceleration Laboratory, Johnsville, Pa. in November 1960 and again at Johnsville during a seven-week period in March and April of 1961.

The helmet was developed specifically for respiratory research. If the closed circuit respiratory system is not required, some adaptation, fitted over the brow and cheek bones with a check strap for the chin, would be sufficient to retain the head in the helmet and prevent rotation during eyeballs-out, eyeballs-down, or eyeballs-down-and-out acceleration. A protective helmet must still be the basis of all head restraint devices. Any force being borne over the face must always be carried on the most stable portions of the face, namely, the brow and the prominences of the cheek bones. The chin is an unstable point, and the lack of tolerance of the jaw joint to pressure makes it an unsuitable point for any restraint purpose other than a check strap.

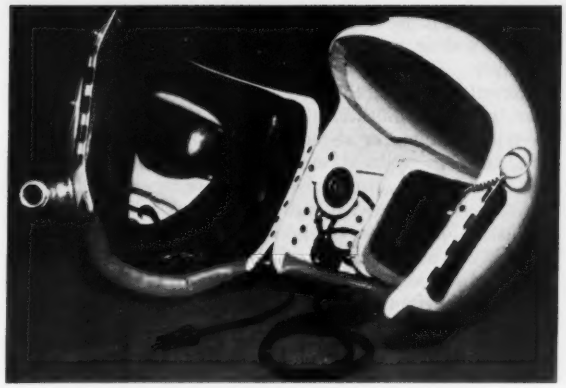

Fig. 4 Mobile support and restraint system: helmet

Whereas the present torso restraint performed satisfactorily in the centrifuge tests, improvements in performance might be gained if the rigid portion of the aluminum framework were extended downward anteriorly over the shoulder to include the area now occupied by the nylon fabric portion of the bib. The inflated back bladder could likewise be extended to include the same area. From this point, which is the level of the nipple line down to the upper margin of the pelvic restraint, the use of the nylon netting seems to be adequate and satisfactory, for this is not and should not be a weight-bearing area. The purpose of the restraint here should only be to maintain body contours and so prevent the radical displacement of internal abdominal organs.

The pelvic and lower limb restraint is more of a problem. Restraining the pelvis itself is a simple matter, but the integration of the pelvic restraint with the g-suit and the leg protective devices present a problem. It is probable that a close fitting leg and pelvic mechanical elastic garment secured by appropriate straps to the basic support structure will be sufficient.

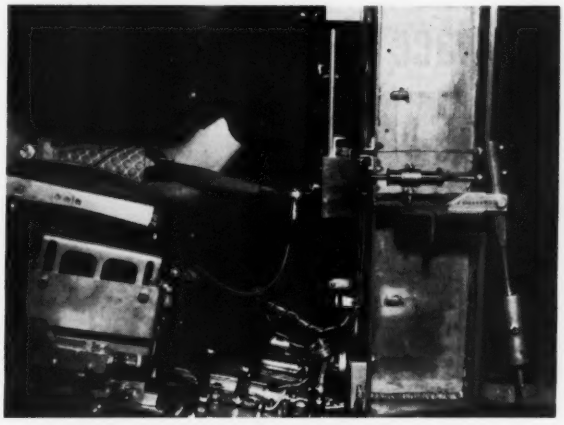

Fig. 5 Mobile support and restraint system: forearm restraint with counter weight

The upper arm restraint is critical only when movement is required to operate a side-arm controller. It does not appear that an upper arm restraint is necessary as long as there is an arm rest and the forearm itself is properly restrained.

This support and restraint system appears to be an answer to some of the many problems that are known to exist in motion flight simulators. Its capability of quick donning (5 min) and rapid attachment or release by the pilot from the basic support, requiring no more time to enter and be fastened

in place than it does for a person to walk into a room and be seated in a chair, makes it highly desirable for use in any type of vehicle. However, since movement in a shirt sleeve environment is a desirable requirement for a space vehicle, some further modification is required that would facilitate the pilot's leaving or re-entering the fabricated torso and limb anterior restraints unassisted. The entire anterior fabricated, or soft, portion of the restraint must be made so that the pilot can enter it and effect closure or exit from it as he chooses for it to be adaptable for flight vehicle use. This capability is not required in flight simulation devices where the entire portable portion of the restraint can be worn into and out of the simulator with considerable ease.

There are two types of acceleration in which this current restraint is untested and probably as yet unsatisfactory. Accelerations that impose lateral transverse forces, either sustained or impact, are in all probability not adequately designed for. The question of any impact capability has not as yet been ascertained, but it is probable that the present restraint, with certain modifications to the bladder system, has considerable capability.

The primary purpose of this support and restraint system, however, has been to permit simulator studies of flight vehicle control under varying conditions of acceleration stress. For this, its primary function, it has performed admirably.

References

1 Bürhrlen, L., "Studies Concerning the Significance of the Direction of Acceleration Forces Acting Upon the Human Body" ("Versuche Über die Bedeutung der Richtung beim Einwirken von Fliehkraften auf den Menschlichen Körper"), *Luftfahrtmedizin*, vol. 1, no. 5, 1939.

2 Gauer, O. and Rubb, S., "The Limits of Endurability for Centrifugal Forces in the Back to Chest Direction" ("Die Erträglichkeitagrenzen fur Fliehkrafte in Richtung Rücken-Brust"), *Luftfahrtmedizin*, vol. 3, no. 3, 1939.

3 Lombard, C. F., "Human Tolerance to Forces Produced by Acceleration," *Rep. ES-21072*, Douglas Aircraft Co., February 1948.

4 Ballinger, E. R. and Dempsey, C. A., "The Effects of Prolonged Acceleration on the Human Body in the Prone and Supine Positions," *WADC TR-52-250*.

5 Bondurant, S., Clark, N. P., Blanchard, W. G., Miller, H., Hessberg, R. R. and Hiatt, E. P., "Human Tolerance to Some Accelerations Anticipated in Space Flight," *USAFMJ*, vol. 9, no. 8, August 1958.

6 Clark, N. P., Bondurant, S. and Leverett, S. D., "Human Tolerance to Prolonged Forward and Backward Accelerations," *J. Aviation Medicine*, vol. 30, no. 1, January 1959.

7 Creer, B. Y., Smedal, H. A. and Wingrove, R. C., "A Centrifuge Study of Pilot Tolerance to Acceleration and the Effects of Acceleration on Pilot Performance," *NASA TN D-337*, 1960.

8 Smedal, H. A., Creer, B. Y. and Wingrove, R. C., "Physiological Effects of Acceleration Observed During a Centrifuge Study of Pilot Performance," *NASA TN D-345*, 1960.

9 Smedal, H. A., Stinnett, G. and Innis, R., "A Restraint System Enabling Pilot Control While Under Moderately High Acceleration in a Varied Acceleration Field," *NASA TN D-91*, 1960.

Directional Solar Reflectances in the Space Vehicle Temperature Control Problem[1]

D. K. EDWARDS[2]

University of California
Los Angeles, Calif.

Directional spectral reflectances of typical spacecraft surface systems are presented. The surface systems reported are aluminum foil, anodized aluminum, aluminum foil coated with oxidized titanium, sandblasted stainless steel, silicon solar cell with glass cover, flame sprayed aluminum oxide, and white paint. Average solar absorptances of elementary geometries with the above surface systems are obtained, and the discrepancy between the actual average absorptance and the near normal value used in design and analysis is presented. The geometries considered are the sphere, cylinder, and cone. Design and analysis with directional spectral reflectances are shown to be especially important for vehicles with large areas exposed to solar irradiation at angles more than 60° from the normal.

SPACE vehicle temperature must be maintained within a range fixed by the requirements of the transported electronic instruments, power supply, or life. Since the temperature of a vehicle is governed by a heat balance (1)[3] that generally involves the amount of solar irradiation absorbed, knowledge of the solar absorptance is necessary for analysis and design of the temperature control system.

Considered as a source of radiation, the sun may be idealized in several ways. At distances far from the sun, the angle

Received Jan. 27, 1961.

[1] This paper is based on part of an annual report submitted to the National Science Foundation for the year 1959–1960 under Grant G 9505.

[2] Assistant Professor.

[3] Numbers in parentheses indicate References at end of paper.

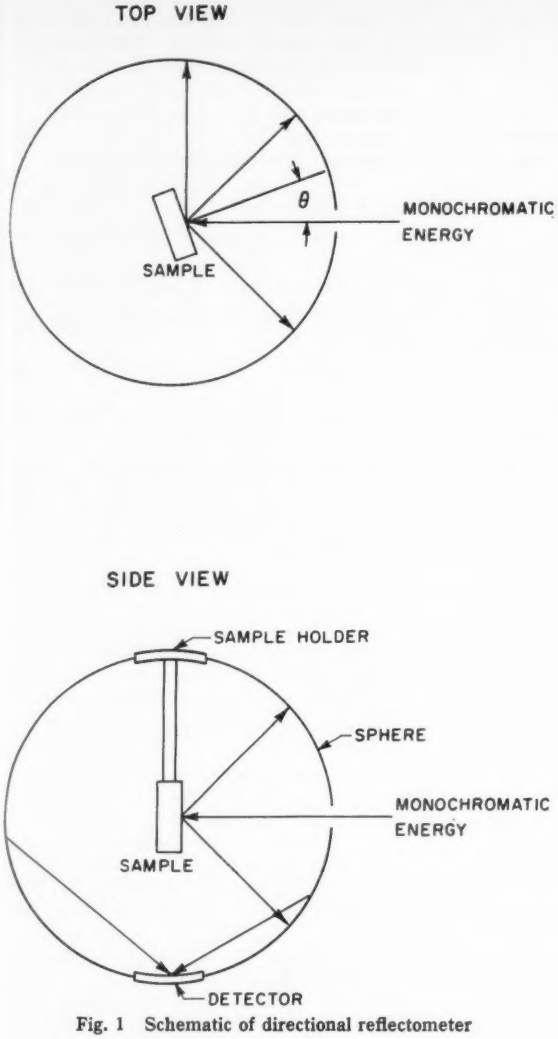

Fig. 1 Schematic of directional reflectometer

subtended by the solar disk is small and may have a negligible influence on the angle of incidence of the solar irradiation on the vehicle. In this case, the sun may be considered a point source. For surfaces closer to the sun so that the angle subtended by the solar disk is appreciable, a better approximation of the solar structure is needed. One such idealization is that the sun is a sphere with a given directional intensity of the sphere surface. The directional intensity is determined from the *darkening to the limb* (2).

In the present treatment, the sun is considered a point source. For such a case the solar radiation is absorbed by a surface element at the rate (1)

$$\alpha_S SF_S = \left[\int_0^\infty \alpha_\lambda(\theta,\Phi)\, S_\lambda d_\lambda\right] \cos\theta \qquad [1]$$

where

$$F_S = \cos\theta \qquad [2]$$

is the geometric shape factor

$$S = \int_0^\infty S_\lambda d_\lambda \qquad [3]$$

is the total solar irradiation, $\alpha_\lambda(\theta,\Phi)$ the directional absorptance of the vehicle surface element, S_λ the monochromatic solar irradiation at wavelength λ, and (θ,Φ) the polar and azimuthal angles of incidence. From Eqs. 1, 2, and 3 the total directional absorptance is seen to be

$$\alpha_S(\theta,\Phi) = \int_0^\infty \alpha_\lambda(\theta,\Phi) S_\lambda d_\lambda \Big/ \int_0^\infty S_\lambda d_\lambda \qquad [4]$$

It has been standard procedure in thermal environment analysis and design to consider space vehicle surfaces as diffuse with $\alpha_\lambda(\theta,\Phi) = \alpha_\lambda$ and $\alpha_S(\theta,\Phi) = \alpha_S$ (1, 3). The value of α_S used in such analysis has usually been the near normal directional value $\alpha_S(\theta \simeq 0)$. However, space vehicle exterior surfaces are usually an isolated system from the standpoint of external irradiation, that is, the external surfaces are convex, so that no interreflected energy forms part of the irradiation. For this reason exact directional characteristics can be used in analysis with little difficulty.

In what follows, directional spectral reflectances of several typical spacecraft materials are given; no attempt to precisely define the surface system is made. Surface-average solar absorptances for a sphere, cylinder, and cone are determined from the data, and the deviation of these average values from the corresponding near normal value is evaluated. The effect of this deviation on the space vehicle temperature control problem is evaluated.

Apparatus and Procedure

Apparatus used consisted of an integrating sphere attached to standard Perkin-Elmer monochromator optics. Fig. 1 shows a schematic of the sphere. Radiant energy from the exit slit of a monochromator is focused either on a sample suspended in the sphere by a rotatable shaft or on the diffuse sphere wall. A detector, with a response essentially independent of angle, located at the base of the sphere detects

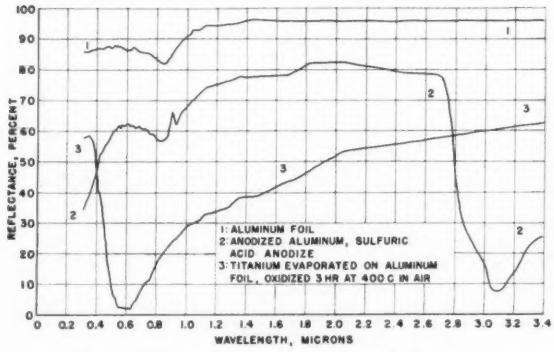
REFLECTANCE, PERCENT
WAVELENGTH, MICRONS
1: ALUMINUM FOIL
2: ANODIZED ALUMINUM, SULFURIC ACID ANODIZE
3: TITANIUM EVAPORATED ON ALUMINUM FOIL, OXIDIZED 3 HR AT 400 C IN AIR

Fig. 2 Spectral near normal reflectances

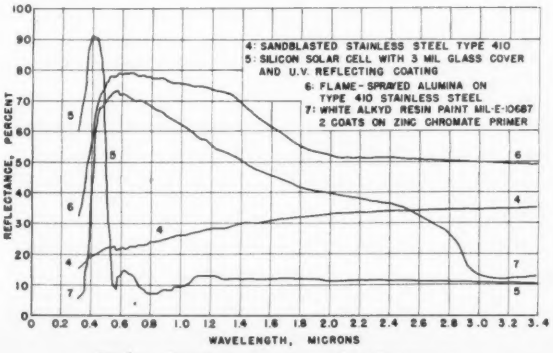
REFLECTANCE, PERCENT
WAVELENGTH, MICRONS
4: SANDBLASTED STAINLESS STEEL TYPE 410
5: SILICON SOLAR CELL WITH 3 MIL GLASS COVER AND U.V. REFLECTING COATING
6: FLAME-SPRAYED ALUMINA ON TYPE 410 STAINLESS STEEL
7: WHITE ALKYD RESIN PAINT MIL-E-10687 2 COATS ON ZINC CHROMATE PRIMER

Fig. 3 Spectral near normal reflectances

energy reflected from the sphere wall. The ratio of the detector signal with the sample irradiated to that with the sphere wall directly irradiated is the absolute directional reflectance. The angle of incidence may be varied by rotation of the sample holder about an axis passing through the sample face. For a detailed description of the apparatus together with a comprehensive error analysis, the reader is referred to (4).

Spectral reflectances for $\theta = 20°$ were obtained at 50 wavelengths in the solar spectrum. Measurements were made relative to a magnesium oxide sample which was held exposed on the back of the sample holder. The absolute reflectance of this standard was determined directly. This procedure was more convenient, as the standard could be rotated into position with a remote controlled servomechanism. Near normal spectral reflectances past 2.5 μ were obtained with a heated cavity reflectometer (5).

Each λ_i of the 50 wavelengths was chosen such that

$$\int_0^{\lambda_i} S_\lambda d\lambda \Big/ \int_0^{\infty} S_\lambda d\lambda = 0.01\, n \qquad [5]$$

$$n = 1, 3, 5 \ldots 99$$

where $\int_0^{\lambda} S_\lambda d\lambda$ was obtained from Johnson's data (6). Further, the spectral slit width $\Delta\lambda_i$ at wavelength λ_i was set approximately equal to

$$\Delta\lambda_i = [\lambda_{i+1} - \lambda_{i-1}]/2 \qquad [6]$$

Thus, each point represented 2% of the solar spectrum, and the average of the 50 points gives $\alpha_S(\theta = 20°)$.

Directional reflectances were obtained relative to the reflectance at $\theta = 20°$ at five of the above wavelengths and with the above mentioned spectral slit width. Checks were made to establish any azimuthal angular dependence by rotating the sample on the sample holder.

Results

Figs. 2 and 3 give descriptions of the seven surface systems investigated along with the directional spectral absorptance for $\theta = 20°$. Normalized directional reflectances of each surface at 0.46, 0.59, 0.81, 1.25, and 2.25 μ are presented in Figs. 4–10. The points shown at $\theta = 90°$ were taken as $1/\rho\ (\theta = 20°)$.

Discussion

In cases where the skin is a good thermal conductor or where some type of average temperature is desired, the total rate of solar energy absorbed by the entire vehicle is of interest (1). This rate is

$$Q_S = S \int_A \alpha_S F_S dA \qquad [7]$$

The average α_S may then be defined as

$$\alpha_{S\text{Avg}} = \int_A \alpha_S F_S dA \Big/ \int_A F_S dA \qquad [8]$$

so that

$$Q_S = S \alpha_{S\text{Avg}} A_N \qquad [9]$$

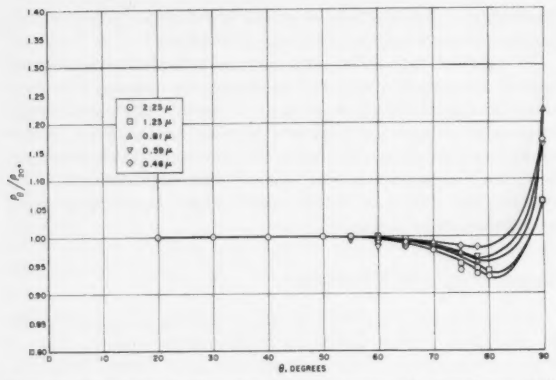

Fig. 4 Normalized directional reflectance of aluminum foil

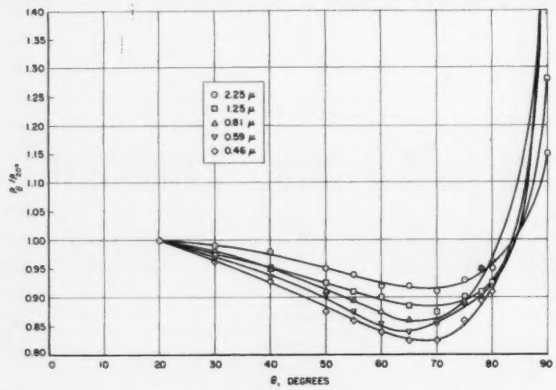

Fig. 5 Normalized directional reflectance of anodized aluminum

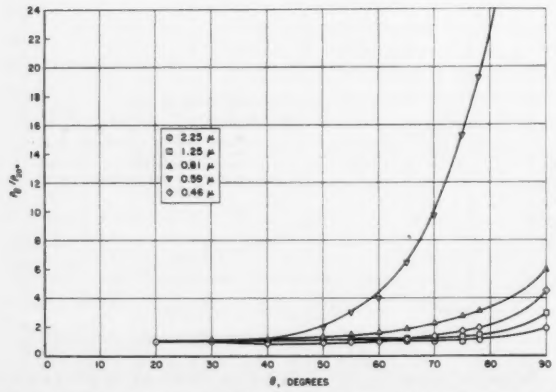

Fig. 6 Normalized directional reflectance of aluminum foil coated with oxidized titanium

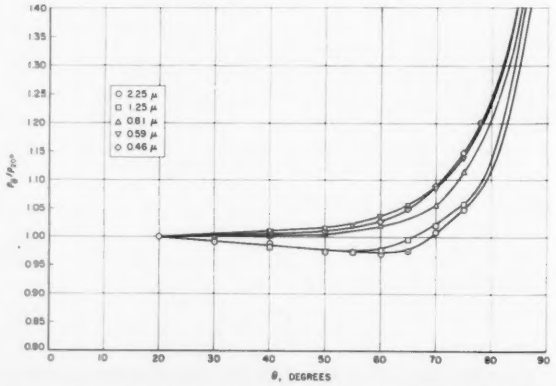

Fig. 7 Normalized directional reflectance of sandblasted stainless steel

Table 1 Ratio of average solar absorptance to near normal solar absorptance

Surface	$\alpha_S(20°)$, %	$\alpha_{SAVG}/\alpha_S(\theta = 20°)$ Sphere	Cylinder	15° Cone[a]	25° Cone[a]
Aluminum foil	11.1	1.023	1.009	1.29	1.13
Anodized aluminum	38.0	1.097	1.062	1.19	1.23
Oxidized titanium	75.7	0.677	0.824	0.693	0.879
Sandblasted stainless steel	76.1	0.991	0.993	0.967	0.992
Silicon cell assembly	74.5	1.023	1.040	0.969	1.073
Flame sprayed alumina	29.1	0.949	0.962	0.910	0.949
White paint	41.2	0.941	0.965	0.856	0.925

[a] Angle is half angle θ_3.

where A_N is the projected area of A in the direction of the irradiation

$$A_N = \int_A F_S dA \qquad [10]$$

Eq. 9 consists of three factors: the environmental solar irradiation S, the surface characteristic α_{SAVG}, and the geometrical projected area A_N. For a perfectly diffuse surface, the surface characteristic and geometrical area are independent of one another, that is, uncoupled. In the case of real surfaces, however, α_{SAVG} depends on both the geometry and surface characteristics. Therefore, in order to assess the overall effect of the angular characteristics on the space vehicle temperature control problem, typical geometries must be considered. For this purpose a sphere, a cylinder with axis normal to the irradiation, and a cone with axis parallel to the irradiation are chosen.

For a sphere of radius r_1, $dA_1 = 2\pi r_1^2 \sin\theta\, d\theta$, and as previously noted $F_S = \cos\theta$ in Eq. 8.

Similarly for a cylinder of radius r_2 and length L normal to the sun's rays $dA_2 = Lr_2 d\theta$ in Eq. 8.

Finally, for a cone of half angle θ_3 and axis directed at the sun, the absorptance is constant and may be removed from under the integral in Eq. 8.

The quantity

$$\int_A \alpha_S(\theta) F_S\, dA = \int_A F_S \int_0^\infty (S_\lambda/S)\alpha_\lambda(\theta)\, d\lambda dA \qquad [11]$$

may be approximated by making the observation that

$$\int_A \alpha_\lambda(\theta)/\alpha_\lambda(\theta = 20°)\, dA$$

is a less rapidly varying function of λ than $\alpha_\lambda(\theta)$ itself is for all the geometries above except the cone with small θ_3. Thus Eq. 11 is rewritten as follows

$$\int_A \alpha_S(\theta)\, F_S dA = \int_0^\infty (S_\lambda/S)\alpha_\lambda(\theta = 20°) \left\{\int_A \left[\frac{\alpha_\lambda(\theta)}{\alpha_\lambda(\theta = 20°)}\right] F_S dA\right\} d\lambda \qquad [12]$$

This equation is in turn approximated by dividing the spectrum into several regions in each of which the quantity in the large brackets is assumed constant.

$$\int_A \alpha_S(\theta)\, F_S dA = \sum_{j=1}^{5} \left\{\int_A \frac{\alpha_{\lambda_j}(\theta)}{\alpha_{\lambda_j}(\theta = 20°)} F_S dA\right\} \sum_{t=t_{-j1}}^{t_j} \alpha_{\lambda_i}(\theta = 20°)\, \frac{\Delta_i S}{S} \qquad [13]$$

As remarked in the procedure, the $\Delta_i S/S$ increments are 2%. Each λ_j represents about 20% of the energy in the solar spectrum.

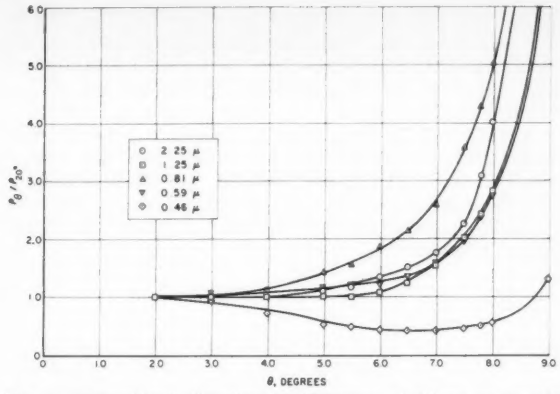

Fig. 8 Normalized directional reflectance of silicon solar cell with cover glass

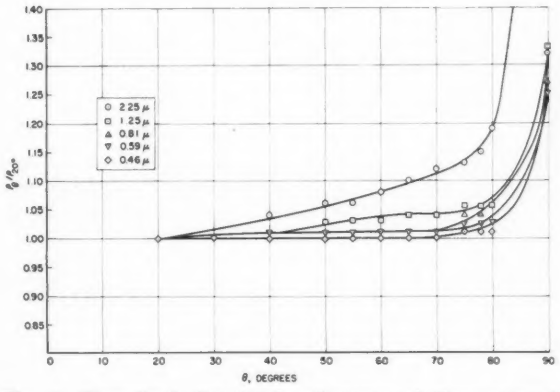

Fig. 9 Normalized directional reflectance of flame-sprayed aluminum oxide

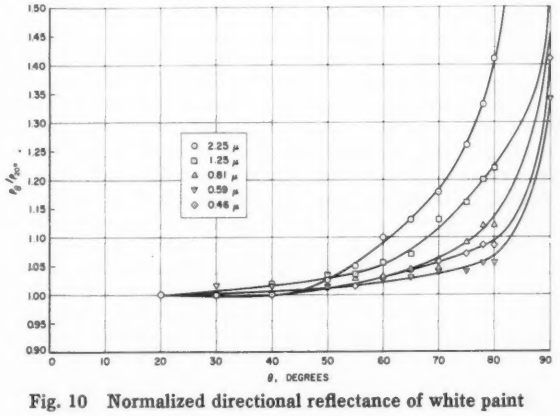

Fig. 10 Normalized directional reflectance of white paint

The quantity summed over j in the first term on the right of Eq. 13 was evaluated graphically for each of the five wavelengths and each geometry. Then these quantities were substituted into Eq. 13 to obtain α_{SAVG}.

Results of these calculations are shown in Table 1. As would be expected from the lack of directional dependence of the data in Figs. 4 and 7, the ratio $\alpha_{SAVG}/\alpha_S(20°)$ differs little from unity for the aluminum foil and sandblasted stainless steel samples. In the case of the solar cell assembly, the directional dependence in the spectral region affected by the reflection coating counters that in the other spectral re-

gions. This behavior explains the otherwise surprising result that the average solar absorptance differs little from the near normal value. The aluminum foil coated with oxidized titanium shows the most marked variation, as would be expected from Fig. 6.

The effect of the deviation of $\alpha_{S\text{Avg}}$ from $\alpha_S(\theta = 20°)$ normally used in analysis must be examined from the point of view of the heat balance equation (1). For simplicity, consider a space vehicle far from any planetary body with negligible internal heat generation and at steady state. The overall heat balance is

$$Q_S = \int_A \epsilon_H \sigma T^4 dA \qquad [14]$$

where T is the temperature of the outer skin and ϵ_H the skin total hemispherical emittance, which is taken constant over the vehicle. The fourth root mean fourth power temperature is then defined as

$$\bar{T} = \left[\frac{Q_S}{\epsilon_H \sigma A}\right]^{1/4} = \left[\frac{\alpha_{S\text{Avg}}}{\epsilon_H} \frac{S}{\sigma} \frac{A_N}{A}\right]^{1/4} \qquad [15]$$

The deviation in $\alpha_{S\text{Avg}}$ from the design value results in a deviation of $\bar{T}$ from the design value $\bar{T}_0$

$$(\bar{T} - \bar{T}_0)/\bar{T}_0 = (1/4)[\alpha_{S\text{Avg}} - \alpha_S(\theta = 20°)]/\alpha_S(\theta = 20°) \qquad [16]$$

If each of the simple geometries is considered to have each of the surfaces investigated at such a distance from the sun that $\bar{T}_0$ is approximately 500°R, the deviation of the temperature may be obtained. These results are indicated in Table 2.

It is seen that use of near normal values of absorptance or reflectance for the design of a conical vehicle pointed at the sun results in large deviations of the actual temperature from the design value, if the cone half angle is small. The deviation of the actual temperature from the design value is small for the case of the cylinder and sphere for nearly all the surface materials. An aluminum sphere covered with evaporated oxidized titanium, however, would have a temperature significantly different from the design value.

The error in $\alpha_{S\text{Avg}}$ caused by the neglect of the directional dependency of α_S should be compared to the uncertainty in α_S due to the uncertainties in measurement. From error analysis (4) the uncertainty in the spectral reflectance measurement is estimated to be 0.015. Thus, in the case of the aluminum foil sample, the experimental uncertainty is larger than the error from neglect of directional variation for the cases of the sphere and cylinder and is of the same order for the cones. Similar observations may be made for the anodized aluminum, flame sprayed alumina, and white paint samples. However, the uncertainty is small compared to the error for the titanium oxide covered aluminum.

The computational procedure summarized in Eq. 13 is not well suited for a cone of small half angle directed at the sun, since $\alpha_\lambda(\theta_3)/\alpha_\lambda(20°)$ may be a strong function of λ in this case. For such a geometry a straightforward procedure would be to measure $\alpha_\lambda(\theta_3)$ directly rather than $\alpha_\lambda(20°)$ and $\alpha_\lambda(\theta_3)/\alpha_\lambda(20°)$. This latter procedure was not carried out in the present instance, as it would have required three times as much spectral data. It is estimated that the use of the former procedure results in an additional uncertainty of about 0.03 for $\alpha_{S\text{Avg}}$ of the oxidized titanium sample in the shape of a cone with 15° half angles. This uncertainty is still much less than the difference between $\alpha_S(20°)$ and $\alpha_{S\text{Avg}}$ for this case, however. Similarly, direct measurement of $\alpha_\lambda(75°)$ in the spectral region affected by the ultraviolet reflection coating disclosed a decrease of 0.02 in α_S (75°) from the value computed using Eq. 13. This change doubles the value shown in Table 2 for the 15° cone of solar cells, but does not change the major conclusion that the effect of directional variation of absorptance is quite small for this sample and configuration.

Table 2 Discrepancy in temperature from assumption of diffuse surfaces for a space vehicle at a distance from the sun such that $\bar{T}_0 = 500°R$

Surface	Temperature difference, °R: Sphere	Cylinder	15° Cone	25° Cone
Aluminum foil	3	1	36	16
Anodized aluminum	12	8	23	29
Oxidized titanium	−40	−22	−38	−15
Sandblasted stainless steel	−1	−1	−4	−1
Silicon cell assembly	3	5	−4	9
Flame sprayed alumina	−6	−5	−11	−6
White paint	−7	−4	−17	−9

$$\Delta T \simeq (1/4)\left[\frac{\alpha_{S\text{Avg}}}{\alpha_S(20°)} - 1\right](500)$$

Summary and Conclusions

Average solar absorptances of typical spacecraft materials obtained for three elementary geometries show that significant error can be introduced into analysis and design of temperature control systems if angular dependence of radiation characteristics is neglected. This fact is particularly true of vehicles with large areas for which polar angles of incidence of solar irradiation exceed 60°. Materials for which errors are less than 10% are sandblasted stainless steel, silicon solar cell assembly with ultraviolet reflection coating, and flame sprayed alumina. Materials for which errors range between 10 and 30% are white paint, anodized aluminum, aluminum foil, and oxidized titanium.

Acknowledgment

The author wishes to express his appreciation to R. Tobin and K. Nelson, who assisted with the experimental measurements. Grateful acknowledgment also is made for support under National Science Foundation Grant 9505.

Nomenclature

A = area
F = geometric factor
n = integer
Q = heat rate
r = radius
S = solar irradiation
α = absorptance
ϵ = emittance
θ = polar angle
ρ = reflectance
Φ = azimuthal angle

Subscripts

1 = sphere
2 = cylinder
3 = cone
Avg = geometric average
H = hemispherical
0 = Design point
N = normal
S = solar
θ = directional characteristic for angle θ
λ = spectral
20° = directional characteristic for $\theta = 20°$

References

1 Camack, W. G. and Edwards, D. K., "Effect of Surface Thermal-Radiation Characteristics on the Temperature-Control Problem in Satellites," *Surface Effects on Spacecraft Materials*, F. J. Clauss (ed.), John Wiley and Sons Inc., New York, 1960.

2 Thomas, R. N., "The Features of the Solar Spectrum as Imposed by the Physics of the Sun," *Trans. of the Conf. on the Use of Solar Energy*, vol. 1, Chap. 1, 1955.
3 Thostesen, T. O., Hibbs, A. R. and Buwalda, E. P., "Temperature Control of the Explorers and Pioneers," *Surface Effects on Spacecraft Materials*, F. J. Clauss (ed.), John Wiley and Sons Inc., New York, 1960.
4 Edwards, D. K., Nelson, K. E., Roddick, R. D. and Gier, J. T., "Basic Studies on the Use and Control of Solar Energy," *Annual Rep. 60-93*, National Science Foundation Grant 9505, Univ. of Calif., Los Angeles, Calif., October 1960, Part 7, and "Integrating Sphere for Imperfectly Diffuse Samples," *J. Opt. Soc. Amer.* (to be published).
5 Gier, J. T., Dunkle, R. V. and Bevans, J. T., "Measurement of Absolute Spectral Reflectivity from 1.0 to 15 Microns," *J. Opt. Soc. Amer.*, vol. 44, no. 558, 1954.
6 Johnson, F. S., "The Solar Constant," *J. Meteorol.*, vol. 11, no. 431, 1954.

Optimization of Multistage Orbit Transfer Processes by Dynamic Programming

F. T. SMITH[1]

The RAND Corp.
Santa Monica, Calif.

This paper discusses the development of a set of variation of parameter equations that define state transformations of a vehicle in terms of some selected set of two-body orbit parameters. The state transformation equations obtained by integration of the variation of parameter equations are substituted in a performance index that is optimized by the methods of dynamic programming. This optimization gives a sequence of incremental velocity vectors to be applied to the vehicle to transfer it from an arbitrary initial orbit to the desired orbit. In addition to the multistage process, three special cases are considered: a single stage process, a double stage process, and a special performance index pertinent to 24-hr communication satellites.

THE PURPOSE of this paper is to expand the idea suggested in (1)[2], i.e., to use a set of variation of parameter equations in an orbit transfer process. The orbit transfer process in the case considered here involves correcting the motion of a space vehicle in some optimum manner.

Two orbit transfer methods are considered in (1). One is a two-stage exact method,[3] and the other is a single stage approximate method that minimizes the sum of the weighted squares of the errors in the orbital parameters existing at the termination of thrust. A generalization of the latter method is discussed here.

Received Feb. 17, 1961.
[1] Guidance and Orbital Mechanics Research, Electronics Dept.
[2] Numbers in parentheses indicate References at end of paper.
[3] The method is exact except for small errors involved in linearizing the equations of motion.

Other references considering optimization of orbit transfer processes are included in the list of references (2–5). These papers use conventional minimization techniques, i.e., setting partial derivatives of functions equal to zero, trial and error methods. This paper considers the optimization of multistage orbit transfer processes by dynamic programming. Further, due to the linearity of the state transformation equations and the quadratic system performance index used, the optimizing control vectors are determined by analytical expressions.

Variation of Parameter Equations

Equations of Perturbed Motion

The motion of a celestial object is approximately defined by a Keplerian orbit that assumes that the only force on the object is due to the force field of the central body. A more

precise determination of the motion of the object requires accounting for the perturbing effects of the gravitational fields of other celestial bodies. In the case of satellites, any nonsphericity of the central body will also perturb the motion.

Integration of equations of motion of a celestial object, when perturbing effects are included, is generally carried out by Cowell's method, Encke's method, or the variation of parameters[4] method (6–8). In what follows, the variation of parameters method will be used to determine the equations of perturbed motion.

The motion of a particle in an inverse-square central force field, subject to a perturbing acceleration, may be described by the following set of second-order differential equations:

$$\frac{d^2x}{d\tau^2} + \frac{\mu x}{r^3} = a_x$$

$$\frac{d^2y}{d\tau^2} + \frac{\mu y}{r^3} = a_y$$

$$\frac{d^2z}{d\tau^2} + \frac{\mu z}{r^3} = a_z$$

where[5]

$\mu = (k/k')^2(m_0 + m_1)$
$\tau = k'(t - t_0)$
a_x, a_y, a_z = components of perturbing force per unit mass.

These three second-order equations may be transformed into a system of six first-order equations (9)

$$\dot{x}_i = g_i(x_j; \tau) + f_i(x_j; \tau) \qquad i, j = 1, \ldots, 6$$

$$x_i(0) = c_i \qquad \dot{x}_i = dx_i/d\tau$$

where

$x_1 = x$	$g_1 = x_2$	$f_1 = 0$
$x_2 = \dot{x}$	$g_2 = -(\mu x_1/r^3)$	$f_2 = a_x$
$x_3 = y$	$g_3 = x_4$	$f_3 = 0$
$x_4 = \dot{y}$	$g_4 = -(\mu x_3/r^3)$	$f_4 = a_y$
$x_5 = z$	$g_5 = x_6$	$f_5 = 0$
$x_6 = \dot{z}$	$g_6 = -(\mu x_5/r^3)$	$f_6 = a_z$

The functions $g_i(x_j; \tau)$ contain the effect of the central force field on the motion of the particle, whereas the functions $f_i(x_j; \tau)$ represent the effect of the perturbing force. The c_i are arbitrary constants of the solution representing the initial values of the position and velocity components at $t = t_0$ or $\tau = 0$. When there is no perturbing force, the system of first-order equations reduces to

$$dx_i/d\tau = g_i(x_j; \tau) \qquad i, j = 1, \ldots, 6$$

where

$$x_i(0) = c_i = x_i(p_1, \ldots, p_6; 0)$$

$p_1, \ldots, p_6$ are a set of orbital parameters defining the two-body orbit. The solution of the two-body equations is given by

$$x_i(\tau) = x_i(p_1, \ldots, p_6; \tau) \qquad i = 1, \ldots, 6$$

A small perturbing force causes the orbital parameters $p_1, \ldots, p_6$ to vary slowly with time. Thus, $p_1, \ldots, p_6$ may be considered as a new set of variables and the solution equations as a set of transformation equations from the variables $p_1, \ldots, p_6$ to $x_1, \ldots, x_6$.

Taking the total derivatives of the transformation equations with respect to time gives

$$\frac{dx_i}{d\tau} = \frac{\partial x_i}{\partial \tau} + \sum_{j=1}^{6} \frac{\partial x_i}{\partial p_j}\frac{dp_j}{d\tau} \qquad i = 1, \ldots, 6$$

Substituting in the equations of motion yields

$$\frac{\partial x_i}{\partial \tau} + \sum_{j=1}^{6} \frac{\partial x_i}{\partial p_j}\frac{dp_j}{d\tau} = g_i(x_j; \tau) + f_i(x_j; \tau) \qquad i = 1, \ldots, 6$$

The partial derivatives $\partial x_i/\partial \tau$ with $p_1, \ldots, p_6$ held constant are identical with $dx_i/d\tau$ in the equations for unperturbed motion. Thus

$$\partial x_i/\partial \tau = g_i(x_j; \tau) \qquad i = 1, \ldots, 6$$

and the equations of perturbed motion become

$$\frac{\partial x_1}{\partial p_1}\frac{dp_1}{d\tau} + \ldots + \frac{\partial x_1}{\partial p_6}\frac{dp_6}{d\tau} = 0$$

$$\frac{\partial x_2}{\partial p_1}\frac{dp_1}{d\tau} + \ldots + \frac{\partial x_2}{\partial p_6}\frac{dp_6}{d\tau} = f_2(x_j; \tau)$$

$$\cdots \cdots \cdots \cdots \cdots$$

$$\frac{\partial x_6}{\partial p_1}\frac{dp_1}{d\tau} + \ldots + \frac{\partial x_6}{\partial p_6}\frac{dp_6}{d\tau} = f_6(x_j; \tau)$$

In matrix form these equations become

$$J(dp/d\tau) = f$$

or

$$\frac{dp}{d\tau} = J^{-1}f = Af$$

where

$$p = [p_1, \ldots, p_6]^T$$
$$f = [0, f_2, 0, f_4, 0, f_6]^T$$

$$J = \begin{bmatrix} \frac{\partial x_1}{\partial p_1} & \frac{\partial x_1}{\partial p_2} & \cdots & \frac{\partial x_1}{\partial p_6} \\ \frac{\partial x_2}{\partial p_1} & \frac{\partial x_2}{\partial p_2} & \cdots & \frac{\partial x_2}{\partial p_6} \\ \cdot & & & \\ & \cdot & & \\ & & & \cdot \\ \frac{\partial x_6}{\partial p_1} & \frac{\partial x_6}{\partial p_2} & \cdots & \frac{\partial x_6}{\partial p_6} \end{bmatrix}$$

The matrix J is the Jacobian matrix of the transformation and has an inverse (9). The vector-matrix equation in expanded form becomes

$$\frac{dp_1}{d\tau} = \frac{J_{21}f_2 + J_{41}f_4 + J_{61}f_6}{|J|}$$

$$\cdots \cdots \cdots \cdots$$

$$\frac{dp_6}{d\tau} = \frac{J_{26}f_2 + J_{46}f_4 + J_{66}f_6}{|J|}$$

where J_{rs} is the cofactor of the element in the rth row and sth column of $|J|$. If the functions $f_i(x_j; \tau)$ are numerically small relative to the functions $g_i(x_j; \tau)$, the right-hand members of the differential equations in the variables $p_1, \ldots, p_6$ are numerically small relative to the right-hand members of the equations in $x_1, \ldots, x_6$, and the parameters $p_1, \ldots, p_6$ will vary more slowly than the coordinates $x_1, \ldots, x_6$. The domain of validity of the solution in $p_1, \ldots, p_6$ is greatly enlarged over that for $x_1, \ldots, x_6$ (9). In fact, if the interval of time over which the equations of perturbed motion are applied is sufficiently short, then the $p_1, \ldots, p_6$ may be assumed constant on the right-hand side of the equation for $dp/d\tau$. The solution is then determined approximately by quadratures, and in vector-matrix form

$$p(\tau_1) = p(0) + \int_0^{\tau_1} Af\, d\tau$$

where

$$p(0) = [p_1(0), \ldots, p_6(0)]^T$$

[4] Also referred to as the variation of elements and variation of arbitrary constants method.

[5] The proper choice of k' in this transformation results in a more convenient unit of time.

Lagrange's Brackets

In a practical case where the orbital parameters $p_1, \ldots, p_6$ are specified and the equations are to be obtained in literal form, it may be simpler to solve for the time derivatives of the parameters by making use of Lagrange's brackets. The virtue of this method lies in the fact that many of the elements of the matrix to be inverted vanish, and possibly the resulting matrix can be reduced to a lower dimension than matrix J before inversion. Let both sides of the vector-matrix differential equation

$$J(dp/d\tau) = f$$

be premultiplied by the matrix J^TE giving

$$J^TE\,J(dp/d\tau) = J^TE\,f$$

where J^T is the transpose of J, and E is the product of three E-matrices that interchange the first and second, third and fourth, and fifth and sixth columns of J^T and multiply the odd columns of the resulting matrix by -1 (10). The matrix E is given by

$$E = \begin{bmatrix} 0 & 1 & 0 & 0 & 0 & 0 \\ -1 & 0 & 0 & 0 & 0 & 0 \\ 0 & 0 & 0 & 1 & 0 & 0 \\ 0 & 0 & -1 & 0 & 0 & 0 \\ 0 & 0 & 0 & 0 & 0 & 1 \\ 0 & 0 & 0 & 0 & -1 & 0 \end{bmatrix}$$

The resulting equation in expanded form may be written as

$$\begin{bmatrix} [p_1, p_1] & [p_1, p_2] & \cdots & [p_1, p_6] \\ [p_2, p_1] & [p_2, p_2] & \cdots & [p_2, p_6] \\ \cdot & \cdot & & \cdot \\ \cdot & \cdot & & \cdot \\ \cdot & \cdot & & \cdot \\ [p_6, p_1] & [p_6, p_2] & \cdots & [p_6, p_6] \end{bmatrix} \begin{bmatrix} \frac{dp_1}{d\tau} \\ \frac{dp_2}{d\tau} \\ \cdot \\ \cdot \\ \cdot \\ \frac{dp_6}{d\tau} \end{bmatrix} = \begin{bmatrix} f_2\frac{\partial x_1}{\partial p_1} + f_4\frac{\partial x_3}{\partial p_1} + f_6\frac{\partial x_5}{\partial p_1} \\ f_2\frac{\partial x_1}{\partial p_2} + f_4\frac{\partial x_3}{\partial p_2} + f_6\frac{\partial x_5}{\partial p_2} \\ \cdot \\ \cdot \\ \cdot \\ f_2\frac{\partial x_1}{\partial p_6} + f_4\frac{\partial x_3}{\partial p_6} + f_6\frac{\partial x_5}{\partial p_6} \end{bmatrix}$$

The elements of the matrix $J^TE\,J$ are known as Lagrange's brackets, and they possess the following properties (11):

$$\left.\begin{aligned} [p_i, p_i] &= 0 \\ [p_i, p_j] &= -[p_j, p_i] \\ \frac{\partial [p_i, p_j]}{\partial t} &= 0 \end{aligned}\right\} \qquad i, j = 1, \ldots, 6$$

where

$$[p_i, p_j] = \frac{\partial x_1}{\partial p_i}\frac{\partial x_2}{\partial p_j} - \frac{\partial x_2}{\partial p_i}\frac{\partial x_1}{\partial p_j} + \frac{\partial x_3}{\partial p_i}\frac{\partial x_4}{\partial p_j} - \frac{\partial x_4}{\partial p_i}\frac{\partial x_3}{\partial p_j} + \frac{\partial x_5}{\partial p_i}\frac{\partial x_6}{\partial p_j} - \frac{\partial x_6}{\partial p_i}\frac{\partial x_5}{\partial p_j} \qquad i, j = 1, \ldots, 6$$

The properties of Lagrange's brackets simplify the matrix $J^TE\,J$ in the following ways:

1 From the first property, the elements on the main diagonal of $J^TE\,J$ vanish.

2 From the first two properties, the matrix $J^TE\,J$ is skew symmetric.

3 From the third property, the brackets do not contain time explicitly, and thus they may be evaluated for any epoch. The choice $t = t_0$ greatly simplified the expressions for the brackets.

The next step in the derivation involves obtaining the required partial derivatives and from them evaluating the nonzero Lagrange's brackets.

Derivatives of the Disturbing Function

For the case of celestial bodies where the components of the perturbing force a_x, a_y, and a_z are the derivatives of a disturbing function R, i.e.,

$$a_x = \frac{\partial R}{\partial x} \qquad a_y = \frac{\partial R}{\partial y} \qquad a_z = \frac{\partial R}{\partial z}$$

The vector $J^TE\,f$ is given by

$$J^TE\,f = \begin{bmatrix} \frac{\partial R}{\partial p_1} \\ \frac{\partial R}{\partial p_2} \\ \cdot \\ \cdot \\ \cdot \\ \frac{\partial R}{\partial p_6} \end{bmatrix}$$

The vector on the right follows from the definitions of f_2, f_4, f_6, x_1, x_3, and x_5 since

$$\frac{\partial R}{\partial x}\frac{\partial x}{\partial p_1} + \frac{\partial R}{\partial y}\frac{\partial y}{\partial p_1} + \frac{\partial R}{\partial z}\frac{\partial z}{\partial p_1} = \frac{\partial R}{\partial p_1}$$

and

$$\begin{aligned} x(\tau) &= x_1(p_1, \ldots, p_6; \tau) \\ y(\tau) &= x_3(p_1, \ldots, p_6; \tau) \\ z(\tau) &= x_5(p_1, \ldots, p_6; \tau) \end{aligned}$$

Inverting the matrix $J^TE\,J$ gives

$$\frac{dp}{d\tau} = (J^TE\,J)^{-1}J^TE\,f = Af$$

Because the first, third, and fifth components of vector f are zero, the matrix A may be rewritten as a 6×3 matrix, and vector f may be written as a 3×1 vector. These revised forms of A and f will be assumed in all that follows.

Multistage Orbit Correction Process

State Transformation Equation

A multistage orbit correction process is defined as consisting of a series of consecutive thrust vectors applied to vehicle so as to transfer it from one orbit or trajectory to another. The process may be more precisely defined by specifying the direction and magnitude of the thrust vector for each separate stage of the process. Alternatively, the change in the acceleration vector of the vehicle produced by each thrust vector or the incremental velocity vector acquired by the vehicle during each stage of the process may be specified. It is assumed that the initial and final orbits have been predetermined by some measuring process.

In the discussion that follows, the variation of parameter equations derived above are used to define the perturbed motion of the vehicle. The method of dynamic programming

is used to select an optimum set of incremental velocity vectors defining the orbit transfer process. The choice of these incremental velocity vectors is based upon minimizing the sum of the squares of the weighted orbital parameter errors at the termination of the multistage process and is constrained by the total amount of propulsive energy available for the process. The equations derived are in such a form that certain of the final orbital parameter errors may be weighted more heavily than others if desired.

The variation of parameter equations for the perturbed motion in vector matrix form are given by

$$dp/d\tau = A f$$

where

p = $[p_1, \ldots, p_6]^T$
A = 6×3 matrix whose elements are functions of $p_1, \ldots, p_6$ and τ implicitly through the true, eccentric, or mean anomaly
f = $[f_1, f_2, f_3]^T$

It was pointed out previously that if the interval of integration is sufficiently short and the components of vector f small enough, then the elements of matrix A may be assumed constant without making important errors. Although vector f may not be small relative to vector g, the duration of integration will be kept small enough relative to the orbital period so that the changes required in $p_1, \ldots, p_6$ will be small.

The acceleration vector f is due to the application of thrust by a rocket motor. If matrix A is assumed constant over the interval $0 \leq \tau \leq \tau_1$ then

$$\int_0^{\tau_1} A f \, d\tau = A \int_0^{\tau_1} f(\tau) \, d\tau = A \, \Delta V(\tau_1)$$

where

$$\begin{aligned} \int_0^{\tau_1} f(\tau) \, d\tau &= \left[\int_0^{\tau_1} f_1(\tau) \, d\tau, \int_0^{\tau_1} f_2(\tau) \, d\tau, \int_0^{\tau_1} f_3(\tau) \, d\tau \right]^T \\ &= [\Delta V_1(\tau_1), \Delta V_2(\tau_1), \Delta V_3(\tau_1)]^T \\ &= \Delta V(\tau_1) \end{aligned}$$

The vector ΔV is the incremental velocity vector acquired during the period of thrust from 0 to τ_1. The vector-matrix differential equation may then be integrated to

$$p(\tau_1) = p(0) + \mathrm{A} \, \Delta V(\tau_1)$$

This equation represents the change in the state of the system as represented by the orbital parameters from an initial state $p(0)$ to some state $p(\tau_1)$, due to acquiring the vector velocity increment $\Delta V(\tau_1)$. The behavior of the acceleration vector f in producing ΔV is unimportant at this point, due to constant thrust, constant acceleration, etc.

A somewhat simplified expression for the state transformation is given by

$$p_{k+1} = p_k + A_k \, \Delta V_k$$

where

p_k = $p(\tau_k)$
p_{k+1} = $p(\tau_{k+1})$
A_k = matrix A with its elements evaluated at $\tau = \tau_{k+1}$
ΔV_k = incremental velocity vector acquired during the time interval from τ_k to τ_{k+1}

To be consistent with the discussion of the variation of parameter equations, the following assumptions are associated with the state transformation equation:

1 The time interval $\tau_{k+1} - \tau_k$ is small relative to the orbital period for all values of $k = 0, 1, \ldots, N$.

2 The elements of the matrix A_k are taken as constants during the time interval $\tau_{k+1} - \tau_k$ and are evaluated at $\tau = \tau_{k+1}$.

System Performance Index

There are two requirements placed on the performance of the system: 1) the sum of the weighted squares of the errors remaining in the orbital parameters at the termination of the orbit correction process is to be a minimum; 2) the total propulsive energy available to accomplish the orbit correction process is limited. The performance index is designed to exhibit system behavior consistent with these two requirements.

Let p_N be the vector representing the desired set of orbital parameters at the termination of the orbit correction process. Then define

$$\delta_k = p_N - p_k$$

as the error remaining in the orbital parameter vector at $\tau = \tau_k$. Using the state transformation equation yields

$$\delta_k = p_N - p_{k-1} - A_{k-1} \Delta V_{k-1}$$

or

$$\delta_N = p_N - p_{N-1} - A_{N-1} \Delta V_{N-1}$$

Here, δ_N represents the errors remaining in the orbital parameters at the termination of the orbit correction process. The sum of the weighted squares of the errors may be expressed as

$$\delta_N{}^T Q_N \delta_N = q_{11}(\delta p_1)^2 + q_{22}(\delta p_2)^2 + \ldots + q_{66}(\delta p_6)^2$$

where

δ_N = $[\delta p_1, \delta p_2, \ldots, \delta p_6]^T$
$\delta p_1, \ldots, \delta p_6$ = errors remaining in orbital elements at the termination of the orbit correction process
Q_N = 6×6 diagonal matrix with diagonal elements $q_{11}, \ldots, q_{66}$
$q_{11}, \ldots, q_{66}$ = weighting factors for orbital parameter errors

The kinetic energy added to or subtracted from the vehicle during the orbit correction process depends on the sum of the squares of the magnitudes of the incremental velocity vectors for all stages of the process.

$$\Delta V_k{}^T \Delta V_k = (\Delta V_k)_1{}^2 + (\Delta V_k)_2{}^2 + (\Delta V_k)_3{}^2$$

where $(\Delta V_k)_1$, $(\Delta V_k)_2$, $(\Delta V_k)_3$ are the components of ΔV_k.

The two requirements on system behavior combine to give the following performance index for an N-stage process beginning at state $\Delta p(0)$:

$$J_N[\Delta p(0); \Delta V_0, \ldots, \Delta V_{N-1}] = \delta_N{}^T Q_N \delta_N + \lambda \sum_{k=0}^{N-1} \Delta V_k{}^T \Delta V_k$$

where λ is a constant determined by available propulsive energy. This performance index is to be minimized by the proper choice of the N incremental velocity vectors $\Delta V_0, \ldots, \Delta V_{N-1}$.

Minimization of Performance Index by Dynamic Programming Method

Minimization of J_N requires the proper choice of N vectors, i.e., it is an N-dimensional problem that would be rather lengthy to solve by conventional methods. The use of dynamic programming reduces the minimization problem to N one-dimensional problems that are much simpler to handle (12, 13).

In what follows dynamic programming will be applied to J_N to derive the necessary recurrence relations to permit the computation J_N, δ_N, and ΔV_k, $k = 0, 1, \ldots, N-1$.

Consider first a one-stage process beginning at τ_{N-1} and terminating at τ_N. The performance index becomes

$$J_1 = \delta_N{}^T Q_N \delta_N + \lambda \Delta V_{N-1}{}^T \Delta V_{N-1}$$

where

$$\begin{aligned} \delta_N &= \Delta p_{N-1} - A_{N-1} \Delta V_{N-1} \\ \Delta p_{N-1} &= p_N - p_{N-1} \end{aligned}$$

Substituting for δ_N in J_1 gives

$$\begin{aligned} J_1 &= [\Delta p_{N-1} - A_{N-1} \Delta V_{N-1}]^T \, Q_N [\Delta p_{N-1} - A_{N-1} \, \Delta V_{N-1}] \\ &\qquad + \lambda \Delta V_{N-1}{}^T \Delta V_{N-1} \\ &= \Delta p_{N-1}{}^T Q_N \Delta p_{N-1} - 2 \Delta V_{N-1}{}^T A_{N-1}{}^T Q_N \Delta p_{N-1} + \\ &\qquad \Delta V_{N-1}{}^T (A_{N-1}{}^T Q_N A_{N-1} + \lambda \, I_3) \, \Delta V_{N-1} \end{aligned}$$

where

$$I_3 = \begin{bmatrix} 1 & 0 & 0 \\ 0 & 1 & 0 \\ 0 & 0 & 1 \end{bmatrix}$$

Differentiating J_1 with respect to ΔV_{N-1}, setting the result equal to zero, and solving for ΔV_{N-1} gives

$$\begin{aligned} \Delta V_{N-1} &= (A_{N-1}{}^T Q_N A_{N-1} + \lambda I_3)^{-1} \, A_{N-1}{}^T Q_N \, \Delta p_{N-1} \\ &= M_{N-1} \, A_{N-1}{}^T \, Q_N \, \Delta p_{N-1} \end{aligned}$$

where

$$M_{N-1} = (A_{N-1}{}^T Q_N \, A_{N-1} + \lambda I_3)^{-1}$$

The above equation gives the vector ΔV_{N-1} that minimizes the one-stage performance index J_1 for the system initially in an arbitrary state p_{N-1}. Substituting this equation in J_1 gives the minimum value of J_1

$$\begin{aligned} \text{Min } J_1[p_{N-1};\, \Delta V_{N-1}] &= \Delta p_{N-1}{}^T \, Q_N \Delta p_{N-1} - 2 \, \Delta p_{N-1}{}^T Q_N{}^T A_{N-1} M_{N-1}{}^T \, A_{N-1}{}^T Q_N \Delta p_{N-1} \\ &\qquad + \Delta p_{N-1}{}^T \, Q_N{}^T A_{N-1} M_{N-1}{}^T M_{N-1}{}^{-1} M_{N-1} A_{N-1}{}^T Q_N \Delta p_{N-1} \\ &= \Delta p_{N-1}{}^T \, [Q_N - Q_N{}^T A_{N-1} M_{N-1}{}^T A_{N-1}{}^T \, Q_N] \, \Delta p_{N-1} \\ &= \Delta p_{N-1}{}^T \, Q_{N-1} \, \Delta p_{N-1} \end{aligned}$$

where

$$Q_{N-1} = Q_N - Q_N{}^T A_{N-1} M_{N-1}{}^T A_{N-1}{}^T Q_N$$

Also

$$\begin{aligned} \delta_N &= \Delta p_{N-1} - A_{N-1} M_{N-1} A_{N-1}{}^T Q_N \Delta p_{N-1} \\ &= (I_6 - A_{N-1} \, M_{N-1} \, A_{N-1}{}^T \, Q_N) \, \Delta p_{N-1} \end{aligned}$$

Next consider a two-stage process beginning with the system in state p_{N-2} and terminating in state p_N. The one-stage process considered above becomes the second stage of the two-stage process, and the expression for J_2 is

$$\begin{aligned} J_2[p_{N-2};\, \Delta V_{N-1},\, \Delta V_{N-2}] &= \delta_N{}^T Q_N \delta_N + \lambda (\Delta V_{N-1}{}^T \times \\ &\qquad \Delta V_{N-1} + \Delta V_{N-2}{}^T \Delta V_{N-2}) \\ &= J_1[p_{N-1};\, \Delta V_{N-1}] + \\ &\qquad \lambda \, \Delta V_{N-2}{}^T \Delta V_{N-2} \end{aligned}$$

At this point the principle of optimality is applied (13), which means the following: An optimal sequence of incremental velocity vectors $\Delta V_0, \Delta V_1, \ldots, \Delta V_{N-1}$ has the property that whatever the initial p_0 may be, and whatever choice is made for ΔV_0, the remaining sequence $\Delta V_1, \ldots, \Delta V_{N-1}$ must constitute an optimal sequence with regard to the state p_1 resulting from the choice of ΔV_0. This principle is applied by replacing $J_1[p_{N-1};\, \Delta V_{N-1}]$ by its minimized form $\Delta p_{N-1}{}^T \, Q_{N-1} \Delta p_{N-1}$ in the expression for J_2 and minimizing J_2 with respect to ΔV_{N-2}

$$\begin{aligned} &\underset{\Delta V_{N-1},\, \Delta V_{N-2}}{\text{Min}} \; J_2[p_{N-2};\, \Delta V_{N-1},\, \Delta V_{N-2}] = \\ &\qquad \underset{\Delta V_{N-2}}{\text{Min}} \; (\Delta p_{N-1}{}^T Q_{N-1} \Delta p_{N-1} + \lambda \, \Delta V_{N-2}{}^T \Delta V_{N-2}) \end{aligned}$$

where from the state transformation equation

$$\begin{aligned} \Delta p_{N-1} &= p_N - p_{N-1} \\ &= p_N - p_{N-2} - A_{N-2} \Delta V_{N-2} \\ &= \Delta p_{N-2} - A_{N-2} \Delta V_{N-2} \end{aligned}$$

The expression to be minimized with respect to ΔV_{N-2} becomes

$$\begin{aligned} &\Delta p_{N-2}{}^T Q_{N-1} \Delta p_{N-2} - 2 \Delta V_{N-2}{}^T A_{N-2}{}^T Q_{N-1} \Delta p_{N-2} + \\ &\qquad \Delta V_{N-2}{}^T (A_{N-2}{}^T Q_{N-1} A_{N-2} + \lambda I_3) \, \Delta V_{N-2} \end{aligned}$$

Proceeding as for J_1 we obtain for the optimal ΔV_{N-2}

$$\begin{aligned} \Delta V_{N-2} &= (A_{N-2}{}^T Q_{N-1} A_{N-2} + \lambda I_3)^{-1} \, A_{N-2}{}^T Q_{N-1} \Delta p_{N-2} \\ &= M_{N-2} A_{N-2}{}^T Q_{N-1} \Delta p_{N-2} \end{aligned}$$

where

$$M_{N-2} = (A_{N-2}{}^T \, Q_{N-1} \, A_{N-2} + \lambda I_3)^{-1}$$

The minimum value of J_2 becomes

$$\underset{\Delta V_{N-1},\, \Delta V_{N-2}}{\text{Min}} \; J_2[p_{N-2};\, \Delta V_{N-1},\, \Delta V_{N-2}] = \Delta p_{N-2}{}^T Q_{N-2} \Delta p_{N-2}$$

where

$$Q_{N-2} = Q_{N-1} - Q_{N-1}{}^T \, A_{N-2} \, M_{N-2}{}^T A_{N-2}{}^T \, Q_{N-1}$$

The expression for δ_N for the two-stage process is somewhat more complicated than for the one-stage process

$$\begin{aligned} \delta_N &= \Delta p_{N-1} - A_{N-1} \, \Delta V_{N-1} \\ &= [I_6 - A_{N-1} \, M_{N-1} \, A_{N-1}{}^T Q_N] \, \Delta p_{N-1} \\ &= [I_6 - A_{N-1} \, M_{N-1} \, A_{N-1}{}^T \, Q_N] \, [\Delta p_{N-2} - A_{N-2} \Delta V_{N-2}] \\ &= [I_6 - A_{N-1} M_{N-1} A_{N-1}{}^T Q_N] \\ &\qquad [I_6 - A_{N-2} M_{N-2} A_{N-2}{}^T Q_{N-1}] \Delta p_{N-2} \end{aligned}$$

The above process may be carried on for N-stages. However, by carrying on for several more stages it is evident that recurrence relations exist for each of the desired quantities. These recurrence relations are

$$\left.\begin{aligned} \Delta V_{N-r} &= M_{N-r} A_{N-r}{}^T Q_{N-r+1} \Delta p_{N-r} \\ M_{N-r} &= (A_{N-r}{}^T Q_{N-r+1} A_{N-r} + \lambda I_3)^{-1} \\ \text{Min } J_r &= \Delta p_{N-r}{}^T Q_{N-r} \Delta p_{N-r} \\ Q_{N-r} &= Q_{N-r+1} - \\ &\qquad Q_{N-r+1}{}^T A_{N-r} M_{N-r}{}^T A_{N-r}{}^T Q_{N-r+1} \\ \delta_N &= \left[\prod_{r=1}^{N} (I_6 - \right. \\ &\qquad \left. A_{N-r} M_{N-r} A^T{}_{N-r} Q_{N-r+1}) \right] \Delta p_0 \end{aligned}\right\} \quad r = 1, \ldots, N$$

The evaluation of the matrix A_{N-r} for each time τ_{N-r+1} presents a problem. For a system described by a linear, constant coefficient differential equation the matrix A_{N-r} is constant. In the problem considered here the matrix A is a function of the components of the state vector p, i.e., the two-body orbital parameters, as well as time. However, as pointed out in (9), if the time interval over which the differential equations are integrated is sufficiently short, the components of vector p entering into the elements of A may be considered as constants for the entire process. This assumption is justified by the fact that the total orbital change as defined by $p_N - p_0$ will have to be small because of restrictions on available fuel.

An alternative procedure involves the following steps:

1 Assume A constant for the entire process and compute the optimal sequence of ΔV_k, $k = 1, \ldots, N-1$.

2 Using the optimal ΔV_k, compute p_k and then A_k.

3 Repeat process using A_k in place of constant A matrix, and determine a new optimal sequence of ΔV_k.

3 Iterate the above procedure until the change in ΔV_k is sufficiently small.

The evaluation of the parameter λ is carried out by choosing several values of λ and computing the corresponding sequences of optimal ΔV_k. The resulting ΔV_k are tested in

$$\sum_{k=0}^{N-1} \Delta V_k{}^T \Delta V_k \leq C$$

For the maximum $p_N - p_0$ expected, the value of λ can be selected to satisfy the above inequality. The constant C on the right side of the inequality is proportional to the total kinetic energy change possible with the available fuel.

Some Special Cases

Single Stage Orbit Correction Process

It is possible to transfer from the initial orbit to one close to the desired orbit by one application of thrust. How close the final orbit and the desired orbit are will depend on the weights assigned to the orbital parameter errors between the initial and desired orbits and the position in the initial orbit at which the correction process is carried out. The possible advantage of a single stage orbit transfer process is that it may result in a final orbit satisfying practical requirements with less expenditure of fuel and with a less complex guidance system mechanization.

The equations derived in the section on the variation of parameters are given by the vector-matrix equation

$$dp/d\tau = Af$$

which integrates to

$$p(\tau_1) = p(0) + \int_0^{\tau_1} Af\, d\tau$$

$$= p(0) + A\ \Delta V(\tau_1)$$

If we define $\Delta p(0)$ as the change required in the orbital parameter vector to transfer from the initial orbit to the desired orbit, then the residual errors in the orbital parameters at the end of the single stage orbit transfer process is given by

$$\delta = \Delta p(0) - A\ \Delta V(\tau_1)$$

where δ is the 6×1 residual orbital parameter error vector. It will be possible to choose $\Delta V(\tau_1)$ to make δ vanish only for certain conditions. Since these conditions will normally not be satisfied in practical cases, it is necessary to choose the components of $\Delta V(\tau_1)$ so that δ will be minimized in accordance with some performance index. The one chosen for discussion here is to minimize the sum of the weighted squares of the components of δ, i.e., to minimize

$$J_1 = \delta^T Q\, \delta$$

where Q is a 6×6 diagonal matrix whose nonzero elements weight the squares of the individual orbital parameter errors. From the multistage process derivation the minimizing velocity vector is given by

$$\Delta V(0) = (A^T Q\, A)^{-1} A^T Q\ \Delta p(0)$$

since $\lambda = 0$ for the performance index considered.

The residual error vector δ is also given by

$$\delta = [I_6 - A(A^T Q A)^{-1} A^T Q]\ \Delta p(0)$$
$$= N\ \Delta p(0)$$

For δ to vanish the matrix N must be singular. It may be shown that this will be true only when

$\Delta r + \alpha\, \Delta \dot{r} = 0$, Δr = error in position vector

$$\alpha \approx \frac{1 - \cos n\tau}{n \sin n\tau}$$

n = mean daily motion

τ = duration of thrust for single stage process

The expression for α assumes that the magnitude of the thrust vector is so controlled that a constant acceleration due to the correcting thrust vector is maintained and the distance from the center of force is constant during the orbit correction process.

Two-Stage Orbit Correction Process

It is shown in (1) that two successive applications of thrust are required in general to remove completely the errors in the orbital parameters. There the system is analyzed in terms of rectangular components of position and velocity, and no constraint is placed on the amount of energy available to make the complete orbit correction. This situation may be treated as a special case of the multistage process if a two-stage process with $\delta_N{}^T \delta_N$ and λ equal to zero is assumed.

Thus

$$\delta_N = p_N - p_{N-1} - A_{N-1}\Delta V_{N-1} = 0$$
$$p_{N-1} = p_{N-2} + A_{N-2}\Delta V_{N-2}$$

or

$$p_N - p_{N-2} - A_{N-1}\Delta V_{N-1} - A_{N-2}\Delta V_{N-2} = 0$$

This equation may be written as

$$A_{N-1}\Delta V_{N-1} + A_{N-2}\Delta V_{N-2} = \Delta p_{N-2}$$

This vector matrix equation represents six linear equations in the six unknown components of ΔV_{N-1} and ΔV_{N-2}. Let ΔV_{N-1} and ΔV_{N-2} make up a 6×1 vector

$$[\Delta V_{N-1} : \Delta V_{N-2}]^T = [(\Delta V_{N-1})_1, (\Delta V_{N-1})_2, (\Delta V_{N-1})_3, (\Delta V_{N-2})_1, (\Delta V_{N-2})_2, (\Delta V_{N-2})_3]^T$$

and the elements of A_{N-1} be designated by α_{jk}, and the elements of A_{N-2} by β_{jk}. This yields

$$\begin{bmatrix} \alpha_{11} & \alpha_{12} & \alpha_{13} & \beta_{11} & \beta_{12} & \beta_{13} \\ \alpha_{21} & \alpha_{22} & \alpha_{23} & \beta_{21} & \beta_{22} & \beta_{23} \\ \cdot & & & & & \\ & \cdot & & & & \\ & & \cdot & & & \\ \alpha_{61} & \alpha_{62} & \cdots & & & \beta_{63} \end{bmatrix} \begin{bmatrix} (\Delta V_{N-1})_1 \\ (\Delta V_{N-1})_2 \\ (\Delta V_{N-1})_3 \\ (\Delta V_{N-2})_1 \\ (\Delta V_{N-2})_2 \\ (\Delta V_{N-2})_3 \end{bmatrix} = \begin{bmatrix} (\Delta p_{N-2})_1 \\ (\Delta p_{N-2})_2 \\ (\Delta p_{N-2})_3 \\ \cdot \\ \cdot \\ (\Delta p_{N-2})_6 \end{bmatrix}$$

If the time between application of the two thrust vectors is short, then the first and fourth, second and fifth, and third and sixth columns of the α β matrix will be almost equal. This means that the determinant of the α β matrix will be quite small, resulting in very large components of velocity for a given parameter error vector.

Special Performance Index

Consider the case of a communication satellite in 24-hr. circular equatorial orbit. Due to perturbing accelerations, such a satellite will wander from its desired reference point and eventually move out of the ground antenna cone of view (assuming a nonsteerable antenna). The problem is to apply thrust periodically to the satellite so as to keep it within the antenna's cone of view.

From the standard equation for a cone of revolution, the following equation can be derived

$$\tan^2 \phi = \frac{(\Delta A \cos h)^2 + (\Delta h)^2}{(1+\Delta\rho/\rho)^2}$$
$$\approx (\Delta A \cos h)^2 + (\Delta h)^2$$

where

ϕ = cone's generating angle
ΔA = angular azimuth error of the satellite position at the ground antenna
Δh = angular elevation error of the satellite position at the ground antenna

If $\Delta A \cos h$ and Δh are expressed in terms of the errors in the six parameters defining the satellite's orbit, $\tan^2 \phi$ becomes a quadratic form in the orbital parameter errors $\Delta p_i, i = 1, \ldots, 6$

$$\tan^2 \phi = \Delta p^T Q \, \Delta p$$

where

$\Delta p = [\Delta p_1, \ldots, \Delta p_6]^T$
Q = 6×6 matrix whose elements are functions of local sidereal time and the position of the satellite in its orbit

At any instant of time the satellite may be assumed to lie on the surface of a right circular cone whose vertex is at the ground antenna and whose axis is the line of sight from the antenna to the preferred satellite position in a perfect 24-hr circular equatorial orbit. If ϕ_r is the generating angle of the antenna cone of view, it is desirable to maintain the following inequality:

$$\tan^2 \phi_r \geq \Delta p^T \, Q \, \Delta p$$

At any instant then, the angle ϕ defined by

$$\phi = \tan^{-1} [\Delta p^T Q \, \Delta p]^{1/2}$$

is a measure of system performance. Since minimizing ϕ is the same as minimizing $\tan^2 \phi$, the performance index for the system is

$$J = \tan^2 \phi = \delta^T Q \delta$$

where δ is a 6×1 vector whose components are the errors in the orbital parameters remaining at the termination of the orbital transfer process.

The performance index $\tan^2 \phi$ may be minimized by dynamic programming techniques, as indicated in the section on multistage orbit correction process, and an energy constant may be included if desired. The matrix Q_N becomes the matrix Q in the above equation and now has time dependent nonzero off diagonal elements. However, since the orbit correction process is normally of short duration relative to the orbital period, the elements of Q may be evaluated for the time of the termination of the process and assumed constant during the process.

Further Considerations

The general multistage orbit transfer process represents an N-dimensional minimization problem. A solution by classical minimization techniques requires solving N simultaneous equations. The use of dynamic programming can reduce the N-dimensional problem to N one-dimensional problems. Further, when the state transformation equation is linear and the system performance index is quadratic, an analytic solution that includes certain types of constraints can be obtained. The method presented in this paper is very flexible since

1 Any constraint that can be related to a quadratic function of velocity may be incorporated.

2 Any desired set of two-body orbital parameters may be used to formulate the equations of motion.

3 By properly choosing the elements of matrix Q_N, the squares of the errors on the terminal orbital elements may be given any desired weight.

4 In the multistage process the spacing of the corrective thrust vectors may be chosen to suit the particular problem at hand, i.e., rendezvous problem, point to point trajectory, satellite orbit.

The recurrence relations were derived assuming a three-dimensional control vector ΔV. Using this formulation, as was pointed out in the discussion of the single stage correction process, it is impossible to drive the terminal errors to zero, even with no constraints, except under special conditions. However, when one or two of the orbital parameter errors are of special significance, they may be weighted very heavily and can be driven to very small values at the termination of the process. An alternative formulation is to use the two-stage process discussed previously as one stage of the multistage process. The α β matrix in the two-stage formulation becomes the A_{N-r} matrix in the recurrence relations, and the ΔV_{N-r} vector is now a six-dimensional vector as defined for the two-stage process. Of course, for $\lambda = 0$ (no constraint) the multistage process degenerates to the two-stage process with zero terminal errors, i.e., $\delta_N = 0$.

A word of caution is in order concerning the use of the method for numerical computations. The variation of parameter equations are based on strong assumptions of linearity. Care must be taken in designing the process so that the resulting changes in orbital parameters during any one stage does not exceed the acceptable linear region of the state transformation equations.

Acknowledgment

This investigation was supported by NASA Contract-NASr-21(02).

References

1 Smith, F. T., "A Discussion of a Midcourse Guidance Technique for Space Vehicles," The RAND Corp., *Research Memo. RM-2581*, Oct. 3, 1960.

2 Breakwell, J. V., "Fuel Requirements for Crude Interplanetary Guidance," *Advances in Astronautical Sciences*, Vol. 5, Plenum Press, New York, 1960.

3 Breakwell, J. V., "The Spacing of Corrective Thrusts in Interplanetary Navigation," presented at the Western National Meeting of the Am. Astronaut. Soc., Seattle, Wash., August 1960 (*preprint no. 60-76*).

4 Lawden, D. F., "Optimal Programme for Correctional Manoeuvres," *Astronautica Acta*, vol. 6, Fasc. 4, 1960, pp. 195–205.

5 Rosenbloom, A., "Final-Value Systems With Total Effort Constraints," First Int. Cong. Int. Fed. Auto. Control, Moscow, USSR, June 1960.

6 Dubyago, A. D., *The Determination of Orbits*, The Macmillan Co., New York, 1961. Chap. 9.

7 Herrick, S., *Astrodynamics*, Van Nostrand, New York, Chap. 17 (to be published).

8 *Planetary Coordinates for the Years 1960–1980*, Her Majesty's Stationary Office, London, 1958, pp. 142–160.

9 Moulton, F. R., *Differential Equations*, Dover Publications Inc., New York, 1958, Chap. 4.

10 Mirsky, L., *An Introduction to Linear Algebra*, Oxford, 1955, Chap. 6.

11 Moulton, F. R., *An Introduction to Celestial Mechanics*, The Macmillan Co., New York, 1914.

12 Bellman, R., *Adaptive Control Processes; A Guided Tour*, Princeton University Press, Princeton, N. J., 1961, p. 57.

13 Smith, F. T., "A Discussion of Several Concepts Used in the Optimization of Control Systems by Dynamic Programming," The RAND Corp., *Paper P-1665*, May 13, 1959.

Method of Calculating Liquid Flow Fluctuations in Rocket Motor Supply Pipes

W. A. WOODS[1]

Mechanical Engineering Dept.
University of Liverpool
Liverpool, England

The connection between oscillatory propellant flow and high frequency combustion instability in rocket motors is outlined, and the object of the present work is discussed. Previous work on the method of characteristics and water hammer is briefly considered. The theory is introduced, first using basic equations and then characteristic equations. Boundary conditions are dealt with in some detail; closed ends, inflow, outflow, cavitation, and a new concept of source and sink type of boundaries are discussed, and boundary charts are given. Calculations for closed pipe and pipe flow systems, such as a rocket motor fuel supply, are included. It is shown that applied disturbances lead to large amplitude waves in a closed pipe but to limited amplitude waves in a pipe flow system.

ONE OF the major problems associated with the development of liquid propellent rocket motors is a high frequency instability phenomenon, often referred to as *screaming*. In an attempt to investigate this condition and factors controlling its initiation, the combustion department at R. P. E. Westcott has embarked on an experimental program in which a controlled, high frequency, mass flow fluctuation is to be superimposed on the fuel supply to the rocket.[2]

The purpose of the present work is to provide a theoretical treatment suitable for describing the flow in fuel pipe lines under transient or oscillatory conditions. The method used, namely the method of characteristics, is developed in a way similar to that employed in one-dimensional gas dynamic studies. By this method two diagrams are constructed; the first, the position diagram, shows the propagation of the pressure waves in a time-distance field, and the second, the state diagram, gives the pressure and velocity of the fluid corresponding to any given point in the position diagram. Various systems are considered, and the methods used for the calculations are discussed in some detail.

Previous Work

The method of characteristics is well established in connection with gas dynamics, in particular for two-dimensional, steady, supersonic, compressible flow and one-dimensional, unsteady, compressible flow, as discussed by Courant and Friedrichs (1).[3] Jenny (2), in pioneer work, developed the method of characteristics to deal with unsteady gas flow in which friction, changes of area and heat transfer effects were present; variations on this and similar work have been discussed by Shapiro (3). Detailed applications of these theories using different techniques have been reported by de'Haller (4), Benson (5), Rudinger (6), and many others. The present work is concerned mainly with the application of the new methods mentioned above to an old problem, i.e., *water hammer*.

The first rational approach to water hammer was made by Joukovski, 1885, and later refined by Allievi, 1913. Since that time graphical methods have been developed independently by Schnyder, 1932 (7), Jaeger, 1933 (8), and Bergeron, 1937 (9), who were essentially concerned with plotting diagrams corresponding to the characteristic diagrams in this article. Many other writers have discussed the topic, and selected references concerned with similar problems are listed at the end of this paper.

In this new approach the problem of water hammer is tackled in a more general and rigorous fashion than formerly by using a modern, theoretical method. The boundary conditions are discussed in some detail, and the treatment is broadly similar to that used in unsteady, gas dynamic problems. The cavitation type of boundary described was used by Bergeron, but, as far as the author is aware, the combination of inflow and outflow boundaries with the source and sink concept is quite new.

Theory

Basic Equations

Considering one-dimensional frictionless adiabatic flow of a liquid in a constant area pipe, the following fundamental equations apply:

Continuity Equation

$$\frac{1}{\rho}\frac{\partial \rho}{\partial t} + \frac{\partial u}{\partial x} + \frac{u}{\rho}\frac{\partial \rho}{\partial x} = 0 \qquad [1]$$

Euler's Momentum Equation

$$\frac{\partial u}{\partial t} + u\frac{\partial u}{\partial x} + \frac{1}{\rho}\frac{\partial p}{\partial x} = 0 \qquad [2]$$

It will be assumed that the following equation applies:

$$a = \sqrt{\frac{K}{\rho}} \qquad [3]$$

Received March 28, 1961.

[1] Lecturer in Mechanical Engineering.

[2] The results of this work will probably be reported by R. P. E. Westcott at a later date.

[3] Numbers in parentheses indicate References at end of paper.

where

a = effective speed of sound of liquid when in an elastic pipe
K = effective adiabatic bulk modulus for the liquid when in an elastic pipe
p = static pressure
t = time
u = velocity of liquid
x = Cartesian coordinate of distance
ρ = density of the liquid in the pipe

The expression for K is given by Allievi's equation (12)

$$K = k\left[\frac{1}{1 + \left(\frac{d}{e}\right)\frac{k}{E}}\right] \qquad [4]$$

Here

k = adiabatic bulk modulus of the liquid
E = Young's modulus for the pipe material (adiabatic)
e = pipe wall thickness (assumed small compared with d)
d = pipe diameter

In addition, it will be assumed that the density is a function of the pressure alone and that the following substitutions can be made:

$$\frac{\partial \rho}{\partial x} = \frac{1}{a^2}\frac{\partial p}{\partial x}$$

$$\frac{\partial \rho}{\partial t} = \frac{1}{a^2}\frac{\partial p}{\partial t}$$

After substitution the previous equations become

$$\frac{\partial p}{\partial t} + K\frac{\partial u}{\partial x} + u\frac{\partial p}{\partial x} = 0 \qquad [5]$$

$$\frac{a^2}{K}\frac{\partial p}{\partial x} + \frac{\partial u}{\partial t} + u\frac{\partial u}{\partial x} = 0 \qquad [6]$$

If the field of flow is continuous, two further equations representing the total differentials can be derived as

$$\frac{\partial u}{\partial x}dx + \frac{\partial u}{\partial t}dt = du \qquad [7]$$

$$\frac{\partial p}{\partial x}dx + \frac{\partial u}{\partial t}dt = dp \qquad [8]$$

Eqs. 5–8 may be shown to be a system of four hyperbolic equations from which the usual characteristic equations can be derived (see Ref. 1, 2 or 3). These are

Direction Condition

$$\frac{dx}{dt} = u \pm a \qquad [9]$$

Compatibility Condition

$$\frac{dp}{du} = \mp\frac{K}{a} \qquad [10]$$

Working Form of Characteristic Equations

Over the range of conditions likely to be encountered in most problems, the values of a and K will be practically constant. For a given problem, therefore, the values of a and K will be regarded as constants.

The velocities of the pressure waves, as represented by Eq. 9, are much higher than the liquid velocities, and, hence, the latter may justifiably be neglected.

The characteristic equations may now be rewritten in a more convenient form.

Direction Condition

$$\frac{dx}{dt} = \pm a \qquad [11]$$

Compatibility Condition

$$\frac{dp}{K} = \mp\frac{du}{a} \qquad [12]$$

The method of characteristics consists of constructing a pair of matched networks on state and position diagrams, by means of Eqs. 11 and 12. One network, in the position diagram, is drawn between known physical boundaries, and the other, in the state diagram, is drawn from boundary curves that represent possible $p - u$ relationships at the physical boundaries. Boundary conditions are of great importance in the application of the method of characteristics and will be considered in some detail in the next section.

Boundary Conditions

The boundary of a position diagram characteristic is defined by the physical boundary of the duct, but the corresponding boundary point in the state diagram is not always obvious. This section is concerned with the determination of the state diagram boundary curves and the ideas introduced by considering simple cases.

Closed end

If a duct has a fixed closed end and the fluid remains in contact with it, then the boundary condition for this type is that liquid velocity be zero at the boundary. Therefore, the boundary curve is a vertical line ($u = 0$) on the state diagram.

On the other hand, if the duct has a moving closed end or a piston, the boundary condition may change with time and will be $u = u\ (\text{piston}) = f(t)$.

Open end

The open end type of boundary is further subdivided according to whether the flow is from or into the pipe, and it is considered in a general way by including a nozzle at the end of the pipe. The same treatment will apply from a plain open end (no nozzle) to a closed end by varying the area ratio of the nozzle, that is, by varying one parameter.

The case of flow from a pipe is considered first.

Outflow

The nozzle and pipe are shown in Fig. 1a. In transient flow applications the axial length of such a nozzle would be small compared with the length of the pipe, and, because of this, at any given instant of time the flow in the region of the nozzle may be regarded as steady flow. Flow that changes gradually with time is usually referred to as quasi-steady.

Following these ideas, the continuity and Bernoulli equations may be used to derive the following expression:

$$\frac{p_1 - p_2}{K} = \frac{1}{2}\left(\frac{u_1}{a}\right)^2\left[\frac{1}{\Phi^2} - 1\right] \qquad [13]$$

In this equation

p = static pressure
u = liquid velocity
a = sonic velocity
K = bulk modulus
$\Phi = \dfrac{\text{effective area of nozzle}}{\text{pipe area}}$

where a and K are effective values consistent with the section on working forms of equations. Suffixes 1 and 2 refer to

the cross section shown in Fig. 1a. Eq. 13 is shown graphically in Fig. 1b for a range of nozzle-area ratios. In this diagram it may be observed that as $\Phi \rightarrow 0$ the corresponding boundary curve approaches a vertical line through the origin, and that $\Phi = 0$ corresponds to the fixed closed end condition. At the other end of the range $\Phi = 1$ corresponds to an open end, and it is seen that the static pressure at the open end must be equal to the ambient pressure.

It should be appreciated that the area-ratio parameter Φ will be an effective value, namely, the product of the geometric ratio and an appropriate discharge coefficient. The mode of flow is important, and work by Northup (10) has shown that in small jets, such as rocket fuel injectors, two modes of flow for a given pressure drop are possible; these are illustrated in Fig. 2. In the first mode the liquid is in contact with solid boundaries, whereas in the second there is a free boundary to the liquid stream that starts at the inlet side of the jet. Each mode of flow has its own effective area; this is illustrated by the discharge coefficients shown in the lower part of Fig. 2.

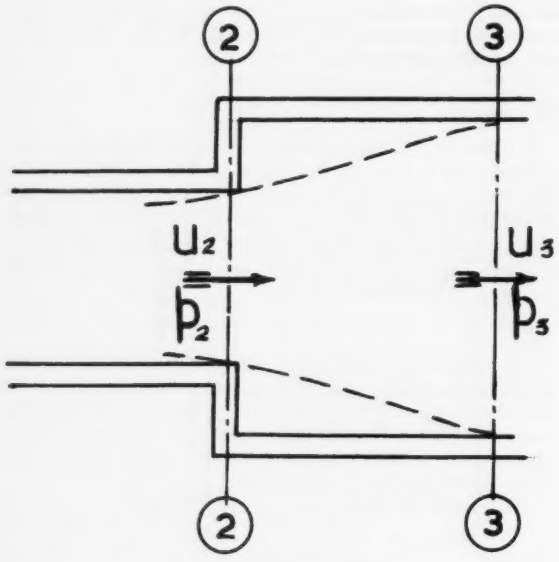

Fig. 1a Nozzle notation

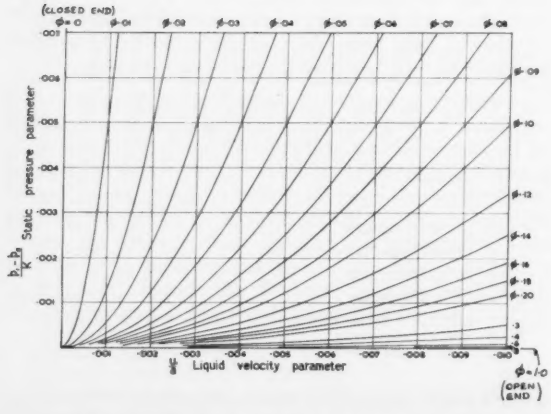

Fig. 1b Theoretical outflow boundary chart

Inflow

A simple system, that of flow into a sudden enlargement, will be considered next; this is shown in Fig. 3a. Here the quasi-steady flow assumption is more questionable than in the previous case; first, because the plane of pressure recovery, that is, where one-dimensional flow is resumed, may be several diameters downstream of the sudden enlargement; and, second, because the instantaneous mode of flow under transient conditions may not be the same as that obtained under steady flow. The latter point has been discussed by Binnie (11), Zienkiewicz and Hawkins (12), and others, and for cases such as the one under discussion the steady flow momentum equation is normally used.

For inflow a similar procedure to that for outflow is used, but the momentum equation is included together with an assumption that the static pressure across the plane of the sudden enlargement is constant. Using the above, the following equation is obtained:

$$\frac{P_2 - p_3}{K} = \left(\frac{u_2}{a}\right)^2 \left(\frac{1}{2\psi^2} + 1 - \frac{1}{\psi}\right) \qquad [14]$$

where

P = stagnation pressure

ψ = (effective flow area just before sudden enlargement / area of downstream pipe (after sudden enlargement))

Suffixes 2 and 3 are the stations shown in Fig. 3a. Eq. 14 is shown graphically for a range of ψ values in Fig. 3b, and the values of ψ are effective values.

The boundary condition for a Borda tube is obtained by considering the curve $\psi = 0.5$, and, similarly, the curve shown by $\psi = 0.62$ gives the boundary condition for an external mouthpiece. These mouthpieces are illustrated in Fig. 4.

At high flow rates such mouthpieces are prone to cavitation and, if this occurs, the value of ψ changes appreciably. Recently, a device has been described by Randall (13) in which a concentric vapor cavity is used as a means of controlling the effective flow area of a venturi tube. As a venturi tube, or similar device, may form an outlet boundary, the degree of cavitation must be known in order to determine outlet boundary conditions. In addition, ψ should be modified to account for the fact that the actual configuration may not be a simple sudden enlargement. This latter modification is

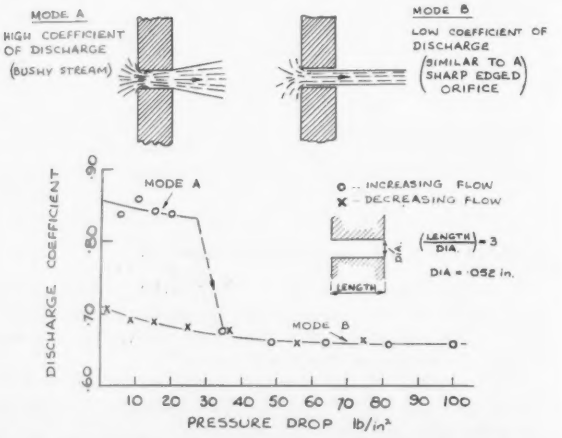

Fig. 2 Two modes of flow through small jets (after Northup Ref. 10, 1951)

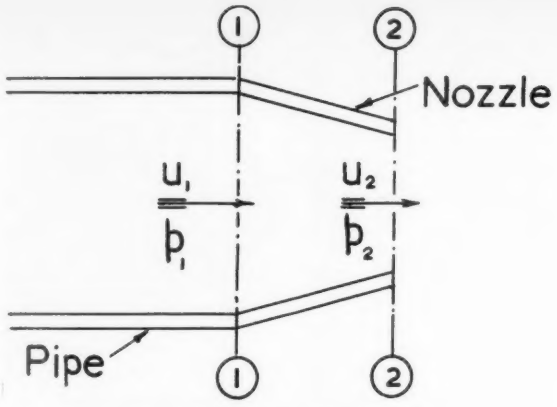

Fig. 3a Sudden enlargement notation

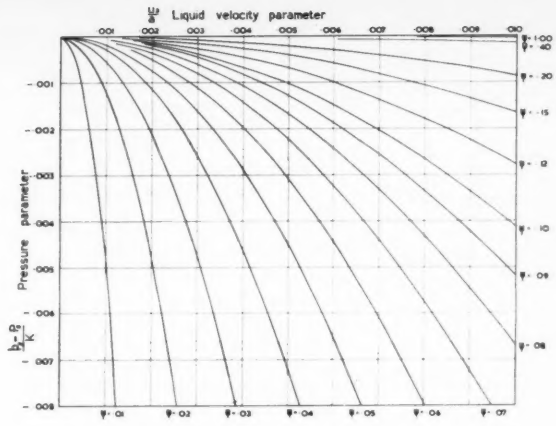

Fig. 3b Theoretical inflow boundary chart

the most difficult, and each configuration warrants a complete investigation. In order to derive a method for calculating transient liquid flows, the above boundary conditions will be used in the applications described later.

Cavitation

In the section concerned with the closed end boundary condition, it was assumed that liquid remained as a liquid and was always in contact with the closed end; however, when an expansion wave is reflected at a closed end, the pressure may be reduced to such a low value that the vapor pressure of the liquid is reached. When this occurs a vapor pocket is formed, and the boundary condition for the closed end is completely changed. The new boundary condition is one that has a constant pressure numerically equal to the vapor pressure of the liquid. The boundary could admit to almost any velocity in a direction away from the closed end boundary; thus the boundary curve becomes a horizontal line in the state diagram.

In order to continue characteristic diagram calculations, it is necessary to draw a separate position diagram showing the time history of the vapor pocket, since it provides the criterion for the type of boundary condition to be used. Once a vapor pocket is established, the boundary can admit to either positive or negative velocities. In general, the life of a vapor pocket will be finite, as subsequent reflected waves may reverse the direction of liquid flow and, thus, reduce the size of the vapor pocket.

It should be mentioned that the treatment of cavitation given here is a simplified one, and it assumes that condensation and evaporation take place in an infinitesimally short space of time. Further refinements could be included following the work of Zwick and Plesset (14), who include heat transfer effects in their equations.

Source and sink boundaries

In order to excite oscillations in the flow, the Combustion Department at Westcott proposes to use a small piston type plunger driven by an electromagnetic vibrator. If this type of device is placed near the end of a pipe, it is possible to modify the normal boundary conditions so that they include the effects of the plunger.

For such a boundary a plane source or sink is assumed to be located adjacent to the conventional boundary. The properties of the source or sink are that it can generate (or abstract) fluid evenly across the plane of the pipe and does not obstruct the flow or admit to a pressure drop across it. The concept is illustrated diagrammatically in Fig. 5. From the above assumptions it follows that:

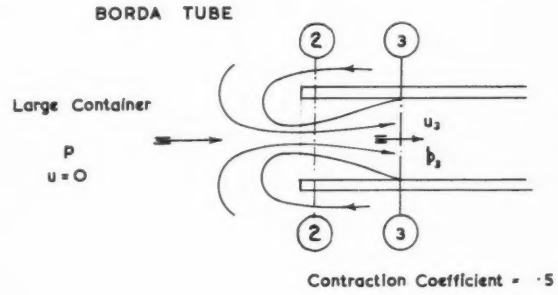

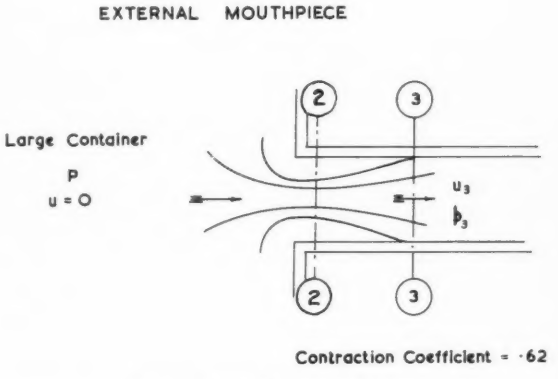

Fig. 4 Types of pipe mouthpieces

For outflow

$$u_1 = u_s + u_1 \qquad [15a]$$

$$p_I = p_1 \qquad [15b]$$

and for inflow

$$u_{III} = u_s + u_3 \qquad [16a]$$

$$p_3 = p_{III} \qquad [16b]$$

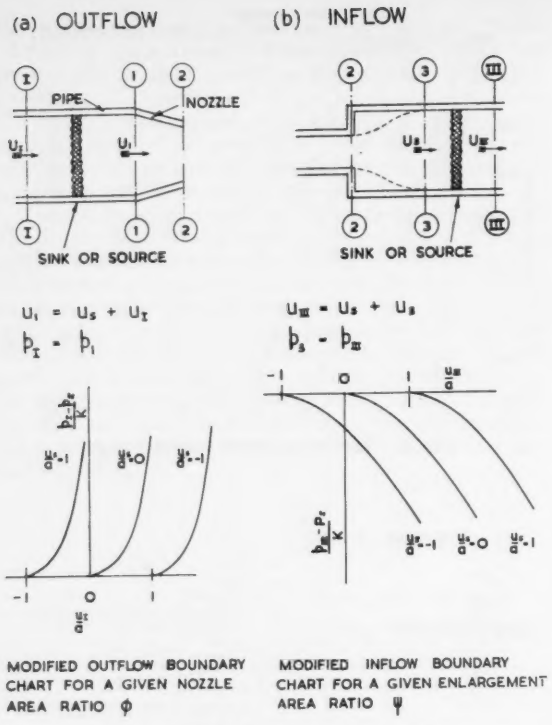
(a) OUTFLOW
(b) INFLOW
PIPE
NOZZLE
SINK OR SOURCE
SINK OR SOURCE
MODIFIED OUTFLOW BOUNDARY CHART FOR A GIVEN NOZZLE AREA RATIO φ
MODIFIED INFLOW BOUNDARY CHART FOR A GIVEN ENLARGEMENT AREA RATIO ψ

Fig. 5 Source-sink boundary conditions

where

$$u_s = \left(\frac{\text{volume of fluid generated by source per second}}{\text{cross-sectional area of pipe}}\right)$$

and the subscript s refers to source or sink.

From Eqs. 15 and 13 an overall relationship may be obtained between p_I and u_I. This is illustrated graphically for a given nozzle in the lower part of Fig. 5a. It can be seen that a change of u_s moves the complete curve horizontally to the left for a source and to the right for a sink.

In a similar way, by considering Eqs. 16 and 14, the modified inflow boundary conditions are obtained (illustrated in the lower part of Fig. 5b). Such boundaries will be used in the next section, which illustrates the applications of the methods previously outlined.

Applications

Closed Pipe Calculations

Nonresonant condition with cavitation

The first calculations were concerned with a straight pipe having a piston plunger at one end; the other end was closed. It was assumed that the piston had the same diameter as the pipe bore and moved with simple harmonic motion; the effects of pipe friction were neglected.

The basic assumptions for the calculation were

Pipe length	10.458 ft
Pipe diameter	0.5 in.
Piston frequency	160 cps
Piston displacement amplitude, i.e., half total movement	0.0075 in.
Sonic velocity in liquid	4910 fps
Adiabatic bulk modulus for liquid	324,000 lb_f/sq in.
Vapor pressure of liquid	0.3 lb_f/sq in.

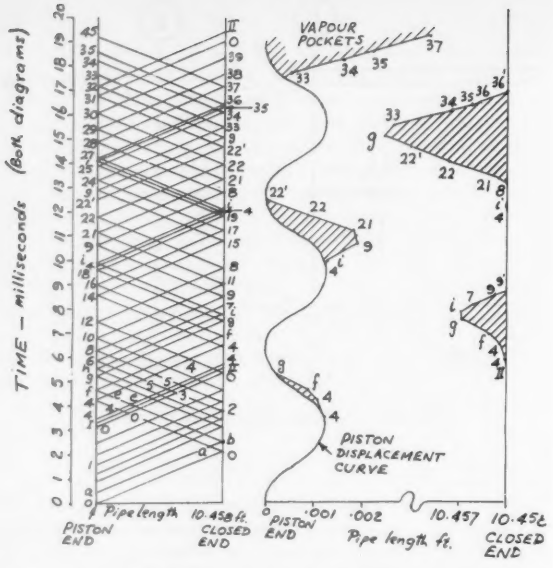

Fig. 6 Closed pipe calculation for nonresonant conditions with cavitation. Left: wave line position diagram. Right: path line position diagram for boundaries

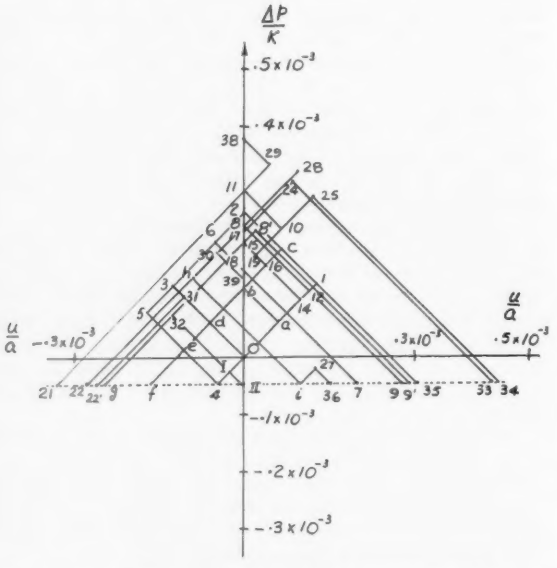

Fig. 7 State diagram for closed pipe calculation for nonresonant conditions with cavitation

In this calculation no allowance for the elasticity of the pipe was made. The piston was assumed to start from rest at its outer position, with the fluid in the pipe being at rest at atmospheric pressure, 14.7 lb_f/sq in. The results for this calculation are shown in Figs. 6, 7 and 8.

Fig. 6 shows two position diagrams; the first, on the left, gives the wave lines or disturbance characteristics, whereas

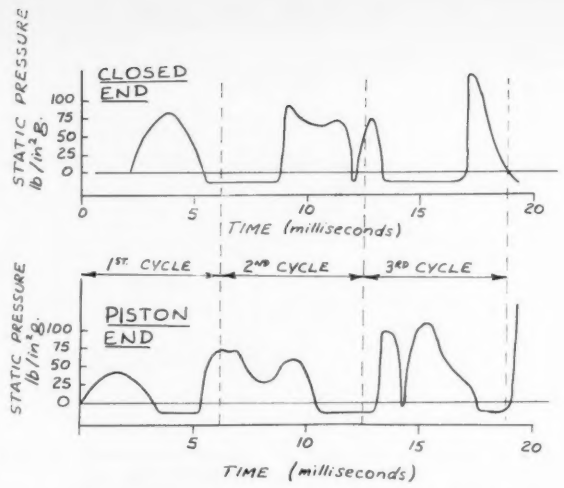

Fig. 8 Indicator diagrams for closed pipe calculation for non-resonant conditions with cavitation

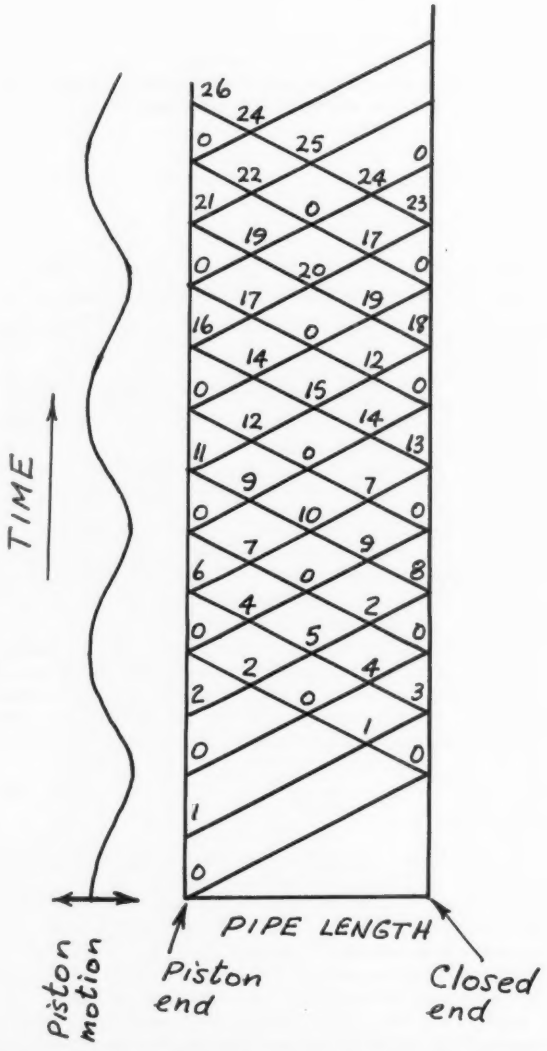

Fig. 9 Position diagram for closed pipe calculation for resonant conditions without cavitation

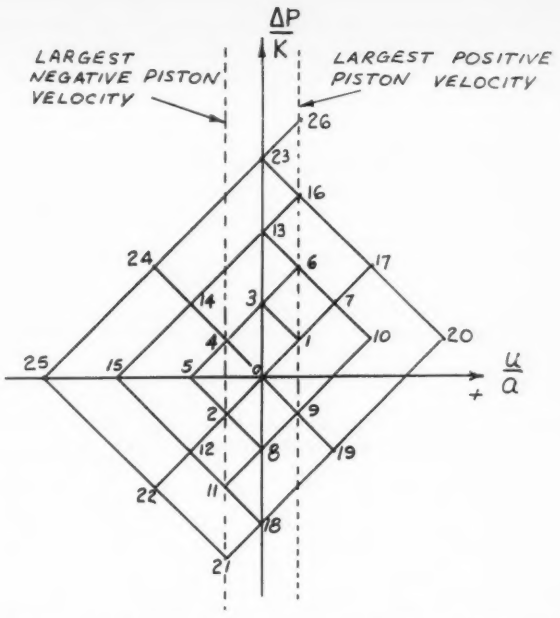

Fig. 10 State diagram for closed pipe calculation for resonant conditions without cavitation

the second, on the right, shows the path lines for the two boundaries. A very large displacement scale has been employed for the latter. The numbering on this diagram is arbitrary, and there is no special significance in numbers, letters, or Roman numerals used. The crosshatched areas on the path line diagram represent regions where cavitation has taken place.

The corresponding state diagram is shown in Fig. 7. The numbering corresponds to that on Fig. 6, and the dotted horizontal line represents the vapor pressure line for the liquid.

The indicator diagrams for the first three cycles are shown in Fig. 8. It is seen that initially the wave has a regular shape, but soon the wave action becomes extremely complex. As friction was neglected, the oscillations increased in magnitude; this is clearly revealed by the increasing size of the vapor pockets, shown in Fig. 6. In this calculation the wave travel time did not correspond to the periodic time of the piston, and, if the calculation had been continued, it would probably have revealed a beat phenomenon.

Resonant conditions without cavitation

The second calculation was intended to be a more realistic approach to an actual test. The velocity of sound in the liquid and the bulk modulus of the liquid were regarded as effective values, and a base pressure sufficiently high to avoid cavitation was assumed. The velocity of sound was selected so that the wave travel time corresponded to the periodic time of the piston. The values used for the calculation were

Piston frequency	160 cps
Effective sonic velocity in liquid	3345 fps
Effective bulk modulus for liquid	150,800 lb_f/sq in.
Pipe length	10.458 ft

As before, the piston was started from its outer position when the fluid was at rest at its base pressure. The diagrams for this calculation are shown in Figs. 9, 10, and 11. From

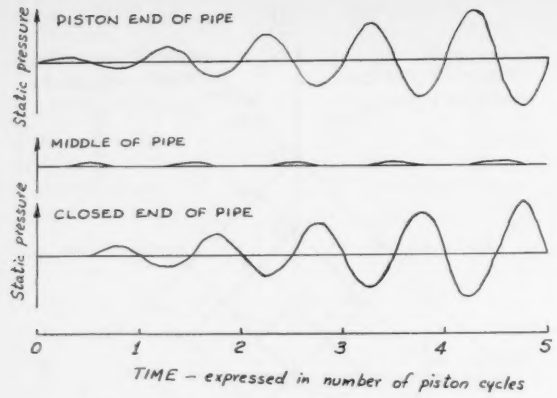

Fig. 11 Indicator diagrams for closed pipe calculation for resonant conditions without cavitation

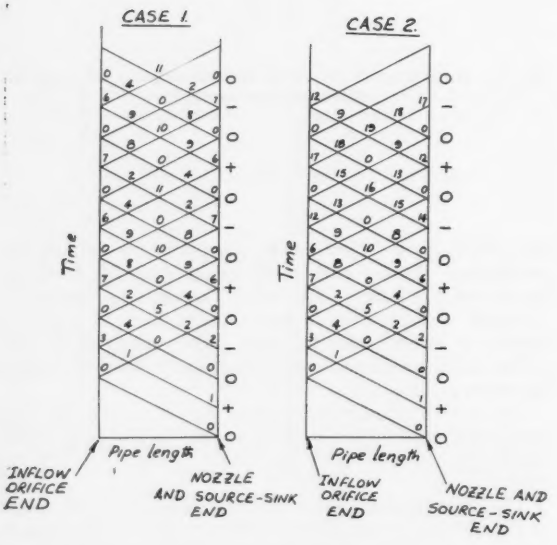

Fig. 12 Position diagrams for pipe flow calculations with source and sink type of disturbance

\+ Source generating fluid at maximum rate
– Sink removing fluid at maximum rate
O No fluid being generated or removed

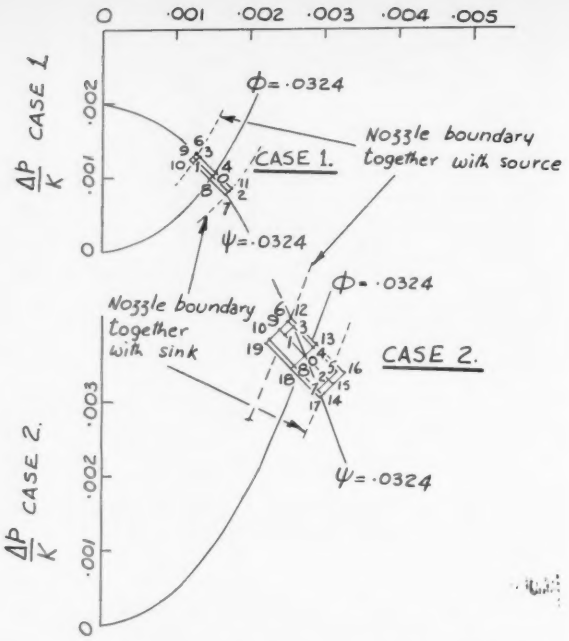

Fig. 13 State diagrams for pipe flow calculations with source and sink type of disturbance; abscissa axis, y/a

Fig. 11 the wave action is again seen to be increasing in magnitude as friction was neglected. Fig. 11 also shows that the pressure fluctuations at the piston end are 180° out of phase with those at the closed end, and a practically constant pressure prevails at the middle of the pipe.

Pipe Flow Calculations

The diagrams shown in Figs. 12, 13, and 14 apply to a pipe system with an entry orifice in which $\psi = 0.0324$. At the opposite end of the pipe there is a nozzle where $\Phi = 0.0324$; the latter was to simulate the rocket combustion chamber injector nozzle. Near this nozzle there is assumed to be a cyclical source-sink type of disturbance. In the following calculations the periodic time of the source-sink disturbance is made equal to the wave travel time for the pipe; this corresponded to a frequency of 419 cps. Other assumptions are

Source-sink dimensionless velocity	$u_s/a = \pm 0.0004$
Pipe length	4 ft
Effective velocity of sound in liquid	3345 fps
Effective bulk modulus of liquid	150,800 lb_f/sq in.
Discharge nozzle back pressure	0 psi gage
Dimensionless supply pressure $(\Delta p/K)$ supply	Case 1—0.002 (approx. 300 lb_f/sq in. gage)
	Case 2—0.007 (approx. 1050 lb_f/sq in. gage)

The base pressure is the static pressure at which the two boundary curves intersect, i.e., the static pressure in the pipe corresponding to steady flow conditions. The effect of the source-sink disturbance is to shift the nozzle boundary. This is shown in Fig. 13 as dotted boundary curves.

In both calculations stable cyclical conditions are rapidly reached. An important result is that, with this type of arrangement, the wave action amplitude reaches a finite limit even without friction. Hence, in practice, the wave action amplitude should be less than that obtained in a closed pipe.

Discussion

A method for estimating the nature of liquid flow under unsteady conditions has been developed. In the present work this method is confined to frictionless adiabatic flow. The treatment is by the method of characteristics, used in a manner similar to that for unsteady gas dynamics problems.

The calculations carried out suggest that an applied disturbance could be arranged in a closed pipe so that it would resonate, and the wave action amplitude would progressively increase. In an actual case, a finite limit to the wave action amplitude should be reached, because frictional viscous damping is present. In addition, if the disturbance was large

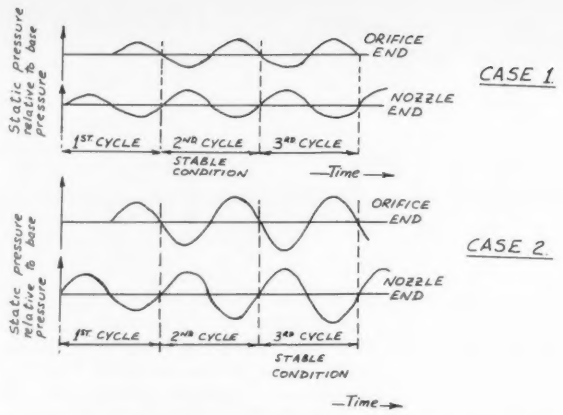

Fig. 14 Indicator diagrams for pipe flow calculations with source and sink type of disturbance

enough or if the base pressure, i.e., static pressure in the pipe before the disturbance was initiated, was low enough, cavitation would take place.

For a flow system in which a disturbance is applied near one end of a pipeline, between an orifice and discharge nozzle, the theoretical calculation showed that a regular, cyclical wave action would be set up with a finite wave action amplitude. The latter system represented the fuel supply line to a small research rocket motor; the orifice was installed for flow measurements, and the discharge nozzle was the fuel spray jet.

Conclusions

The method of characteristics may be applied to problems involving unsteady flow of a compressible liquid. The use of this method along the lines adopted for gas dynamics is somewhat similar to the Schnyder-Jaeger-Bergeron graphical method for water hammer problems.

The theory reveals a progressively increasing wave action amplitude for a resonant disturbance in a closed pipe. This suggests that eventually cavitation would inevitably occur. In a practical case, frictional damping would lead to a finite limit being reached for the wave action amplitude.

The case of a flow system is somewhat different, and the theory suggests that in the resonant condition a finite amplitude is attained. This suggests that the maximum wave action amplitude obtained in a flow system is less than that obtained in a closed pipe.

Acknowledgments

This work was carried out at the Ministry of Aviation Rocket Propulsion Establishment, Westcott, and the author wishes to thank the Director for permission to publish this paper and the members of the Combustion Department for their help and advice.

References

1 Courant, R. and Friedrichs, K. O., *Supersonic Flow and Shock Waves*, Interscience Publishers Inc., New York, 1948.

2 Jenny, E., "Berechnungen und Modellversuche über Druckwellen grosser Amplituden in Auspuff-Leitungen," Thesis, E.T.H. Zurich, Ameba-Druck, Basel, 1949. Part of this appears in *The Brown Boveri Review*, vol. 37, no. 11, 1950, p. 447.

3 Shapiro, A. H., *Dynamics and Thermodynamics of Compressible Fluid Flow*, Vol. 2, The Ronald Press, New York, 1954.

4 de'Haller, P., "The Application of a Graphic Method to Some Dynamics Problems in Gases," *Sultzer Tech. Rev.*, no. 1, 1945, p. 6.

5 Benson, R. S., "Discharge of Gas from Cylinder to Atmosphere," *The Engineer*, vol. 199, 1955, p. 546.

6 Rudinger, G., *Wave Diagrams for Nonsteady Flow in Ducts*, D. Van Nostrand Co. Inc., New York, 1955.

7 Schnyder, O., "Über Druckstösse in Rohrleitungen," *Wasserkraft und Wasserwirtshaft*, vol. 27, no. 5, p. 49, and no. 6, p. 64, 1932.

8 Jaeger, C., *Théorie Générale du Coup de Bélier*, Dunod, Paris, 1933.

9 Bergeron, L.,"A General Graphical Method of Calculating the Propagation of Plane Waves," (Translated), *Mémoires Soc. des Ing. Civils de France*, no. 4, 1937, p. 407.

10 Northup, R. P., "Flow Stability in Small Orifices," paper prepared for presentation to the American Rocket Society on Nov., 30, 1951, at the Annual Meeting of the A.S.M.E. in Atlantic City, N. J.

11 Binnie, A. M., "Protective Air Vessels for Rising Pipe-Lines," *Proc. Inst. of Mech. Engrs.*, vol. 153, London, 1945, p. 15.

12 Zienkiewicz, O. C. and Hawkins, P., "Transmission of Water Hammer Pressures through Surge Tanks," *Proc. Inst. of Mech. Engs.*, vol. 168, no. 23, London, 1954, p. 629.

13 Randall, L. N., "Rocket Applications of the Cavitating Venturi," JARS, vol. 22, January–February 1952, p. 28.

14 Zwick, S. A. and Plesset, M. S., "On the Dynamics of Small Vapor Bubbles," *J. Math., Phys.*, vol. 33, 1955, p. 308.

Technical Notes

Radiation Shielding of Space Vehicles by Means of Superconducting Coils[1]

RICHARD H. LEVY[2]

AVCO-Everett Research Laboratory, Everett, Mass.

ONE OF the major problem areas in connection with manned space flight is that of providing adequate protection against the various forms of ionizing radiation known to be present in space. There are three principal forms of this radiation; the first is due to the inner and outer Van Allen belts that are present at all times in specified regions in the vicinity of Earth. The second is the so-called background cosmic radiation that is present throughout the galaxy. The third, and in many respects the most important, originates in the beams of energetic protons emitted from the sun in solar flares; these vary widely in strength and also in frequency, maximum frequency occurring with sunspot maximum.

General Discussion

Shielding against the Van Allen belts is no longer the problem it was once thought to be. Dosage received in passing through them can be minimized by suitable trajectory shaping, and a quite modest amount of shielding appears to be sufficient to reduce the dose received in passing twice through each belt to a reasonable value on the order of 5 rem. The galactic cosmic rays form a quite different problem. In the first place the level is generally quite low (of the order of 5 to 12 rem/yr), so that trips of six months or so may be planned without taking special precautions against them. On the other hand it is fortunate that this is the case, since the typical energy of the galactic cosmic rays is so high that appreciable reduction of the dose rate is prohibitively expensive in terms of weight. The most important shielding problem, however, is posed by solar flares. It seems likely at present that prediction schemes can be devised that will make possible trips lasting up to a maximum of about two weeks for which the statistical probability of encounter of a large flare can be reduced to acceptable levels. However, trips longer than about two weeks will almost certainly involve shielding against large flares. Much of the information given above may be found, for instance, in (1).[3]

A simplified view of the shielding problem, and one that will be adequate for the purposes of this note, involves the specification of a proton energy such that if all protons of less than this energy are removed from the flux before striking the body, the resultant dose is tolerable. Given such a proton energy, the problem of solid shielding becomes a simple exercise; range-energy curves for protons are given for many substances in many references. Excluding hydrogen as too bulky and impractical, a number of elements have very similar stopping powers, including carbon, aluminum, and copper. Water is also considered by many as typical of this group. The difference between these substances is largely their rate of production of secondary neutrons; carbon appears to be best from this point of view, but water is not much worse. It should be noted that secondary neutron effects may play an important role in the determination of the critical proton energy.

For a two-week lunar type mission, the cutoff energy is around 200 Mev, resulting in water thicknesses on the order of 25 gm/sq cm. This in turn gives shielding weights that are high but not unreasonably so. The real problem is in longer trips, for which the cutoff energy is considerably higher. There are some conflicting estimates of just how high it is, and it is not the purpose of this note to attempt the resolution of that particular problem; 500 Mev to 1 Bev can be estimated with some confidence, and this gives thicknesses of the order of 100 to 300 gm/sq cm. When translated into reasonable surface areas for spacecraft, the resultant weights come out very high. Furthermore, these weights are mandatory in the sense that there is no room for reduction. In this note a possible alternative scheme of shielding will be discussed, which, whereas it does not appear to offer greatly reduced weights at present, is nevertheless capable of improvement, at least in principle, depending on the production of materials with higher strength to weight ratios.

Analysis of Magnetic Shielding

This alternative scheme is shielding by means of magnetic fields. Such a scheme has been considered (2), but rejected on the grounds of the excessive power needed to maintain the large fields required. This objection must be reconsidered in view of the introduction of the new high field superconductors. A coil made of such a material could be charged once and for all; then, provided only that it was protected by insulation against external heat sources, it would act as a permanent magnet.

The calculation of the shielding effect of a magnetic dipole has been well understood for many years in connection with the effect of Earth's field on cosmic rays. The results of this calculation are as follows: given a dipole of magnetic moment m and a particle with momentum to charge ratio p/e, the so-called Stormer radius $c = (em/4\pi p)^{1/2}$ can be defined. Then, if θ is the colatitude, the region inside the surface $r/c = [(1 + \sin^3\theta)^{1/2} - 1]/\sin\theta$ is inaccessible to particles that originate at infinity and have the specified value of p/e or less. It is worth noting that when $\theta = \pi/2$ (in the equatorial plane) the shielded region extends only out to 41% of the Stormer radius. An axially symmetric space

Received Aug. 8, 1961.

[1] This research was supported by Headquarters, Ballistic Systems Div., Air Force Systems Command, USAF under Contract No. AF 04(647)-278.

[2] Principal Research Scientist. Member ARS.

[3] Numbers in parentheses indicate References at end of paper.

EDITOR'S NOTE: The Technical Notes and Technical Comments sections of ARS JOURNAL are open to short manuscripts describing new developments or offering comments on papers previously published. Such manuscripts are usually published without editorial review within a few months of the date of receipt. Requirements as to style are the same as for regular contributions (see masthead page).

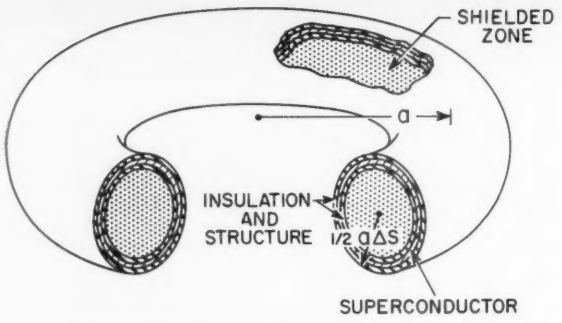

Fig. 1 Schematic of superconducting coil for radiation shielding

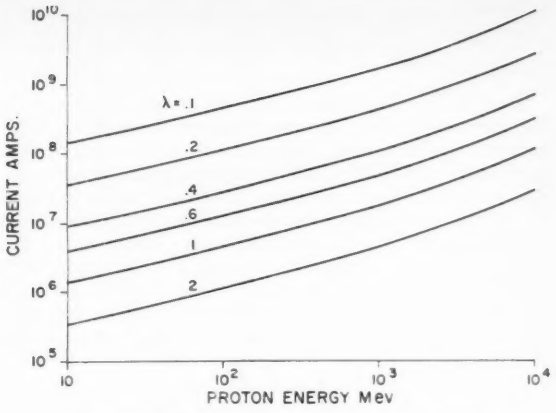

Fig. 2 Value of parameter $\lambda = a/c = (4p/\mu_0 eI)^{1/2}$

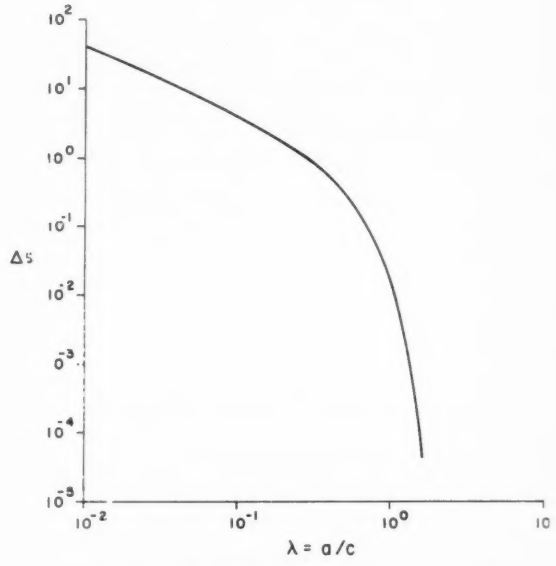

Fig. 3 Extent of radiation free zone in equatorial plane

vehicle of the shape defined above with a dipole with magnetic moment appropriate to the cutoff energy at its center would then be shielded, except against those particles arriving precisely from the polar directions.

Whereas this result is interesting, it will be shown later that the dipole configuration is undesirable from the structural point of view. If the magnetic field is to be generated by a current carrying superconductor, a realistic configuration would be a single turn coil made from a hollow tube of superconductor. Other configurations have been studied, but do not yield basically different results. It can be shown that for the single turn coil there is a toroidal shielded region surrounding the wire, roughly circular in cross section. It is clearly expedient, in order to avoid wasted field, to place the superconductor at the boundary of the shielded region; this will not alter the field in the region of interest. Living quarters inside such a superconducting torus will then be radiation free (up to the design particle energy). A schematic diagram of such a device is shown in Fig. 1.

Quantitatively, the shielding calculation may be summarized as follows: if I is the circulating current, a nondimensional parameter $\lambda = a/c = (4p/\mu_0 eI)^{1/2}$ can be defined. Values of λ are shown in Fig. 2. The cross-sectional radius of the shielded torus is then given by $r_s = (1/2)a\Delta s$, where Δs is a function of λ and is plotted in Fig. 3. It can be seen that Δs falls very rapidly with increasing λ, whereas small values of λ imply very large values of I. It may be anticipated that on closer analysis an optimum value of λ will appear.

This closer analysis involves a more detailed look at the principal components of a coil of the type being described. For the present purposes the coil may be thought of as consisting of the superconducting coil itself, the structure required to support the magnetic forces, and the insulation necessary to maintain the appropriate low temperatures. It will appear that the structure is by far the most important of these three items. It will be sufficient to consider as representative the structure required to support the bursting hoop stress on the coil. If ρ_s and σ_w are the density and working stress of the structural material to be used, simple considerations (4) show that the mass of structure required is given by

$$(\mu_0 \rho_s I^2 a/2\sigma_w)\ (1 + \ln a/r_s)$$

The variation of this quantity with the square of the current is a natural consequence of the energy connected nature of the structure. It is this structural term that will prevent λ from being as small as we like. The mass of the actual superconductor turns out to be far less than the mass of structure, based upon an aluminum structure at 50,000 psi, a superconductor with a density of about 8.4 gm/cu cm, a current carrying capacity of about 10^5 amps/sq cm, and a critical field in the general neighborhood of 10^5 gauss. (These properties correspond roughly to the niobium tin compound discussed in (3), but may be thought of as the first in a new series of greatly improved superconductors.) If we denote the density and current carrying capacity of the superconductor by ρ_c and j_c respectively, the mass of superconductor is easily shown to be $2\pi\rho_c Ia/j_c$. The insulation needed to maintain the superconductor at the required temperature is proportional to the surface area of the device and increases with the mission length. However, all cases studied resulted in such low values that this item will not be considered any further here.

If a given shielded volume $V = (1/2)\pi^2 a^3(\Delta s)^2$ is decided on, then for a given cutoff energy the shape and total mass of the coil for various currents can be found. As indicated above, such an analysis yields an optimum value for λ; this value turns to be about 0.6. The mass is not too sensitive to it. Using the optimum value of λ, the mass of a superconducting shield can be plotted against the shielded volume. Using the range energy curves for protons in water, similar curves for a spherical solid shield can be plotted. These

results are shown in Fig. 4 and constitute the essential results of this note.

Conclusions

The following conclusions may be drawn from Fig. 4: first, the superconducting shield is lighter for a given proton energy when either large volumes or very energetic protons are considered; second, the absolute masses involved are very large by present day standards, but it must be remembered that shielding of the type described will be positively required for all manned space missions lasting more than about two weeks, so that these missions are not possible at all until vehicles of this size can be used; third, the advantage of the superconducting shield is considerably enhanced, since in the shielding process the protons do not strike the coil but are deflected; as a result there is no generation of secondary neutrons, so that comparisons should not be made on the basis of the same proton energy; rather, for a given mission, the cutoff energy appropriate to the solid shield will be higher than that appropriate for the superconductor.

To conclude, it may be of interest to calculate various parameters for a particular case. Choose, for example, a coil capable of protecting 100 m³ (corresponding to 20 or 30 men) against 1 Bev protons. We find the optimum λ is 0.7, $a = 13$ m, $r_s = 0.62$ m, $I = 3.7 \times 10^7$ amps, and the total mass is 3.76×10^5 kg, of which 92% is structure. In contrast, a water shield protecting the same volume (but in the shape of a 2.9-m radius sphere) weighs 8.5×10^5 kg without considering the secondaries.

Further details of the work described in this note may be found in (4).

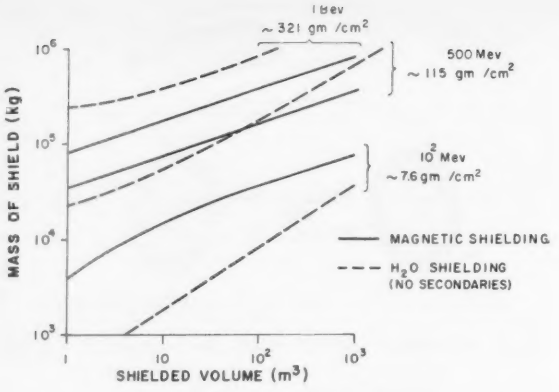

Fig. 4 Optimized shielding weights

References

1 Newell, H. E. and Naugle, J. E., "Radiation Environment in Space," *Science*, vol. 132, no. 3438, Nov. 18, 1960, pp. 1465–72.

2 Dow, N. F., "Structural Implications of the Ionizing Radiation in Space," *Proc.* Manned Space Stations Symposium, Los Angeles, Calif., April 20–22, 1960.

3 Kunzler, J. E., Beuhler, E., Hsu, F. S. L. and Wernick, L. F., "Superconductivity in Nb_3Sn at High Current Density in a Magnetic Field of 88 K Gauss," *Physical Review Letters*, vol. 6, Feb. 1, 1961, pp. 89–91.

4 Levy, R. H., "Radiation Shielding of Space Vehicles by Means of Superconducting Coils," *Avco-Everett Research Lab. Research Rep. 106*, August 1961.

Lunar Landing Vehicle Propulsion Requirements[1]

J. RICHARD WROBEL[2]
ROBERT R. BRESHEARS[3]

Jet Propulsion Laboratory
California Institute of Technology
Pasadena, Calif.

THE PURPOSE of this analysis is to develop generally applicable criteria for the design of a lunar-landing vehicle propulsion system. Variations of the landing maneuver, such as oblique entry, hovering, lateral translation, and multiple burning phases, have been omitted in this first analysis of the problem. The effect of any of these variations would perhaps best be studied in a specific vehicle analysis since needs vary, depending on the mission chosen. A weighted average value of gravity appropriate for the altitude spread encountered may be used for those situations in which the ignition altitudes are appreciably large compared with the lunar radius. An appropriate choice of the gravity value and impact velocity will make this analysis applicable for use in computing the optimum vertical descent on any atmosphere-free celestial body.

The characteristics of lunar transfer trajectories have been discussed rather thoroughly in the recent literature by several authors (1–4).[4] The trajectory parameter of interest is the relative velocity with which an unbraked vehicle would strike the lunar surface. This velocity is determined by integrating the effect of the forces acting on the vehicle as it traverses the Earth-Moon transfer trajectory. Values of this impact velocity are available in the literature for various Earth-Moon transit times. A plot of the average impact velocity vs. transit time from Earth is presented in Fig. 1. The impact velocity represents the impulsive velocity decrement that would be necessary to stop the vehicle if applied just prior to contact with the lunar surface. For finite thrust levels (nonimpulsive velocity additions), the total effective decrement is greater than this impact velocity due to the kinematic inefficiency of burning while traversing a gravitational field.

The descent under power is simplified by the following five assumptions, leaving the trajectory equations linear and solvable in closed form.

1 Gravity g is constant during deceleration.

2 Descent is made vertical to the lunar surface.

3 Propellant exhaust velocity and mass rate of expulsion are constant with time.

4 The descent to the surface is free of atmospheric drag forces.

5 Vehicle velocity and altitude are simultaneously zero at the end of burning.

Under these assumptions, the form of the differential

Presented at the ARS Semi-Annual Meeting, Los Angeles, Calif., May 9–12, 1960; revision received Sept. 5, 1961.

[1] This paper presents the results of one phase of research carried out at the Jet Propulsion Laboratory, California Institute of Technology, under Contract No. NASw-6, sponsored by NASA.

[2] Development Engineer, Propulsion Div. Member ARS.

[3] Development Engineer, Propulsion Div.

[4] Numbers in parentheses indicate References at end of paper.

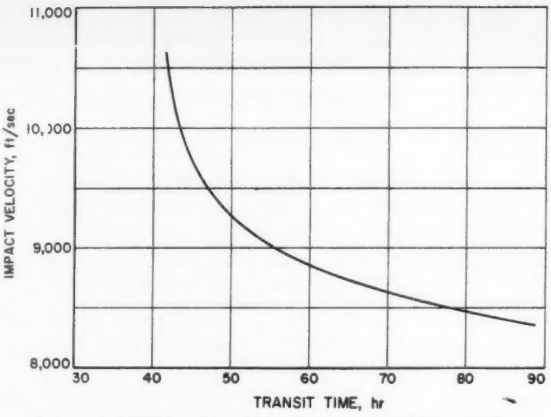

Fig. 1 Lunar impact velocity vs. transit time from Earth

equations of motion is identical with that of the simple vertical ascent sounding rocket equation (5).

When the conservation of momentum is applied to a body of mass m ejecting mass with an exhaust velocity c while descending vertically through a drag-free constant gravity field, the familiar result is,

$$m(d^2h/dt^2) = -c(dm/dt) - mg \qquad [1]$$

To obtain the altitude-time function $h(t)$, Eq. 1 must be integrated twice with respect to time and the following boundary conditions applied at ignition:

$$m = m_0 \text{ at } t = 0 \qquad h = h_0 \text{ at } t = 0$$

at burnout

$$m = m_b \text{ at } t = t_b \qquad h = 0 \text{ at } t = t_b$$

The velocity at ignition may be determined from energy considerations. Without a retrorocket, the spacecraft would strike the lunar surface at velocity V. At an altitude h_0 the vehicle already has the velocity V_0, the difference in velocity being due to potential and kinetic energy exchange. Continuing with the assumption of constant gravity g in the lunar proximity, these simple functional relationships evolve.

$$V_0^2 = V^2 - 2gh_0 \qquad [2]$$

$$gh_0/c^2 = -[(1-\xi)/a_0][1 + (1-\xi)/2a_0 + (\ln\xi)/(1-\xi)] \qquad [3]$$

$$a_0 = [2(1-\xi) + 2\xi \ln\xi][(\ln\xi)^2 - (V/c)^2]^{-1} \qquad [4]$$

$$t_b g/c = (1-\xi)/a_0 \qquad [5]$$

where $\xi \equiv m_b/m_0$, and a_0 is the initial acceleration in multiples of g.

The mass of the propulsion system plays an important role in determining the thrust level for which a given vehicle lands with maximum usable payload. The propulsion system as discussed here is meant to include the following: thrust chamber, propellant tanks, tank structure, propellant transfer system, propellant holdup, propellant reserves, plumbing, valves, and thrust-level control system. For a given propulsion scheme the system mass will vary with the propellant load and the thrust level. For liquid propulsion systems this mass dependence varies somewhat from system to system depending on the propellant transfer method, the properties of the propellant, and the thrust chamber design.

For a given propellant combination and propellant transfer scheme, there will be some values of the constants of proportionality such that over an arbitrary range of thrust level and propellant load the system mass may be assumed to be a linear function of the thrust F and the propellant load m_p.

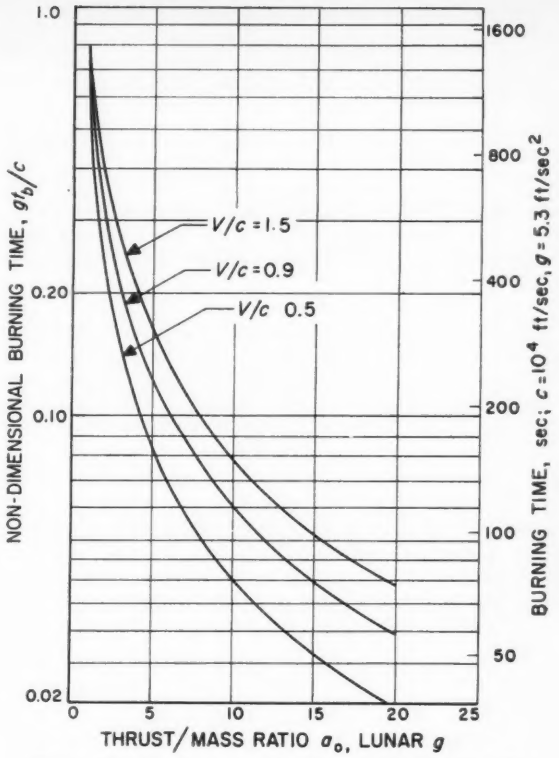

Fig. 2 Burning time as a function of thrust/mass ratio

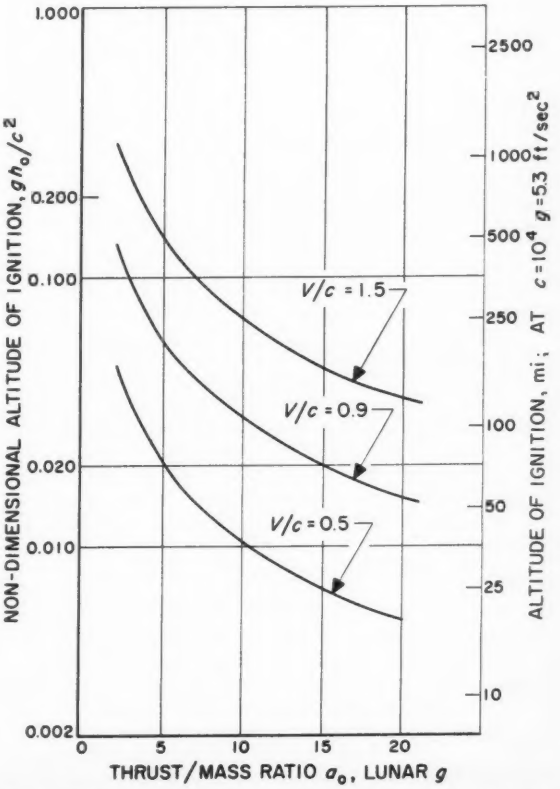

Fig. 3 Ignition altitude as a function of thrust/mass ratio

Functionally, this dependence may be described as

$$m_{ps} = A + Bm_p + CF \quad [6]$$

The gross soft landed payload of the vehicle is defined to be the difference between burnout mass m_b and propulsion system mass m_{ps}. The dimensionless payload ratio λ is the mass of nonpropulsive payload landed per unit of initial gross mass m_0.

$$\lambda = \xi - (A/m_0) - B(1 - \xi) - Ca_0g \quad [7]$$

where a_{0g} has been substituted for the ratio of thrust to initial gross mass. The payload ratio for any vehicle is, therefore, determined as a function of a_0g and ξ. To maximize the usable payload, the derivative of λ with respect to a_0 must be equated to zero. This results in another independent equation

$$d\xi/da_0 = g\,C/(1 + B) \quad [8]$$

The parameter $C/(1 + B)$ evolves as the only propulsion-system characteristic needed to find the thrust level which results in the maximum payload. Taking the derivatives of Eq. 4 and eliminating $d\xi/da_0$ with Eq. 8 results in an implicit expression for the optimum value ξ_{opt} of ξ

$$g\,C/(1 + B) = [(\ln\xi_{opt})^2 - (V/c)^2]^2/\{[(\ln\xi_{opt})^2 - (V/c)^2]2(\ln\xi_{opt}) - 4(\ln\xi_{opt})^2 - 4(1 - \xi_{opt})(\ln\xi_{opt})/\xi_{opt}\} \quad [9]$$

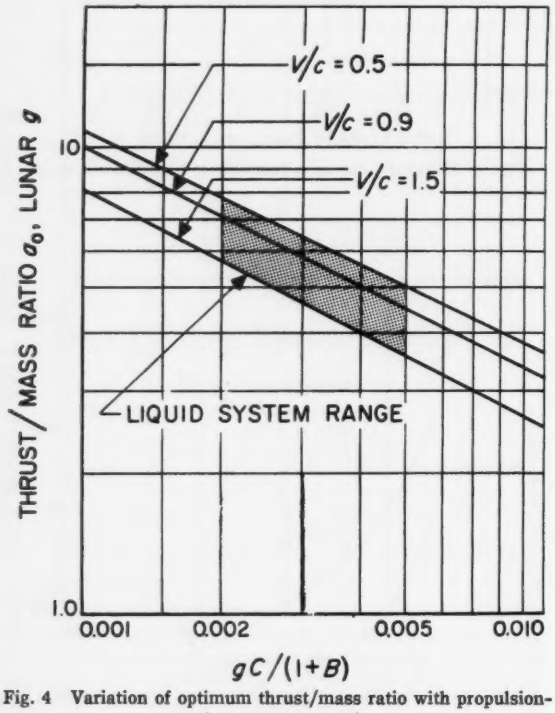

Fig. 4 Variation of optimum thrust/mass ratio with propulsion-system mass parameter

Eqs. 3, 4, and 5 form a set that describes the dynamics of the descent. The solution of these equations of motion are presented graphically in Figs. 2 and 3. Fig. 2 illustrates the variation of burning time with choice of thrust to mass ratio for pertinent velocity ratios V/c. Fig. 3 illustrates the dependence of ignition altitude on thrust to mass ratio. The ordinate of each of these curves is presented in dimensional form for a specific example of lunar g as well as in dimensionless form for general applications.

It should be noted that this set of equations possesses one degree of freedom. If the optimum payload condition is desired, then Eq. 9 must be included. This fixes all the variables for any given set of parameters, V, c, g, and $C/(1 + B)$. Fig. 4 represents the functional relationship of optimum thrust to mass ratio to the propulsion-system mass parameter $C/(1 + B)$. The range of interest for lunar landing vehicles incorporating liquid propellant systems includes values of thrust to mass ratio from 4 to 7 lunar g, as shown in the shaded region of Fig. 4. The parameter C in Eq. 6 for solid propellant systems is, in general, much smaller than that for liquid systems. That is, the inert system mass for a solid rocket is largely dependent upon the propellant mass (or total impulse), and not strongly dependent on thrust level. The optimum thrust level for solid rockets may result in accelerations greater than a typical spacecraft can tolerate.

In some instances, the maximum payload condition may result in ignition altitudes, accelerations, or burning times which are inconsistent with guidance or scientific requirements. Another situation that could arise is that, for expediency, some propulsion systems available at the appropriate time might be modified for retrorocket applications. The thrust level of such an engine would then not necessarily result in the maximum payload for a given launch vehicle. In these situations, it is desirable to determine the penalties in payload incurred.

If, after determining the optimum thrust mass ratio for a vehicle, it is found that the values selected for the propulsion system characterizing parameters A, B, and C are inapplicable in the derived range of thrust and propellant load, new values of the parameters may be chosen and a new optimum determined.

References

1 Stearns, E. V., "Propulsion Requirements for a Lunar Soft Landing," presented at Flight Propulsion Meeting, IAS, March 10, 1960.

2 Clement, G. H., "The Moon Rocket," *P-833*, Rand Corp., Santa Monica, Calif., May 1956.

3 Lieske, H. A., "Lunar Trajectory Studies," *P-1293*, Rand Corp., Santa Monica, Calif., Feb. 26, 1960.

4 Smith, R. A., "Landing on Airless Planets," *J. British Interplanetary Soc.*, vol. 12, no. 4, 1953, pp. 149–155.

5 Cross, C. A., "An Analogue Computer for the Vertical Rocket Landing and Takeoff Problems," *J. British Interplanetary Soc.*, vol. 15, no. 1, 1956, pp. 7–17.

Binder Crystallization in Polysulfide Propellant

W. E. HUNTER,[1] E. T. FOSTER,[2] and G. F. MANGUM[3]

Thiokol Chemical Corp., Huntsville, Ala.

The packing of high polymer structural units into a highly ordered geometric pattern results in formation of crystalline areas within the polymer. The effects of crystallization on polymer properties are: 1) decrease in elongation; 2) increase in tensile strength; 3) increase in modulus; and 4) decrease in volume. Degree, rate, and temperature of crystallization (or disappearance of crystallization) can be determined by a number of methods. Three approaches were studied in attempts to eliminate crystallization in polysulfide propellants: 1) increase in structural heterogeneity; 2) immobilization of molecular segments by increasing the extent of crosslinking; and 3) plasticization by using commercial plasticizers exhibiting wide temperature range compatibility. Increase in structural heterogeneity through block polymerization of three-component mixtures of low molecular weight liquid polymers was most effective in eliminating crystallization of polysulfide propellants within the time limits of the experiments. Evidence is presented to the effect that crystallization of a binder does not necessarily mean failure or even abnormal operation of a particular rocket motor.

EVIDENCE of the occurrence of binder crystallization in solid composite propellants was reported as early as 1956 by Thiokol Chemical Corp. During a large motor development program, propellant cracking was observed at low temperatures in low stress areas of case-bonded propellant charges, whereas more highly stressed areas were unaffected. The crack pattern was similar in several motors stored at a low temperature, i.e., longitudinal cracks in the propellant charge were evidently initiated in the low stress region of the star tip and progressed radially toward the motor case. Measurements of physical properties of the propellant after various time-temperature programs led to the conclusion that crystallization could be induced in the propellant by prolonged storage at certain low temperatures. The results of programs conducted by Thiokol to eliminate crystallization in polysulfide propellants are reported in this paper.

The formation of crystallites in high polymers is a well-known phenomenon that results from the packing of polymer structural units into a highly ordered geometric pattern. The common properties associated with crystals result from this orderly arrangement of ions, atoms, molecules, or molecular segments into unique patterns typical of the material. In the case of crystalline polymers, the structural units are generally not molecules, but segments of molecules. Portions of a long chain molecule can lie in close association with neighboring molecules or molecular segments to form oriented or crystalline regions, and yet other portions of the molecule can extend beyond in random fashion to yield noncrystalline or amorphous regions.

The effect of crystallization on the properties of a polymer can be qualitatively described as producing: 1) decrease in elongation; 2) increase in tensile strength; 3) increase in modulus; 4) decrease in volume. A quantitative prediction of the effect of crystallization on polymer properties is, in general, not possible because the simple case of a polymer with completely crystalline regions or completely amorphous regions does not occur. In practice, all possible degrees of order exist in a so-called crystalline polymer. Volume fraction of crystallites, crystallite sizes, and arrangements of crystallites with respect to each other also affect polymer properties.

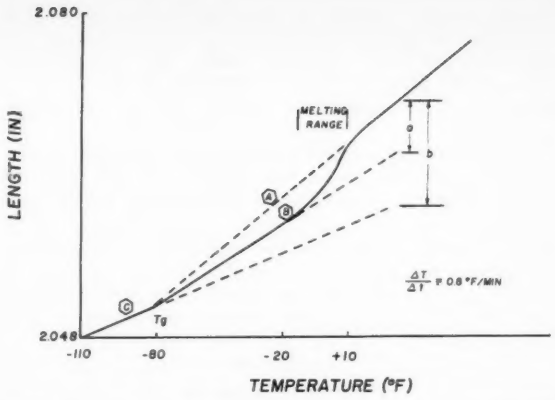

Fig. 1 Typical linear thermal expansion curve for a crystallized propellant

Experimental

A number of methods for determining degree, rate, and temperature of crystallization have been applied in studying this phenomenon in solid propellants.

The melting point and the relative degree and rate of crystallization were measured by storing samples at various temperatures for various periods of time, then cooling the sample rapidly to a temperature below the glass transition temperature and measuring change in volume or length of the sample as the temperature was increased at a low constant rate. The results of a measurement of this type are illustrated in Fig. 1. In that figure, Curve A is a plot of linear expansion vs. temperature in the absence of crystallization. Curve B deviates from Curve A because of crystallization, and Curve C is a plot of linear expansion vs. temperature of the sample below the second-order transition temperature. The ratio of a (the difference in slope between Curve A and Curve B) to b (the difference in slope between Curve A and Curve C) is a measure of the relative degree of crystallization. This ratio will vary with storage temperature and time, thus providing a measure of the rate of crystallization and the temperature at which the maximum rate of crystallization occurs.

Another test that has been used extensively in studying crystallization in propellants is based on changes of physical properties resulting from crystallization. Tensile specimens are stored at various temperatures for various periods of time, and then tensile properties are measured at a constant rate of elongation. If two samples are tested at the same temperature, the one in which crystallization has occurred has markedly less elongation and correspondingly higher modulus. In some cases, relatively long induction periods are required before the detrimental effects of crystallization are noted.

Increase in Structural Heterogeneity

Three approaches were studied in attempts to eliminate crystallization in polysulfide propellants: 1) Block copolymerization of low molecular weight polysulfide polymer mixtures; 2) copolymerization of several species of polysulfide monomers; 3) internal plasticization using copolymerization of materials with bulky groups.

The use of blends of low molecular weight polysulfide polymers having mutual solubilities and equal reactivities

Presented at the ARS Solid Rocket Propellant Conference, Salt Lake City, Utah, Feb. 1–3, 1961; revision received Sept. 15, 1961.

[1] Chief, Advanced Propellant Section.

[2] Chief, Propellant Development Section.

[3] Project Manager.

in place of single polymers as propellant binders produces a heterogeneous polymer system composed of blocks of the individual polymers. In some cases, this heterogeneity increases the time required for crystallization to occur; in other cases, crystallization appears to be completely eliminated.

Butyl formal polysulfide polymer as a propellant binder crystallizes in minutes at temperatures around −20° to −40°F (Fig. 2). However, crystallization did not occur in the region of −50° to −100°F. This is believed to be caused in small test pieces by the rapid cool-out that does not allow time for significant crystallite growth to occur at temperatures of near optimum growth rate. This effect has been observed both with small test specimens and in small motors with thin (0.5-in.) webs. In motors with thick propellant webs, the thermal transients are generally such that crystallization does occur. To provide assurance that crystallization will not occur, tests for crystallization must be extended over considerable periods of time.

A blend of butyl formal polysulfide polymer and butyl ether polysulfide polymer as a propellant binder has not crystallized during 30 days storage at previous low temperatures (Fig. 2). This blend does crystallize if stored for longer periods of time. A blend of three polysulfide polymers (Fig. 2) has shown no crystallization after storage for 6 months at various low temperatures.

Random butyl formal-butyl ether polysulfide copolymers were prepared by copolymerization of a mixture of chlorobutyl formal and chlorobutyl ether. Crystallization studies on these copolymers over a wide range of temperatures for long periods of time showed no evidence of crystallization. No change in propellant elongation occurred during 20 weeks of storage at temperatures of −20°, −40°, and −60°F. Under similar conditions, butyl formal polysulfide polymer,

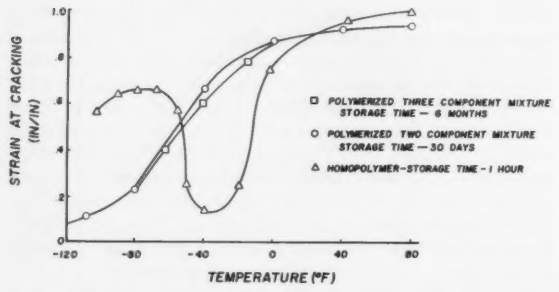
STRAIN AT CRACKING (IN/IN)
TEMPERATURE (°F)
POLYMERIZED THREE COMPONENT MIXTURE STORAGE TIME — 6 MONTHS
POLYMERIZED TWO COMPONENT MIXTURE STORAGE TIME — 30 DAYS
HOMOPOLYMER-STORAGE TIME - 1 HOUR

Fig. 2 Effects of binder heterogeneity on crystallization tendencies of polysulfide propellants

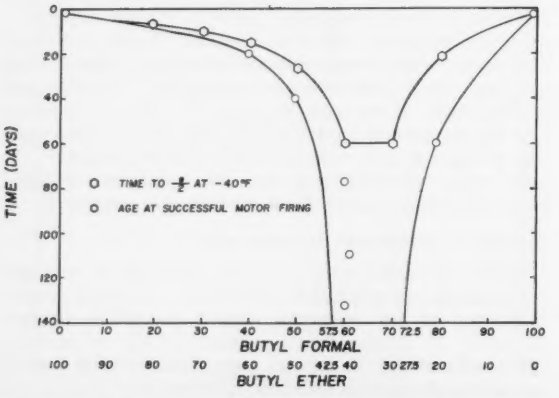

Fig. 3 Phase diagram for polysulfide block copolymers based on propellant tensile properties

butyl ether polysulfide polymer, and block copolymers of these two materials, as propellant binders, were previously shown to crystallize in relatively short periods of time. Although crystallization of polysulfide propellant binders was eliminated by the use of random copolymers, certain copolymer production problems were encountered that made this solution less desirable than the use of block terpolymer systems.

Attachment of bulky groups, such as phenol groups, and of side chains, such as epoxidized castor oil, onto the polymer chain resulted in decreased crystallization tendencies in some cases. This approach, however, did not result in completely eliminating propellant binder crystallization.

Immobilization of Molecular Segments by Increasing Extent of Cross Linking

Effects of cross linking were studied over a range of ½ to 5 mole per cent in several polysulfide polymers. Within the range studied, increased cross linking did not appear to be effective in eliminating crystallization.

Plasticization by Use of Commercial Plasticizers Exhibiting Wide Temperature Range Compatibility

The addition of plasticizers to a polymeric system is a well-known means of lowering the glass transition temperature and, as applied to solid propellants, of lowering the temperature at which motors operate successfully. The addition of a plasticizer to a solid propellant that is known to crystallize should also lower the temperature at which the maximum rate of crystallization occurs. The addition of plasticizers to a number of polysulfide propellants that are known to crystallize has consistently resulted in no change in the propellant binder crystallization temperature. The rate of crystallization is, in fact, actually increased by the addition of many plasticizers, and the temperature of maximum rate of crystallization is essentially unchanged. This increased rate of crystallization is probably the result of increased mobility of segments of polymer molecules, which results in ease of alignment of structural units into a crystalline pattern.

Although crystallization of a propellant binder generally results in large changes in propellant tensile properties, such changes can be tolerated in some rocket motors. Many thin wall flight type motors have been successfully fired over a pressure range of 1000 to 1500 psi at low temperatures after having been subjected to various cyclic and long term, low temperature environmental storage conditions. Yet tensile test data obtained on samples of the same propellant, stored under similar conditions of time and temperature in the laboratory, have exhibited significant changes in tensile properties indicative of crystallization. Fig. 3 illustrates this point. The upper curve represents the time, at −40° F, required for reduction of uniaxial tensile strain to one half of its initial value for propellants made with various proportions of butyl ether and butyl formal block copolymer binders. The circles below this curve represent successful static tests of the corresponding propellants that were stored at −40° F and successfully fired at, or below, this temperature without prior warmup.

Where the performance requirements of the motor permit a design that will operate reliably in spite of binder crystallization, that solution is quite acceptable. When such designs cannot be used, however, the avoidance of crystallization is essential to reliable operation.

Of the approaches studied for eliminating crystallization of polysulfide propellants, an increase in structural heterogeniety was found to be the most effective. Within the time limitations of the experiment, crystallization was eliminated by the use of random polysulfide copolymers and three-component block polymers. From the standpoint of many practical considerations, the use of three-component block polymers has been the most favorable solution to the polysulfide crystallization problem.

Determination of Electron Density and Mobility in Slightly Ionized Cesium

GEORGE J. MULLANEY[1]

NORMAN R. DIBELIUS[2]

General Electric Co.
Schenectady, N. Y.

THERE are a number of experimental techniques available for determining electron concentrations in ionized gases. These include, for example, microwave (1–3),[3] magnetic fields with search coils (4), interferometric (5), and probe techniques (6) other than the one discussed in this note. Since each type of measurement has its limitations, it may be useful to consider the following method for determining electron densities in a partially ionized gas.

The electrical conductivity of a plasma is given by

$$\sigma_0 = \frac{e^2}{m_e} \frac{n_e}{\nu} \qquad [1]$$

where e is the charge of an electron, m_e its mass, n_e electron density, and ν the electron collision frequency.

$\omega_e \tau_e$, where ω_e is the electron cyclotron frequency and τ_e is the time interval between collisions of the electrons with the neutral gas in the conducting plasma, is also expressed by

$$\omega_e \tau_e = \frac{e}{m_e} \frac{B}{\nu} = \mu B \qquad [2]$$

B is the magnetic flux density and μ the electron mobility, since in the presence of a d-c electric field $\mu = e/m_e \, 1/\nu$. From Eqs. 1 and 2

$$n_e = \frac{B}{e} \frac{\sigma_0}{(\omega_e \tau_e)} \qquad [3]$$

The electron density is thus determined by measurements of B, σ_0, and $\omega_e \tau_e$. Conductivity measurements described in this note were made with a cell using concentric electrodes (Fig. 1) and Hall current completely free to flow. The conductivity of the quiescent plasma with a magnetic field parallel to the long axis of the tube is given by

$$\sigma = \frac{\sigma_0}{1 + (\omega_e \tau_e)^2} \qquad [4]$$

and therefore

$$n_e = \frac{B}{e} \frac{\sigma_0}{\sqrt{\sigma_0/\sigma - 1}} \qquad [5]$$

Collision ionization is not taken into account, and electrons are assumed to be the only mobile charge carriers. The total resistance R_0 of a hydromagnetic capacitor, the geometry of which is similar to the cell in our experiment, is derived by Chang and Lundgren (7)

$$R_0 = \frac{\ln(r_2/r_1)\, M}{4\pi\sigma h \tanh M} \qquad [6]$$

In the presence of a uniform magnetic field when an emf is applied across the electrodes, the plasma will rotate about the polar axis at such a rate that the viscous force balances the Lorentz force. If the Hartmann number M is large, the total resistance will increase. Even though the gas is rotating for our experimental conditions, the calculated maximum velocity is less than 100 cm/sec, M is only 0.01, and $M/\tanh M$ approaches unity. A change in plasma conductivity in the presence of a magnetic field should only reflect changes due to $\omega_e \tau_e$.

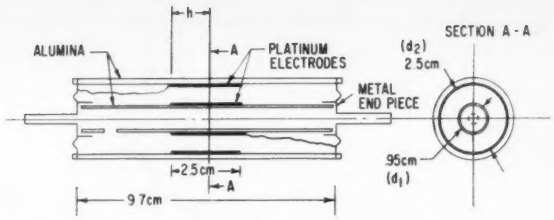

Fig. 1 Concentric electrode conductivity cell

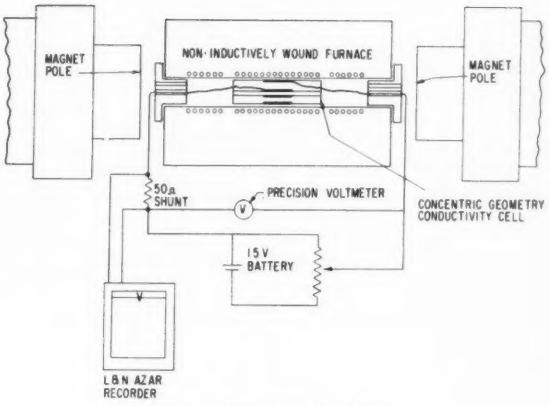

Fig. 2 Experimental setup

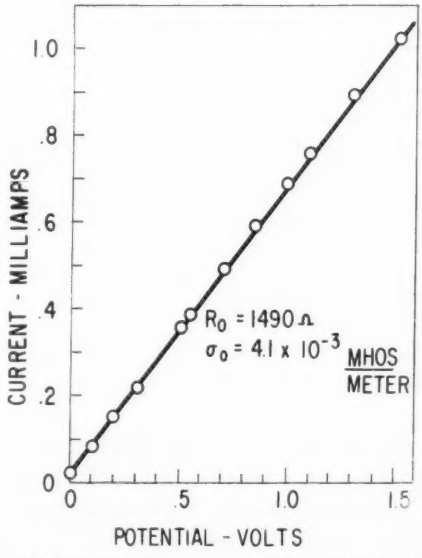

Fig. 3 Typical current-voltage curve. Temperature at electrode 1125° K

Received May 25, 1961.

[1] Mechanical Engineer, Research Lab.

[2] Mechanical Engineer, General Engineering Lab.

[3] Numbers in parentheses indicate References at end of paper.

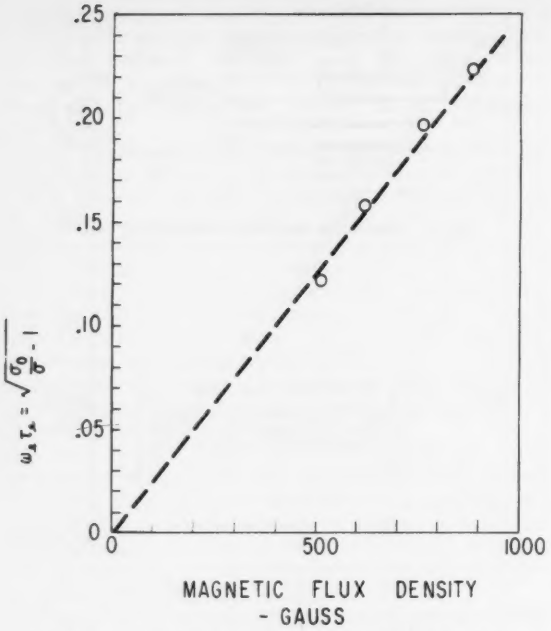

Fig. 4 $\omega_e\tau_e$ **varies linearly with magnetic flux density**

The experimental setup used to demonstrate this method of electron density determination is shown in Fig. 2. After loading the conducting cell with 50 mg of cesium, it was placed inside of the electric furnace and heated to 1125° K. The current-voltage curve (Fig. 3), obtained when a potential was applied across the electrodes, gave a direct measurement of σ_0. Installation of the furnace cell unit between the 4-in. diam pole pieces of an electromagnet provided a magnetic field parallel to the axis of the cell and at right angles to the radial electric field. The magnitude of $\omega_e\tau_e$ was determined by the currents measured across the electrodes with and without the presence of the magnetic field. $\omega_e\tau_e$ vs. magnetic flux density B is shown in Fig. 4. For $\omega_e\tau_e = 0.25$ and $B = 1000$ gauss in Eq. 3

$$n_e = 1.03 \times 10^{10} \quad \text{electrons/cu cm}$$

Electron mobility in atomic cesium at the temperature and pressure of these experiments is determined from the relation

$$\mu = \frac{\omega_e\tau_e}{B} = 25{,}000 \text{ sq cm/volt-sec}$$

The measured conductivity and the calculated electron density make it possible to obtain a collision cross section of electrons with cesium atoms

$$Q = \frac{0.385 \times 10^{-7}}{\sqrt{T}} \frac{n_e}{n} \frac{1}{\sigma_0}$$

$$Q = 3.6 \times 10^{-15} \text{ sq cm}$$

The most important uncertainty in these experiments is the cesium pressure. It was hoped that the pressure would be known from the cesium vapor pressure-temperature curve, since the temperature distribution in the furnace was measured and the temperature profile of the conductivity cell known. The conductivity experiments were performed over a period of several weeks and were repeatable. However, titration measurements after the tests were terminated and the conductivity cell opened showed that only about 8 mg of cesium were present. The cesium pressure corresponding to this amount of cesium was 0.12 atm at 1125°K. This is in fair agreement with the calculated pressure (0.05 atm) using the Saha equation and the electron density determined from the magnetic field experiments but only about 10% of the pressure expected from the original 50 mg added. A large part of the cesium has either been adsorbed by or chemically reacted with the walls at the operating temperatures of these experiments.

The authors are indebted to L. Tonks, L. P. Harris, G. E. Moore, and R. A. Alpher for many valuable discussions.

References

1 Margenau, H., "Conductivity and Dispersion of Ionized Gases at High Frequencies," *Phys. Rev.*, vol. 69, 1946, p. 508.
2 Biondi, M., "Measurement of the Electron Density in Ionized Gases by Microwave Techniques," *Rev. Scien. Instr.*, vol. 22, 1951, p. 500.
3 Persson, K. B., "A Method for Measuring the Conductivity in a High Electron Density Plasma," *Gen. Elec. Research Lab. Rept. 61-RL-2638C*, 1961.
4 Lin, S., Resler, E., and Kantrowitz, A., "Electrical Conductivity of Highly Ionized Argon Produced by Shock Waves," *J. Appl. Phys.*, vol. 26, 1955, p. 95.
5 Alpher, R. A. and White, D. R., "Interferometric Measurement of Electron Concentration in Plasmas," *Phys. Fluids*, vol. 1, 1958, p. 452.
6 Langmuir, I. and Mott-Smith, H., "Studies of Electric Discharge in Gases at Low Pressure," *Gen. Elec. Review*, vol. 27, 1924, p. 449.
7 Chang, C. and Lundgren, T., "Flow of an Incompressible Fluid in a Hydromagnetic Capacitor," *Phys. Fluids*, vol. 2, 1959, p. 627.

Comparison of the Exact and Approximate Methods for Predicting Free Molecule Aerodynamic Coefficients

LEE H. SENTMAN[1]

Lockheed Aircraft Corp., Sunnyvale, Calif.

The aerodynamic coefficients for a body in a free molecule flow were computed using kinetic theory and several approximate theories. A comparison of the results shows that, for molecular speed ratios at satellite altitudes, the approximate theories which do not completely account for the random motion of the impinging molecules are satisfactory for the prediction of C_N and C_M; however, for elongated bodies at small angles of attack, they are inadequate for the prediction of C_A.

Received May 25, 1961.

[1] Graduate Study Engineer-Scientist, Missile and Space Co. Member ARS.

ANALYSIS of the trajectory and the attitude control of near-Earth satellites requires a knowledge of the forces and moments caused by molecular impingement. A detailed analysis of these molecular impingement forces and moments which act on the satellite must be carried out and incorporated into the vehicle design.

The determination of the aerodynamic force acting on a satellite is a free molecule flow problem. A closed form solution for the free molecule aerodynamic coefficients can

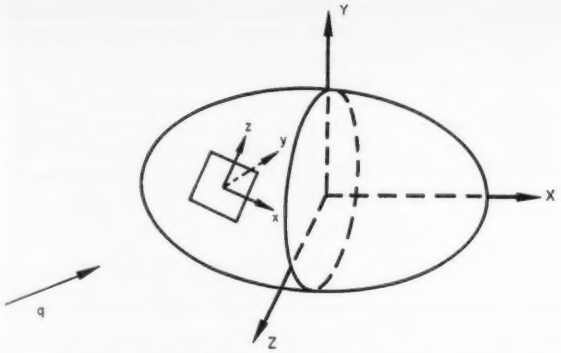

Fig. 1 Definition of the coordinate systems

be obtained only for a flat plate and the cylinder. For this reason, several approximate methods were developed by Gustafson (1)[2] and Schrello (2). The theory of (1) completely neglects the random motion of the incident molecules, that is, it assumes the molecular speed ratio S is infinite. The theory of (2), however, partially takes into account the random motion of the molecules. Unfortunately, both of these solutions break down at small molecular speed ratios and at small angles of attack for all values of molecular speed ratio. An exact analysis is necessary in many cases and is presented in this note.

Theory

Consider an element of a surface that is fixed with respect to a body axis system $X\ Y\ Z$ (Fig. 1). The coordinate system $X\ Y\ Z$ is stationary with the gas molecules moving relative to it with a mass velocity q. Choose a local coordinate system $x\ y\ z$ on the element of surface area with the positive y-axis being the inward directed normal to the surface, the x- and z-axes being tangent to the surface element. Let u, v, w be the velocity components of the molecules in the local x, y, z directions respectively. Then, with the assumption of free molecule flow, the expression for the number of molecules impinging on unit area per unit time N_i is

$$N_i = n_i q \left[\frac{\gamma}{2} (1 + \operatorname{erf} \gamma S) + \frac{1}{2S\sqrt{\pi}} \exp^{(-\gamma^2 S^2)} \right] \quad [1]$$

Assuming diffuse reflection, the expression for the force coefficient in a particular direction on a convex element of area is

$$dc = \frac{1}{A_{ref}} \left\{ (\epsilon k + \gamma l + \eta t) \left[\gamma(1 + \operatorname{erf} \gamma S) + \frac{1}{S\sqrt{\pi}} \exp^{(-\gamma^2 S^2)} \right] + \frac{l}{2S^2} (1 + \operatorname{erf} \gamma S) + \frac{l}{2} \sqrt{\frac{T_r}{T_i}} \left[\frac{\gamma\sqrt{\pi}}{S} (1 + \operatorname{erf} \gamma S) + \frac{1}{S^2} \exp^{(-\gamma^2 S^2)} \right] \right\} dA \quad [2]$$

where ϵ, γ, η are the direction cosines between the mass velocity q and the local x, y, z axes respectively, k, l, t are the direction cosines between direction in which the force is desired and the local x, y, z axes respectively, and S is the molecular speed ratio. To obtain the aerodynamic coefficients of a particular body at an angle of attack, the appropriate expressions for the direction cosines k, l, t, ϵ, γ, η in terms of the particular body geometry are substituted into Eq. 2, which is then integrated over the entire surface area of the body.

The basic assumption of free molecule flow is that the body does not disturb the flow. Thus, it is permissible to resolve a complicated body into simple shapes, compute the coefficients for each section, and then add them together to obtain the total coefficients for the entire vehicle. Since most satellites are composed of flat plates, cylinders, cones, and spherical segments, the expressions for the normal, axial, and pitching moment coefficients were obtained for these shapes.

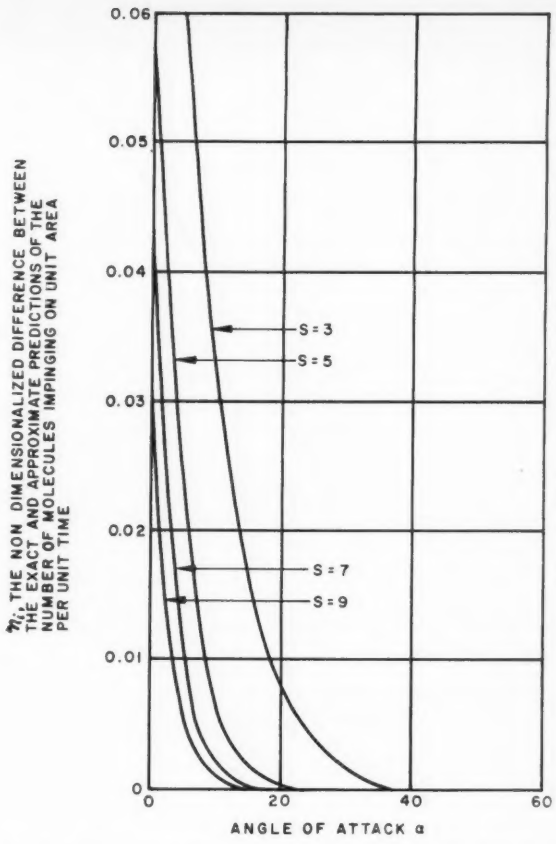

Fig. 2 Difference in the number of molecules impinging on unit area per unit time

In (3), it is shown that the resulting expressions for the aerodynamic coefficients can be written in the following functional form

$$C = g(L,r) \left[I_1(S,\alpha,\beta) + \sqrt{\frac{T_r}{T_i}}\, I_2(S,\alpha,\beta) \right] \quad [3]$$

where $g(L,r)$ is a function of the length dimensions of the shape only, $I_1(S,\alpha,\beta)$ and $I_2(S,\alpha,\beta)$ are functions only of the moleular speed ratio S, angle of attack α, and in the case of the cone and spherical segment a geometric angle β. For the cone, the geometric angle β is the semivertex angle, and for the spherical segment, β is half the included angle of the segment. Since the I's are functions of S, α, and β only,

[2] Numbers in parentheses indicate References at end of paper.

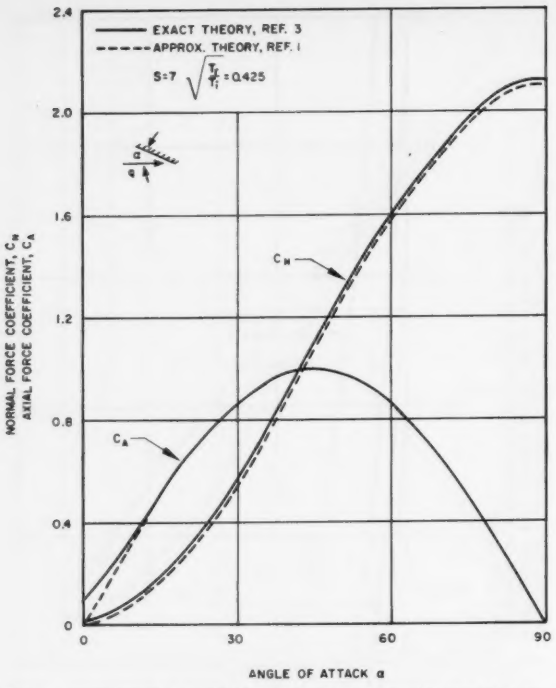

Fig. 3 Aerodynamic coefficients for a flat plate with one side exposed to the flow assuming complete thermal accommodation
A_{ref} = plan form area of the plate

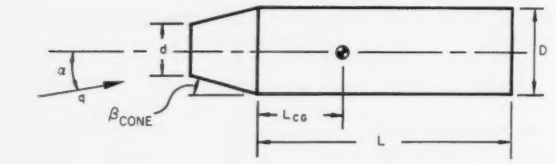

$\beta_{CONE}=15°$ $\frac{d}{D}=0.834$ $\frac{L_{CG}}{D}=1.0$ $\frac{L}{D}=3.0$

Fig. 4 Idealized satellite shape

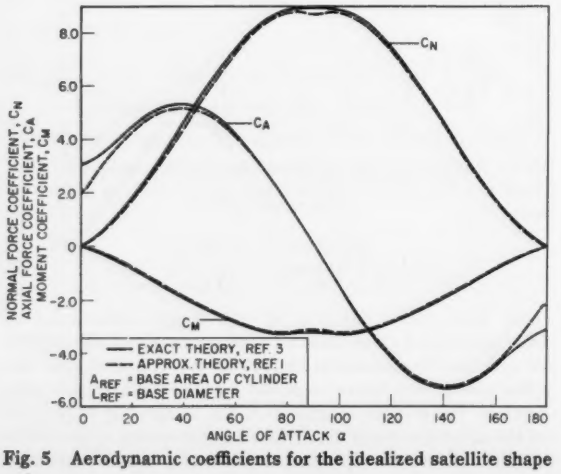

Fig. 5 Aerodynamic coefficients for the idealized satellite shape

they may be considered as general free molecule flow functions that are independent of the length, radius, etc., of the particular shape under consideration. Once they are known, the aerodynamic coefficients for the particular shape can be computed. In general, the I's are complicated integrals that can be evaluated in closed form only for the flat plate and cylinder. For this reason, they were evaluated on the IBM 7090 computer and are presented in tabular form in (3) for the following ranges of the parameters S, α, and β:

$$1 \leq S \leq 13 \qquad 0 \leq \alpha \leq 180°$$

$$5° \leq \beta_{cone} \leq 85° \qquad 5° \leq \beta_{sphere} \leq 180°$$

where β_{cone} and β_{sphere} increase in increments of 5°.

Results

The exact theory includes completely the random motion of the molecules, whereas the approximate theories do not. The fundamental effect of the inclusion of the random motions of the incident molecules is an increase in the number of molecules impinging on unit area of surface per unit time. This is illustrated by considering the difference between N_i as given by Eq. 1 and N_i as given by the theory of (1). According to this theory

$$N_i = n_i q \gamma \qquad [4]$$

Then

$$\mathfrak{N}_i = \frac{N_{iexact} - N_{iapprox}}{n_i q} = \frac{\gamma}{2}(\text{erf } \gamma S - 1) + \frac{1}{2S\sqrt{\pi}} \exp(-\gamma^2 S^2) \qquad [5]$$

In Fig. 2, $\mathfrak{N}_i$ is plotted against the angle of attack α of the surface for several values of the molecular speed ratio S. As seen in Fig. 2, for values of S greater than 5, which are pertinent to a near-Earth satellite, the random motion effect is confined to small surface inclinations. As such, the primary effect would be an increase in the axial force coefficient, with a relatively small effect on the normal force coefficient. This is shown in Fig. 3, where the axial and normal force coefficients for a surface element are plotted as a function of surface inclination. From Fig. 3 it can readily be seen that the approximate theory is quite adequate for the prediction of the normal force at all surface inclination angles but is inadequate for the prediction of the axial force when the surface is closely aligned to the free stream.

It is interesting to apply these results to an idealized satellite shape such as that shown in Fig. 4. The aerodynamic force and moment coefficients are presented in Fig. 5. The computations were performed for a molecular speed ratio of 7 and, assuming complete thermal accomodation, $\sqrt{T_r/T_i} = 0.425$, which are typical of the conditions at satellite altitudes.[3] In computing the coefficients, the forward end of the cone and the aft end of the cylinder were considered as flat plates. The results using the theory of (2) are omitted for clarity of presentation, since they would fall between the exact and approximate results of (1).

As seen in Fig. 5, the primary difference between the approximate and exact methods lies in the prediction of the axial force coefficient at small angles of attack. This difference, as we have seen previously, is due to the effect of the random molecular motions. Since the conical surface elements are inclined 15° to the flow at $\alpha = 0$, and the cylindrical surface elements are parallel to the flow at $\alpha = 0$, the difference between the exact and approximate predictions of C_A is primarily due to molecular impingement on the

[3] The value of the wall temperature that was used to compute $\sqrt{T_r/T_i}$ is an average skin temperature resulting from a thermodynamic analysis of a particular satellite. The value used above is typical of those, encountered in practice, that have been tentatively supported by experimental data.

surface of the cylinder. This conclusion is made on the basis of the results shown in Fig. 2. The magnitude of this difference, which is a linear function of the L/D of the cylindrical part of the body, is presented in Fig. 6. As noted from the analysis of a unit surface element, the approximate theory appears adequate for the prediction of C_N and C_M at all angles of attack, but is inadequate for the prediction of C_A for an elongated body at small angles of attack.

Nomenclature

A = area
C_A = axial force coefficient
C_M = moment coefficient
C_N = normal force coefficient
$\text{erf } x = \frac{2}{\sqrt{\pi}} \int_0^x \exp^{-y^2} dy$
g = function of the length dimensions of a body
I_1, I_2 = general free molecule flow functions
k, l, t = direction cosines between the direction in which the force is desired and the local x, y, z axes respectively
L = length of a body
n_i = number density of incident molecules
N_i = number of molecules impinging on unit area per unit time
$\mathfrak{N}_i = \frac{N_{i\text{exact}} - N_{i\text{approx}}}{n_i q}$
q = mass velocity of the gas
r = radius of a body
S = molecular speed ratio. $S = q/c_m$ where c_m is the most probable speed of the molecules
T = temperature
u, v, w = velocity components of the molecules in the local x, y, z directions, respectively
x, y, z = local axis system
X, Y, Z = body axis system
α = angle of attack

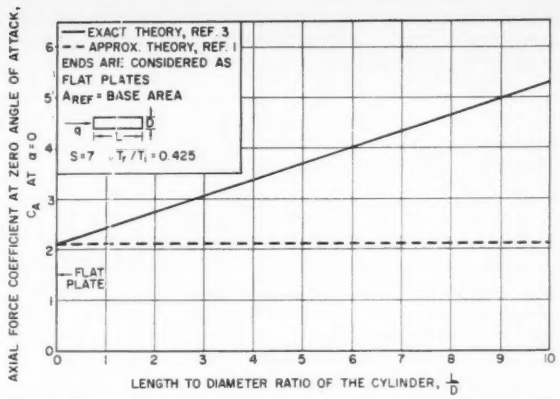
EXACT THEORY, REF. 3
APPROX. THEORY, REF. 1
ENDS ARE CONSIDERED AS FLAT PLATES
AREF = BASE AREA
S=7 Tr/Ti=0.425
FLAT PLATE
AXIAL FORCE COEFFICIENT AT ZERO ANGLE OF ATTACK, CA AT α=0
LENGTH TO DIAMETER RATIO OF THE CYLINDER, L/D

Fig. 6 Variation of the axial force at zero angle of attack with L/D for a cylinder

β = general geometric angle
ϵ, γ, η = direction cosines between the mass velocity q and the local x, y z axes, respectively

Subscripts

i = incident molecules
r = reflected molecules

References

1 Gustafson, W. A., "The Newtonian Diffuse Method for Computing Aerodynamic Forces," *LMSD T.M. 5132*, Lockheed Aircraft Corp. Missile and Space Div., Sunnyvale, Calif., August 28, 1958.

2 Schrello, D. M., "Approximate Free Molecule Aerodynamic Characteristics," ARS JOURNAL, vol. 30, no. 8, August 1960, pp. 765–767.

3 Sentman, L. H., "Free Molecule Flow Theory and Its Application to the Determination of Aerodynamic Forces," *LMSC Tech. Rep. 448614*, Lockheed Missiles and Space Co. Sunnyvale, Calif., October 1961.

Suggested Method for Small Changes in Nodal Longitude for Polar Orbits

PAUL D. ARTHUR[1] and REINHARD LAHDE[2]

Lockheed Aircraft Corp., Burbank, Calif.

IF THE injection point is not in the plane of the desired polar orbit, maneuvers are required. One method is to inject due north or south and then make a cross firing at the next pole crossing to establish the correct orbit. To decrease the magnitude of the required cross fire, this note suggests injection slightly east or west of due north or south. The possible saving is a function of the injection latitude.

Consider establishing a circular orbit in a polar plane not passing through an injection point in the northern hemisphere (Fig. 1). If the correct circular speed V_c exists at the injection point λ_1 N lat, when the transfer orbit intersects the desired polar plane the south latitude λ_2 is given by

$$\tan \lambda_2 = \frac{\alpha}{A_1 \cos \lambda_1} - \tan \lambda_1$$

where A_1 is the azimuth measured from due south of the injection velocity, and α is the longitude angle between the injection point and the desired polar final orbit plane. As small values of α, A_1, and A_2, are of practical interest, these angles will approximate their sines and tangents. The cosines are taken as unity. No approximation is made with λ_1 and λ_2, as their values range from 0 to $\pi/2$. At the intersection

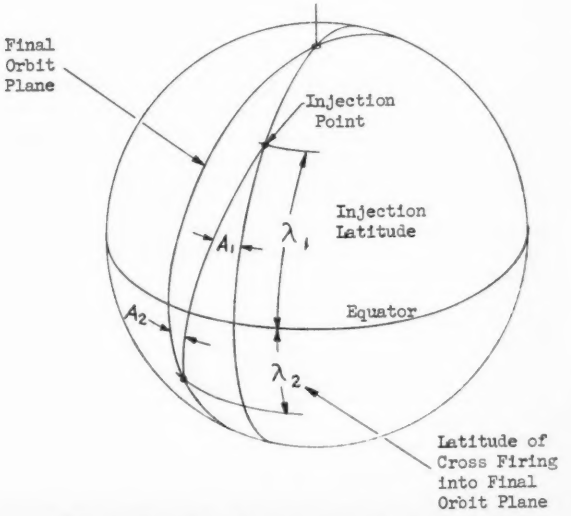

Fig. 1 Transfer orbit to change modal longitude

Received April 10, 1961.

[1] Consultant, Spacecraft Engineering.

[2] Staff Engineer, Spacecraft Engineering.

with the final polar orbit plane, the vehicle azimuth, A_2 from north, is the rotation angle required to transfer into the polar orbit and is given by

$$A_2 = A_1 \frac{\cos \lambda_1}{\cos \lambda_2}$$

The impulse velocity of this cross fire maneuver is

$$\Delta V = V_c A_2$$

As the injection azimuth A_1 is increased from zero due south, the intersection latitude λ_2 moves north from the south pole. The rotation angle A_2 decreases from α, the value if maneuver occurs at the south pole, to a minimum at $\lambda_2 = 90° - \lambda_1$ and then increases for larger A_1.

The minimum rotation angle A_2 and, thus, impulse velocity ΔV values are found to be

$$A_{1_{opt}} = \alpha \sin \lambda_1$$

$$\lambda_{2_{opt}} = \pi/2 - \lambda_1$$

$$A_{2_{opt}} = \alpha \cos \lambda_1$$

$$\Delta V_{opt} = V_c \alpha \cos \lambda_1$$

The fractional saving over the crossfire at the next pole crossing by use of this optimum trajectory is

$$(\alpha - A_{2opt})/\alpha = 1 - \cos \lambda_1$$

This problem is the minimization of the angle between a desired great circle plane and a great circle plane through the injection point.

In general, the minimum angle occurs for intersection 90° away from the injection point. If the injection point is near the desired plane, this 90° spacing becomes the latitude difference, as explicitly derived above.

The derivation gives the azimuth angles in inertial space. For near-polar orbits, the azimuth measured on the surface of the rotating Earth is farther west by

$$\frac{1522 \cos \lambda_1}{57.3\ V_c} \text{ deg}$$

1522 fps being the linear motion of Earth at the Equator.

The derivation and sketch have been presented for a launch from the Northern Hemisphere in a southward direction. The same technique can be applied to the other three combinations. Not considered here is the possiblity of lateral component thrusting during boost.

Class of Minimum Altitude Variation Orbits About an Oblate Earth

L. RIDER[1]

Aerospace Corp., El Segundo, Calif.

The results of Anthony and Fosdick concerning near-circular orbits in an oblate potential field are used to determine the characteristics of orbits with the property that the maximum altitude variation over an oblate Earth during a complete revolution is minimized. The analysis considers all near-circular orbits with arbitrary inclination and apse location. The solution orbits are found to have apses over the Equator and at extreme latitude. Polar orbits experience the greatest altitude variation; equatorial orbits can be constructed which show no altitude variation and hence are truly circular. In general, the altitude variation depends upon average altitude and orbital inclination.

THE DESCRIPTION of near-circular orbits about an oblate Earth with no atmosphere has received considerable attention in recent literature. Such analyses have usually been concerned with the differences between first-order oblateness and the classical inverse-square results, as obtained by Anthony and Fosdick in (1).[2] For certain missions, however, it is of interest to examine the physical characteristics of near-circular orbits referred not to a truly circular orbit, but rather to the Earth's surface. Those near-circular orbits with the property that the maximum altitude excursion during a complete revolution about Earth be minimal are of particular interest for photographic missions.

Expression for Local Satellite Altitude

The second-order solution for radial distance of near-circular orbits of arbitrary inclination i and arbitrary apse location ξ_0 is given in (2) as

$$r = r_0 \left(1 + \eta - \eta \cos(\xi - \xi_0) - \frac{J}{6}\left(\frac{R}{r_0}\right)^2 \{6[1 - \cos(\xi - \xi_0)] + \sin^2 i[-(9 - 6\cos 2\xi_0) + (9 - 5\cos 2\xi_0)\cos(\xi - \xi_0) - (2\sin 2\xi_0)\sin(\xi - \xi_0) - (\cos 2\xi_0)\cos 2(\xi - \xi_0) + (\sin 2\xi_0)\sin 2(\xi - \xi_0)]\}\right) \quad [1]$$

where

- r_0 = initial value of r at an apse
- J = coefficient of the second harmonic in the gravitational potential function for an oblate Earth
- R = equatorial radius
- ξ = approximate central angle travel of the satellite measured from the equatorial position
- i = orbital inclination to the equatorial plane
- η = $(v_0/v_{c_0})^2 - 1$, analog of eccentricity
- v_0 = initial speed at r_0
- v_{c_0} = circular speed for a spherical Earth at $r = r_0$
- ξ_0 = initial value of ξ

A good approximation for the local radius R' of an oblate Earth spheroid with polar flattening of 11.6 n miles is given by

$$R' = R(1 - f^2 \sin^2 i \sin^2 \xi) \quad [2]$$

where f^2 is the ellipticity of the surface ellipse cut out by a plane passing through both the center and the poles.

Received July 5, 1961.

[1] Staff Engineer, Orbital Mechanics Dept. Member ARS.

[2] Numbers in parentheses indicate References at end of paper.

The difference between Eqs. 1 and 2 provides the local satellite altitude h as

$$h = \bar{h} - r_0 \left\{ \left[\left(\frac{v_0}{v_{c_0}} \right)^2 - 1 + \frac{J}{6} \left(\frac{R}{r_0} \right)^2 (-6 + (9 - 5\cos 2\xi_0) \sin^2 i) \right] \cos(\xi - \xi_0) + \left[\frac{f^2}{2} \left(\frac{R}{r_0} \right) - \frac{J}{6} \left(\frac{R}{r_0} \right)^2 \right] \sin^2 i \cos 2\xi - \left[\frac{J}{3} \left(\frac{R}{r_0} \right)^2 \sin^2 i \sin 2\xi_0 \right] \sin(\xi - \xi_0) \right\} \quad [3]$$

where

$$\bar{h} = r_0 \left\{ \left(\frac{v_0}{v_{c_0}} \right)^2 - \left(\frac{R}{r_0} \right) \left[1 + J \left(\frac{R}{r_0} \right) \right] + \left(\frac{R}{r_0} \right) (\sin^2 i) \left[\frac{f^2}{2} - J \left(\frac{R}{r_0} \right) \left(\cos 2\xi_0 - \frac{3}{2} \right) \right] \right\} \quad [4]$$

Eq. 3 can be put in the form

$$h = \bar{h} - A^2 \cos 2\xi - B^2 \sin(\xi - C) \quad [5]$$

where

$$A^2 = r_0 \left[\frac{f^2}{2} \left(\frac{R}{r_0} \right) - \frac{J}{6} \left(\frac{R}{r_0} \right)^2 \right] \sin^2 i \quad [6]$$

$$B^2 = r_0 \left(\left\{ \left(\frac{v_0}{v_{c_0}} \right)^2 - 1 + \frac{J}{6} \left(\frac{R}{r_0} \right)^2 [-6 + (9 - 5\cos 2\xi_0) \sin^2 i] \right\}^2 + \left\{ \frac{J}{3} \left(\frac{R}{r_0} \right)^2 \sin^2 i \sin 2\xi_0 \right\}^2 \right)^{1/2} \quad [7]$$

$$C = \xi_0 + \arctan \left(\frac{- \left\{ \left(\frac{v_0}{v_{c_0}} \right)^2 - 1 + \frac{J}{6} \left(\frac{R}{r_0} \right)^2 [-6 + (9 - 5\cos 2\xi_0) \sin^2 i] \right\}}{\left[\frac{J}{3} \left(\frac{R}{r_0} \right)^2 \sin^2 i \sin 2\xi_0 \right]} \right) \quad [8]$$

Minimization of the Altitude Variation

Since $\bar{h}$ is not a latitude-dependent term, the altitude variation of the orbit about the Earth spheroid will be given by $-g$, where

$$g = A^2 \cos 2\xi + B^2 \sin(\xi - C) \quad [9]$$

and

$$A^2 = A^2(f, R, r_0, J, i)$$

$$B^2 = B^2 \left(\frac{v_0}{v_{c_0}}, R, r_0, J, i, \xi_0 \right)$$

$$C = C \left(\frac{v_0}{v_{c_0}}, R, r_0, J, i, \xi_0 \right)$$

..... [10]

Note that the periodic terms of Eq. 9 are linearly independent; hence, in order to eliminate all variation in altitude, it would be necessary to make each of the amplitude coefficients vanish. Except for the special case $\sin^2 i = 0$ (equatorial orbit), A^2 vanishes only when $r_0 = (J\ R/3f^2)$, which corresponds to a radius interior to the surface of Earth.

For an equatorial orbit A^2 vanishes, and B^2 can be reduced to zero by choosing

$$\left(\frac{v_0}{v_{c_0}} \right)^2 = 1 + J \left(\frac{R}{r_0} \right)^2 \quad [11]$$

The resulting orbit then exhibits no variation in altitude. For a nonzero inclination, however, it is not possible to eliminate A^2, but it will now be demonstrated that the altitude excursion can be minimized by choosing initial conditions which make $B \equiv 0$.

The function g may be considered as a function of three independent variables: ξ, B, and C. (There exists a transformation of coordinates which maps $(\xi_0, v_0/v_{c0})$ into (B, C), since the Jacobian of B and C is not identically zero.) Thus

$$g(\xi, B, C) = A^2 \cos 2\xi + B^2 \sin(\xi - C) \quad [12]$$

and the necessary conditions for an extremum are given by

$$\partial g/\partial \xi = -2A^2 \sin 2\xi + B^2 \cos(\xi - C) = 0 \quad [13]$$

$$\partial g/\partial B = 2B \sin(\xi - C) = 0 \quad [14]$$

$$\partial g/\partial C = -B^2 \cos(\xi - C) = 0 \quad [15]$$

The simultaneous realization of Eqs. 14 and 15 requires $B = 0$, and the satisfaction of Eq. 13 for $i \neq 0$ requires $\xi = 0, \pi/2, \pi$, or $(3/2)\pi$.

Characteristics of the Minimum Altitude Variation Orbit

From Eq. 7, the condition that $B = 0$ requires that $\sin 2\xi_0 = 0$, which corresponds to an initial apse over the Equator ($\xi_0 = 0, \pi$) or at extreme latitude ($\xi_0 = \pi/2, 3\pi/2$). Symmetry considerations indicate it is only necessary to consider the cases $\xi_0 = 0, \pi/2$.

The initial speed requirements, again resulting from Eq. 7, are given by

$$\left(\frac{v_0}{v_{c_0}} \right)^2_{\xi_0 = 0} = 1 + \frac{J}{3} \left(\frac{R}{r_0} \right)^2 (3 - 2\sin^2 i) \quad [16]$$

and

$$\left(\frac{v_0}{v_{c_0}} \right)^2_{\xi_0 = \pi/2} = 1 + \frac{J}{3} \left(\frac{R}{r_0} \right)^2 (3 - 7\sin^2 i) \quad [17]$$

The resulting altitude variation is thereby specialized to

$$h = \bar{h} - r_0 \left[\frac{f^2}{2} \left(\frac{R}{r_0} \right) - \frac{J}{6} \left(\frac{R}{r_0} \right)^2 \right] \sin^2 i \cos 2\xi \quad [18]$$

where

$$\bar{h}_{\xi_0 = 0} = r_0 \left\{ 1 - \left(\frac{R}{r_0} \right) + \left(\frac{R}{r_0} \right) \left[\frac{f^2}{2} - \frac{J}{6} \left(\frac{R}{r_0} \right) \right] \sin^2 i \right\} \quad [19]$$

and

$$\bar{h}_{\xi_0 = \pi/2} = r_0 \left\{ 1 - \left(\frac{R}{r_0} \right) + \left(\frac{R}{r_0} \right) \left[\frac{f^2}{2} + \frac{J}{6} \left(\frac{R}{r_0} \right) \right] \sin^2 i \right\} \quad [20]$$

The radial distances for the two cases resulting from substitution of Eqs. 16 and 17 and the appropriate ξ_0 values in

with the final polar orbit plane, the vehicle azimuth, A_2 from north, is the rotation angle required to transfer into the polar orbit and is given by

$$A_2 = A_1 \frac{\cos \lambda_1}{\cos \lambda_2}$$

The impulse velocity of this cross fire maneuver is

$$\Delta V = V_c A_2$$

As the injection azimuth A_1 is increased from zero due south, the intersection latitude λ_2 moves north from the south pole. The rotation angle A_2 decreases from α, the value if maneuver occurs at the south pole, to a minimum at $\lambda_2 = 90° - \lambda_1$ and then increases for larger A_1.

The minimum rotation angle A_2 and, thus, impulse velocity ΔV values are found to be

$$A_{1_{opt}} = \alpha \sin \lambda_1$$

$$\lambda_{2_{opt}} = \pi/2 - \lambda_1$$

$$A_{2_{opt}} = \alpha \cos \lambda_1$$

$$\Delta V_{opt} = V_c \alpha \cos \lambda_1$$

The fractional saving over the crossfire at the next pole crossing by use of this optimum trajectory is

$$(\alpha - A_{2_{opt}})/\alpha = 1 - \cos \lambda_1$$

This problem is the minimization of the angle between a desired great circle plane and a great circle plane through the injection point.

In general, the minimum angle occurs for intersection 90° away from the injection point. If the injection point is near the desired plane, this 90° spacing becomes the latitude difference, as explicitly derived above.

The derivation gives the azimuth angles in inertial space. For near-polar orbits, the azimuth measured on the surface of the rotating Earth is farther west by

$$\frac{1522 \cos \lambda_1}{57.3\ V_c} \text{ deg}$$

1522 fps being the linear motion of Earth at the Equator.

The derivation and sketch have been presented for a launch from the Northern Hemisphere in a southward direction. The same technique can be applied to the other three combinations. Not considered here is the possiblity of lateral component thrusting during boost.

Class of Minimum Altitude Variation Orbits About an Oblate Earth

L. RIDER[1]

Aerospace Corp., El Segundo, Calif.

The results of Anthony and Fosdick concerning near-circular orbits in an oblate potential field are used to determine the characteristics of orbits with the property that the maximum altitude variation over an oblate Earth during a complete revolution is minimized. The analysis considers all near-circular orbits with arbitrary inclination and apse location. The solution orbits are found to have apses over the Equator and at extreme latitude. Polar orbits experience the greatest altitude variation; equatorial orbits can be constructed which show no altitude variation and hence are truly circular. In general, the altitude variation depends upon average altitude and orbital inclination.

THE DESCRIPTION of near-circular orbits about an oblate Earth with no atmosphere has received considerable attention in recent literature. Such analyses have usually been concerned with the differences between first-order oblateness and the classical inverse-square results, as obtained by Anthony and Fosdick in (1).[2] For certain missions, however, it is of interest to examine the physical characteristics of near-circular orbits referred not to a truly circular orbit, but rather to the Earth's surface. Those near-circular orbits with the property that the maximum altitude excursion during a complete revolution about Earth be minimal are of particular interest for photographic missions.

Expression for Local Satellite Altitude

The second-order solution for radial distance of near-circular orbits of arbitrary inclination i and arbitrary apse location ξ_0 is given in (2) as

$$r = r_0 \left(1 + \eta - \eta \cos (\xi - \xi_0) - \frac{J}{6}\left(\frac{R}{r_0}\right)^2 \{6[1 - \cos (\xi - \xi_0)] + \sin^2 i[-(9 - 6 \cos 2\xi_0) + (9 - 5 \cos 2\xi_0) \cos (\xi - \xi_0) - (2 \sin 2\xi_0) \sin (\xi - \xi_0) - (\cos 2\xi_0) \cos 2(\xi - \xi_0) + (\sin 2\xi_0) \sin 2(\xi - \xi_0)]\}\right) \quad [1]$$

where

- r_0 = initial value of r at an apse
- J = coefficient of the second harmonic in the gravitational potential function for an oblate Earth
- R = equatorial radius
- ξ = approximate central angle travel of the satellite measured from the equatorial position
- i = orbital inclination to the equatorial plane
- η = $(v_0/v_{c_0})^2 - 1$, analog of eccentricity
- v_0 = initial speed at r_0
- v_{c_0} = circular speed for a spherical Earth at $r = r_0$
- ξ_0 = initial value of ξ

A good approximation for the local radius R' of an oblate Earth spheroid with polar flattening of 11.6 n miles is given by

$$R' = R(1 - f^2 \sin^2 i \sin^2 \xi) \quad [2]$$

where f^2 is the ellipticity of the surface ellipse cut out by a plane passing through both the center and the poles.

Received July 5, 1961.

[1] Staff Engineer, Orbital Mechanics Dept. Member ARS.

[2] Numbers in parentheses indicate References at end of paper.

The difference between Eqs. 1 and 2 provides the local satellite altitude h as

$$h = \bar{h} - r_0 \left\{ \left[\left(\frac{v_0}{v_{c_0}} \right)^2 - 1 + \frac{J}{6} \left(\frac{R}{r_0} \right)^2 (-6 + (9 - 5\cos 2\xi_0) \sin^2 i) \right] \cos(\xi - \xi_0) + \left[\frac{f^2}{2} \left(\frac{R}{r_0} \right) - \frac{J}{6} \left(\frac{R}{r_0} \right)^2 \right] \sin^2 i \cos 2\xi - \left[\frac{J}{3} \left(\frac{R}{r_0} \right)^2 \sin^2 i \sin 2\xi_0 \right] \sin(\xi - \xi_0) \right\} \quad [3]$$

where

$$\bar{h} = r_0 \left\{ \left(\frac{v_0}{v_{c_0}} \right)^2 - \left(\frac{R}{r_0} \right) \left[1 + J \left(\frac{R}{r_0} \right) \right] + \left(\frac{R}{r_0} \right) (\sin^2 i) \left[\frac{f^2}{2} - J \left(\frac{R}{r_0} \right) \left(\cos 2\xi_0 - \frac{3}{2} \right) \right] \right\} \quad [4]$$

Eq. 3 can be put in the form

$$h = \bar{h} - A^2 \cos 2\xi - B^2 \sin(\xi - C) \quad [5]$$

where

$$A^2 = r_0 \left[\frac{f^2}{2} \left(\frac{R}{r_0} \right) - \frac{J}{6} \left(\frac{R}{r_0} \right)^2 \right] \sin^2 i \quad [6]$$

$$B^2 = r_0 \left(\left\{ \left(\frac{v_0}{v_{c_0}} \right)^2 - 1 + \frac{J}{6} \left(\frac{R}{r_0} \right)^2 [-6 + (9 - 5\cos 2\xi_0) \sin^2 i] \right\}^2 + \left\{ \frac{J}{3} \left(\frac{R}{r_0} \right)^2 \sin^2 i \sin 2\xi_0 \right\}^2 \right)^{1/2} \quad [7]$$

$$C = \xi_0 + \arctan \left(\frac{- \left\{ \left(\frac{v_0}{v_{c_0}} \right)^2 - 1 + \frac{J}{6} \left(\frac{R}{r_0} \right)^2 [-6 + (9 - 5\cos 2\xi_0) \sin^2 i] \right\}}{\left[\frac{J}{3} \left(\frac{R}{r_0} \right)^2 \sin^2 i \sin 2\xi_0 \right]} \right) \quad [8]$$

Minimization of the Altitude Variation

Since $\bar{h}$ is not a latitude-dependent term, the altitude variation of the orbit about the Earth spheroid will be given by $-g$, where

$$g = A^2 \cos 2\xi + B^2 \sin(\xi - C) \quad [9]$$

and

$$A^2 = A^2(f, R, r_0, J, i)$$

$$B^2 = B^2 \left(\frac{v_0}{v_{c_0}}, R, r_0, J, i, \xi_0 \right)$$

$$C = C \left(\frac{v_0}{v_{c_0}}, R, r_0, J, i, \xi_0 \right) \quad [10]$$

Note that the periodic terms of Eq. 9 are linearly independent; hence, in order to eliminate all variation in altitude, it would be necessary to make each of the amplitude coefficients vanish. Except for the special case $\sin^2 i = 0$ (equatorial orbit), A^2 vanishes only when $r_0 = (J\ R/3f^2)$, which corresponds to a radius interior to the surface of Earth.

For an equatorial orbit A^2 vanishes, and B^2 can be reduced to zero by choosing

$$\left(\frac{v_0}{v_{c_0}} \right)^2 = 1 + J \left(\frac{R}{r_0} \right)^2 \quad [11]$$

The resulting orbit then exhibits no variation in altitude. For a nonzero inclination, however, it is not possible to eliminate A^2, but it will now be demonstrated that the altitude excursion can be minimized by choosing initial conditions which make $B \equiv 0$.

The function g may be considered as a function of three independent variables: ξ, B, and C. (There exists a transformation of coordinates which maps $(\xi_0, v_0/v_{c0})$ into (B, C), since the Jacobian of B and C is not identically zero.) Thus

$$g(\xi, B, C) = A^2 \cos 2\xi + B^2 \sin(\xi - C) \quad [12]$$

and the necessary conditions for an extremum are given by

$$\partial g/\partial \xi = -2A^2 \sin 2\xi + B^2 \cos(\xi - C) = 0 \quad [13]$$

$$\partial g/\partial B = 2B \sin(\xi - C) = 0 \quad [14]$$

$$\partial g/\partial C = -B^2 \cos(\xi - C) = 0 \quad [15]$$

The simultaneous realization of Eqs. 14 and 15 requires $B = 0$, and the satisfaction of Eq. 13 for $i \neq 0$ requires $\xi = 0, \pi/2, \pi$, or $(3/2)\pi$.

Characteristics of the Minimum Altitude Variation Orbit

From Eq. 7, the condition that $B = 0$ requires that $\sin 2\xi_0 = 0$, which corresponds to an initial apse over the Equator ($\xi_0 = 0, \pi$) or at extreme latitude ($\xi_0 = \pi/2, 3\pi/2$). Symmetry considerations indicate it is only necessary to consider the cases $\xi_0 = 0, \pi/2$.

The initial speed requirements, again resulting from Eq. 7, are given by

$$\left(\frac{v_0}{v_{c_0}} \right)^2_{\xi_0 = 0} = 1 + \frac{J}{3} \left(\frac{R}{r_0} \right)^2 (3 - 2\sin^2 i) \quad [16]$$

and

$$\left(\frac{v_0}{v_{c_0}} \right)^2_{\xi_0 = \pi/2} = 1 + \frac{J}{3} \left(\frac{R}{r_0} \right)^2 (3 - 7\sin^2 i) \quad [17]$$

The resulting altitude variation is thereby specialized to

$$h = \bar{h} - r_0 \left[\frac{f^2}{2} \left(\frac{R}{r_0} \right) - \frac{J}{6} \left(\frac{R}{r_0} \right)^2 \right] \sin^2 i \cos 2\xi \quad [18]$$

where

$$\bar{h}_{\xi_0 = 0} = r_0 \left\{ 1 - \left(\frac{R}{r_0} \right) + \left(\frac{R}{r_0} \right) \left[\frac{f^2}{2} - \frac{J}{6} \left(\frac{R}{r_0} \right) \right] \sin^2 i \right\} \quad [19]$$

and

$$\bar{h}_{\xi_0 = \pi/2} = r_0 \left\{ 1 - \left(\frac{R}{r_0} \right) + \left(\frac{R}{r_0} \right) \left[\frac{f^2}{2} + \frac{J}{6} \left(\frac{R}{r_0} \right) \right] \sin^2 i \right\} \quad [20]$$

The radial distances for the two cases resulting from substitution of Eqs. 16 and 17 and the appropriate ξ_0 values in

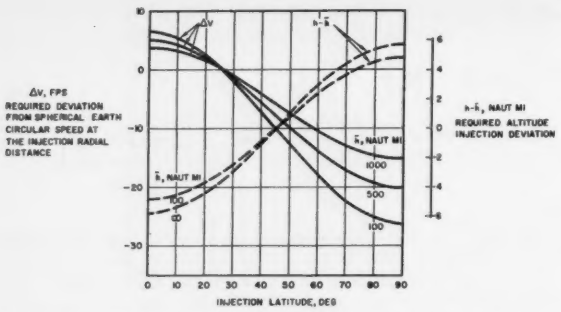

Fig. 1 Injection speed and altitude for minimum altitude variation polar orbits about an oblate Earth

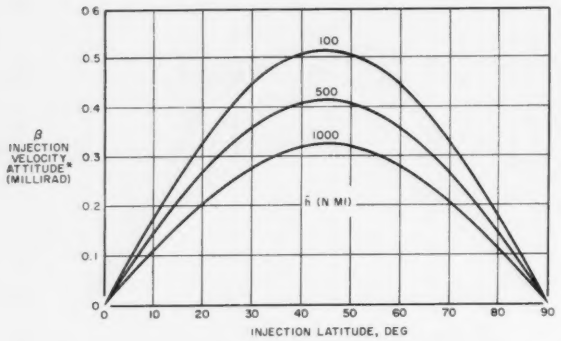

* FOR INJECTION LATITUDES IN THE NORTHERN HEMISPHERE: INJECTION VELOCITY SHOULD HAVE A DOWNWARD COMPONENT (β NEG) FOR NORTHERLY LAUNCHES, AND AN UPWARD COMPONENT (β POS) FOR SOUTHERLY LAUNCHES.

Fig. 2 Injection speed attitude from the local horizontal for minimum altitude polar orbits about an oblate Earth

Eq. 1 are given by

$$r_{\xi_0=0} = r_0\left[1 - \frac{J}{6}\left(\frac{R}{r_0}\right)^2 (\sin^2 i)(1 - \cos 2\xi)\right] \quad [21]$$

and

$$r_{\xi_0=\pi/2} = r_0\left[1 + \frac{J}{6}\left(\frac{R}{r_0}\right)^2 (\sin^2 i)(1 + \cos 2\xi)\right] \quad [22]$$

from which it can be determined that the difference between the two orbits is of size only, the orbit with the initial apse at $\xi_0 = \pi/2$ being at an altitude $r_0(J/3)(R/r_0)^2 \sin^2 i$ higher than the orbit with apse at $\xi_0 = 0$. The difference in radial distance is exactly equal to the perturbation in radial distance due to the oblate Earth potential at a point of extreme latitude for an orbit with initial apse over the Equator. Hence, the duality of the solution orbit is essentially artificial, brought about by the method of initializing the problem. Henceforth, with no loss in generality, consider only $\xi_0 = 0$.

From the general equation for speed in a near-circular orbit as taken from (2), the speed variation of the minimum altitude excursion orbit is

$$v = v_0\left[1 - \frac{J}{3}\left(\frac{R}{r_0}\right)^2 (\sin^2 i)(1 - \cos 2\xi)\right] \quad [23]$$

It should be noted that the expression for local altitude, Eq. 18, contains the term $\bar{h}$, which is not a function of time but about which equal time-dependent periodic excursions occur. It thus provides a natural definition for *average* orbital altitude.

An interesting characteristic of this orbit has been verified by numerical integration on the IBM 7090. The lines of apsides do not exhibit the characteristic secular rotation in the orbital plane; thus if the orbit is originated with an apse over the Equator, this orientation will remain constant. An analytic proof of this characteristic, for solutions through first order in J, has been obtained by Hall (3). These orbits then correspond to the class of nonprecessing orbits discussed by MacMillan in (4).

Injection Conditions as a Function of Latitude

Once *average* orbital altitude and orbital inclination are specified, it becomes possible to solve Eq. 19 for r_0. Thus

$$r_0 = \frac{1}{2}\left(\bar{h} + R\left(1 - \frac{f^2}{2}\sin^2 i\right) + \left\{\left[\bar{h} + R\left(1 - \frac{f^2}{2}\sin^2 i\right)\right]^2 + \frac{2}{3}J R^2 \sin^2 i\right\}^{1/2}\right) \quad [24]$$

This value of r_o, when substituted in Eq. 18, will define the required injection altitude as a function of latitude.

The required inertial injection speed as a function of latitude can be obtained from the triple product given by

$$\frac{v}{v_{c_r}} = \left(\frac{v_0}{v_{c_0}}\right)\cdot\left(\frac{v_{c_0}}{v_{c_r}}\right)\cdot\left(\frac{v}{v_0}\right) \quad [25]$$

where the first product term is obtained from Eq. 16, the second from Eq. 21, and the relation $v_{c0}/v_{c_r} = (r/r_0)^{1/2}$ and the third from Eq. 23. Defining Δv by relation

$$\frac{v}{v_{c_r}} = 1 + \frac{\Delta v}{v_{c_r}} \quad [26]$$

and carrying out the indicated multiplication of Eq. 25 results in

$$\frac{\Delta v}{v_{c_r}} \approx \frac{J}{12}\left(\frac{R}{r_0}\right)^2 [6 - (9 - 5\cos 2\xi)\sin^2 i] \quad [27]$$

The quantities Δv and $(h - \bar{h})$ are shown in Fig. 1 for several values of $\bar{h}$ for a polar orbit.

The radial speed at injection can be obtained from Eq. 21 by time differentiation. Thus

$$\dot{r} = -(r_0)\frac{J}{3}\left(\frac{R}{r_0}\right)^2 \sin^2 i \sin 2\xi\dot{\xi} \quad [28]$$

Since

$$\dot{\xi} \approx (v_{c_r}/r_.)$$

then

$$\dot{r} \approx -v_{c_r}\frac{J}{3}\left(\frac{R}{r_0}\right)^2 \sin^2 i \sin 2\xi$$

and the vertical injection speed is given by

$$\frac{\Delta v_v}{v_{c_r}} \approx -\frac{J}{3}\left(\frac{R}{r_0}\right)^2 \sin^2 i \sin 2\xi \quad [29]$$

It should be noted that an apse will occur above both the Equator and the positions of extreme latitude. The injection velocity attitude $\beta = \Delta v_v/v_{c_r}$ is shown in Fig. 2 for a polar orbit.

References

1 Anthony, M. L. and Fosdick, G. E., "Planar Motions About an Oblate Planet," presented at the ARS Semi-Annual Meeting, Los Angeles, Calif., 1960 (*ARS preprint no. 1231-60*).

2 Anthony, M. L. and Fosdick, G. E., "Satellite Motions About an Oblate Planet," IAS National Summer Meeting, June 1960 (*IAS paper no. 60-57*).

3 Hall, N. S., personal communication.

4 Moulton, F. R., *Periodic Orbits*, Carnegie Inst. of Washington, Washington, D. C., 1920.

Measurement of Small Discharge Rate of an Intermittent Exhaust Jet[1]

WILLIAM J. GUMAN[2]

Plasma Propulsion Laboratory, Republic Aviation Corp.
Farmingdale, N. Y.

AT REPUBLIC pulsed plasma accelerators are used to eject gaseous propellant at rates varying from about 10^{-8} to about 10^{-5} lb per pulse. The ejected fluid is extracted from a high pressure reservoir (several hundred psi) and must be remotely monitored and measured while the device is delivering thrust in a vacuum environment. The technique that was developed for determining these extremely small mass flow rates is based on a differential pressure measurement. When gaseous propellant is extracted from the high pressure reservoir, the reservoir pressure drops slightly. This change in pressure was measured relative to the pressure that originally existed in the reservoir by permitting gas to be trapped at the original pressure in a reference plenum. The difference in the pressure existing between the reference plenum and the plenum from which the gas is extracted was measured accurately with a differential pressure transducer.

Schematically, Fig. 1 illustrates the components used to carry out the mass transfer measurement. Reservoir A is the reservoir from which gaseous propellant is extracted. Line B is a lead connecting the sensing equipment to the main reservoir, thus facilitating remote location of the sensing elements. When reservoir A is pressurized, valve C is left open so that the differential pressure transducer E is not subjected to a pressure differential. Valve C is closed after the filling process. The extraction of a minute quantity of gas lowers the reservoir pressure and is detected by the differential pressure transducer, which measures pressure changes relative to the pressure in reference plenum D. Valve C can always be opened to return the entire system to a new zero level.

The amount of gas extracted ΔW was evaluated from the differential pressure reading Δp and a reading of the initial temperature T of the gas in reservoir A. It was necessary to know the volume V of reservoir A and the leads to valve C.

Since an extremely small quantity of gas is extracted from the reservoir (about 1 ppm), the fluid in the reservoir changes its state essentially isothermally. Thus from the equation of state one has (in appropriate units)

$$\Delta W = V\Delta p/RT$$

It is of interest to note that if the fluid were extracted so that the state of gas in the reservoir varied nearly isentropicly, then the relation to be used would be very nearly

$$\Delta W \simeq V\Delta p/\gamma RT$$

where γ is the ratio of specific heats. Experiments (1)[3] have shown that when gas is extracted from a storage tank at a moderate rate, the state of gas in the reservoir changes in a manner given between the values predicted by the isothermal and the isentropic case. For the very small extraction rates, such as are described herein, it is believed that the isothermal case more nearly describes the process inside the reservoir. From a logarithmic differentiation, it can be seen that the percentage error in computing the mass extracted will depend on the percentage error in the differential pressure reading, the percentage error in establishing the volume, and the percentage error in the temperature reading. It is believed that the error in the mass determination using the isothermal relation is less than 5%.

This technique has been used to measure extraction rates as low as 8×10^{-8} lb per pulse of propellant from a 200-psi container. One part per million has been accurately monitored with a straingage type pressure transducer. A differential micromanometer capable of measuring differential gas pressure down to ± 0.00016 in. of water in a 1000-psi line has recently been reported in the literature. Such a transducer can provide measurements better than 1 ppm. The actual equipment used in one of the tests is shown in Fig. 2. Since electrically operated solenoid valves tend to change the temperature and thus the pressure of the trapped gas in the reference plenum, it has been found necessary to use a leak proof bellow type hand valve as the shutoff valve C. To preclude thermal effects, the entire sensing unit except the shutoff valve is located in the vacuum thrust chamber.

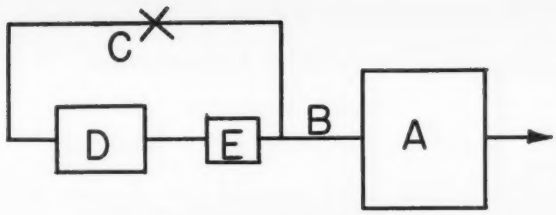

Fig. 1 Schematic of components

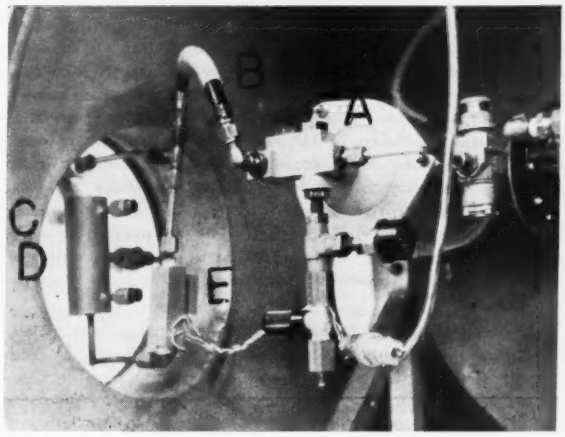

Fig. 2 Actual sensing system

Reference

1 Granet, I., "Summary Report on Tests to Determine the Expansion Process of Air in High Pressure Storage Tanks," *RN-39*, Foster Wheeler Corp., Research Dept., Aug. 6, 1951.

Received July 14, 1961.
[1] This work was sponsored in part by the office of Naval Research under Contract Nonr-2851(00).
[2] Specialist Scientific Research Engineer.
[3] Numbers in parenthesis indicate Reference at end of paper.

Effect of Rapid Pressure Decay on Solid Propellant Combustion

CARL C. CIEPLUCH[1]

NASA Lewis Research Center, Cleveland, Ohio

Rapid pressure decay transients were imposed on a burning, composite propellant charge by suddenly opening a chamber vent. Measurements of light emission and chamber pressure with high frequency response instrumentation indicated that pressure decay rates too low to permanently extinguish combustion could extinguish it momentarily, whereupon combustion was resumed at a steady reduced pressure. It was found that there is a minimum chamber pressure decay rate required to extinguish combustion permanently. For an aluminized composite propellant this rate was 74,000 psi/sec at an initial chamber pressure of 540 psia. The minimum rate of chamber pressure decay increased linearly as the initial chamber pressure increased. The combustion process was found to be quite sensitive to pressure decrease since it could be extinguished momentarily by pressure decay rates nearly an order of magnitude lower than required to extinguish combustion permanently.

THE ABILITY to stop and restart solid propellant rocket motors would significantly increase their flexibility and usefulness for space applications. It appears feasible that an ignition system, such as one that relies on the reaction between a hypergolic fluid and the propellant for ignition (1),[2] could be developed for the multiple ignition requirement of a restartable motor. One technique to stop the motor is to suddenly decrease the chamber pressure in order to extinguish combustion. This method has been used successfully in conjunction with ballistic missile thrust termination and as a research tool in the laboratory. With the advent of new propellants with higher impulse, however, the use of a rapid decrease in pressure to extinguish combustion completely may become more difficult.

The purpose of this investigation was to study the effect of rapid pressure decay on solid propellant combustion with a view toward a more basic understanding of the phenomenon. This article presents some of the results that have been obtained to date during investigation. Several studies along this line have been reported. In (2), observations were made of a burning strand of propellant during the sudden expansion developed by puncturing a diaphragm in the chamber. In (3), photographic studies were made of a burning strand of propellant subjected to rapid pressure decrease in a specially developed bomb. In the present investigation a propellant size and chamber combination were chosen such that the combustion environment more closely approximated that which is obtained in an actual motor, and at the same time was not so large as to lose all the simplicity and flexibility of the strand type of test. Measurements were made of combustion luminosity variation during the pressure drop and of the chamber pressure decay rate required to extinguish combustion.

Presented at the National IAS-ARS Joint Meeting, Los Angeles, Calif., June 13–16, 1961.

[1] Aerospace Research Scientist.

[2] Numbers in parentheses indicate References at end of paper.

Apparatus and Procedure

An isometric sketch of the propellant charge positioned in the chamber is shown in Fig. 1. The propellant slab was 3-in. wide by 5-in. long by 1-in. thick. The propellant was ignited by a standard type pyrotechnic ignitor. Combustion was confined to the upper flat surface, and the chamber vent was actuated after about $^3/_8$ in. of propellant was consumed. The propellant composition was

	Per cent by weight
Epoxy crosslinked copolymer of butadiene and a carboxylic monomer	18.8
Magnesium oxide	0.2
Ammonium perchlorate	72.0
Aluminum	9.0

The propellant had the following burning rate equation:

$$\text{Burning rate} = 0.0324\ P^{0.337}\ \text{ips}$$

where P is the chamber pressure in psia.

Rapid chamber pressure decrease was obtained by suddenly opening a chamber vent hole. The vent hole cover was attached to a pivot arm (Fig. 1), which was suddenly released by an explosive bolt. The electrical signal for the explosive bolt to fire was obtained from a burn out wire which was imbedded in the propellant during casting. The chamber pressure decay rate could be varied by two different methods. One method consisted of varying the size of vent that was suddenly opened. The second method consisted of using a simple dashpot, connected to the pivot arm, which restricted the rate at which the pivot arm, and consequently the vent cover, opened. Using this technique and a large vent hole, the rate of chamber pressure decay was an inverse function of the dashpot resistance.

A quartz window located on the side of the chamber was used to view combustion across the burning surface. A small amount of nitrogen bleed was used to reduce the clouding of the window. A 0.025 to 0.030 in. molybdenum plate with a properly sized drilled hole to maintain the desired chamber pressure was used as the nozzle. The thin nozzle plate limited aluminum oxide buildup in the nozzle. The chamber was mounted by means of the mounting flange onto an altitude exhaust system equipped with an air ejector. All runs were made at an ambient pressure of 3.5 mm of mercury.

Chamber pressure was measured with a high frequency response pressure transducer which was water-cooled. Com-

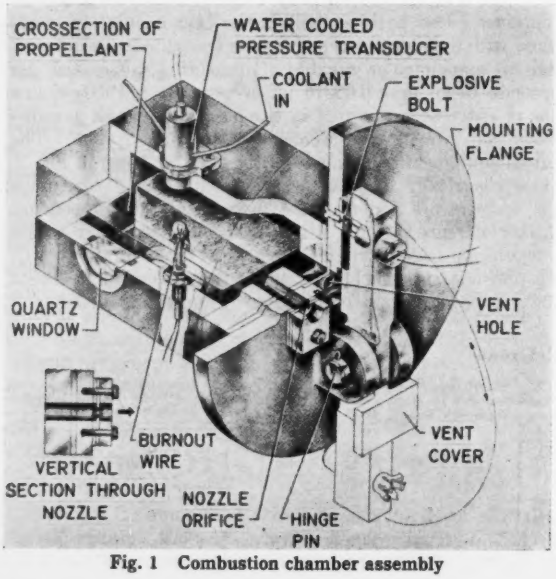

Fig. 1 Combustion chamber assembly

bustion luminosity was measured by viewing through the quartz window with an RCA no. 5582 phototube. The tube had an S-4 response which was sensitive primarily to the visible light region with a peak sensitivity at 4000 Å. The phototube viewed a region of the flame, extending from the propellant surface up to $^1/_2$ in. above it, through a $^7/_8$-in. diam tube. The electrical output of these instruments was amplified as required and recorded on a direct recording oscillograph. Paper speed was 80 ips.

Results and Discussion

Effect of rapid pressure decay on combustion luminosity

Typical oscillograph records of combustion luminosity and chamber pressure during pressure decay transients obtained by suddenly opening the chamber vent are shown in Fig. 2. The solid line records represent a case in which the propellant continued burning after the pressure drop. For this case the chamber pressure leveled out at about 35 psia, dropping from a steady pressure of 547 psia. It is interesting to note that for this case the luminosity record decreased sharply to a minimum, which was only 7% of its original value, 0.0055 sec after the pressure decrease was initiated. This minimum luminosity point occurred at a chamber pressure of 145 psia, which was considerably above the final chamber pressure. From the minimum point the luminosity then recovered to almost its original value in 0.035 sec. This sharp drop in luminosity to almost zero during the early stages of the pressure decrease indicated that the flame was for the most part extinguished or quenched momentarily. However, the strength of the pressure drop, or in other words, the pressure decay rate, was not sufficient to prevent the flame from reestablishing at a lower pressure.

The dashed line represents the results obtained from a higher pressure decay rate (increased vent size). In this case the combustion was extinguished, and chamber pressure dropped to ambient, which was 3.5 mm of mercury, in about 0.04 sec. The luminosity record also dropped very sharply for this case. However, after an initial attempt to recover, the luminosity subsequently dropped to zero, and combustion was extinguished.

The effect of chamber pressure decay rate on the minimum luminosity during the pressure drop and luminosity recovery after the pressure drop are shown in Fig. 3. Chamber pressure decay rate was varied by varying the size of the vent. Since pressure did not vary linearly with time but

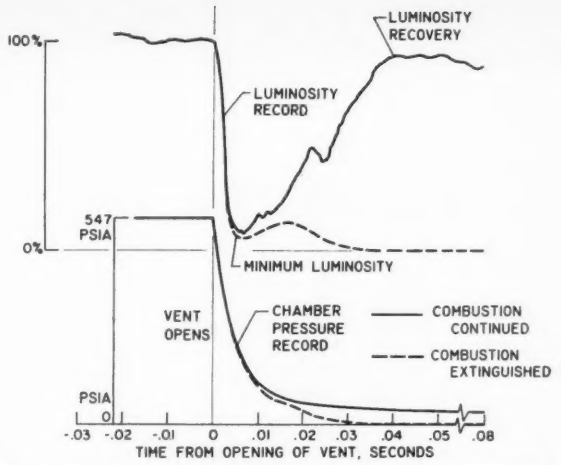

Fig. 2 Typical luminosity and chamber pressure transient records during rapid pressure decay

was an exponential function, a representative or effective value was calculated for the pressure decay rate. It was defined as $\Delta P/\Delta t$, where ΔP was a 50% reduction in chamber pressure and Δt the corresponding time for this pressure change. At low pressure decay rates the luminosity recovered to approximately 100% of the original value, indicating combustion continued after the pressure drop. Above a pressure decay rate of about 74,000 psi/sec luminosity did not recover completely, and combustion ceased. This critical pressure decay rate for combustion extinction is probably unique for the propellant composition used in this investigation. It can be seen from the minimum flame luminosity curve in Fig. 3 that the gas phase flame is sensitive to a wide range of pressure decay rates. The flame apparently was extinguished or quenched momentarily for pressure decay rates as low as 10,000 to 15,000 psi/sec, which is almost an order of magnitude lower than that required to extinguish the flame completely. The relative sensitivity of the flame to rapid pressure decrease may be a contributing factor to

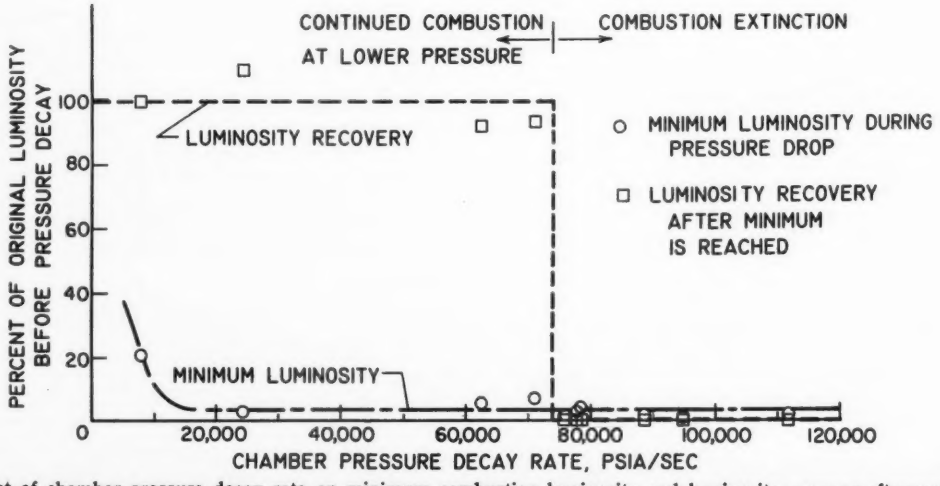

Fig. 3 Effect of chamber pressure decay rate on minimum combustion luminosity and luminosity recovery after pressure decay. Nominal chamber pressure, 540 psia

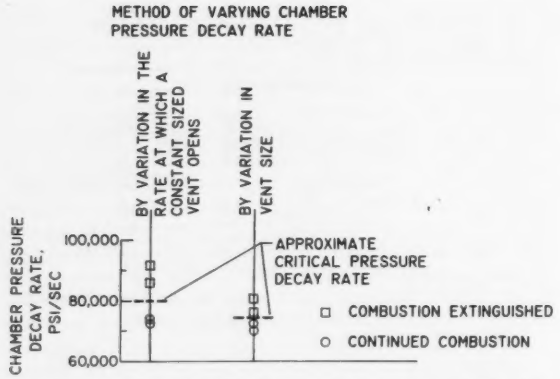
METHOD OF VARYING CHAMBER PRESSURE DECAY RATE
BY VARIATION IN THE RATE AT WHICH A CONSTANT SIZED VENT OPENS
BY VARIATION IN VENT SIZE
CHAMBER PRESSURE DECAY RATE, PSI/SEC
100,000
80,000
60,000
APPROXIMATE CRITICAL PRESSURE DECAY RATE
COMBUSTION EXTINGUISHED
CONTINUED COMBUSTION

Fig. 4 Comparison of critical pressure decay rate obtained by two different methods. Nominal chamber pressure, 540 psia

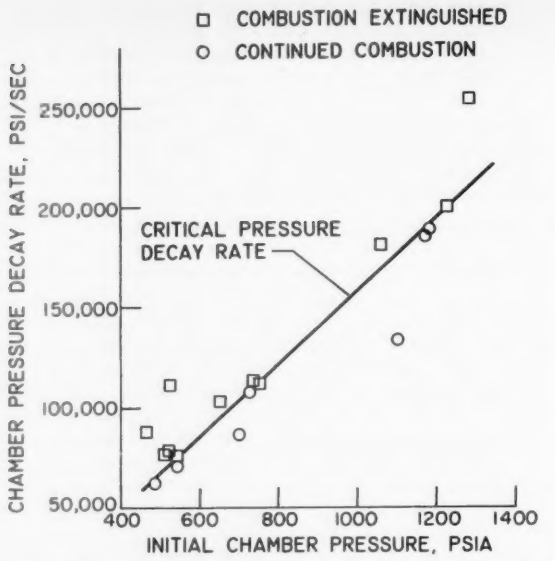

Fig. 5 Effect of initial chamber pressure on critical chamber decay rate

the combustion instability that is often encountered in solid propellant motors. During the expansion part of an instability wave the resulting reduction in flame intensity or reaction rate can act to amplify the pressure decrease.

Comparison of critical pressure decay rate obtained by two different methods

Variation in the chamber vent size varies not only the pressure decay rate but also the final chamber pressure. For example, as the vent size is increased, the pressure decay rate increases and final combustion pressure decreases, provided of course the combustion is not extinguished during the pressure drop. The pressure decay rate can be varied independently, however, by using a constant vent size and varying the rate at which the vent is opened. The pressure-time curves obtained by these techniques were quite similar in shape. A comparison of the critical pressure decay rate (minimum required to extinguish combustion) obtained by these two methods is shown in Fig. 4. Although there is some uncertainty as to the precise critical pressure decay rate because of the data spread, it appears as though the value is nearly the same in both cases. This indicates that the pressure decay rate was of primary importance in extinguishing combustion by sudden pressure decrease.

Combustion extinction as referred to in this article means a permanent termination of the combustion process. In all runs at an ambient pressure of 3.5 mm of mercury (equivalent to an altitude of 23 miles) in which the pressure decay rate was higher than critical, combustion was halted with no indication of any subsequent spontaneous reignition causing a low pressure burnout of the propellant. During some exploratory runs at ambient pressure about 700 mm of mercury, however, several instances were observed where the propellant reignited several seconds after combustion had apparently been completely extinguished. It appears that once combustion has been extinguished by a rapid pressure decrease, the propellant will not subsequently reignite in a low ambient pressure environment.

Effect of chamber pressure on critical decay rate

The variation of critical pressure decay rate (minimum required for combustion extinction) for a range of initial chamber pressures from 500 to 1200 psia is shown in Fig. 5. The chamber pressure decay rate was varied by varying the vent size. The circular and square symbols represent nonextinction and extinction points respectively. The line drawn between the extinction and nonextinction points represents the variation of critical chamber pressure decay rate with original chamber pressure level. The critical pressure decay rate was found to increase linearly as the chamber pressure level increased for the range of chamber pressure investigated. The critical pressure decay rate was approximately 74,000 psi/sec for an initial chamber pressure of 540 psia.

Summary of Results

The following summarizes the results of the initial phases of a study of the effect of rapid pressure decrease on combustion of an aluminized solid propellant.

1 There is a minimum rate of the decay of chamber pressure required to extinguish combustion. This minimum rate was 74,000 psia/sec for an initial chamber pressure of 540 psia.

2 Combustion luminosity measurements indicated that the flame was very sensitive to rapid pressure decrease, since it could be extinguished or quenched momentarily by pressure decay rates nearly an order of magnitude lower than required to extinguish the flame permanently.

3 The minimum pressure decay rate for extinction increased linearly as the chamber pressure increased.

References

1 Ciepluch, C. C., Allen, H., Jr. and Fletcher, E. A., "Ignition of Solid-Propellant Rocket Motors by Injection of Hypergolic Fluids," ARS JOURNAL, vol. 30, no. 7, July 1960.

2 Price, E. W., "Analysis of Results of Combustion Instability Research on Solid Propellants," presented at the Solid Propellant Rocket Research Conf., Princeton, N. J., Jan. 28–29, 1960 (*ARS preprint no. 1068-60*).

3 Chaille, J. L. and Brown, L. M., Bulletin of the 13th Meeting of the Joint Army-Navy-Air Force Solid Propellant Group, June 4–6, 1957.

Interaction of Centered Expansion Waves[1]

GEORGE RUDINGER[2]

Cornell Aeronautical Laboratory Inc., Buffalo, N. Y.

Exact solutions for two cases of reflection of centered expansion waves from a closed end of a duct are presented. It is shown that the reflected wave, in general, is not centered and that its deviation from a centered expansion wave increases rapidly with decreasing ratios of the specific heats.

NONSTEADY flows in ducts frequently involve the interaction of two expansion waves. It is the purpose of this note to show that, if the waves are centered before interacting, they are, in general, not centered after leaving the interaction region. A general proof for this statement does not seem feasible, but it is sufficient to present one particular case for which an exact proof can be given. A second case will be described to provide better understanding of the phenomena.

Let a centered expansion wave be reflected from a closed end of a duct. For reason of symmetry, the resulting flow is the same as if two equal waves facing in opposite directions interacted. A wave diagram for such a flow is shown in Fig. 1. The incident and reflected waves separate regions 0, 1, and 2, where uniform flow conditions prevail, and their characteristics are straight lines outside the interaction region. The time and position coordinates of the center of the incident wave are given by $t = 0$ and $x = L$, respectively. It is convenient to express the flow velocity u and the local speed of sound a in terms of the sound speed a_0 of the initially undisturbed gas and to use the dimensionless coordinates $\xi = x/L$ and $\tau = a_0 t/L$. For a perfect gas, the characteristics are then described by the well-known conditions (1,2)[3]

$$P = \frac{2}{\gamma - 1}\frac{a}{a_0} + \frac{u}{a_0} = \text{const} \quad \text{for} \quad \frac{d\xi}{d\tau} = \frac{u + a}{a_0} \qquad [1a]$$

$$Q = \frac{2}{\gamma - 1}\frac{a}{a_0} - \frac{u}{a_0} = \text{const} \quad \text{for} \quad \frac{d\xi}{d\tau} = \frac{u - a}{a_0} \qquad [1b]$$

where P and Q are the Riemann variables, and γ is the ratio of the specific heats of the gas.

Fig. 1 shows the head and tail of the incident and reflected waves. The points where the reflected characteristics leave the region of interaction are labeled A and B. The path of an arbitrary intermediate characteristic is also shown; it leaves the closed end at D and the interaction region at C. To check whether or not the backward extensions of the characteristics of the reflected wave (broken lines) pass through one common point, the coordinates and flow conditions along the line ACB are required.

The exact solution for the flow within the interaction region was given by Riemann in terms of hypergeometric functions. Any point within this region can be specified by the values of P and Q associated with the characteristics that intersect there. The time coordinate of this point is then given by (Ref. 1, p. 195)

$$\tau(P,Q) = \left(\frac{P_0 + Q_0}{P + Q}\right)^{\lambda} F(1 - \lambda; \lambda; 1; z) \qquad [2]$$

where

$$\lambda = \frac{1}{2}\frac{\gamma + 1}{\gamma - 1} \qquad [3]$$

F is the hypergeometric function (3) of the argument

$$z = -(P_0 - P)(Q_0 - Q)/(P_0 + Q_0)(P + Q) \qquad [4]$$

and for the parameters given in Eq. 2, it takes the form

$$F(z) = 1 + \frac{(1 - \lambda)\lambda}{1 \cdot 1}z + \frac{(1 - \lambda)(2 - \lambda)\lambda(\lambda + 1)}{1 \cdot 2 \cdot 1 \cdot 2}z^2 + \ldots \qquad [5]$$

with $|z| < 1$.

If λ is an integer, $F(z)$ reduces to a polynomial of order $\lambda - 1$. In particular, one obtains $F(z) = 1 - 2z$ for $\lambda = 2$, corresponding to $\gamma = 5/3$. Since the gas is initially at rest $P_0 = Q_0 = 2/(\gamma - 1) = 3$, Eq. 2 then assumes the form

$$\tau(P,Q) = \frac{36}{(P + Q)^2}\left[1 + \frac{(3 - P)(3 - Q)}{3(P + Q)}\right] \qquad [6]$$

The corresponding value of ξ may be obtained from the condition for a characteristic of the reflected wave

$$\frac{d\xi}{d\tau} = \frac{u + a}{a_0} = \frac{\gamma + 1}{4}P - \frac{3 - \gamma}{4}Q \qquad [7]$$

or

$$\frac{d\xi}{d\tau} = \frac{2P - Q}{3} \quad \text{for } \gamma = \frac{5}{3} \qquad [8]$$

where P must be treated as a constant parameter that defines the particular characteristic.

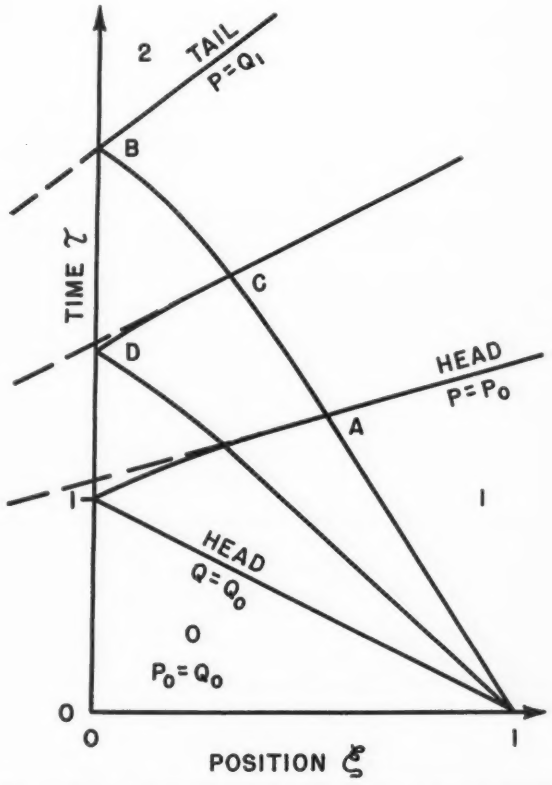

Fig. 1 Reflection of a centered expansion wave from a closed end. The head, tail, and an arbitrary intermediate characteristic of the incident and reflected wave are shown

Received July 21, 1961.

[1] This work was carried out as part of Project SQUID, which is supported by the Office of Naval Research under Contract Nonr-1858(25). Reproduction in full or in part is permitted for any use of the United States Government.

[2] Principal Physicist. Member ARS.

[3] Numbers in parentheses indicate References at end of paper.

Table 1 Flow conditions at points A, B, and C of Fig. 1, for $\gamma = 5/3$ and $Q_1 = 3/2$ (all values are exact)

Point	P	u/a_0	a/a_0	τ	ξ
A	3	3/4	3/4	16/9	1
B	2	1/4	7/12	1152/343	239/343
C	3/2	0	1/2	5	0

Table 2 Intersection of the characteristics through points A, B, and C of Fig. 1 for the example of Table 1 (values rounded off to two decimal places)

Points	ξ^*	τ^*
A,B	−2.65	−0.65
A,C	−3.10	−1.19
B,C	−2.92	−0.83

Table 3 Intersection of the head of the reflected wave with the neighboring characteristic (*) and with the tail (**) of the reflected wave for $Q_1 = 0$ (rounded off to one decimal place)

γ	5/3	7/5	6/5
λ	2	3	5.5
τ^*	−2.0	−8.0	−101.8
τ^{**}	+1.5	+2.3	+8.0
ξ^*	−7.0	−19.0	−92.8
ξ^{**}	0	0	0

Integration of Eq. 8 yields

$$\xi = (2/3)P - (1/3)\int Q d\tau + \text{const}$$

The integration constant can be determined, because the characteristic leaves the closed end at the point for which the conditions $\xi = 0$, $\tau = \tau_e$, and $Q = P$ are satisfied (point D of Fig. 1). Thus one obtains

$$\xi = \frac{2}{3}P(\tau - \tau_e) - \frac{1}{3}\int_P^Q Q\,\frac{d\tau}{dQ}\,dQ \qquad [9]$$

where the value of τ_e follows from Eq. 6 for $Q = P$; the same equation also yields the derivative in the integrand. After carrying out the indicated operations, the result can be expressed in the form

$$\xi = 2 + \frac{2}{3}P(\tau - \tau_e) + \frac{9}{P^2} - \frac{8P}{P+Q} + \frac{10P^2 - 54}{(P+Q)^2} + \frac{4P(9-P^2)}{(P+Q)^3} \qquad [10]$$

The strength of the incident wave is prescribed by the change of Q from $Q_0 = P_0 = 3$ to some value Q less than Q_0. The characteristics of the reflected wave are specified by their P-values, which range from $P_A = P_0$ to $P_B = Q_1$.

Eqs. 6 and 10 thus represent the border of the interaction region if one sets $Q = Q_1$. The equations of the straight lines which form the P-characteristics of the reflected wave outside the interaction region are then given by

$$\xi - \xi_i(P, Q_1) = [\tau - \tau_i(P,Q_1)](2P - Q_1)/3$$

where the quantities with subscript i are functions of the variable P and the constant parameter Q_1, according to Eqs. 6, 8, and 10. It would be quite difficult to determine whether or not this family of straight lines can ever have a common center. To show that, in general, no common center exits, it is sufficient to give one numerical example. Suppose $Q_1 = 3/2$ is chosen. The head and tail of the reflected wave are then given by $P_A = 3$ and $P_B = 3/2$. For an intermediate characteristic, the value $P_e = 2$ may arbitrarily be chosen. If these numbers are substituted in Eqs. 6 and 10, the results collected in Table 1 are obtained. For these values, it is readily established that the characteristics through A, B, and C do not pass through one common point. Their individual intersection points (ξ^*, τ^*) are given in Table 2.

The foregoing result is sufficient proof that, in general, the reflected wave is not centered, but a wave diagram drawn to scale shows that the wave is not too far from being centered in the particular example selected. It therefore becomes of interest to investigate the behavior of the reflected wave for values of γ lower than 5/3. Although the hypergeometric function reduces to a polynomial for certain values of γ, the required algebraic work would be excessive, and a different approach will be used.

Consider the expansion wave for which $Q_1 = 0$. When the tail of this wave reaches the closed end (point B of Fig. 1), the condition of zero flow velocity requires that $P_B = Q_B = 0$. Consequently, both a and u are zero at this point, which can be reached by the characteristic only after an infinite time. Since $u_B + a_B = 0$, the time axis becomes the backward extension of the tail of the reflected wave, and its intersection with the head of the wave, for which $P_A = P_0$, can be determined. If a third characteristic is then chosen so that $P_e = P_0(1 - \epsilon)$, the hypergeometric function again becomes linear in z if ϵ tends to zero, so that terms of higher powers of ϵ can be neglected. Eq. 4 then yields

$$z = -\frac{\epsilon}{2}\frac{P_0 - Q}{P_0 + Q} + \text{terms of higher order of } \epsilon$$

The calculation proceeds in the same manner as in the first case, and after considerable algebraic manipulation, the coordinates of point C and the slope of the reflected characteristic are obtained

$$\xi_0 = (\lambda - 1)2^\lambda + 1 + \lambda(\lambda^2 - 1)2^{\lambda-1}\epsilon \qquad [11]$$

$$\tau_c = 2^{\lambda-1}[2 + \lambda(\lambda - 1)\epsilon] \qquad [12]$$

and

$$(u_c + a_c)/a_0 = \lambda(1 - \epsilon) \qquad [13]$$

The intersection of the characteristic described by Eqs. 11–13 with the neighboring head of the wave, for which $\epsilon = 0$, yields the *effective instantaneous center* of the head of the reflected wave as

$$\xi^* = 1 + 2\lambda - 2\lambda^2 - 2^\lambda \qquad [14]$$

and

$$\tau^* = -(\lambda - 1)2^{\lambda-1} \qquad [15]$$

The intersection of the head of the reflected wave with its tail (time axis) is located at

$$\xi^{**} = 0$$

$$\tau^{**} = (2^\lambda - 1)/\lambda \qquad [16]$$

Eqs. 3 and 14–16 yield the values listed in Table 3 for three values of γ.

It is again found that the reflected waves are not centered, and it can also be seen that the discussed intersection points rapidly move apart as the value of γ is decreased below 5/3. In view of these results, it seems extremely unlikely that any combinations of Q_1 and γ exist for which the reflected wave turns out to be centered, but this particular point has not been

rigorously proven.

From the presented analysis, it may be concluded that the interaction of centered expansion waves leads to waves that are not, in general, centered. It has also been shown that such deviations from a centered expansion wave increase rapidly with decreasing values of γ.

References

1 Courant, R. and Friedrichs, K. O., *Supersonic Flow and Shock Waves*, Interscience Publishers Inc., New York, 1948.

2 Rudinger, G., *Wave Diagrams for Nonsteady Flow in Ducts*, D. Van Nostrand Co. Inc., Princeton, N. J., 1955.

3 Whittaker, E. T. and Watson, G. N., *A Course of Modern Analysis*, Cambridge University Press, 1958, 4th ed., p. 281.

Impulse Programming for Turbine Boost

J. J. MARCINEK[1] and R. E. GOLDSTEIN[2]

General Dynamics Corp., Pomona, Calif.

IN MANY practical situations rotating power-supplying machines must be boosted or accelerated to operating speed in comparatively short periods of time. Very short reaction times are required by many military systems. In commercial usage, although reaction times are usually less stringent, emergency power may be urgently required in the case of breakdown of conventional utility sources.

Boost energy for many missile on-board power supplies and for some aircraft jet engines is obtained from solid propellant gas generators. However, the rate of gas generation from solid propellants is dependent, sometimes notoriously so, on temperature. This problem then poses the question, "What are the effects of impulse programming on the end of boost rotational speed of the turbine?"

In the typical solid propellant-turbine system, boost impulse is nominally constant. However, the rate at which momentum is delivered to the wheel varies with temperature. An understanding of the time effects associated with such a system can be obtained from the elementary analysis that follows.

The angular acceleration of the turbine rotor is given by

$$I\ddot{\theta} + \mu\dot{\theta} = T(t)$$

where the symbols have the conventional meaning.

For simplicity assume that

$$\mu = \text{const}$$

$$\int_0^\tau T dt = \text{const}$$

with the understanding that for a particular case T is also constant. Thus, a small T indicates a large τ and vice versa.

For the case of an impulse turbine, where the blade to spouting velocity ratio is about 0.1 and the jet and blade angles are of conventional design, velocity diagrams will yield the driving torque relationship

$$T = K\dot{m}(V - \dot{\theta}r)r$$

With the assumptions already made, $K < 2$ and will vary slightly with rotor velocity in a range of about $1.6 \leq K \leq 1.8$. In the present analysis, K will be assumed nominally constant.

On the basis of the above, the mass rate of flow can also be assumed constant, and similarly V, the tangential component of the spouting velocity, is constant. Blade interference effects are neglected.

Now, if

$$M = \dot{m}\tau$$

then

$$T = K(M/\tau)(V - \dot{\theta}r)r$$

Integrating the momentum equation

$$\ddot{\theta} + \frac{\mu}{I}\dot{\theta} = \frac{KM}{I\tau}(V - \dot{\theta}r)r$$

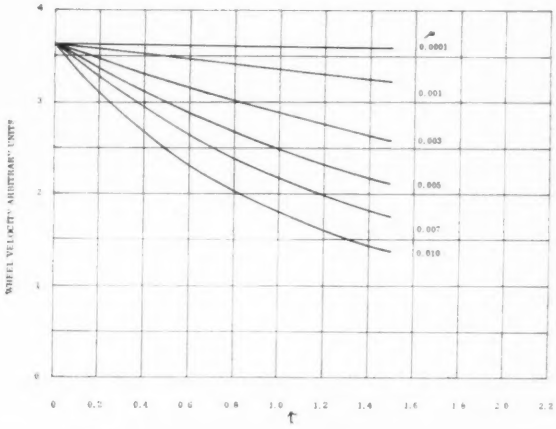

Fig. 1 Effect of rotor loading on end of boost velocity; turbine wheel velocity vs. impulse time

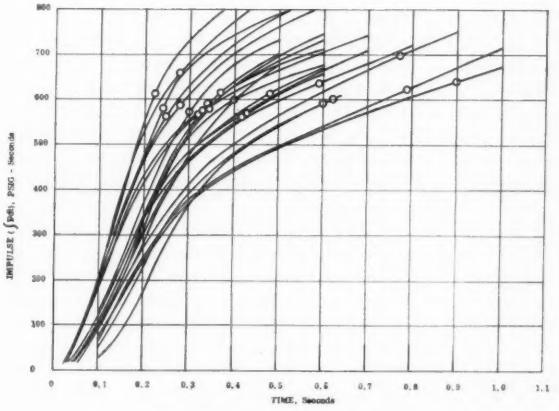

Fig. 2. Electrical system: impulse vs. time
Conditions
Two types of solid propellants
Two types of grain configurations
Four firing temperatures
○ Turbine wheel at 23,000 rpm

Received August 7, 1961.

[1] Chief of Advanced Programs. Member ARS.

[2] Thermo-Mechanics Group Supervisor. Member ARS.

provides

$$\dot{\theta} = \frac{KMV}{\mu\tau + 2Mr^2}\left(1 - \exp\left[-\left(\frac{\mu\tau}{I} + \frac{KM}{I}\,r^2\right)\right]\right)$$

As $\mu \to 0$, $\dot{\theta}$ becomes independent of τ. If μ is large, τ should be small to minimize the effect on $\dot{\theta}$.

Consider the case of a small turbine with the following characteristics:

$$\begin{aligned} I &= 0.00595 \text{ in.-lb-sec}^2 \\ r &= 2 \text{ in.} \\ M &= 9.05 \times 10^{-5} \text{ lb-sec}^2/\text{in.} \\ V &= 63600 \text{ ips} \end{aligned}$$

The plot of Fig. 1 graphically shows the influence of rotor loading on the end of boost rotor velocity. For small loads, the velocity is insensitive to boost programming. A heavily loaded rotor demands careful control of the boosting time to attain the desired rotational velocity.

A considerable test history has been accumulated at General Dynamics/Pomona with solid propellant charges and the rapid boosting of turbines to provide missile hydraulic and electric power. Figs. 2 and 3 summarize some of these results for the following: 1) two types of propellants; 2) two grain configurations; 3) four firing temperatures.

Note that

$$\dot{m}\tau = M \propto \int_0^\tau p\,dt$$

As might be anticipated from the curves of Fig. 1, the constant speed slopes for the electrical system are much flatter than those of the hydraulic system. The viscous

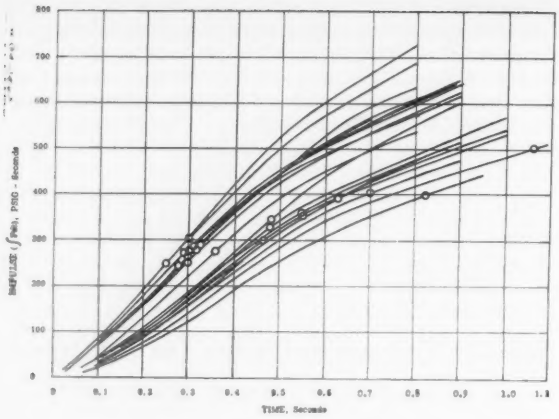

Fig. 3. Hydraulic system: impulse vs. time
Conditions
Two types of solid propellants
Two types of grain configurations
Four firing temperatures
Hydraulic oil at various temperatures
○ Turbine wheel at 10,000 rpm

effects over the temperature range of operation are significantly lower for the electrical power system.

From this it can be concluded that, for a given available impulse, the turbine wheel speed at end of boost is not greatly affected by variations in the programming of the impulse if the torque loadings are fairly light.

Analysis of Large Amplitude Re-Entry Oscillations

GEORGE S. CAMPBELL[1]

Hughes Aircraft Co., Culver City, Calif.

Simple approximate relations are developed for calculating the oscillatory behavior of a vehicle re-entering the atmosphere with an arbitrarily large initial angle of attack. Comparison is made with results calculated using complete three degree of freedom equations of motion. The approximate damping results, when used in conjunction with results from a previous linear theory, are in good agreement with the exact calculations.

THE OSCILLATORY behavior of a re-entering space vehicle can have an important influence on aerodynamic loads, re-entry heating, and acceleration inputs to internal components. Direct numerical solution of the complete equations of motion is costly in machine time, and yet present analytical methods, such as (1),[2] are restricted to small angles of attack. The present analysis extends Tobak and Allen's results to arbitrarily large amplitudes. Results of the approximate theory are compared with three degree of freedom results for a representative lunar return vehicle.

Received Aug. 15, 1961.

[1] Senior Staff Engineer. Member ARS.

[2] Numbers in parentheses indicate References at end of paper.

Decay Envelope

For sufficiently large entry angles, a symmetric vehicle re-enters the atmosphere at approximately constant flight path angle during the early portion of its trajectory (2). Also, velocity remains approximately constant during any one cycle of the short period oscillation, and so an approximate pitching-moment equation may be written

$$\frac{d^2\alpha}{dy^2} = \frac{C_m \rho SD}{2I \sin^2 \gamma} \qquad [1]$$

The pitching-moment coefficient is assumed to depend only on angle of attack. The omission of a damping in pitch term restricts the results to altitudes for which the relative density $\rho SD/m$ is sufficiently small.

A first integral of Eq. 1 is

$$\left(\frac{d\alpha}{dy}\right)^2 = \left(\frac{d\alpha}{dy}\right)_0^2 + \frac{SD}{I \sin^2 \gamma}\int_{\alpha_0}^{\alpha} C_m\, \rho\, d\alpha \qquad [2]$$

The amplitude decay envelope may be obtained by applying Eq. 2 at successive peaks in the oscillation so that

$$\left(\frac{d\alpha}{dy}\right)_1 = \left(\frac{d\alpha}{dy}\right)_0 = 0$$

using the notation defined in Fig. 1. The angle of attack at 1 is less than at 0 by the amount

$$\Delta\alpha = \alpha_0 + \alpha_1$$

The integral in Eq. 2 is evaluated by using a constant average

density over each quarter cycle

$$\rho = \rho_0 - \tfrac{1}{4}(d\rho/dy)_0 \Delta y \qquad 0 < \alpha < \alpha_0$$

$$\rho = \rho_0 - \tfrac{3}{4}(d\rho/dy)_0 \Delta y \qquad \alpha_1 < \alpha < 0$$

Carrying out the integration in Eq. 2 for small $\Delta\alpha$ and an antisymmetric pitching moment gives

$$\Delta\alpha = \frac{-(d\rho/dy)_0}{\rho_0} \frac{\int_0^{\alpha_0} C_m d\alpha}{C_m(\alpha_0)} \frac{\Delta y}{2} \qquad [3]$$

Eq. 3, taken in the limit for small $\Delta\alpha$ and Δy, is the differential equation for the amplitude decay envelope. Its solution, in terms of an undetermined constant C that depends on initial conditions, is

$$\int_0^{\alpha} C_m(\alpha) d\alpha = C\rho^{-1/2} \qquad [4]$$

where the subscript 0 has been dropped.

For a linear pitching moment and small angles of attack, Eq. 4 is in agreement with Tobak and Allen's Eq. 67, specialized to small relative densities.

Oscillation Frequency

The frequency of the short period oscillations may be estimated by fitting a sine wave to Eq. 2 at a peak and the adjacent zero in the α vs. y curve (points 0 and M in Fig. 1). The sine wave

$$\alpha = \alpha_0 \sin ky$$

has a maximum slope of

$$(d\alpha/dy)_m = k\alpha_0$$

at the point

$$\alpha_m = 0$$

Assuming constant density over the quarter cycle, substitution of these values into Eq. 2 gives the wave number

$$k^2 = -\frac{\rho SD}{I \sin^2 \gamma} \frac{1}{\alpha^2} \int_0^{\alpha} C_m d\alpha \qquad [5]$$

The subscript 0 has again been omitted.

Eqs. 4 and 5 determine the dependence of k on density. Use of the simple kinematic relation

$$\omega = kV \sin \gamma$$

provides the equation for angular frequency of the oscillations.

$$\omega^2 = -\frac{\rho V^2 SD}{I} \frac{1}{\alpha^2} \int_0^{\alpha} C_m d\alpha \qquad [6]$$

This result is in agreement with Eq. 67 of (1) when C_m is linear with α. The Allen-Eggers result may be used to give the required dependence of velocity on altitude

$$\frac{V}{V_E} = \exp\left(\frac{-C_D \rho S}{2\beta m \sin \gamma}\right) \qquad [7]$$

Comparison With Exact Results

Results using the approximate equations, Eqs. 4 and 6, are compared in Figs. 2 and 3 with numerical solution of the complete three degree of freedom equations of motion. The initial conditions chosen correspond to vertical re-entry at 179° initial angle of attack and superorbital flight velocity. Aerodynamic coefficients used in the calculations are given in Fig. 4; damping in pitch ($C_{mq} + C_{m\dot{\alpha}}$) was taken as zero. Newtonian theory was used to calculate the aerodynamics of the double cone body. Pitching moments are taken about a center of gravity 0.47 diam from the body's nose. The matching point used to determine the unknown constant in Eq. 4 is indicated on the decay envelope (Fig. 2).

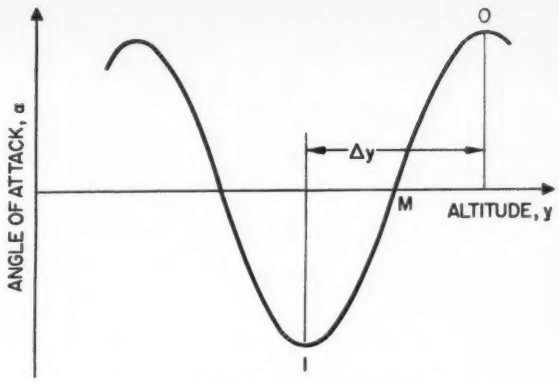

Fig. 1 Notation for approximate theory

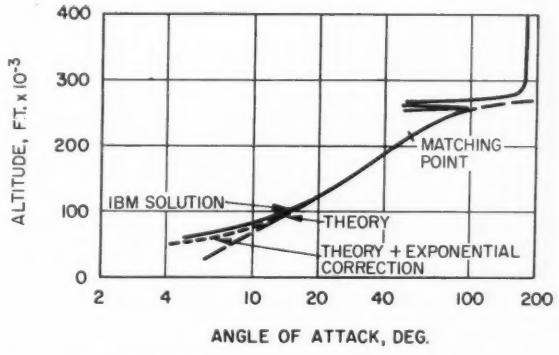

Fig. 2 Re-entry oscillation envelope; comparison of approximate theory with IBM solution

$\gamma_E = 90°$ $\quad W/S = 26.3$ psf
$V_E = 36{,}500$ fps $\quad \sigma/D = 0.201$

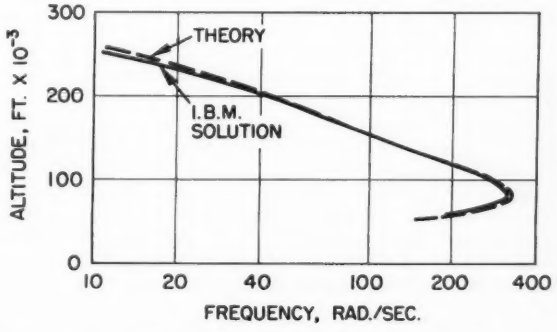

Fig. 3 Re-entry oscillation frequency; comparison of approximate theory with IBM solution

$\gamma_E = 90°$ $\quad W/S = 26.3$ psf
$V_E = 36{,}500$ fps $\quad \sigma/D = 0.201$

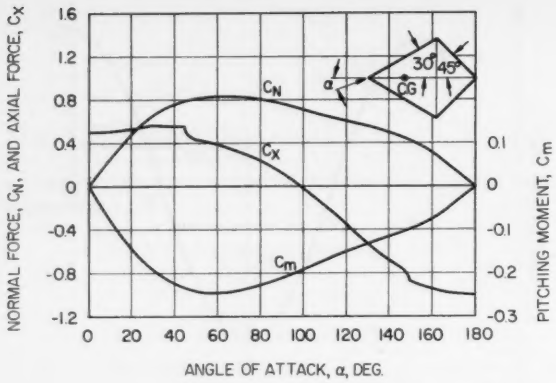

Fig. 4 Aerodynamic coefficients used for trajectory calculations

The approximate damping theory (labeled *theory* in Fig. 2) departs from exact results somewhat below $\alpha = 20°$. At this angle of attack linear theory becomes applicable so that the results of (1) may be applied

$$\frac{\alpha}{\alpha_1} = \left(\frac{\rho_1}{\rho}\right)^{1/4} \exp \lambda_1(\rho - \rho_1)$$

$$\lambda_1 = \frac{S}{4\beta m \sin \gamma}\left[C_D - C_{L_\alpha} + (C_{m_q} + C_{m_{\dot\alpha}})\left(\frac{D}{\sigma}\right)^2\right]$$

The combined use of the two theories (*theory + exponential correction* in Fig. 2) provides good prediction of the damping envelope over the complete angle of attack range. Limited numerical calculations are required to establish the constant C, but continuation of the step by step calculations to the high frequency portion of the trajectory has been found expensive in machine time.

The approximate equation for oscillation frequency, Eq. 6, is compared with IBM results in Fig. 3. In applying Eq. 7 to obtain velocity, an average value of C_D depending on α amplitude at each altitude was used. The approximate results are in good agreement with results using the complete equations of motion.

Nomenclature

C_D = drag coefficient, 2 (drag)/$\rho V^2 S$
C_L = lift coefficient, 2 (lift)/$\rho V^2 S$
C_{L_α} = lift-curve slope, $dC_L/d\alpha$
C_m = pitching moment coefficient, 2 (pitching moment)/$\rho V^2 SD$
C_{m_q} = damping in pitch, $\frac{\partial C_m}{\partial \dot\theta D/V}$
$C_{m_{\dot\alpha}}$ = damping in plunge, $\frac{\partial C_m}{\partial \dot\alpha D/V}$
C_N = normal force coefficient, 2 (normal force)/$\rho V^2 S$
C_X = axial force coefficient, 2(axial force)/$\rho V^2 S$
D = body diameter
I = moment of inertia in pitch
k = wave number, 2π/wavelength
m = vehicle mass
S = body cross-sectional area
V = velocity
V_E = initial entry velocity
y = altitude
α = angle of attack
ρ = atmospheric density
γ = flight-path angle, positive down
ω = angular frequency, 2π/period
β = atmospheric exponent, $-d(\log \rho)/dy$
σ = radius of gyration, $\sqrt{I/m}$
θ = pitch attitude, $(\alpha - \gamma)$

References

1 Tobak, M. and Allen, H. J., "Dynamic Stability of Vehicles Traversing Ascending or Descending Paths Through the Atmosphere," *NACA TN 4275*, 1958.

2 Allen, H. J. and Eggers, A. J., Jr., "A Study of the Motion and Aerodynamic Heating of Missiles Entering the Earth's Atmosphere at High Supersonic Speeds," *NACA TN 4047*, 1957.

Polar Hodograph for Ballistic Missile Trajectories

S. P. ALTMAN[1] and J. S. PISTINER[2]

Hamilton Standard Division, United Aircraft Corp. Windsor Locks, Conn.

SINCE a ballistic missile trajectory (as shown in Fig. 1) is essentially an orbit that intersects Earth's surface at the launch and impact points (assuming flight in vacuum), a hodograph analysis can be used to define and study ballistic missile trajectories, as shown by Paul (1).[3] Prior to his work, a comparable analysis was developed for the orbital transfer problem (2–4) by use of a polar hodograph. This type of hodograph provides all trajectory characteristics in a more concise form useful for trajectory design applications by transforming the surface of the spherical Earth into a straight line.

Received Sept. 22, 1961.

[1] Supervisor, System Design. Member ARS.

[2] Senior Engineer, Control Systems. Member ARS.

[3] Numbers in parentheses indicate References at end of paper.

Polar Hodograph

The following energy equation for the planar orbit (in vacuum) of a vehicle in the central force field of a spherical celestial body was considered:

$$E = \frac{m}{2}(v_\phi^2 + v_r^2) - \frac{\mu m}{r}$$
$$= \text{total orbital energy} = \text{const} \qquad [1]$$

Since

$$l = mrv_\phi = \text{total angular momentum} = \text{const} \qquad [2]$$

Eq. 1 may be rewritten as

$$R^2 = v_r^2 + (v_\phi - C)^2 \qquad [3]$$

where

$$C = \mu m/l = \mu/rv_\phi \qquad [4]$$

$$R = \sqrt{(2E/m) + (\mu m/l)^2} = \sqrt{(2E/m) + C^2} \qquad [5]$$

Eq. 3 represents a hodograph circle (as shown in Fig. 2) with radius R displaced along the v_ϕ-axis by the amount C. Then it is seen that

$$v_r = R \sin \phi \qquad [6]$$

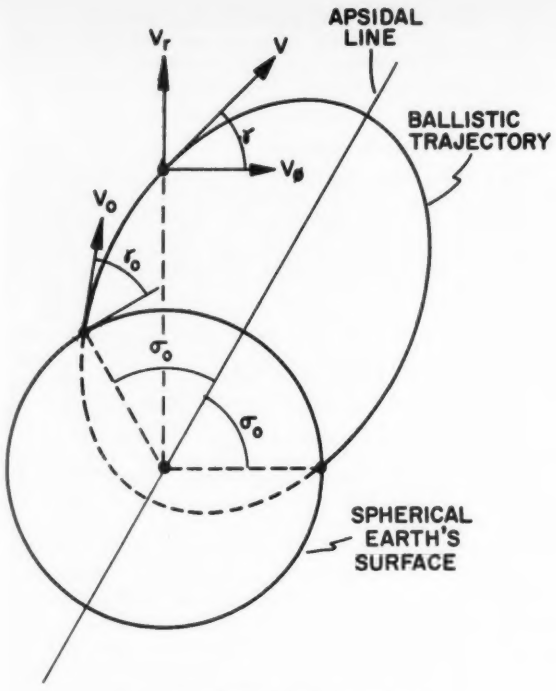

Fig. 1 The ballistic missile trajectory

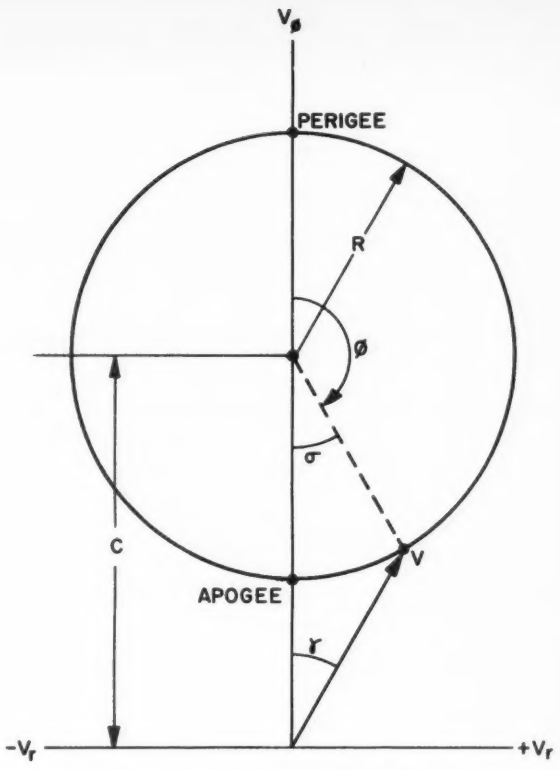

Fig. 2 The polar hodograph of an orbit

$$v_\phi = C + R\cos\phi \quad [7]$$

$$v^2 = v_r^2 + v_\phi^2 = C^2 + R^2 + 2CR\cos\phi \quad [8]$$

The following transformations from conic parameters to hodograph parameters can easily be obtained:

$$e = R/C \quad [9]$$

$$a = \mu/(C^2 - R^2) \quad [10]$$

As shown in Fig. 2, the flight path angle γ defines the angle between the v_ϕ-axis and the velocity v. The anomaly ϕ and its supplement σ are defined by the angles between the hodograph radius to the subject point of the orbit and the v_ϕ-axis directed down or up respectively from the hodograph circle center.

If Eqs. 6 and 7 are multiplied by C, then

$$Cv_r = CR\sin\phi \quad [6a]$$

$$Cv_\phi = C^2 + CR\cos\phi \quad [7a]$$

are obtained, which describe the modified polar hodograph (shown in Fig. 3). All angular relations of this hodograph are invariant, while the quantity

$$Cv_\phi = \mu/r \quad [11]$$

is expressed graphically as a straight line parallel to the v_r-axis. The hodograph for a circular orbit at Earth's surface, i.e., at orbital altitude = r_e, is represented by the point E, so that

$$(Cv_\phi)_e = \mu/r_e \quad [12]$$

is the locus of all points of trajectory intersection with Earth's surface. In general, a line parallel to the v_r-axis is the locus of all points at a given radial distance from the center of the celestial body.

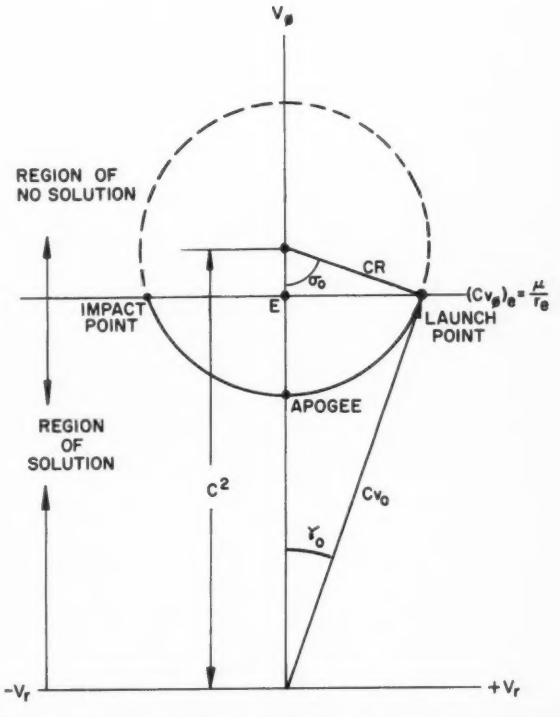

Fig. 3 The modified polar hodograph of the ballistic missile trajectory

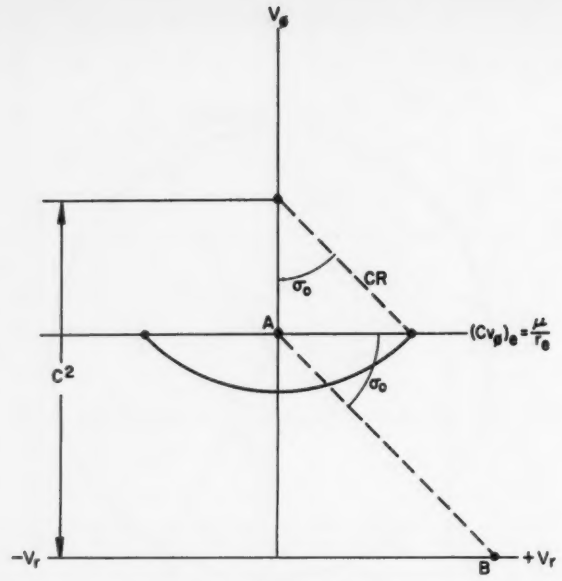

Fig. 4 The modified polar hodograph of the minimum energy trajectory

Ballistic Missile Trajectory

The modified polar hodograph of a ballistic missile trajectory will intersect the $(Cv_\phi)_e$-line, as shown in Fig. 3. The entire region lying above the $(Cv_\phi)_e$-line does not provide trajectory solutions. That is, all ballistic missile trajectories are represented by hodograph circle segments between the $(Cv_\phi)_e$-line and the v_r-axis. The two points of intersection of the hodograph with the $(Cv_\phi)_e$-line are the launch and impact points of the trajectory. The intersection of the hodograph with the v_ϕ-line is the apogee point.

The hodograph parameters can be defined in terms of the launch conditions and/or range angle, as follows:

$$C = (\mu/r_e)/(v_0 \cos \gamma_0) \quad [13]$$

$$R = [C^2 + (v_0^2 - 2\mu/r_e)]^{1/2} = v_0(\sin \gamma_0/\sin \sigma_0) \quad [14]$$

Consequently, the ballistic missile trajectory can be defined on the modified polar hodograph by sets of specified flight data, i.e., velocity, flight-path angle, or range angle. For example, let the magnitude of the launch velocity v_0 and the launch flight path angle γ_0 be specified. From the origin, direct a line at the angle γ_0 from the v_ϕ-axis, and select a length of that line to represent Cv_0. Assign a scalar value for velocity, so that the scalar length of the known velocity v_0 is established. Then the length for C is derived from Cv_0, so that the point for C^2 is obtained. The modified hodograph circle radius is the distance from that point to the end of the Cv_0-line.

The modified polar hodograph provides the values for σ, γ, Cv, Cv_ϕ, and Cv_r directly, for any given point on the missile trajectory. The values for v, v_ϕ, v_r, and r are obtainable by simple arithmetic operation. The flight time can be obtained by the use of analytic relations presented in (3).

Minimum Energy Trajectory

For a given range angle $2\sigma_0$, an infinite set of trajectory solutions is possible. The one ballistic trajectory that requires the least magnitude of launch velocity v_0 (for the given range angle) is the minimum energy trajectory. For this trajectory, the hodograph circle center displacement can be shown to be

$$C^2 = \mu/(r_e \sin \sigma_0) \quad [15]$$

and the modified hodograph circle radius

$$CR = \left[\frac{1 - \sin \sigma_0}{1 + \sin \sigma_0}\right]^{1/2} C^2 = \left|\frac{\cos \sigma_0}{1 + \sin \sigma_0}\right| C^2 \quad [16]$$

The hodograph for the minimum energy trajectory is simply constructed by use of Eq. 15, as shown in Fig. 4. From the intersection point A between the v_ϕ-axis and the $(Cv_\phi)_e$-line, direct a line at an angle σ_0 from the $(Cv_\phi)_e$-line until its intersection with the v_r-axis at point B. By the trigonometric relation of Eq. 15, $\overline{AB} = C^2$. Then the hodograph circle center is located on the v_ϕ-axis, and the radius CR is obtained by directing a line from the circle center at an angle σ_0 to the v_ϕ-axis until intersection with the $(Cv_\phi)_e$-line. The hodograph of the trajectory is then the circle segment lying below the $(Cv_\phi)_e$-line, as shown.

Nomenclature

- a = semimajor axis of the ellipse
- C = velocity parameter of the orbit
- e = eccentricity of the ellipse
- E = total potential and kinetic energy of the orbital body
- l = total angular momentum of the orbital body
- m = mass of the orbital body
- r = radial distance between the gravitational centers of the orbital and celestial bodies
- R = velocity parameter of the orbit
- v = linear velocity
- γ = angle between the hodograph v_ϕ-axis and the hodograph radius R to the orbital body on the hodograph
- μ = gravitational constant for the given celestial body
- 2σ = total range angle
- ϕ = true anomaly of the body in orbit

Subscripts

- e = spherical Earth's surface
- 0 = launch point
- r = radial
- ϕ = normal

References

1 Paul, E. W., "The Hodograph and Ballistic Missile Trajectory Problems," *Aerospace Engng.*, vol. 20, no. 2, February 1961, pp. 24–25, 70–72.

2 Altman, S. P., "Orbital Transfer for Satellites," *Fourth BMD Symposium on Ballistic Missiles and Space Technology 1959*, Pergamon Press, New York, 1961.

3 Pistiner, J. S., "Some Characteristics of the Planar Satellite Orbit," ARS JOURNAL, vol. 30, no. 3, March 1960, pp. 275–277.

4 Altman, S. P. and Pistiner, J. S., "Hodograph Analysis of the Orbital Transfer Problem for Coplanar, Nonaligned Elliptical Orbits," ARS JOURNAL, vol. 31, no. 9, September 1961, pp. 1217–1225.

Notes on Heat Sink Analysis

K. A. ADAMS[1] and M. R. SEIZEW[2]

Chrysler Corp., Advanced Projects Organization
Centerline, Mich.

When considering a solid material for use in a heat sink application, a most important parameter is the rate of penetration of some critical temperature, e.g., melting temperature, into the material. Accompanying this penetration is a change in the thermodynamic properties of the material which complicates the solution of the conductivity equations by normal analytical methods. This paper presents a method of solution which uses dimensional analysis to relate the conductivity equations and transform them from partial differential equations to the more easily solved ordinary differential equations.

WHEN heat is applied to a solid material, the conduction of this heat is governed by the conductivity equation

$$\frac{\partial T}{\partial t} = \alpha \frac{\partial^2 T}{\partial x^2} \qquad [1]$$

If the temperature being considered is critical, i.e., a temperature at which the thermodynamic properties of the material change, the solution is no longer a simple one; it now involves two simultaneous differential equations of the same type as Eq. 1. By using dimensional analysis, it is possible to relate these equations and transform them into solvable ordinary differential equations. Certain limitations and conditions are imposed in this analysis: 1) the property changes, thermal conductivity, and diffusivity are distinct; 2) latent heat is neglected to simplify the problem; 3) the temperature at the surface of the material is constant; 4) the material can be considered to have infinite thickness in positive x direction; 5) the solution is applicable only during the time of external heat application.

Referring to Fig. 1 for $t > 0$, we have two property regions of the medium: the first region has reached critical temperature and the thermodynamic properties are changed; the second region is below critical or noncritical temperature.

The heat conduction equation for the critical temperature region is

$$\frac{\partial T}{\partial t} = \alpha_1 \frac{\partial^2 T}{\partial x^2} \qquad [2]$$

and for the noncritical temperature region is

$$\frac{\partial T}{\partial t} = \alpha_2 \frac{\partial^2 T}{\partial x^2} \qquad [3]$$

The boundary conditions for the specified situation are

$$T(\infty,t) = 0 \qquad T(x,0) = 0$$
$$T(x + 0,t) = T(x - 0,t) \qquad [4]$$
$$K_1 \left(\frac{\partial T}{\partial X}\right)_{x+0} = K_2 \left(\frac{\partial T}{\partial x}\right)_{x-0}$$

It can be shown that the use of dimensional analysis yields a solution of the simultaneous differential equations, Eqs. 2 and 3, which has the form

$$T = T_0 - T_0 f(x/\sqrt{\alpha_1 t}, \Gamma, \delta) \qquad [5]$$

and

$$x/\sqrt{\alpha_1 t} = E[(T_0 - T)/T_0, \Gamma, \delta] \qquad [6]$$

where f and E are dimensionless functions of their dimensionless arguments. Differentiation of Eq. 5 once with respect to time and twice with respect to distance gives

$$\frac{\partial T}{\partial t} = \frac{T_0}{2} \frac{\partial f}{\partial E} \cdot \frac{x}{\sqrt{\alpha_1}\, t^{3/2}} \qquad [7a]$$

$$\frac{\partial^2 T}{dx^2} = -T_0 \frac{\partial^2 f}{dE^2} \cdot \frac{1}{\alpha_1 t} \qquad [7b]$$

Substituting Eqs. 7 into Eqs. 2 and 3 gives

$$\frac{d^2 f}{dE^2} + \frac{E}{2} \frac{df}{dE} = 0 \qquad x_c > x \quad [8]$$

$$\frac{d^2 f}{dE^2} + \frac{\delta E}{2} \frac{df}{dE} = 0 \qquad x_c > x \quad [9]$$

Eqs. 8 and 9 are integrated with the aid of the substitution $df/dE = Y$, yielding the results

$$df/dE = c_1 e^{-E^2/4} \qquad x_c > x \quad [10]$$

$$df/dE = c_2 e^{-\delta E^2/4} \qquad x_c < x \quad [11]$$

Using boundary condition at the interface $E = E_c$ where

$$E_c[(T_0 - T_c)/T_0, \Gamma, \delta] = x_c/\sqrt{\alpha_1 t}$$

gives

$$df = [\Gamma c_2 e^{-E_c^2(\delta^{-1})/4}] e^{-E^2/4}\, dE \qquad x_c > x \quad [12]$$

$$df = c_2 e^{-E^2\delta/4}\, dE \qquad x_c < x \quad [13]$$

Integrating both sides of Eqs. 12 and 13 gives

$$f(E_c) - f(0) = \Gamma c_2 e^{-E_c^2(\delta^{-1})/4} \int_0^{E_c} e^{-E^2/4}\, dE \qquad [14]$$

$$f(\infty) - f(E_c) = c_2 \int_{E_c}^{E\infty} e^{-\delta E^2/4}\, dE \qquad [15]$$

Inserting the boundary condition in Eqs. 14 and 15 yields

$$1 - \frac{T_c}{T_0} = [\Gamma c_2 e^{-E_c^2(\delta^{-1})/4}] \int_0^{E_c} e^{-E^2/4}\, dE \qquad [16]$$

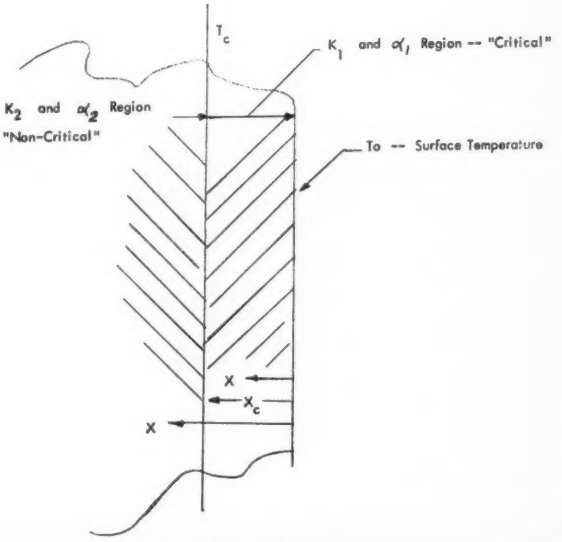

Fig. 1 Illustration to discussion

Received Aug. 17, 1961.

[1] Staff Engineer, Technical Staff. Member ARS.

[2] Staff Engineer, Operations Research Staff.

and

$$\frac{T_c}{T_0} = C_2\left[\int_0^{E\infty} e^{-\delta E^2/4}\,dE - \int_0^{E_c} e^{-\delta E^2/4}\,dE\right] \quad [17]$$

Dividing Eq. 16 by Eq. 17 to eliminate C_2 yields

$$\frac{T_0 - T_c}{T_c} = \frac{\Gamma e^{-E_c^2(\delta-1)/4}\int_0^{E_c} e^{-E^2/4}\,dE}{\int_0^{E\infty} e^{-\delta E^2/4}\,dE - \int_0^{E_c} e^{-\delta E^2/4}\,dE} \quad [18]$$

or rewriting Eq. 18 in the normal form gives

$$\frac{T_0 - T_c}{T_c} = \frac{\Gamma[\sqrt{2\pi}\phi\,(\sqrt{\delta - 1/2})E_c\;[2\sqrt{\pi}A(E_c/\sqrt{2})}{2\sqrt{\pi/\delta}[1 - A\,(\sqrt{\delta/2}E_c)]} \quad [19]$$

where A and ϕ are tabular values of the error integral and the error function respectively. Eq. 19 has unique solutions in E_c, corresponding to given materials and applied temperatures.

Solving for E_c, X_c can then be determined from

$$x_c = E_c\sqrt{\alpha_1 t} \quad [20]$$

and the rate of critical temperature penetration is

$$dx_c/dt = (1/2)E_c\sqrt{\alpha_1/t} \quad [21]$$

Example: A new material is considered for heat sink applications. *Problem:* To find the penetration rate and depth after one hour for some critical temperature at which the thermodynamic properties change.
Given conditions:

$T_0 = 5000°F$
$T_c = 2500°F$
$K_2 = 30$ Btu/hr-ft-°F
$K_1 = 15$ Btu/hr-ft-°F
$\alpha_2 = 0.7$ ft²/hr
$\alpha_1 = 0.35$ ft²/hr
$\delta = 0.5$
$\Gamma = 2$

Substituting the above values into Eq. 19 and trying various values of E_c gives for $E_c = 2.3$

$$1 = \frac{0.5e^{0.125(2.3)^2}\,[2\sqrt{\pi}\,A(2.3/\sqrt{2})]}{2\sqrt{\pi/0.5}[1 - A\,\{\sqrt{0.25}\,(2.3)\}]}$$

$$1 = \frac{(0.966)(3.544)(0.448)}{2.51[1 - 0.375]} = \frac{1.54}{1.57} \approx 1$$

Using $E_c = 2.3$ in Eq. 21 penetration rate

$$\frac{dx_c}{dt} = (1/2)(2.3)\sqrt{\frac{0.35}{1}}$$

$$\frac{dx_c}{dt} = 0.680 \text{ ft/hr}$$

Using $E_c = 2.3$ in Eq. 20 penetration depth

$$x_c = (2.3)\sqrt{0.35(1)}$$

$$x_c = 1.36 \text{ ft}$$

Nomenclature

E_c = critical dimensionless parameter
K_1 = thermal conductivity of the medium at critical temperature
K_2 = thermal conductivity of the medium below critical temperature
T_0 = absolute temperature at the surface
T_c = absolute critical temperature
t = time
x_c = critical temperature penetration depth
α_1 = thermal diffusivity of the medium at critical temperature
α_2 = thermal diffusivity of the medium below critical temperature
Γ = K_2/K_1 ratio
δ = α_1/α_2 ratio

One-Dimensional Solid Propellant Oscillatory Burner

M. D. HORTON[1]

U. S. Naval Ordnance Test Station, China Lake, Calif.

FOR SOME time the problem of oscillatory burning has plagued solid propellant rocket designers, and in the last few years much work, both experimental and theoretical, has been devoted toward understanding and controlling the phenomenon. Because of the complexity of the phenomenon, most theories concerning oscillatory burning (1–3)[2] have used a one-dimensional combustion model with the appropriate acoustical equations for the combustion chamber. Until recently there was no experimental justification for the use of a one-dimensional combustion model, as oscillatory burning had not been observed in chambers that approximated the one-dimensional situation. That such models might be valid was shown experimentally by Brownlee (4), who produced traverse oscillations in a slab burner, and Price (5), who succeeded in designing a burner that oscillated in the Helmholtz mode.

Received July 24, 1961.
[1] Chemical Engineer, Research Dept.
[2] Numbers in parentheses indicate References at end of paper.

In an attempt to produce a burner that would closely approximate the one-dimensional situation and would permit unambiguous experimental measurements, the author has developed two arrangements of a simple burner which exhibit oscillatory burning. The successful production of oscillatory burning in this chamber seems to be dependent on the minimization of chamber damping, the lack of which probably prevented previous investigators from obtaining oscillatory burning in a similar burner (5). These burners employ end-burning grains in a cylindrical, steel, side-vented chamber and are shown schematically in Fig. 1. Rather extensive tests with various lengths of the Type A burner have yielded first-mode longitudinal oscillations in the frequency range of 250 to 3000 cps. Neither tangential nor radial oscillations have been observed in the chamber. For the pressure range of 100 to 500 psi, used to date, several double-base and composite propellants have exhibited oscillatory behavior in this burner. The peak to peak amplitudes of the oscillations are characteristically about 10% of the mean pressure level in the chamber. A typical test record is shown in Fig. 2. Although limited tests have been conducted in the Type B burner, oscillations of a much higher amplitude (peak to peak values are about 30% of the mean chamber pressure) have been observed, as is illustrated in Fig. 3.

Of special interest is the fact that the oscillations shown in Fig. 3 were recorded by a transducer in contact with the rear

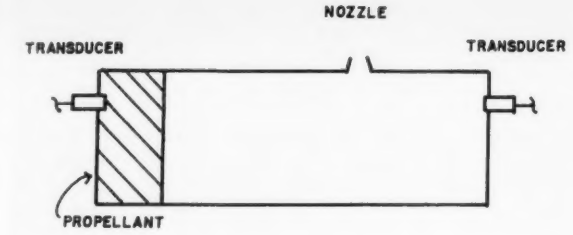

TYPE A

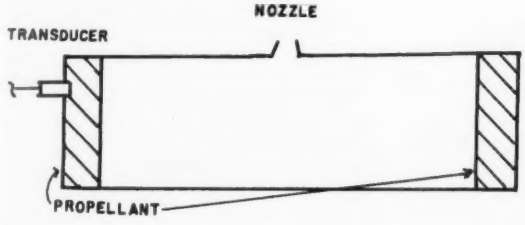

TYPE B

Fig. 1 Schematic drawings of chambers used to study oscillatory burning

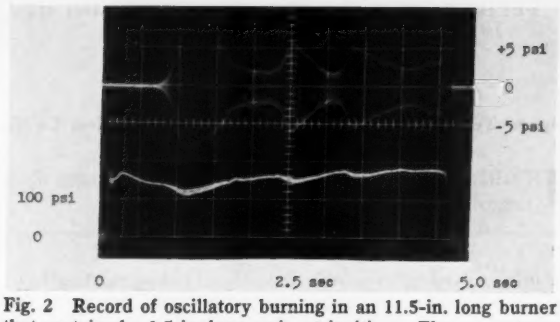

Fig. 2 Record of oscillatory burning in an 11.5-in. long burner that contained a 1.5-in. long grain at ignition. The upper trace is the envelope of the oscillations, and the lower is an unfiltered record of the pressure

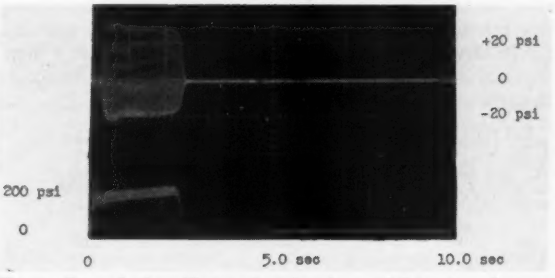

Fig. 3 Record of oscillatory burning in a 12.5-in. long burner that contained 1.0-in. long grains of propellant in each end at ignition. The upper trace is the envelope of the oscillations, and the lower is an unfiltered record of the pressure

surface of the propellant. The theory of McClure (6) predicts that the undamped pressure oscillations of the propellant are always at least as great as those of the combustion gases. The experimental data (7) agree with the theory and show that the propellant oscillations range from the same amplitude to ten times the amplitude of those in the gas.

Another interesting feature of the oscillatory burning in the chamber is revealed by Fig. 1. The mean chamber pressure is observed to decrease as the amplitude of the oscillations increases. If this effect is interpreted as being due to an interaction between the oscillations and the burning rate of the propellant, then, as Crump reports (8), pressure oscillations decrease the burning rate of the propellant.

The burners have many experimental applications, among which is their use to determine the acoustical admittance of the burning propellant surface. To do this, one would fire a burner of each type under suitable conditions to produce the same oscillatory wavelengths. During the onset of the oscillatory burning, the logarithmic increments of the pressure oscillations would be measured, and from these increments the rates of acoustical energy accumulation would be determined. The difference in the rates of accumulation would be caused by a doubling of the driving force, whereas the damping would be approximately unchanged. This difference then could be used to calculate both the chamber damping and the acoustical admittance of the burning propellant surface.

For experimental evaluation of the many current theories, considerable experimental ingenuity must be applied. The author believes that the task can be considerably simplified by the use of these one-dimensional oscillatory burners.

References

1 Hart, R. W. and McClure, F. T., "Combustion Instability: Acoustic Interaction With a Burning Propellant Surface," *J. Chem. Phys.*, vol. 30, no. 6, June 1959, p. 1501.

2 Shinnar, R. and Dishon, M., "Heat Transfer Stability Analysis of Solid Propellant Rocket Motors," *Progress in Astronautics and Rocketry (Solid Propellant Rocket Research*, Vol. 1), M. Summerfield (ed.), Academic Press, New York, 1960, p. 359.

3 Smith, A. G. "A Theory of Oscillatory Burning of Solid Propellants Assuming a Constant Surface Temperature," *Progress in Astronautics and Rocketry (Solid Propellant Rocket Research*, Vol. 1), M. Summerfield (ed.), Academic Press, New York, 1960, p. 375.

4 Brownlee, W. G. and Marble, E. F., "An Experimental Investigation of Unstable Combustion in Solid Propellant Rocket Motors." *Progress in Astronautics and Rocketry (Solid Propellant Rocket Research*, Vol. 1), M. Summerfield (ed.), Academic Press, New York, 1960, p. 455.

5 Price, E. W., Mathes, H. B., Crump, J. E. and McGie, M. R., "Experimental Research in Combustion Instability of Solid Propellants," *Combustion and Flame*, vol. 5, June 1961, pp. 149–162.

6 McClure, F. T., Hart R. W. and Bird, J. F., "Solid Propellant Rocket Motors as Acoustic Oscillators," *Progress in Astronautics and Rocketry (Solid Propellant Rocket Research*, Vol. 1), M. Summerfield (ed.), Academic Press, New York, 1960, p. 295.

7 Horton, M. D. "Oscillatory Burning of Solid Rocket Propellants," unpublished Ph.D. thesis, University of Utah, May 1961.

8 Crump, J. E. and Price, E. W., "The Effect of Acoustic Environment on the Burning Rate of Double Base Solid Propellants," ARS JOURNAL, vol. 31, no. 7, July 1961, pp. 1026–1029.

Terminating the Iterative Solution of Kepler's Equation

OLIVER K. SMITH[1]

Space Technology Laboratories Inc. Los Angeles, Calif.

IN ORBIT calculations, particularly those carried out on a large digital computer, Kepler's equation

$$E - e \sin E = M \qquad [1]$$

is often solved by Newton's method. That is, starting from some initial estimate E_0, a sequence $E_0, E_1, E_2 \ldots$ is generated

$$E_{i+1} = E_i + \delta E_i$$

$$\delta E_i = \frac{M - E_i + e \sin E_i}{1 - e \cos E_i}$$

If at the nth step $|\delta E_{n-1}|$ is less than some preassigned positive constant ϵ, then the sequence is terminated with E_n. Frequently the choice of ϵ has been arbitrary, but a more scientific selection is possible with the aid of the following theorem proved by Ostrowski (1).[2]

Let $f(x)$ be a real function of the real variable x, $f(x_0)f'(x_0) \neq 0$, $h_0 = -f(x_0)/f'(x_0)$, $x_1 = x_0 + h_0$. Consider the interval J_0: $[x_0, x_0 + 2h_0]$ and assume that $f''(x)$ exists in J_0, max $|f''(x)| = M$ in J_0 and

$$2|h_0|M \leqslant |f'(x_0)|$$

Starting with x_0, form the sequence x_v by the recurrence formula

$$x_{v+1} = x_v - f(x_v)/f'(x_v) \qquad (v = 0, 1, \ldots)$$

Then all x_v lie in J_0 and we have

$$x_v \to \zeta \quad (v \to \infty)$$

where ζ is the only root in J_0. Further, we have the relations

$$\frac{|x_{v+1} - x_v|}{|x_v - x_{v-1}|^2} \leqslant \frac{M}{2|f'(x_v)|} \qquad (v = 1, 2, \ldots)$$

$$|\zeta - x_{v+1}| \leqslant \frac{M}{2|f'(x_v)|} |x_v - x_{v-1}|^2 \qquad (v = 1, 2, \ldots)$$

Applying this result to Eq. 1 and taking e as a bound for the second derivative of $E - e \sin E$ gives the following:

Suppose that for some n

$$|\delta E_n| \leqslant (1/2)(1 - e \cos E_n) \qquad [2]$$

then Eq. 1 has only one solution E^* in the closed interval $[E_n, E_n + 2\delta E_n]$, and the Newton iteration sequence starting from E_n (and hence the entire sequence) converges to E^*. Furthermore, we have the relations

$$|E_{n+1} - E_n| \leqslant \frac{e}{2} \frac{(\delta E_n)^2}{1 - e \cos E_n} \qquad [3]$$

$$|E^* - E_{n+1}| \leqslant \frac{e}{2} \frac{(\delta E_n)^2}{1 - e \cos E_n} \qquad [4]$$

These expressions make it easy to establish a variety of suitable convergence criteria. Since Eq. 4 can be simplified to

$$|E^* - E_{n+1}| \leqslant \frac{1}{2} \frac{e}{1 - e} (\delta E_n)^2 \qquad [5]$$

we find that if we choose $\epsilon = 10^{-5}$ radian, then for $e \leqslant 0.99$ and any E_{n+1} such that $|\delta E_n| \leqslant \epsilon$, the sequence is convergent, and the truncation error is less than 0.5×10^{-8} radian. In case E lies in the interval in which $\cos E_n < 1/2$, then even with $\epsilon = 10^{-4}$ radian, the truncation error remains less than 10^{-8} for any e less than one.

Since Kepler's equation is usually solved repeatedly for the same eccentricity, it may be worthwhile to make the test depend upon e, for instance, by computing

$$\epsilon = 10^{-4} \sqrt{(1 - e)/e} \qquad [6]$$

each time the eccentricity changes. The resultant truncation error is less than 10^{-8} radian, and the test is often less stringent than the others suggested.

These results show that in several computer programs the convergence criterion could be relaxed considerably. Experience to date has confirmed the analysis.

Received May 5, 1961.

[1] Associate Manager, Mathematical Analysis Dept.

[2] Numbers in parentheses indicate Reference at end of paper.

Reference

1 Ostrowski, A. M., *Solution of Equations and Systems of Equations*, Academic Press, New York, 1960, p. 44.

Technical Comments

Proposal for a Simple Visual Tracking Arrangement for Space Probes

STEPHEN A. KALLIS JR.[1]

Dunedin, Fla.

A CLEAR advantage in location and tracking was demonstrated by the Echo I balloon satellite. As well as its intended purpose of being a communication relay, it was in addition an easily recognizable landmark in the sky, owing to its rapid relative motion.

It is possible to utilize a variation of this effect to produce a simple tracking arrangement. One such arrangement would be to include an Echo type sphere with every space probe and allow it to inflate once the atmosphere has been effectively left behind. This solution would seem to be impractical for a number of reasons; one is that a sacrifice of instrumentation space to the collapsed sphere would result.

An alternate suggestion is to manufacture two reflecting leaves which could be wrapped about the body of the probe. Once the atmosphere has been left behind, a slight axial rotation of the vehicle would cause the leaves to unfurl, and the centrifugal force of the rotation would be sufficient to keep them taut. If these leaves were manufactured of metallized mylar, their mass would probably be rather slight. For example, a piece of mylar of $^1/_2$-mil thickness and with an area of 7.2×10^3 sq in.has a weight of less than 20 oz.

Such a probe would not only be able to utilize the light of the sun for a visual identification, but the rotation of the device would itself be a means of visual identification as said rotation would produce an occulting effect to observers. This would be extremely useful for naked eye observational identification when the relative motion against the background of stars becomes less pronounced than in Echo I's case, such as in a lunar probe.

It must, of course, be pointed out that the proper positioning of the vehicle is necessary for the success of the operation, but this can and should be accomplished before the reflecting leaves are released.

Received Nov. 21, 1960.

[1] Lieut., USNR. Associate Member ARS.

New Patents

George F. McLaughlin, *Contributor*

Directional thrust control (2,981,501). E. T. Schaefer, Houston, Tex.

Pilot enclosing capsule with at least four rocket engines on universal connections allowing their simultaneous movement in a 360-degree path to control direction of capsule movement.

Clamp ring release for aircraft booster (2,982,497). W. E. Worley (ARS member), Mishawaka, Ind., assignor to The Bendix Corp. (ARS corporate member).

Pressure responsive means connected to a clamp releaser aircraft or missile upon movement of a valve actuated in response to acceleration forces.

Rocket motor attachments (2,982,503). T. C. Campbell, St. Annes-on-Sea, England, assignor to The English Electric Co., Ltd.

Dual purpose aircraft for high-thrust range and high-endurance long range, without structural change. A pressurized ventral auxiliary fuel tank and rocket motor are fitted to structure.

Rocket fuels (2,982,636). W. B. Reynolds, Bartlesville, Okla., assignor to Phillips Petroleum Co.

Solid rocket propellant containing nitrated hydroxylated polymers and a solid inorganic oxidizing salt admixed with fuel component.

Motor fuel composition (2,982,637). H. W. Kruse, China Lake, Calif., assignor to the U. S. Navy.

About 44.5 to 62.5 mole per cent proparagyl alcohol, and the remainder hydrazine. Freezing point range varies from about −49.2° to −55.6°C.

Nitrocellulose propellants (2,982,638). Dr. R. A. Cooley (ARS member), and H. A. Bruson, North Haven, Conn., assignors to Olin Mathieson Chemical Corp. (ARS corporate member).

Smokeless powder grain of gelatinized vitrocellulose and about 0.5 to 5% lead salt of an aliphatic acid. Lead salt has more than six carbon atoms, and is uniformly dispersed.

Means to prevent perforation of starter disk during ignition delay (2,982,090). B. M. Adelman (ARS member), Los Angeles, Calif., assignor to Phillips Petroleum Co.

Wire mesh member positioned between starter disk and aft end of combustion chamber and spaced from blowout disk.

Compound ramjet turbo-rocket engines (2,982,093). B. L. Belcher (and 8 others), London, England, assignors to D. Napier and Son, Ltd.

Rocket type generator and a turbine driven by gas. Compressor coupled to turbine delivers air to combustion chamber.

Gas generating device (2,982,095). P. B. Campbell (ARS member), Kansas City, Mo., assignor to Westinghouse Electric Corp. (ARS corporate member).

Primary combustible charge within a housing, and a second charge initially blocking flow of gaseous products, but being consumable within a predetermined time after ignition.

Torque limiter (2,982,096). E. J. Bevers and R. J. Wente, Indianapolis, Inc., assignors to General Motors Corp. (ARS corporate member).

Flowmeter connected to fuel line in a gas turbine limits fuel flow to a predetermined value of torque output.

Rocket motor (2,982,097). E. H. Hull (ARS member), Scotia, N. Y., assignor to the U. S. Army.

Reactant head comprising a disk-shaped back plate. Rearward part has equiangularly-spaced inwardly and rearwardly inclined conduits of progressively increasing size.

Control system (2,984,971). H. E. Corbitt, R. W. Cunningham and R. M. Hill Jr., Azusa, Calif., assignors to Aerojet-General Corp. (ARS corporate member).

Electrical system, responsive to changes in fluid pressure, transduces such changes to mechanical movement for control of flight direction.

Variable area nozzle (2,984,972). R. L. Davidson, Lynnfield Center, Mass., assignor to General Electric Co. (ARS corporate member).

Flow restrictor in gas flow path comprising two parts, one of a material for disintegrating over one range of flow conditions, and another part for disintegrating over a second range of conditions.

Liquid-solid propellant rocket (2,984,973). A. F. Stegelman, Bartlesville, Okla., assignor to Phillips Petroleum Co.

Piston in a casing forms a fluid-tight container between piston and payload section. Solid propellant bonded to piston in combustion chamber.

Control for cartridge starter (2,984,976). E. A. Volk Jr., Hasbrouck Heights, N. J., assignor to The Bendix Corp. (ARS corporate member).

Solid propellant for turbine engines. Gas generated actuates pneumatic means when a control is actuated by a predetermined turbine speed or gas pressure.

Liquid cutting of hard materials (2,985,050). B. G. Schwacha, Anaheim, Calif., assignor to North American Aviation, Inc. (ARS corporate member).

Discharge nozzle twenty thousandths of an inch ejects liquid pressurized to thousands of atmospheres of pressure in needlelike jet at supersonic velocity.

Composite rubber base propellant (2,985,526). E. D. Guth, Bartlesville, Okla., assignor to Phillips Petroleum Co.

Solid Propellant consisting of 50 to 90 weight per cent of a solid oxidizer admixed with 10 to 50 weight per cent of self-curing binder.

Mechanism for simulating relative movements of the Earth, the celestrial sphere and an Earth satellite (2,985,969). R. H. Farquhar, St. Davids, Pa.

Transparent celestial sphere disposed about Earth sphere for rotation at constant speed about N-S poles. Satellite at free end of sweep arm is mounted on a radial arm between spheres.

Shock absorbing means for rocket propellant grains (2,986,001). Dr. L. Green Jr. (ARS member), West Covina, Calif., assignor to Aerojet-General Corp. (ARS corporate member).

Annular space between grain and combustion chamber wall contains layer of dilatant liquid for absorbing shock of grain ignition.

Leaky-type exhaust nozzle (2,986,002). A. Ferri (ARS member), Rockville Centre, N. Y., assignor to Curtiss-Wright Corp.

Nozzle having a portion comprising tapering segments with smaller ends downstream. Segments separated by triangular gaps through which part of exhaust gases escape.

Freestream ram air turbine (2,986,219). W. P. Boardman Jr, (ARS member), G. P. Carver, W. W. Carlton, and J. C. Wise, Cleveland, Ohio, assignors to The Marquardt Corp. (ARS corporate member).

Blades on a rotor mounted for movement through openings in a turbine casing. Area of blades presented to freestream varied to maintain constant turbine speed.

Aircraft cockpit arrangement (2,986,361). G. E. Codding (ARS member), Lawndale, Calif.

Spherical sealable compartment in nose housing detachably connected to fuselage. Receptacle units for hands and feet of pilot operate controls of vehicle.

High speed far infrared detector and heat seeking control for guided missiles (2,986,637). Dr. F. E. Null (ARS member), Shalimar, Fla.

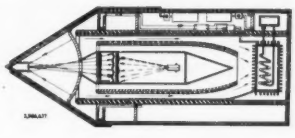

Cells arranged as a mosaic. Resistance of film surrounding central condenser varies with completeness of absorbed layer of water molecules as controlled by incident radiation. (Note: Application for patent filed August 1946.)

EDITOR'S NOTE: Patents listed above were selected from the Official Gazette of the U. S. Patent Office. Printed copies of patents may be obtained from the Commissioner of Patents, Washington 25, D. C., at a cost of 25 cents each; design patents, 10 cents.

Book Notes

Plastic Flow and Structure in Solids, Tracy Y. Thomas (Graduate Institute for Mathematics and Mechanics, Indiana University, and Applied Mathematics Staff, U. S. Naval Research Laboratory), Academic Press Inc., New York, 1961, 263 pp. $8.50.

Chapters: 1) Basic Invariants in the Mechanics of Continuous Media; 2) Conditions of Compatibility; 3) Waves in Elastic Media; 4) Perfectly Plastic Solids; 5) Characteristic Surfaces and Wave Propagation; 6) Instability and Fracture. *Appendix:* Equilibrium Theory of Luders Bands.

This is the second volume of "Mathematics in Science and Engineering," a series of monographs and textbooks edited by Richard Bellman. It is devoted mainly to a study of the propagation, growth, and decay of discontinuities in solids. The material is based largely on articles published by the author in various mathematical journals during the preceding five years.

Optimal Design of Chemical Reactors, a Study in Dynamic Programming, Rutherford Aris (Department of Chemical Engineering, Institute of Technology, University of Minnesota), Academic Press Inc., New York, 1961, 183 pp. $7.00.

Chapters: 1) Introduction; 2) Principal Notions of Dynamic Programming; 3) Mathematical Models for Reactor Design; 4) the Objective Function; 5) Continuous Flow Stirred Tank Reactor; 6) Multibed Adiabatic Reactor; 7) Tubular Reactor; 8) Stochastic Problems; 9) Optimal Operation of Existing Reactors.

This third volume of "Mathematics in Science and Engineering" considers problems of chemical reactor engineering and shows how the principal optimal problems of chemical reactor design can be solved by dynamic programming.

Reliability: Theory and Practice, Igor Bazovsky (Design Engineer, Research and Development Dept., United Control Corp.), Prentice-Hall Inc., Englewood Cliffs, N. J., 1961, 286 pp. $10.95.

Contents: 26 chapters on such subjects as the concept of reliability, the exponential case of chance failures, useful life of components, exponential and Poisson distributions, reliability of stand-by systems, safety and reliability of aircraft and airborne systems, design analysis examples, confidence limits, and state of art reliability.

This volume is one of a space technology series edited by C. W. Besserer and Floyd E. Nixon. It encompasses the entire field of reliability engineering. The implications of component parts reliabilities are analyzed and discussed, and a new concept of the life function of components is presented.

Gyroscopes: Theory and Design, with Applications to Instrumentation, Guidance, and Control, edited by Paul H. Savet (Staff Scientist, Arma Div., American Bosch Arma Corp., and Adjunct Professor, Polytechnic Institute of Brooklyn), McGraw-Hill Book Co. Inc., New York, 1961, 396 pp. $12.75.

Contents: 12 chapters contributed by different authors. 1) Fundamentals of Vector and Operational Calculus; 2) Theory of the Gyroscope—Part 1; 3) Theory of the Gyroscope—Part 2; 4) Functional Characteristics and Restraints; 5) the Gyrocompass; 6) the Gyro Vertical; 7) Inertial Navigation—Part 1; 8) Inertial Navigation—Part 2; 9) Fundamentals of Gyro Design; 10) Gyroscopic Elements; 11) Electrical Design of Gyros; 12) Gyro Evaluation.

This book is a detailed account of modern engineering theory and practice in high precision gyroscopes, reflecting the thinking of 11 scientists currently working on gyro research and development. It is designed to serve as a foundation in the theory of gyroscopes and includes coverage of the gyrocompass, stable gyro verticals, and inertial guidance systems.

Heat-Transfer Calculations by Finite Differences, George Merrick Dusinberre (Professor of Mechanical Engineering, Pennsylvania State University), International Textbook Co., Scranton, Pa., 1961, 280 pp. $12.75.

Chapters: 1) Thermal Properties; 2) Fundamental Equations; 3) Alternative Formulations; 4) Analytical and Analog Methods; 5–8) Transients; 9) Steady State—Simple Systems; 10) Steady State—Complex Systems; 11) Variable Properties; 12) Digital Computers; 13) Miscellaneous Examples; 14) Problems. *Appendix:* Elrod's Coefficients, the Graphical Method, the Liebmann Method, etc.

This book is intended as a guide to finite difference methods for heat transfer calculations. It is built around a series of examples which cover a variety of applications.

Combustion, Flames, and Explosions of Gases, 2nd ed., edited by Bernard Lewis and Guenther von Elbe (both of Combustion and Explosives Research Inc.), Academic Press Inc., New York, 1961, 708 pp. $22.00.

Contents: Part 1) Chemistry and Kinetics of the Reactions Between Gaseous Fuels and Oxidants; Part 2) Flame Propagation; Part 3) State of the Burned Gas; Part 4) Problems in Technical Combustion Processes.

The purpose of this volume is to provide the chemist, physicist, and engineer with a basis for understanding combustion phenonema. In this new edition particular emphasis has been placed on the modification of combustion wave propagation due to heat loss to the unburned medium and to localized changes of mixture composition by diffusional processes.

Progress in Very High Pressure Research, Proceedings of an International Conference, edited by F. P. Bundy, W. R. Hibbard Jr. and H. M. Strong (Staff Members of the Research Laboratory, General Electric Co.), John Wiley & Sons Inc., New York, 1961, 314 pp. $12.00.

Contents: Introductory addresses and a total of 27 technical papers on such subjects as high pressure apparatus, optical studies at high pressure, thermodynamics of activated processes, state of matter at high pressure, properties of semiconductors at high pressures, nuclear magnetic resonance in solids and liquids under pressure, and large pressure units.

This book consists of the papers and discussions presented at an International Conference held at Lake George, N. Y., June 13 and 14, 1960. The conference was sponsored jointly by the Materials Central Wright Air Development Div., USAF, and the Research Laboratory of General Electric Co. The sessions were arranged to bear mainly on the topics of equipment and technique, structures of materials formed under high pressure, and behavior of matter under high pressure. The book includes a review of high pressure work in the USSR presented by L. F. Vereshchagin.

Medical and Biological Aspects of the Energies of Space, edited by Paul A. Campbell (Medical Corps, USAF), Columbia University Press, New York, 1961, 470 pp. $10.00.

Contents: 24 chapters contributed by different authors. Part 1) Delineation; Part 2) Application; Part 3) Protection. *Appendices:* 1) Definitions of Terms, Quantities, and Units; 2) Conversion Factors.

This volume has been compiled from papers delivered at the October 1960 symposium sponsored by the School of Aerospace Medicine of the USAF Aerospace Medical Center at Brooks Air Force Base, Texas. The symposium was arranged by the Southwest Research Institute of San Antonio. The papers delineate the energies of space, describe their potential applications, and explain their dangers for man.

The books listed here are those recently received by the ARS from various publishers who wish to announce their current offerings in the field of astronautics. The order of listing does not necessarily indicate the editors' opinion of their relative importance or competence.

Technical Literature Digest

M. H. Smith, *Associate Editor*
The James Forrestal Research Center, Princeton University

Propulsion and Power (Combustion Systems)

Control of Gas-Turbine and Ramjet Engines, by L. A. Zalmanzon and B. A. Cherkasov, *NASA Tech. Translation* F-41, July 1961, 257 pp. (Transl. of book of Govt. Defense Industry Press, Moscow, 1956.)

Investigation of Veil Cooling for Radial-Flow Turbines, by W. U. Rossler and J. W. Mitchell, *Garrett Corp., Air Res. Manufacturing Div. Air Res. Rep.* K-451-R, May 1961, 164 pp., 19 refs.

Design of a Large, Two-Stage, Light-Gas Model Launcher, by W. B. Stephenson and D. E. Anderson, *Arnold Engng. Dev. Center,* AEDC-TR-61-6, June 1961, 55 pp.

A Single Chart System of Interior Ballistics, by R. C. Strittmater, *Aberdeen Proving Ground, Ballistic Res. Labs., BRL Rep.* 1126, March 1961, 12 pp.

Advanced Ignition System for Solid Propellant Rocket Motors, by J. J. Priapi, ARS JOURNAL, vol. 31, no. 7, July 1961, pp. 1029–1031.

Solid Rockets for Space Vehicles, by William Cohen, ASTRONAUTICS, vol. 6, no. 8, Aug. 1961, pp. 22–25, 50–56.

What Costs for Big Boosters? by James Schad, ASTRONAUTICS, vol. 6, no. 8, Aug. 1961, pp. 26–27, 56–57.

Thermodynamics of Ramjet Flow Processes, by F. Bader and E. A. Bunt, *Johns Hopkins Univ., Appl. Phys. Lab.* TG 370-2, Feb. 1960, 177 pp.

An Investigation of Transverse Mode Combustion Instability in Liquid Propellant Rocket Motors, by Frederick H. Reardon, *Princeton Univ., Dept. Aeron. Engng., Rep.* 550, 1961, 123 pp., 58 figs. (Thesis, Ph.D.)

Kinetics, Equilibria and Performance of High Temperature Systems; Proceedings of the First Conference, (Combustion Institute Western States Section, 1st Conference, Los Angeles, Nov. 1959) Gilbert S. Bahn and Edward E. Zukoski (eds.), Butterworth & Co., London, 1960, 255 pp.

The Computation of High Temperature Engine Performance, by H. E. Brandmaier and J. J. Harnett, pp. 171–180.

Perturbation Technique for Fitting Jet Engine Performance Parameters, by Wayne E. Simon, pp. 186–192.

An Analysis of Rocket Engine Performance with Nearly Constant Temperature Burning in the Combustion Chamber and Exhaust Nozzle, by Perry L. Blackshear Jr., pp. 199–208.

Automatic Control of Aviation Engines, A. A. Sheviakava (ed.), Moskva, Gos., Izdatel. Obor. Prosh., 1959, 183 pp. (In Russian.)

Investigation of the Characteristic Regulation of Compressed Gas Ratios, for Use in Reaction Motors, by L. A. Zalmanson, Iu. L. Mach, and G. Paitch Stepanov, pp. 5–73.

EDITOR'S NOTE: Contributions from Professors E. R. G. Eckert, E. M. Sparrow and W. E. Ibele of the Heat Transfer Laboratory, University of Minnesota, are gratefully acknowledged.

Investigation of the Laminar Flow of Air in Capillary Tubes of Pneumatic Systems, by A. V. Bogacheva, pp. 74–113.

A Calculation of a Centrifugal Atomizer, by A. M. Prakhov, pp. 113–183.

Verification of Nozzle Admittance Theory by Direct Measurement of the Admittance Parameter, by Luigi Crocco, Rodolfo Monti and Jerry Grey, ARS JOURNAL, vol. 31, no. 6, June 1961, pp. 771–775.

Selection of a Pressurization System for a Storable Liquid Propellant Rocket Engine, by C. J. Kaplan, ARS JOURNAL, vol. 31, no. 6, June 1961, pp. 786–792.

Correction Factor for Annular Nozzles, by N. D. Vlachos, ARS JOURNAL, vol. 31, no. 6, June 1961, pp. 822–823.

Propulsion and Power (Noncombustion)

Radial Flux or Field of an Isotropic, Cylindrical Source of Finite Extent, by Edmund E. Callaghan and Lawrence Flax, *NASA Tech. Note* D-873, July 1961, 27 pp.

Magnetohydrodynamic Power Generation Experiment, by F. C. Foshag and A. E. Were, *Gen. Electric Co., Missile and Space Vehicle Dept.* T.I.S. R59SD447, Dec. 1959, 12 pp., 10 figs.

Gaseous Fission Reactors for Booster Propulsion, by Robert V. Meghreblian, *Calif. Inst. Tech., Jet Propulsion Lab. Tech. Rep.* 32–94, March 1961, 15 pp.

Thrust-Unit Requirements for Electrically Propelled Spacecraft, by David G. Elliott and Jerome H. Molitor, *Calif. Inst. Tech., Jet Propulsion Lab. Tech. Rep.* 32-117, June 1961, 9 pp.

Power Input to a Small Flat Plate from a Diffusely Radiating Sphere, With Application to Earth Satellites, by F. G. Cunningham, *NASA Tech. Note* D-710, July 1961, 15 pp.

Pressure Energy Exchange Principle, by John E. Minardi, Charles E. Pax and Harold E. Wright, *Air Force Res. Div., Aeron. Res. Labs.,* ARL 45, May 1961, 24 pp.

Thermionic Conversion of Heat to Electricity, by W. B. Nottingham, G. N. Hatsopoulos and E. N. Carabateas, *Aerospace Engng.,* vol. 20, no. 7, July 1961, pp. 14–15, 82–85.

Feasibility of Turbulent Vortex Containment in the Gaseous Fission Rocket, by M. L. Rosenzweig, W. S. Lewellen and J. L. Kerrebrock, ARS JOURNAL, vol. 31, no. 7, July 1961, pp. 873–883.

Propulsion System Using a Cavity Reactor and Magnetohydrodynamic Generator, by Richard J. Rosa, ARS JOURNAL, vol. 31, no. 7, July 1961, pp. 884–889.

Photochemistry and Space Power Generation, by J. N. Pitts, J. David Margerum and Wm. E. McKee, ARS JOURNAL, vol. 31, no. 7, July 1961, pp. 890–895.

Internal Design Consideration for Cavity-Type Solar Absorbers, by Charles W. Stephens and Alan M. Haire, ARS JOURNAL, vol. 31, no. 7, July 1961, pp. 896–901.

Applications for Lower-Power Nuclear Rockets, by Ralph S. Cooper, ASTRONAUTICS, vol. 6, no. 8, Aug. 1961, pp. 34–36, 66–69.

The Pluto Program, by Harry L. Reynolds, ASTRONAUTICS, vol. 6, no. 8, Aug. 1961, pp. 37–39, 72.

Spectral Response of Solar Cells, by Brian Dale and F. P. Smith, *J. Appl. Phys.,* vol. 32, no. 7, July 1961, pp. 1377–1381.

Theory of an Electromagnetic Mass Accelerator for Achieving Hypervelocities, by Karlheinz Thom and Joseph Norwood, Jr., *NASA Tech. Note* D-886, June 1961, 36 pp.

A Review of Republic's Pinch Engine Experimental Program, by Irving Granet and William J. Guman, *Republic Aviation Corp., Plasma Propulsion Lab.* PPL-60-15 (160), Oct. 1960, 40 pp.

On Energy Problems of Interstellar Space Flight, by G. Marx, *Astronautica Acta,* vol. 6, no. 6, 1960, pp. 366–372. (In German.)

Thermionic Reactor Systems, by R. C. Howard, *Nuclear Sci. and Engng.,* vol. 10, no. 2, June 1961, pp. 173–182.

Application of Rapid Fission Gas Analyses to an Off-Gas System Test, by R. C. Koch, G. L. Grandy and J. A. Roll, *Nuclear Sci. and Engng.,* vol. 10, no. 2, June 1961, pp. 183–189.

Some Properties of Cesium Plasma in a Thermoelectronic Energy Converter, by N. D. Morgulis and Yu. P. Korchevoi, *Soviet Phys.: Doklady,* vol. 6, no. 1, July 1961, pp. 71–73.

Reactor Core Temperature Measurement, by L. H. Shinault and T. F. McGrath, ARS JOURNAL, vol. 31, no. 6, June 1961, pp. 799–803.

Power Supplies for Space Vehicles, by N. W. Snyder, *Astronautica Acta,* vol. 6, no. 6, 1960, pp. 271–310.

Status of the Ion-Propulsion Effort, by Eugene Urban, ASTRONAUTICS, vol. 6, no. 6, June 1961, pp. 34–35.

Nuclear Rocket Engine Control, by R. R. Mohler and J. E. Perry Jr., *Nucleonics,* vol. 19, no. 4, April 1961, pp. 80–84.

Gaseous Propulsion Reactors, by R. V. Meghreblian, *Nucleonics,* vol. 19, no. 4, April 1961, pp. 95–99.

The Case for Nuclear Energy, by H. B. Finger, *Nucleonics,* vol. 19, no. 4, April 1961, pp. 58–63.

Power Plants for Outer Space, by J. M. Allen, *Battelle Tech. Rev.,* vol. 10, no. 2, Feb. 1961, pp. 3–6.

Compact Reactors for Space Power, by H. M. Dieckamp, R. Balent and J. R. Wetch, *Nucleonics,* vol. 19, no. 4, April 1961, pp. 73–76.

Radionuclide Power for Space Missions, by D. G. Harvey and J. G. Morsel, *Nucleonics,* vol. 19, no. 4, April 1961, pp. 69–72.

Lightweight Solar Concentrator Development, by R. Gillette, H. E. Snyder and T. Timar, *Solar Energy,* vol. 5, no. 1, Jan.-March 1961, pp. 24–28.

KIWI Tests Pave Way to Rover, by R. E. Schreiber, *Nucleonics,* vol. 19, no. 4, April 1961, pp. 77–79.

The State of Development of Propulsion Systems for Space Flight, by G. F. Au, *Luftfahrttechnik*, vol. 7, no. 1, Jan. 10, 1961, pp. 15–25. (In German.)

Electrical Propulsion in Space, by G. Giannini, *Scien. Amer.*, vol. 204, no. 3, March 1961, pp. 57–65.

Cut-off Parameter of the Impulse Dispersion Coefficients of Systems with Long-Range Interaction, by G. Ecker and D. Voslamber, *Zeitschrift fur Naturforschung*, vol. 15A, no. 12, Dec. 1960, pp. 1107–1108. (In German.)

Optical Characteristics of Silicon Solar Cells and of Coatings for Temperature Control, by C. A. Escoffery and W. Luft, *Solar Energy*, vol. 4, no. 4, Oct. 1960, pp. 1–10.

Randomly Rotating Spherically Arrayed Silicon Solar Energy Converters, by W. Luft, *Solar Energy*, vol. 4, no. 4, Oct. 1960, pp. 33–39.

Propellants and Combustion

Statistical Analysis of Gallery Variables Affecting the Probability of Ignition by Explosives, by R. L. Grant and R. W. Van Dolah, *Bureau of Mines, Rep. of Investigations* 5760, 1961, 25 pp.

The Nature of the Fluctuation Bands of Boric Acid, by A. A. Mal'tsev, V. K. Mateev and V. M. Tatevskii, *The Johns Hopkins Univ. Appl. Phys. Lab.* TG 230-T238, May 1961, 5 pp. (Transl. from *Doklady Akademii Nauk SSSR*, vol. 137, no. 1, 1961, pp. 123–125.)

Approximate Calculations of Spectral Emissivities in the Infrared for HCl in the Strong-Line Approximation, by L. D. Gray, *Calif. Inst. Tech., Daniel and Florence Guggenheim Jet Propulsion Center Tech. Rep.* 37, May 1961, 6 pp.

Absolute Infrared Intensity Measurements for NO_2 and N_2O_4, by A. Guttman, *Calif. Inst. Tech., Daniel and Florence Guggenheim Jet Propulsion Center*, June 1961, 112 pp., 62 figs.

Model Experiments on Atomization of Liquids, by Mintscho Popov, *NASA Tech. Translation* F-65, July 1961, 33 pp. (Transl. from *Revue de Mécanique Appliquée*, Rumania, vol. 1, no. 1, 1956, pp. 71–88.)

Measurements of the Dissociation Rate of Molecular Oxygen, by Charles J. Schesnayder Jr. and John S. Evans, *NASA Tech. Rep.* R-108, 1961, 37 pp.

Burning Rate Measurement of Solid Propellants, by Lawrence Spenadel, *Rev. Scien. Instr.*, vol. 32, no. 7, July 1961, pp. 837–839.

Universal Apparatus for Determining Rates of Evaporation and Decomposition of Various Substances in a Vacuum, by D. V. Ignatov and Yu. N. Lebedev, *Instruments and Experimental Techniques*, no. 6, June 1961, pp. 967–969.

Effect of Acoustic Environment on the Burning Rate of Double-Base Solid Propellants, by J. E. Crump and E. W. Price, ARS JOURNAL, vol. 31, no. 7, July 1961, pp. 1026–1029.

Progress in Combustion Science and Technology, Vol. 1, by J. Ducarmé, Melvin Gerstein and H. Lefebre, Pergamon Press, New York, 1960, 226 pp.

Flow Visualization Techniques, by E. F. Winter, pp. 1–36, 80 refs.

Chemical Analysis in Combustion Chamber Development, by B. Toone, pp. 37–59, 17 refs.

Aerodynamic Influences on Flame Stability, by M. V. Herbert, pp. 61–109, 35 refs.

Geometric-Optical Techniques in Combustion Research, by F. J. Weinberg, pp. 111–144, 93 refs.

Flame Quenching, by A. E. Potter Jr., pp. 145–181, 78 refs.

Ignition in Liquid Propellant Rocket Engines, by Edward A. Fletcher and Gerald Morrell, pp. 183–216.

Ozone Chemistry and Technology (International Ozone Conference, Chicago, Nov. 1956), American Chemical Society, Washington, D. C., 1959, 465 pp.

Laboratory Techniques for Handling High-Concentration Liquid Ozone, by A. C. Jenkins, pp. 13–21.

Physical Properties of Liquid Ozone-Oxygen Mixtures: Density, Viscosity, and Surface Tension, by C. K. Hersh, A. W. Berger and J. R. Callaway Brown, pp. 22–27.

Detonation Properties of Ozone, by S. A. Harper and W. E. Gordon, pp. 28–37.

Pure Ozone Flame and the Combustion of Various Fuel Gases in Pure Ozone, by A. G. Streng and A. V. Grosse, pp. 38–43.

Separation of Ozone from Oxygen by a Sorption Process, by G. A. Cook, A. D. Kiffer, C. V. Klumpp, A. H. Malik and L. A. Spence, pp. 44–52.

Transfer of Ozone from Oxygen to a Carrier Gas, by F. R. Balcar, W. Dennis and J. J. Rendos, pp. 53–56.

Mechanism of Gas Phase Decomposition of Ozone. Thermal and Photochemical Reactions, by A. E. Axworthy Jr. and S. W. Benson, pp. 388–397.

Implications of Data on the Gas Phase Decomposition of Ozone, by S. W. Benson and A. E. Axworthy Jr., pp. 398–404.

Experimental Investigation of Heat Flux at the Upper Limit of Nucleate Boiling for Two Mixtures of Hydrazine and Unsymmetrical Dimethylhydrazine, by Arvel B. Witte, *Calif. Inst. Tech., Jet Propulsion Lab. Tech. Rep.* 32–78, April 1961, 8 pp.

Physical Gas Dynamics (Transl. from the Russian by R. C. Murray and D. R. H. Phillips), A. S. Predvoditelev (ed.), Pergamon Press, New York, 1961, 183 pp.

Formation of Shock Discontinuity Before a Flame Front, by G. D. Salamandra and O. A. Tsukhanova, pp. 164–178.

Interaction of a Flame with a Shock Discontinuity, by G. D. Salamandra, pp. 179–183.

Kinetics, Equilibria and Performance of High Temperature Systems; Proceedings of the First Conference, (Combustion Institute Western States Section, 1st Conference, Los Angeles, Nov. 1959), Gilbert S. Bahn and Edward E. Zukoski (eds.), Butterworth & Co., London, 1960, 255 pp.

Chemical Species in High Temperature Systems, by R. S. Scheffe and C. B. Henderson, pp. 1–4.

Estimation of the Heats of Formation of Gaseous Combustion Product Molecules, by C. J. O'Brien, J. R. Perrin and J. Perrine, pp. 5–17.

Some Provisional Tables of Species Thermodynamic Properties, by R. R. Koppang, C. M. Sherwood and G. S. Bahn, pp. 18–29.

Automatic Computation of Ideal Gas Thermodynamic Functions for Diatomic Molecules, by J. S. Gordon and R. Robinson, pp. 30–34.

On the Apparent Divergence of the Thermodynamic Properties of Dilute Gases at High Temperatures: Thermodynamic Functions for Diatomic Molecules, by L. Haar, pp. 35–38.

The Thermodynamic Properties of the Products of H_2-O_2 Combustion at Elevated Temperatures, by W. C. Moffatt, F. D. Skinner and R. J. Zaworski, pp. 53–57.

Equilibria at High Temperatures for the Formation of the Molecular Species C_2, C_3, Cu_2 and Si_2, by S. Zaff, L. E. Ashley and C. M. Cobb, pp. 58–65.

Performance Calculations for Reaction Engines: Pt. I. Performance Parameters, by D. G. McMahon, pp. 66–68. **Pt. II. A Brief Survey of Past and Current Methods of Solution for Equilibrium Composition,** by H. E. Brandmaier and J. J. Harnett, pp. 69–73.

Calculation of the Thermodynamic Properties of Multi-Compound Systems and Evaluation of Propellant Performance Parameters, by Stuart R. Brinkley Jr., pp. 74–81.

Analysis of the Mathematical Model for Chemical Equilibrium, by John H. Hancock and Theodore S. Motzkin, pp. 82–89.

Propellant Thermodynamic Performance Calculations for Rocket Engines, by P. G. Baer, R. Greene, H. Smith and J. Wortman, pp. 90–104.

Machine Computation of Chemical Equilibria in Reacting Systems, by David G. McMahon and Richard Roback, pp. 105–114.

Programme for Computing Equilibrium Temperature and Composition of Chemical Reactions, by R. M. Mentz, pp. 115–122.

Note on the Linearization Method for Computing Chemical Equilibrium in Complex Systems, by Roger L. Wilkins, pp. 123–127.

Performance Calculations Using an IBM 650 Computer, by J. D. Breazeale, pp. 128–136.

Hand Calculation of Equilibrium Compositions as a Learned Habit, and Speed-up Effected with the IBM 610 Computer, by Gilbert S. Bahn, pp. 137–140.

Computation of Complicated Combustion Equilibria on a High-Speed Digital Computer, by D. S. Villars, pp. 141–151.

A Practical Approach to Computer Programming for Specific Impulse Calculations, by L. J. Gordon and H. E. Boerlin, pp. 152–160.

Calculation of Thermodynamic Properties of Combustion Gases with a Small Punch-Card Electronic Computer, by Robert W. Smith Jr. and Edwin Cook, pp. 161–165.

Extension to Multiphase Systems of the RAND Method for Determining Equilibrium Compositions, by B. R. Kubert and S. E. Stephenou, pp. 166–170.

Computing Complex Chemical Equilibria by Minimizing Free Energy, by Leonard M. Naphtali, pp. 181–183.

A Note on the Newton-Raphson Technique, by Leonard M. Naphtali, p. 184–192.

A Spray Combustion Model with Droplet Breakup, by Samuel Z. Burstein and Leonard M. Naphtali, pp. 193–198.

Methods for Computing the Theoretical Behavior of Premixed Reacting Flowing Gases, by H. A. Friedman and E. F. Eckel, pp. 209–218.

Studies of Chemical Non-equilibrium in Hypersonic Nozzle Flows, by J. Gordon Hall and Anthony L. Russo, pp. 218–231.

Criteria for Design and Development of Automatic, Self-Linearizing, Self-Editing, Electronically Calibrated Trans-

ducers, by George Birkel Jr., pp. 232–240.

The Expansion Parameter as a Tool in First-Cut Comparisons of Exotic Ramjet Fuel Formulations, by Gilbert S. Bahn and Richard R. Koppang, pp. 241–247.

Thermodynamics of High-Temperature Gas Mixtures: Propellants Containing Boron, by John S. Gordon, William Mitchell, David Goland and Marianne P. Stoltenberg, pp. 248–255.

Theory of Mixing and Chemical Reaction in the Opposed-Jet Diffusion Flame, by D. B. Spalding, ARS JOURNAL, vol. 31, no. 6, June 1961, pp. 763–771.

Heat Sink Strand Bomb for Determining Ballistic Properties of Solid Propellants, by E. K. Ives, J. Dominik and W. A. Proell, ARS JOURNAL, vol. 31, no. 6, June 1961, pp. 783–785.

Thermal Conductivity of Kerosine D. Eng. R. D. 2495 Between 15 and 325° at Pressures up to 200 Atm., by H. Ziebland and M. T. Duprée, ARS JOURNAL, vol. 31, no. 6, June 1961, pp. 845–848.

A Further Note on a Diffusion Problem with Chemical Reaction, by E. H. Wissler and R. S. Schechter, *Appl. Sci. Res., Section A,* vol. 10, no. 3–4, 1961, pp. 198–204.

Thermal Stresses and Strains in Elastic Cylindrial and Case-Bonded Grains, by J. A. C. Vandenkerckhove, *Astronautica Acta,* vol. 6, no. 6, 1960, pp. 342–353.

Safety-Evaluating the Explosive Character of Chemicals, by R. W. Van Dolah, *I/EC, Ind. Engng. Chem.,* vol. 53, no. 7, July 1961, pp. 59–63.

Computed Compositions and Thermodynamic Properties of Deuterium-Air Flames, by Edwin B. Cook and Robert W. Smith Jr., *Project Squid Tech. Rep.* BUM-31-R, June 1961, 22 pp.

Methodology for Experimental Studies of the Over-All Kinetics of the Combustion of Gases, by Z. S. Leonteva, *Johns Hopkins Univ., Appl. Phys. Lab.* TG 230-T224, March 1961, 6 pp. (Transl. from *Inzhenerno-Fizicheskii Zhurnal,* vol. 3, no. 2, Feb. 1960, pp. 12–16.)

Fundamental Studies Relating to Systems Analysis of Solid Propellants, by M. L. Williams, P. J. Blatz and R. A. Schapery, *Calif. Inst. Tech., Guggenheim Aeron. Lab., Final Rep.* GALCIT SM 61–5, Feb. 1961, 295 pp.

The Modified Wagon Wheel Grain Design $w_1 > w_2 > w_3$, by Max. W. Stone, *Rohm & Haas Co. Rep.* 5–30, May 1961, 1 vol.

Experimental Investigation of the Ignition Process of Solid Propellants in a Practical Motor Configuration, by Robert W. Lancaster, *Princeton Univ., Dept. Aeron. Engng., Rep.* 548, May 1961, 26 pp., 19 figs. (Thesis, M.S.)

Comparison of Solid Propellant Rates in Strands and Rocket Motors, by Clarke E. Hermance, *Princeton Univ., Dept. Aeron. Engng., Rep.* 556, May 1961, 37 pp., 24 figs. (Thesis, M.S.)

Research and Technologic Work on Explosives, Explosions, and Flames: Fiscal Years 1955 and 1956, *Bureau of Mines, Info. Circ.* 7999, 1961, 31 pp.

High Temperature Heat Capacity Equations and Thermodynamic Properties of Combustion Gases, by Mary M. Williams, *Bureau Naval Weapons, NAVWEPS Rep.* 7699, Feb. 1961, 34 pp.

Shock Tube Determination of Dissociation Rates of Oxygen, by John P. Rink, Herbert T. Knight and Russell E. Duff, *J. Chem. Phys.,* vol. 34, no. 6, June 1961, pp. 1942–1949.

Gaseous Detonations, XV. Expansion Waves in Gaseous Detonations, by Hajime Miyama and Paul Kydd, *J. Chem. Phys.,* vol. 34, no. 6, June 1961, pp. 2038–2045.

Deviations from Thermal Equilibrium Along Reactant Molecules, by B. Widom, *J. Chem. Phys.,* vol. 34, no. 6, June 1961, pp. 2050–2056.

Diffusional Transport of Atomic Hydrogen Through Molecular Hydrogen at Elevated Temperatures, by Henry Wise, *J. Chem. Phys.,* vol. 34, no. 6, June 1961, pp. 2139–2141.

Surface-Catalyzed Excitations in the Oxygen System, by Gene Mannella and Paul Harteck, *J. Chem. Phys.,* vol. 34, no. 6, June 1961, pp. 2177–2180.

Heats of Combustion and Formation of Trimethylborane, Triethylborane and Tri-n-butylborane, by Walter H. Johnson, Marthada V. Kilday and Edward J. Prosen, *J. Res. National Bur. Standards (A. Physics and Chem.),* vol. 3, May–June 1961, pp. 215–220.

An Experimental Study Concerning the Pressurization and Stratification of Liquid Hydrogen, by A. F. Schmidt, J. R. Purcell, W. A. Wilson and R. V. Smith, *J. Res. National Bur. Standards (C. Engng. and Instrumentation),* vol. 65, no. 2, April–June 1961, pp. 81–88.

The Effect of Bubbles in Shock Detonation in a Liquid, by R. I. Soloukhin, *Soviet Phys.: Doklady,* vol. 6, no. 1, July 1961, pp. 16–17.

Dissociation of Molecular Hydrogen Ions in Collisions with Gas Molecules, by L. I. Pivovar, V. M. Tubaev and M. T. Novikov, *Soviet Phys.: JETP,* vol. 13, no. 1, July 1961, pp. 23–26.

Materials and Structures

A Study of Several Aerothermoelastic Problems of Aircraft Structures in High-Speed Flight, by John Cornelius Houbolt, *Zurich, Eidgenossische Technische Hochschule* (ETH) Prom. Mr. 2760, 1958, 108 pp. (Thesis, Dr. Sci.)

On the Erosion of Satellite Surfaces Due to Sputtering in the Free Molecular Flow Region, by D. N. Vachon, *General Elec. Co., Missile and Space Vehicle Dept.,* TIS R61SDO41, March 1961, 11 pp.

Experimental Method of Producing Porous Tungsten for Ion Rocket Engines, by Neal T. Saunders, **Appendix: Metallographic Preparation of Porous Tungsten,** by Anne R. Kendra, *NASA Tech. Note* D-864, June 1961, 23 pp.

Analysis of Tapered Shells on the Basis of V. Z. Vlasov's Variational Method, by B. A. Konovalov, *Johns Hopkins Univ., Appl. Phys. Lab.* TG 230-T234, April 1961, 12 pp.

The Aerothermaldynamic Behavior of Pyrolytic Graphite During Sustained Hypersonic Flight, by E. J. Nolan and S. M. Scala, *General Elec. Co., Missile and Space Vehicle Dept.* TIS R61SDO51, March 1961, 71 pp., 41 refs.

The Effect of Axial Constraint on the Instability of Thin Conical Shells Under External Pressure, by Josef Singer, *Israel, Inst. Tech., Dept. Aeron. Engng. Tech. Note* 2, Dec. 1960, 12 pp., 5 figs. (AFOSR TN 60-860).

Influence Coefficients of Shallow Spherical Shells, by H. E. Williams, *Calif. Inst. Tech., Jet Propulsion Lab. Tech. Rep.* 32–51, Feb. 1961, 11 pp.

Electrical Properties of Pyrolytic Graphites, by Claude A. Klein, *Raytheon Co., Res. Div. Tech. Rep.* R-58, Feb. 1961, 83 pp.

SERVO IR Report

Bolometer Range Expanded By New Line of Standards

Expansion Based On Series Approved For Army Signal Corps Use

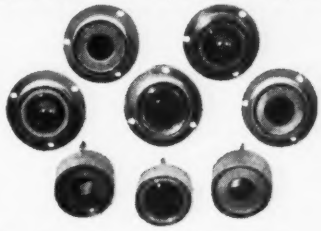

Following rigid Army Signal Corps environmental tests, a broad new line of SERVOTHERM® infrared detectors is now being produced by Servo Corporation under an "Industrial Preparedness Contract" with the U.S. Army Signal Supply Agency.

The new line, now being offered for broad military, industrial, and laboratory use, includes a wide selection of infrared thermistor bolometer models with various window materials, flake sizes, and plain or flange mountings. Regular and immersed thermistor bolometers are offered, as well as stem types, with germanium and silver chloride windows as standard.

SERVOTHERM bolometers can also be supplied with SERVOFRAX® arsenic trisulfide glass, and conventional types of optical glass, calcium fluoride, silicon, KRS-5, and other infrared transmitting materials. Custom designs, including high-ambient and multi-element types, are available.

The further development of production techniques has resulted in reduced costs while improving performance and reliability.

From a simple infrared lens, to a complex infrared system . . . look to Servo

Infrared Optics

Standard and special optical shapes available in all sizes and transmitting materials. Infrared wavelengths from less than 1 to more than 20 microns. Excellent refractive and reflective optics for research, laboratory, industrial, and military use.

IR detectors and associated circuitry

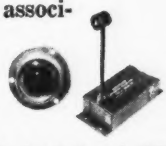

Uniformly sensitive thermistor detectors for fast, accurate, remote detection of radiation from visible through far infrared. Wide variety of time constants, capsule configurations, and window materials. SERVOTHERM® circuitry exploits speed, sensitivity, wide range, low noise, compactness, and flexibility of heat detector cells.

Call or write for further information...or a Servo applications engineer.

SERVO CORPORATION OF AMERICA

111 New South Road • Hicksville, Long Island, N.Y. • WE 8-9700

Investigation of Oxidation-Resistant Coatings on Graphite and Molybdenum in Two Arc-Powered Facilities, by Roger W. Peters and Thomas A. Rasnick, *NASA Tech. Note* D-838, July 1961, 29 pp.

The Wedge-Ring Joint, by W. Hillmer, *Naval Ordnance Test Station,* NOTS TP 2643, June 1961, 6 pp.

Ablation, Heat Sink and Radiation: The Materials that Make them Work, by J. O. Collins and S. Speil, *Materials in Design Engng.*, vol. 53, no. 3, March 1961, pp. 114–118, 149–150.

High-Temperature Materials for Rocket Reactors, by D. P. MacMillan, *Nucleonics,* vol. 19, no. 4, April 1961, pp. 85–88.

Meteoroid Hazard to Nuclear Spacecraft, by R. L. Bjork, *Nucleonics,* vol. 19, no. 4, April 1961, pp. 91–92.

Selectively Emissive Materials for Solar Heat Absorbers, by R. B. Gillette, *Solar Energy,* vol. 4, no. 4, Oct. 1960, pp. 24–32.

Present and Future Problem Areas for High Temperature Inorganic Coatings, by J. D. Walton Jr., *Amer. Ceramic Soc. Bull.*, vol. 40, no. 3, March 1961, pp. 136–141.

Fluid Dynamics, Heat Transfer, and MHD

On the Meteor Ablation in the Atmosphere, by F. Veriani, *Nuovo Cimento,* vol. 19, no. 3, Feb. 1, 1961, pp. 415–442.

Liquid Flow in Tubes, IV, The Transition Process and Turbulent Flow Related to Tube Diameter and Microscopic Surface Properties, by E. R. Lindgren, *Arkiv för Fysik,* vol. 18, no. 5, 1961, pp. 449–464.

The Pressure Pulse Produced by a Large Explosion in the Atmosphere, by V. H. Weston, *Canadian J. Phys.*, vol. 39, no. 7, July 1961, pp. 993–1009.

Waves in a Rarefied Ionized Gas Propagated Transverse to an Exernal Magnetic Field, by Tomiya Watanabe, *Canadian J. Phys.*, vol. 39, no. 7, July 1961, pp. 1044–1057.

Method of Measuring Heat Capacity of Condensed Gases Above their Boiling Point, by A. V. Voronel' and P. G. Strelkov, *Instruments and Experimental Techniques,* no. 6, June 1961, pp. 970–971.

The Two-Dimensional Turbulent Wall-Jet, by W. H. Schwarz and W. P. Cosart, *J. Fluid Mechanics,* vol. 10, part 4, June 1961, pp. 481–495.

On the Stability of Solutions of the Nonlinear Equations of Heat Conduction, by B. A. Kostandian, *PMM; J. Appl. Math. and Mech.*, vol. 24, no. 6, 1960, pp. 1686–1689.

On the Conservation of Vorticity in the Magnetohydrodynamics of Plasma with Many Components, by N. V. Saltanov, *PMM; J. Appl. Math. and Mech.*, vol. 24, no. 6, 1960, pp. 1703–1704.

On the Structure of Turbulence in the Small-Scale Range, by G. S. Golitsyn, *PMM; J. Appl. Math. and Mech.*, vol. 24, no. 6, 1960, pp. 1705–1713.

Flow of Visco-Elastic Maxwell Fluid Through Tubes under Exponential Pressure Gradient, by S. K. Datta, *Zeitschrift für Angewandte Mathematik und Mechanik,* vol. 41, no. 5, May 1961, p. 219.

Propagation of Forced Plane Compression Waves of Small Amplitude in a Viscous Gas When Radiation is Taken into Account, by V. A. Prokof'ev, ARS JOURNAL, vol. 31, no. 7, July 1961, pp. 988–997.

Solution of Several Problems of Air Motion in the Presence of Dissociation and Ionization, by S. S. Kvashina and V. P. Korobeinikov, ARS JOURNAL, vol. 31, no. 7, July 1961, pp. 997–1002.

Analytic Study of Induced Pressure on Long Bodies of Revolution with Varying Nose Bluntness at Hypersonic Speeds, by Vernon Van Hise, *NASA Tech. Rep.* R-78, 1961, 18 pp.

An Investigation of Free Piston Compression of Shock Tube Driver Gas, by R. J. Stalker, *Canada, National Res. Council, Div. Mech. Engng.*, NRC MT-44, May 1961, 24 pp., 17 figs.

Effect of Impingment Angle on Drop-Size Distribution and Spray Pattern of Two Impinging Water Jets, by Marcus F. Heidmann and Hampton H. Foster, *NASA Tech. Note* D-872, July 1961, 34 pp.

Free-Flight Measurement of Local Turbulent Skin Friction on an RM-10 Vehicle, by J. C. Westkaemper, D. R. Moore and C. E. Murphey Jr., *Texas Univ., Defense Res. Lab.* CF-2913, Jan. 1961, 30 pp.

On Turbulent Free Mixing of Parallel Streams of Two Different Gases, by Shigeo Uchida, *Brooklyn Polytech. Inst., Dept. Aerospace Engng. and Appl. Mech., PIBAL Rep.* 635, June 1961, 59 pp., 12 figs.

Compressible Flow Table k = 1.24; Simple Gas Injection Without Forward Velcoty y = 0, *Army Ballistic Missile Agency,* ABMA RA-TR-61-10, June 20, 1961, 89 pp.

Research on Unsteady Flow, by W. P. Jones, *Inst. Aerospace Sciences, 1961 Minta Martin Lecture,* March 1961, 55 pp.

The Experimental Evaluation of the Surface Impact Probe Technique of Measuring Local Skin Friction under Conditions of Moderate Heat Transfer, by Jim King Davidson, *Texas Univ., Defense Res. Lab.*, CF-2931, June 1961, 29 pp. (Thesis, M.S.)

Monte Carlo Application to Molecular Flows, by J. K. Haviland, *Mass. Inst. Tech., Fluid Dynamics Res. Lab., Rep.* 61-5, May 1961, 231 pp., 66 refs.

Simple Formulas for Stagnation-Point Convective Heat Loads in Lunar Return, by Frederick C. Grant, *NASA Tech. Note* D-890, July 1961, 21 pp.

Application of Biot's Variational Principle in Heat Conduction, by Thomas J. Lardner and Frederick V. Pohle, *Brooklyn, Polytech. Inst., Dept. Aerospace Engng. Appl. Mech., PIBAL Rept* 587, May 1961, 90 pp., 23 figs. (AFOSR 932).

Heat Transfer by Simultaneous Conduction and Radiation in an Absorbing Medium, by R. Viskanta and R. J. Grosh, *ASME Paper* 61-SA-34, 1961, 10 pp.

The Effect of Subcooled Liquid on Laminar Film Boiling, by E. M. Sparrow and R. D. Cess, *ASME* 61 SA-29, 1961, 7 pp.

Analysis of Pressure Drop and Heat Transfer of a Pebble-Bedstorage Heater for a Hypersonic Wind Tunnel, by D. E. Randall and A. Bedford, *Atomic Energy Commission,* SC-4591, (RR), May 1961, 33 pp.

The Measurement of the Thermal Conductivity of Gases at High Temperatures with a Shocktube; Experimental Results in Argon at Temperatures Between 1000°K and 3000°K, by Edward F. Smiley, *Catholic Univ. of America,* 1957, 32 pp., 11 figs. (Thesis, Ph.D.).

A Thermal Rayleigh Problem in a Viscous Relaxing Gas, by J. T. Curtis and W. E. Gibson, *Cornell Aeron. Res. Lab. Rep.* AF-1285-A-6, April 1961, 45 pp.

Radiation From Hot Nitrogen, by R. A. Allen, J. C. Camm and J. C. Keck, *Avco-Everett Res. Lab., Avco-Everett Res. Rep.* 102, April 1961, 15 pp.

Expansion and Diffusion of a Layer of Hot Gas in the Presence of Thermal Radiation, by Chuen-Yen Chow, *Mass. Inst. Tech., Fluid Dynamics Res. Lab. Rep.* 61-2, March 1961, 41 pp.

Experimental Determination of Potassium Vapor Pressure in the 550° to 1280°C Temperature Range, by N. S. Grachev and P. L. Kirilov, *NASA Tech. Transl.* F-66, July 1961, 7 pp. (Trans. from *Inzherno-Fizicheskii Zhurnal,* vol. 3, no. 6, June 1960, pp. 62–65.)

Low Frequency Oscillations in Gas Discharges, by Francis F. Chen, *Princeton Univ., Plasma Physics Lab.* MATT-78, June 1961, 10 pp., 5 figs.

Diffusion for a Slightly Ionized Region in a Uniform Flow, by A. C. Pipkin, *Maryland Univ., Inst. Fluid Dynamics Appl. Math. Tech. Note* BN-240, April 1961, 19 pp.

Hydromagnetic Stability of Toroidal Equilibria with an Externally Imposed Rotational Transform, by John L. Johnson and John M. Greene, *Princeton Univ., Plasma Physics Lab.* MATT-76, June 1961, 38 pp.

Plasma Theory of Electron-Phonon Interaction II, by Oldwig von Roos, *Calif. Inst. Tech., Jet Propulsion Lab. Tech. Rep.* 32-106, June 1961, 18 pp.

Experimental Study of Hydromagnetic Waves in Plasma, by Alan W. DeSilva, *Atomic Energy Commission,* UCRL 9601, March 1961, 104 pp.

Build-up of Electromagnetic Waves in a Stream Moving Through a Plasma in the Presence of a Magnetic Field, by V. O. Rapoport, *Johns Hopkins Univ., Appl. Phys. Lab.* TG-230-T226, March 1961, 12 pp. (Transl. from *Izvestiia Vysshikh Uchebnykh Zavedenii Radiofizika,* vol. 3, no. 5, Sept.–Oct. 1960, pp. 737–745.)

Recent Soviet Advances in Inviscid Hypersonic Aerodynamics, by Ronald F. Probstein, *Aerospace Engng.*, vol. 20, no. 7, July 1961, pp. 10–11, 68–81, 63 refs.

High Temperature Rarefied Hypersonic Flow Over a Flat Plate, by H. T. Nagamatsu, R. E. Sheer Jr. and J. R. Schmid, ARS JOURNAL, vol. 31, no. 7, July 1961, pp. 902–910.

Plasma Physics, James E. Drummond (ed.), McGraw-Hill Book Co. Inc., New York, 1961, 386 pp.

Oscillations in Plasmas, by J. E. Drummond, pp. 1–32, 94 refs.

The Spectra of Systems of Interacting Particles, by Y. Klimontovich and V. P. Silin, pp. 35–87, 105 refs.

Statistical Mechanics of Reversible Processes in Plasma Dynamics, by E. Meeron, pp. 88–123, 38 refs.

Amplifying and Evanescent Waves; Convective and Nonconvective Instabilities, by P. A. Sturrock, pp. 124–140, 26 refs.

How to Distinguish Between Attenuating and Amplifying Waves, by O. Buneman, pp. 143–164.

A Review of Magnetohydrodynamics, by Y. A. Yoler, pp. 167–201, 58 refs.

The Bennett Pinch, by O. Buneman, pp. 202–223, 12 refs.

Electrical Properties of High-Altitude Ionized Shock Waves, by P. A. Goldberg, pp. 245–269, 35 refs.

Transverse Plasma Waves and Plasma Vortices, by O. Buneman, pp. 270–292, 10 refs.

Plasma Power Absorption, by J. E. Drummond, pp. 293–306, 10 refs.

Proceedings (Heat Transfer and Fluid Mechanics Institute, Univ. of Southern California, June 1961), R. C. Binder, M. Epstein, R. L. Mannes and H. T. Yang (eds.), Stanford Univ. Press, Stanford, Calif., 1961, 236 pp.

Some Hot-Wire Anemometer Measurements in a Hypersonic Wake, by A. Demetriades, pp. 1–9, 10 refs.

Turbulence Field Near the Stagnation Point on Blunt Bodies of Revolution, by A. M. Kuethe, W. W. Willmarth and G. H. Crocker, pp. 10–22, 10 refs.

Axially Symmetric Free Mixing with Swirl, by M. H. Steiger and M. H. Bloom, pp. 23–37.

On the Interaction of the Reflected Shock Wave with the Laminar Boundary Layer on the Shock Tube Walls, by S. Byron and N. Rott, pp. 38–54, 16 refs.

On the Finite Difference Solution of Laminar Boundary Layer Problems, by J. C. Wu, pp. 55–69, 14 refs.

Heat Transfer to Steam-Water Flows, by H. S. Isbin, A. Kvamme, Y. Yamazaki, I. Garcia Jr. and C. M. Stendahl, pp. 70–78, 14 refs.

Critical Two-Phase, Steam-Water Flows, by H. Fauske, pp. 79–89.

The Use of Acoustic Vibrations to Improve Heat Transfer, by I. A. Raben, pp. 90–103, 12 refs.

Liquid Disintegration by an Air Stream with Secondary Air Mass Augmentation, by H. F. Hrubecky, pp. 104–113, 15 refs.

Investigation of Spray-Type Condensers with Mercury and Water, by L. Hays, J. Collins and J. Neustein, pp. 114–129.

Void Volume, Site Density and Bubble Size for Subcooled Nucleate Pool Boiling, by E. E. Duke and V. E. Schrock, pp. 130–145.

Hypersonic Strong Viscous Interaction of a Flat Plate with Surface Mass Transfer, by T. Y. Li and J. F. Bross, pp. 146–160.

Hypersonic Shock-Layer Theory of the Stagnation Region at Low Reynolds Number, by H. K. Cheng, pp. 161–175, 17 refs.

Ionization Trails, by P. S. Lykoudis, pp. 176–192, 11 refs.

Experiments on the Transpiration Cooled Anode of an Electric Arc, by P. A. Schoeck and E. R. G. Eckert, pp. 193–207.

Heat Transfer Through a Melting Layer with External Gas Flow, by B. L. McFarland and D. B. Harmon, pp. 208–221, 12 refs.

Analysis of Quartz and Teflon Shields for a Particular Re-entry Mission, by E. W. Adams, pp. 222–236, 13 refs.

Analysis of Convective Heat Tranfers in Rocket Nozzles, by Ernest Mayer, ARS JOURNAL, vol. 31, no. 7, July 1961, pp. 911–917.

Surface Temperatures of High Speed, Radiation Cooled Bodies in Dissociating Atmospheres, by Daniel E. Rosner, ARS JOURNAL, vol. 31, no. 7, July 1961, pp. 1013–1015.

Hypersonic Viscous Effects in Wind Tunnels, by Robert H. Johnson, ARS JOURNAL, vol. 31, no. 7, July 1961, pp. 1022–1024.

On "Numerical Comparison Between Exact and Approximate Theories of Hypersonic Inviscid Flow Past Slender Blunt-Nosed Bodies," by K. H. Cheng and A. L. Chang, ARS JOURNAL, vol. 31, no. 7, July 1961, pp. 1024–1026.

Wanted

TECHNICAL EDITOR

Top post, leading technical journal. Science or engineering background, editorial administrative experience required. Salary open.

Send complete resume, salary requirements to:

Editor
P.O. Box 307
Bronxville, N. Y.

Temperature Measurement by Measurement of Radiation, by H. Muller, *Archiv für Technisches Messen,* no. 304, May 1961, pp. 99–102. (In German.)

Study of the Disturbance Caused by a Moving Body in a Partially Ionized Gas, by F. Marcel Devienne and A. Roustan, *Laboratoire Mediterranéen de Recherches Thermodynamiques,* Jan. 1961, 60 pp. (AFOSR 566).

Exact Solutions for Nonequilibrium Expansions of Air with Coupled Chemical Reactions, by Alan Q. Eschendroeder, Donald W. Boyer and J. Gordon Hall, *Cornell Aeron. Lab. Rep.* AF-1413-A-1, May 1961, 21 pp. (AFOSR 622).

Shock Waves in a Plasma, by K. T. Yen, *General Elec. Co., Missile and Space Vehicle Dept.* TIS R61SD089, June 1961, 14 pp.

Shock Wave Structure in a Relaxing Diatomic Gas, by L. Talbot and S. M. Scala, *General Elec. Co., Missile and Space Vehicle Dept.* TIS R60SD850, Nov. 1960, 23 pp., 14 figs.

Method of Determining the Rates and Kinetic Constants of Complex Chemical Reactions in Flow, by G. M. Panchenkov and Iu. Zhorov, *Johns Hopkins Univ., Appl. Phys. Lab.* TG 230-T229, April 1961, 6 pp. (Transl. from *Doklady Akademii Nauk SSSR,* vol. 135, no. 5, 1960, pp. 1172–1175.)

Constant Density Approximations for the Flow Behind Axisymmetric Shock Waves, by Albert G. Munson, *NASA Tech. Note* D-857, May 1961, 29 pp.

Recent Advances in Condensation and Evaporation, by Welby G. Courtney, ARS JOURNAL, vol. 31, no. 6, June 1961, pp. 751–756. 114 refs.

Gas Particle Flow in an Axisymmetric Nozzle, by W. S. Bailey, E. N. Nilson, R. R. Serra and T. F. Zupnik, ARS JOURNAL, vol. 31, no. 6, June 1961, pp. 793–798.

Application of Heat Flux Potentials to the Calculation of Convective Heat Transfer in Chemically Reacting Gases, by Daniel E. Rosner, ARS JOURNAL, vol. 31, no. 6, June 1961, pp. 816–818.

Methods of Hypersonic Flow Theory, by Christoph V. Costa, *Munich, Tech. Hochschule, Math. Inst. Tech. Note* 3, Feb. 1961, 39 pp. (AFOSR 809).

A Calculation Method for Three-Dimensional Turbulent Boundary Layers, by J. C. Cooke, *Great Brit. Aeron. Res. Council, R & M* No. 3199, Oct. 1958, 19 pp.

Heat Transfer and Laminar-Boundary-Layer Separation in Steady Compressible Flow Past a Wall with Non-uniform Temperature, by N. Curle, *Great Brit., Aeron. Res. Council, R & M* No. 3179, Dec. 1958, 16 pp.

An Experiment with a Transpiration-Cooled Nozzle, by Richard P. Bernicker, *Mass. Inst. Tech., Naval Supersonic Lab., Tech. Rep.* 447, July 1960, 73 pp. (AFOSR TN 60-1484).

An Analytical and Experimental Investigation of Steady and Unsteady Flow in Tubing, with Special Application to Simulated Missile Pressure Sensing Systems, by Arnold L. Ducoffe and Frank M. White Jr., *Atomic Energy Commission,* SC-4544-(RR), May 1961, 93 pp.

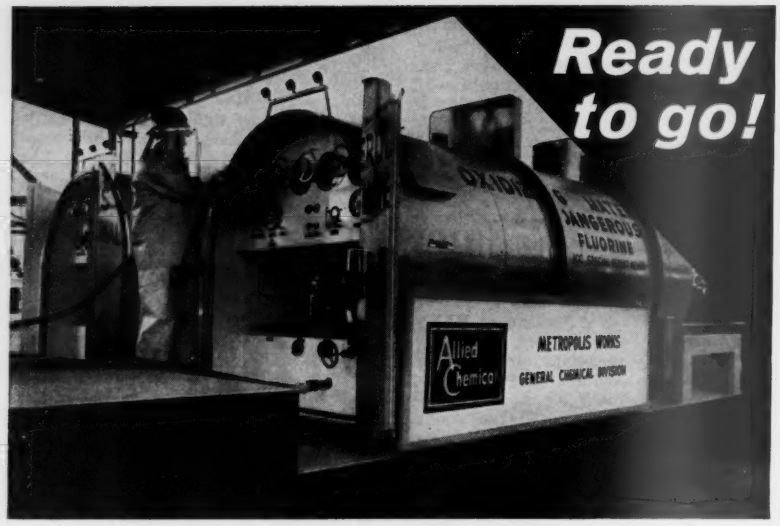

The Ultimate Oxidizer...

ALLIED CHEMICAL

LIQUID FLUORINE

Every major propulsion program working with fluorine has been supplied by Allied Chemical. With the largest privately-owned facilities in the free world, we are equipped to make bulk shipment of liquid fluorine anywhere in the U.S.—right now!

Out of our long experience with fluorine we've developed the storage and handling techniques that make this super-high-energy oxidizer as easy for you to handle as any other advanced propellant. This useful knowledge is freely available when you're ready to put liquid fluorine to work. For the full story on liquid fluorine, and how it's being used today, just write us!

Allied Chemical

GENERAL CHEMICAL DIVISION
40 Rector Street, New York 6, N. Y.

The Effect of a Magnetic Field on the Flow of a Conducting Fluid Past a Body of Revolution, by W. Chester, *J. Fluid Mech.*, vol. 10, part 3, May 1961, pp. 459–465.

The Effect of a Magnetic Field on the Flow of a Conducting Fluid Past a Circular Disk, by W. Chester and D. W. Moore, *J. Fluid Mech.*, vol. 10, part 3, May 1961, pp. 466–472.

Instability Waves in Magnetically Confined Plasmas, by A. A. Ware, *J. Nuclear Energy (Part C: Plasma Phys.)*, vol. 3, no. 2, April 1961, pp. 93–97.

The Shock Model of the Dynamic Pinch, by J. A. Reynolds and J. M. P. Quinn, *J. Nuclear Energy (Part C: Plasma Phys.)* vol. 3, no. 2, April 1961, pp. 135–139.

Plasma Density Fluctuations in a Magnetic Field, by E. E. Salpeter, *Phys. Rev.*, vol. 122, no. 6, June 15, 1961, pp. 1663–1674.

Electrostatic Sound Wave Modes in a Plasma, by F. W. Crawford, *Phys. Rev. Letters*, vol. 6, no. 12, June 15, 1961, pp. 663–664.

Temperature Measurements of Shock Waves and Detonations by Spectrum-Line Reversal, III, Observations with Chromium Lines, by A. G. Gaydon and I. R. Hurle, *Proc., Royal Society, London*, vol. A262, no. 1308, June 1961, pp. 38–50.

On Statistical Dynamics of an Incompressible Turbulent Fluid, by B. I. Davydov, *Soviety Phys.: Doklady*, vol. 6, no. 1, July 1961, pp. 10–12.

Concerning Disturbances Produced by a Body Moving in a Plasma, by L. P. Pitayevskii and V. Z. Kresin, *Soviet Phys.: JETP*, vol. 13, no. 1, July 1961, pp. 185–191.

Oscillatory Flow Near the Entry of a Circular Tube, by H. B. Atabek and Ch. C. Chang, *Zeitschrift für angewandte Math. und Physik*, vol. 12, no. 3, May 1961, pp. 185–201.

Magneto - Fluid - Dynamics of Thin Bodies in Oblique Fields, by K. Stewartson, *Zeitschrift für angewandte Math. und Physik*, vol. 12, no. 3, May 1961, pp. 261–271.

A Thermo-Gasdynamic Diagram for Air Plasma, by Otto Lutz, *Zeitschrift für Flugwissenschaften*, vol. 9, no. 4–5, April–May 1961, pp. 113–117. (In German.)

International Practical Temperature Scale of 1948, by H. F. Stimson, *J. Res. National Bur. Standards (A. Physics and Chem.)*, vol. 65, no. 3, May–June 1961, pp. 139–146.

Flight Mechanics

On the Long Period Luni-Solar Effect in the Motion of an Artificial Satellite, by Peter Musen, *NASA Tech. Note* D-1041, July 1961, 17 pp.

Theory of an Accurate Intermediary Orbit for Satellite Astronomy, by John P. Vinti, *National Bur. Standards, Rep.* 7154, May 1961, 67 pp. (AFOSR 690).

Velocity Requirements for Aport from the Boost Trajectory of a Manned Lunar Mission, by Robert E. Slye, *NASA Tech. Note* D-1038, July 1961, 41 pp.

Earth Oblateness and Relative Sun Motion Considerations in the Determination of an Ideal Orbit for the Nimbus Meteorological Satellite, by William R. Bandeen, *NASA Tech. Note* D-1045, July 1961, 10 pp.

Relating Geodetic Latitude and Altitude to Geocentric Latitude and Radius Vector, by E. W. Purcell and W. B. Cowan, ARS JOURNAL, vol. 31, no. 7, July 1961, pp. 932–934.

Eclipses of Artificial Earth Satellites, by Lawrence G. Stoddard, *Astronaut. Sci. Rev.*, vol. 3, no. 2, April–June 1961, pp. 9–14, 16.

Nonmatrix Formulation of an Eulerian Angle Vector Transformation, by Richard F. Leach, ARS JOURNAL, vol. 31, no. 6, June 1961, pp. 830–831.

The Application of Periodic Surface Theory to the Study of Satellite Orbits, by S. P. Diliberto, W. T. Kyner and R. B. Freund, *Astronom. J.*, vol. 66, no. 3, April 1961, pp. 118–128.

On Satellite Orbits with Very Small Eccentricities, by I. G. Izsak, *Astronom. J.*, vol. 66, no. 3, April 1961, pp. 129–131.

Note on the Motion of a Close Earth Satellite with a Small Eccentricity, by Y. Kozai, *Astronom. J.*, vol. 66, no. 3, April 1961, pp. 132–134.

On the Almost Periodicity of Satellite Motion, by E. D. Callender, *Astronom. J.*, vol. 66, no. 3, April 1961, pp. 134–137.

On Tidal Torque and Eccentricity of a Satellite's Orbit, by G. W. Groves, *Royal Astronom. Soc., Monthly Notices*, vol. 212, no. 5, 1960, pp. 497–502.

On Mr. King-Hele's Theory of the Effect of the Earth's Oblateness on the Orbit of a Close Satellite, by P. J. Message, *Royal Astronom. Soc., Monthly Notices*, vol. 121, no. 1, 1960, pp. 1–4.

A Geometrical Derivation of the Satellite Equations, by R. A. Struble, *J. Math. Analysis and Applications*, vol. 1, no. 3, 4, Dec. 1960, pp. 300–307.

The Theory of Artificial Satellites in Terms of the Orbital True Longitude, by P. Musen, *J. Geophys. Res.*, vol. 66, no. 2, Feb. 1961, pp. 403–409.

The Gravitational Field of the Earth

Derived from Motions of Three Satellites, by Y. Kozai, *Astronom. J.*, vol. 66, no. 1, Feb. 1961, pp. 8–10.

Some Remarks on the Motion of a Satellite of an Oblate Planet, by R. B. Barrar, *Astronom. J.*, vol. 66, no. 1, Feb. 1961, pp. 11–15.

Space Refueling, by C. E. Kaempen, *Space World*, vol. 1, no. 7, April 1961, pp. 37–39, 54–55.

Rotation Period of the Artificial Satellite 1958 δ 1, by P. Notni, H. Oleak and C. R. Faulkner, *Nature*, vol. 189, no. 4766, March 4, 1961, p. 737.

Vehicle Design, Testing, and Performance

Safety Margins Established by Combined Environmental Tests Increase Atlas Missile Component Reliability, by C. C. Campbell, *IRE Trans. on Reliability and Quality Control*, vol. RQC-10, no. 1, March 1961, pp. 1–6.

Use of Balloons and High-Altitude Aircraft for Precursor Satellite Studies, by J. Strong, *Astronom. J.*, vol. 66, no. 2, March 1961, pp. 54–55.

The Explorer IX Atmospheric-Density Satellite, *Natl. Acad. Sci., IGY Bull.*, no. 46, April 1961, pp. 12–16.

Space Vacuum Poses Design Problems, by L. D. Jaffe, *Nucleonics*, vol. 19, no. 4, April 1961, pp. 93–94.

A Systems Analysis of Fast Manned Flights to Venus and Mars Part II: Storage of Liquid and Solid Hydrogen on Nuclear-Powered Interplanetary Vehicles, by K. A. Ehricke, *ASME, Trans., Series B-J., Engng. for Industry*, vol. 83, no. 1, Feb. 1961, pp. 13–28.

Mobots, by J. W. Clark, *Space World*, vol. 1, no. 7, April 1961, pp. 28–31, 44–46.

New Monitors for Astro-Science, by H. Dryden, *Space World*, vol. 1, no. 7, April 1961, pp. 14–17, 56–58.

Saturn Our Best Hope, by W. von Braun, *Space World*, vol. 1, no. 8, June 1961, pp. 10–13, 42–44.

The Tiros II Cloud-Cover and Infrared Satellite, *Natl. Acad. Sci., IGY Bull.*, no. 43, Jan. 1961, pp. 9–13.

The U. S. Booster Rocket Program, by W. von Braun, *Weltraumfahrt*, vol. 11, no. 4, Dec. 4, 1960, pp. 99–106. (In German.)

A Comparison of Computers, by F. G. Curl, *Calif. Inst. Tech., Jet Propulsion Lab. Tech. Rep.* 32-74, March 1961, 20 pp.

Measurements of Sheath Currents and Equilibrium Potential on the Explorer VIII Satellite (1960 ξ), by R. E. Bourdeau, J. L. Donley, G. P. Serbu and E. C. Whipple Jr., *NASA Tech. Note* D-1064, July 1961, 25 pp.

Juno II Summary Project Report, Vol. I, Explorer VII Satellite, *Marshall Space Flight Center, NASA Tech. Note* D-608, July 1961, 356 pp.

Proceedings, Conference on Results of the First U. S. Manned Suborbital Space Flight, Washington, D. C., June 1961, Sponsored by NASA in cooperation with Natl. Inst. of Health and Natl. Academy of Sci., Gov't Printing Office, Washington, D. C., 1961, 76 pp.

Flight Plan for the MR-3 Manned Flight, by Christophor C. Kraft Jr., pp. 7–10.

Mercury Spacecraft Systems, by Aleck C. Bond, pp. 11–18.

Distribution of the Stages of a Missile to Obtain Minimum Take-Off Weight, Minimum Cost, and Maximum Payload Kinetic Energy, by D. Dini, *L'Aerotecnica*, vol. 41, no. 1, Feb. 1961, pp. 3–13. (In Italian.)

Soviet Space Experiments and Astronautics, by F. J. Krieger, *Aerospace Engng.*, vol. 20, no. 7, July 1961, pp. 8–9, 28–37.

Soviet Aeronautical Scientists: How they Work and Where they Publish, by Leon Trilling, *Aerospace Engng.*, vol. 20, no. 7, July 1961, pp. 12–13, 38–42.

A Study of Manned Nuclear-Rocket Missions to Mars, by S. C. Himmel, J. F. Dugan Jr., R. W. Luidens and R. J. Weber, *Aerospace Engng.*, vol. 20, no. 7, July 1961, pp. 18–19, 51–58.

Rocket Boost Vehicle Mission Optimizations, by R. T. Stancil and L. J. Kulakowski, ARS JOURNAL, vol. 31, no. 7, July 1691, pp. 935–943.

High Energy, Low Thrust Jupiter Missions, by Robert H. Fox, ARS JOURNAL, vol. 31, no. 7, July 1961, pp. 1018–1021.

Maximum Error in Total Emissivity Measurements Due to Non-Grayness of Samples, by D. K. Edwards and K. E. Nelson, ARS JOURNAL, vol. 31, no. 7, July 1961, pp. 1021–1022.

The Drive for Lifting Re-Entry Vehicles, by R. Fredette and F. Orazio, ASTRONAUTICS, vol. 6, no. 8, Aug. 1961, pp. 40–42, 76–84, 20 refs.

An Orbital Air-Scooping Vehicle, by Morton Camac and Felix Berner, ASTRONAUTICS, vol. 6, no. 8, Aug. 1961, pp. 40–42, 76–84, 20 refs.

Determination of the Shape of a Body of Minimum Drag at Hypersonic Speed, by A. L. Gonor, *PMM; J. Appl. Math. and Mech.*, vol. 24, no. 6, 1960, pp. 1628–1635.

The Storable Rocket Power in

ALLIED CHEMICAL **CTF**

You may be familiar with the boost in rocket range that chlorine trifluoride can deliver. But do you also know about the ease of shipping, handling and storing that's possible with this powerful oxidizer?

Safe, storable chlorine trifluoride is tried, tested, proved! It's available now in tonnage quantities anywhere in the U.S. We have been producing CTF for over 10 years, on a commercial basis. We know it well—and would be glad to share this knowledge with you. Our technical bulletin, "Chlorine Trifluoride", gives full details. For your copy, just write us on your company letterhead.

Allied Chemical

GENERAL CHEMICAL DIVISION
40 Rector Street, New York 6, N.Y.

Space Programs Summary No. 37-8, Vol. I, *Calif. Inst. Tech., Jet Propulsion Lab.*, April 1961, 40 pp.

The Virtual Mass of Clustered Boosters, by Holt Ashley and Gifford W. Asher, ARS JOURNAL, vol. 31, no. 6, June 1961, pp. 757–763.

Staging of Cruising Vehicles, by M. Arens, ARS JOURNAL, vol. 31, no. 6, June 1961, pp. 824–825.

Capabilities of Multistaged Chemical Rocket Systems, by J. E. Froehlich, *Astronautica Acta*, vol. 6, no. 6, 1960, pp. 311–321.

Monographs to Determine Velocity Requirements for Interplanetary Trips to Mars and Venus, by John V. Breakwell, Rollin W. Gillespie and Stanley Ross, *Astronaut. Sci. Rev.*, vol. 3, no. 2, April–June 1961, pp. 15–16.

Lifting Re-Entry Vehicles, by Edwin G. Czarnecki, ASTRONAUTICS, vol. 6, no. 6, June 1961, pp. 27–31, 50, 52.

Launch Operations Challenge, by William A. Fleming, ASTRONAUTICS, vol. 6, no. 6, June 1961, pp. 20–23, 48.

Response to the "Plasma Hypothesis," by Dandridge Cole, ASTRONAUTICS, vol. 6, no. 6, June 1961, pp. 36–39, 76–80.

Guidance and Control

Adaptive Control Systems, Eli Mishkin and Ludwig Braun (eds.), McGraw-Hill Book Co. Inc., New York, 1961, 533 pp.

The Concept of Adaptive Control, by John G. Truxal, pp. 1–22.

Linear Control Systems—A Signal Flow Graph Viewpoint, by William A. Lynch, pp. 23–49.

Identification of Process Dynamics, by John G. Truxal, pp. 50–90.

Control Systems—Some Unusual Design Problems, by John G. Truxal, pp. 91–118.

Sampled-Data] Systems, by Martin L. Shooman, pp. 119–183.

Design of Intentionally Nonlinear Systems, by Kenneth R. Kaplan, pp. 184–233.

Analysis and Design in the Phase Plane, by Eli Mishkin, pp. 234–263.

The Analytical Theory of Nonlinear Systems, by Eli Mishkin, pp. 264–290.

Automatic Methods of Process Identification, by Richard A. Haddad and Ludwig Braun Jr., pp. 293–322.

Adaptive Control Systems, by Joseph J. Bongiorno Jr., pp. 323–343.

Computer-Controlled Adaptive Control Systems, by Ludwig Braun Jr., pp. 344–381.

Some Unusual but Nonadaptive Systems, by Richard A. Haddad, pp. 382–400.

Digital Techniques, by Melvyn M. Drossman, pp. 401–451.

Analysis of Competitive Situations, by Lawrence P. Grayson, pp. 452–478.

Decision Theory, by John G. Truxal and Joseph J. Padalino, pp. 479–501.

Analysis of Queueing Systems, by Eli Mishkin, pp. 502–517.

Multistage Decision Processes, by John G. Truxal, pp. 518–533.

Self-Contained Navigational System for Determination of Orbital Elements of a Satellite, by K. N. Satyendra and R. E. Bradford, ARS JOURNAL, vol. 31, no. 7, July 1961, pp. 949–956.

Determining the Transfer Functions for Certain Systems with Varying Parameters, by B. E. Rudnitskii, *Automation and Remote Control* (Transl. of *Avtomatika i Telemekhanika*), vol. 21, no. 12, Dec. 1960, pp. 1115–1125.

On Methods for Realizing a Finite Automation Whose Cylical Nature is Determined by the Variation of the Input State, by M. A. Aizerman, L. A. Gusev, L. I. Rozonoer and others, *Automation and Remote Control* (Transl. of *Avtematika i Telemekhanika*), vol. 21, no. 12, Dec. 1960, pp. 1126–1143.

The Effect of the Characteristics of an Electrical Control Element on the Choice of the Parameters for a Hydraulic Amplifier, by I. M. Krassov, L. I. Radovskii and B. G. Turbin, *Automation and Remote Control* (Transl. of *Avtomatika i Telemekhanika*), vol. 21, no. 12, Dec. 1960, pp. 1171–1174.

A Self-Optimizing Non-linear Control System, by J. L. Douce and R. E. King, *Institution Elect. Engrs., Proc., Part B, Electronic and Communication Engng.*, vol. 108, no. 40, July 1961, pp. 441–448.

On Certain Properties of Motion in the Presence of Gyroscopic Forces, by Ia. L. Geronimus, *PMM; J. Appl. Math. and Mech.*, vol. 24, no. 6, 1960, pp. 1549–1557.

A Study of Injection Guidance Accuracy as Applied to Lunar and Interplanetary Missions, by H. J. Gordon, *Calif. Inst. Tech., Jet Propulsion Lab., Tech. Rep.* 32-90, May 1961, 46 pp.

Analysis of Error Progression in Terminal Guidance for Lunar Landing, by P. J. deFries, *NASA Tech. Note* D-605, July 1961, 27 pp.

Contributions to the Theory of Nonlinear Oscillations, vol. 5, S. Lefschetz (ed.), Princeton Univ. Press, Princeton, N. J., 1960, 286 pp.

The Time Optimal Control Problem, by J. P. LaSalle, pp. 1–24.

On the Motion of Nonlinear Gyroscopic Systems, by V. S. Novoselov, *PMM; J. Appl. Math. and Mech.*, vol. 24, no. 6, 1960, pp. 1566–1575.

Stability of Motion of a Gyroscope with a Cardan Suspension, by L. M. Markhashor, ARS JOURNAL, vol. 31, no. 7, July 1961, pp. 958–961.

The Theory of Time Optimal Processes in Linear Systems, by R. V. Gamkrelidze, *Calif. Univ., Los Angeles, Dept. Engng. Rep.* 61-7, Jan. 1961, 33 pp. (AFOSR 572). (Transl. from *Izvestia Akademii Nauk SSSR*, vol. 2, 1958, pp. 449–474.)

Study of the Use of a Terminal Controller Technique for Re-Entry Guidance of a Capsule-Type Vehicle, by Edwin C. Foudriat, *NASA Tech. Note* D-828, May 1961, 29 pp.

A Study of Time Optimal Control, by Bernard H. Paiewonsky, *Princeton Univ., Dept. Aeron. Engng.*, 1961, 114 pp., 17 figs., 99 refs. (Thesis, Ph.D.)

Capabilities and Limitations of Reaction Spheres for Attitude Control, by Ralph D. Ormsby and Mahlon C. Smith, ARS JOURNAL, vol. 31, no. 6, June 1961, pp. 808–812.

Magnetorquer—A Satellite Orientation Device, by L. J. Kamm, ARS JOURNAL, vol. 31, no. 6, June 1961, pp. 813–815.

Unique Cross-Spin Control Concept for Fixed Fin Sounding Rockets, by Russell A. Nidey, ARS JOURNAL, vol. 31, no. 6, June 1961, pp. 824.

Energy Requirements for Satellite Stabilization of the Gravitational Gradient, by Robert R. Wolfe, John M. Corgan and Peter B. Teets, ARS JOURNAL, vol. 31, no. 6, June 1961, pp. 836–838.

Attitude Stabilization Using Focused-Radiation Pressure, by Robert R. Hibbard, ARS JOURNAL, vol. 31, no. 6, June 1961, pp. 844–845.

Saturn Payload to a 24-hr Orbit, by Walter Haeussermann, ASTRONAUTICS, vol. 6, no. 6, June 1961, pp. 24–26, 68–70.

Satrac-Space Rendezvous System, by Lawrence J. Kamm, ASTRONAUTICS, vol. 6, no. 6, June 1961, pp. 32–33, 44, 46.

Lunar Flight Control Display, by T. E. Garrigan, ASTRONAUTICS, vol. 6, no. 6, June 1961, pp. 42, 56–59.

The Dynamics of Self-Adaptive Systems with External Continuous Adjustment of the Compensating Network in the Presence of Random Disturbances, by I. E. Kazakov, *Automation and Remote Control* (*Transl. of Avtomatika i Telemekhanika*), vol. 21, no. 11, Nov. 1960, pp. 1040–1046.

The Stability of a Certain Nonlinear Controlled System, by Chang Jen-Wei, *Automation and Remote Control* (*Transl. of Avtomatika i Telemekhanika*), vol. 21, no. 11, Nov. 1960, pp. 1047–1050.

Foundations for the Application of the Harmonic Linearization Method to an Investigation of Periodic Oscillations in Systems with Lag, by V. S. Kislyakov, *Automation and Remote Control* (*Transl. of Avtomatika i Telemekhanika*), vol. 21, no. 11, Nov. 1960, pp. 1051–1056.

An Approximate Determination of Jet Reaction in a "Nozzle-Flapper" Hydraulic Amplifier, by I. M. Krassov, L. I. Radovskii and B. G. Turbin, *Automation and Remote Control* (*Transl. of Avtomatika i Telemekhanika*), vol. 21, no. 11, Nov. 1960, pp. 1091–1092.

Plotting Logarithmic Frequency Responses for Servosystems with Combined Control, by A. I. Guzenko, *Automation and Remote Control* (*Transl. of Avtomatika i Telemekhanika*), vol. 21, no. 11, Nov. 1960, pp. 1101–1105.

On Synthesizing Control Programs in Systems that Include a Digital Computer, by P. F. Klubnikin, *Automation and Remote Control* (*Transl. of Avtomatika i Telemekhanika*), vol. 21, no. 11, Nov. 1960, pp. 1106–1110.

On a Property of Optimal Controllers with Boundedness Constraints, by Herbert L. Grognsky, *Inst. Radio Engrs., Trans. on Automatic Control*, vol. 6, no. 2, May 1961, pp. 98–110.

A Minimal Time Discrete System, by C. A. Desoer and J. Wing, *Inst. Radio Engrs., Trans. on Automatic Control*, vol. 6, no. 2, May 1961, pp. 111–124.

Theory and Design of High-Order Bang-Bang Control Systems, by M. Athanassiades and O. J. M. Smith, *Inst. Radio Engrs., Trans. on Automatic Control*, vol. 6, no. 2, May 1961, pp. 125–134.

A Parameter-Perturbation Adaptive Control System, by R. J. McGrath, V. Rajaraman and V. G. Rideout, *Inst. Radio Engrs., Trans. on Automatic Control*, vol. 6, no. 2, May 1961, pp. 154–161.

Transfer-Function Tracking and Adaptive Control Systems, by C. N. Weygandt and N. N. Puri, *Inst. Radio Engrs., Trans. on Automatic Control*, vol. 6, no. 2, May 1961, pp. 162–166.

Adaptive Servo Tracking, by A. I. Talkin, *Inst. Radio Engrs., Trans. on Automatic Control*, vol. 6, no. 2, May 1961, pp. 167–172.

A Modified Lyapunov Method for Nonlinear Stability Analysis, by D. R. Ingwerson, *Inst. Radio Engrs., Trans. on Automatic Control*, vol. 6, no. 2, May 1961, pp. 199–210.

A General Performance Index for Analytical Design on Control Systems, by Z. V. Rakasius, *Inst. Radio Engrs., Trans.*

on Automatic Control, vol. 6, no. 2, May 1961, pp. 217–221.

Sensitivity Considerations for Time-Varying Sampled-Data Feedback Systems, by J. B. Cruz Jr., *Inst. Radio Engrs., Trans. on Automatic Control*, vol. 6, no. 2, May 1961, pp. 228–236.

Data Handling by Computers and Utilization of the Resultant Information in Control Loops, by E. Krochmann, *Regelungstechnik*, vol. 9, no. 4, April 1961, pp. 137–143. (In German.)

The Initial Conditions of Linear Transfer Devices, by O. Follinger, *Regelungstechnik*, vol. 9, no. 4, April 1961, pp. 149–152. (In German.)

Hot-Gas Systems Control Attitude in Extreme Environments, by W. W. Chao, *Space/Aeronautics*, vol. 35, no. 3, March 1961, pp. 65–66, 69.

Instrumentation and Communications

Satellite Communications, by B. McMillan, J. B. Fisk and J. R. Pierce, *Yale Scien. Magazine*, vol. 35, no. 6, March 1961, pp. 8–15.

Deep-Space Communications, by E. Rechtin, ASTRONAUTICS, vol. 6, no. 4, April 1961, pp. 37, 42–46.

Problems of Space Cpmmunication, I. Sensitivity of Linear Receivers, by C. T. McCoy, *Electronic Industries*, vol. 20, no. 4, April 1961, pp. 116–120.

Propagation and Generation of Low-Frequency Electromagnetic Waves in the Upper Atmosphere, by B. N. Gershman and V. A. Ugarov, *Soviet Physics-Uspekhi*, vol. 3, no. 5, March–April 1961, pp. 743–764.

Satellite-Borne Instrumentation for Observing Flux of Heavy Primary Cosmic Radiation, by H. Hanson, P. Shwed, M. A. Pomerantz and H. Benjamin, *Franklin Inst., J.*, vol. 571, no. 4, April 1961, pp. 275–291.

Minimum Range to Artificial Earth Satellites, by K. Toma, *Nature*, vol. 190, no. 4773, April 22, 1961, pp. 333–334.

Satellite Flashing Light System, by R. Freed and L. S. Klivans, *Electronics Industries*, vol. 20, no. 4, April 1961, pp. 94–98.

Photogrammetric Refraction Angle: Satellite Viewed from Earth, by B. L. Jones, *J. Geophys. Res.*, vol. 66, no. 4, April 1961, pp. 1135–1138.

Behaviour of Broadcast Frequency Waves at Oblique Incidence During an Annular Eclipse, by R. K. MacCrone and F. R. N. Nabarro, *J. Atmospheric and Terrestrial Phys.*, vol. 20, no. 2–3, March 1961, pp. 200–205.

Current Developments in Pyrheliometric Techniques, by A. J. Drummond, *Solar Energy*, vol. 5, no. 1, Jan.–March 1961, pp. 19–23.

Refraction Compensation in a Spherically Stratified Ionosphre, by S. M. Harris, *IRE Trans. on Antennas and Propagation*, vol. AP-9, no. 2, March 1961, pp. 207–210.

Radio Communication Using Earth-Satellite Repeaters, by L. Pollack, *Engineers' Digest*, vol. 22, no. 2, Feb. 1961, pp. 90–92.

A Transatlantic Communication Experiment Via ECHO 1 Satellite, by H. Carru, R. Gendrin and M. Reyssat, *Nature*, vol. 189, no. 4761, Jan. 28, 1961, pp. 268–271.

Multiple Parameter Presentation of Radar Meteor Echoes, by C. Ellyett and A. C. Stanbury, *IRE Trans. on Antennas and Propagation*, vol. AP-9, no. 2, March 1961, p. 221.

Radar Astronomy, by J. V. Evans, *Contemporary Physics*, vol. 2, no. 2, Dec. 1960, pp. 116–142.

Radio Astronomy, by M. Laffineur, *Amer. J. Phys.*, vol. 29, no. 3, March 1961, pp. 198–206.

The 140-Foot Radio Telescope of the National Radio Astronomy Observatory, by O. Struve, R. M. Emberson and J. W. Findlay, *Astronom. Soc. Pacific, Publ.*, vol. 72, no. 429, Dec. 1960, pp. 439–458.

Ionospheric Scattering of Satellite Transmissions, by J. Mawdsley and I. R. Richards, *Nature*, vol. 189, no. 4768, March 18, 1961, pp. 906–907.

The Refractive Approach to Telemetry, by J. Parry, *Space World*, vol. 1, no. 8, June 1961, pp. 27–28, 54–56.

Data Transmission for the NRL Space Surveillance System, by M. G. Kaufman and F. X. Downey, *IRE Trans. on Space Electronics and Telemetry*, vol. SET-7, no. 1, March 1961, pp. 15–20.

Properties of Orbiting Dipole Belts, by W. E. Morrow Jr. and D. C. MacLennan, *Astronom. J.*, vol. 66, no. 3, April 1961, pp. 107–113.

Report of the Effects of Project West Ford on Optical Astronomy, by W. Liller, *Astronom. J.*, vol. 66, no. 3, April 1961, pp. 114–116.

Project West Ford—Properties and Analysis, by L. Goldberg, *Astronom. J.*, vol. 66, no. 3, April 1961, pp. 105–106.

Radio Properties of an Orbiting Scattering Medium, by A. E. Lilley, *Astronom. J.*, vol. 66, April 1961, pp. 116–118.

High Frequency Radio Propagation and Communication, by F. A. Polkinghorn, *Columbia Engng. Quar.*, vol. 14, no. 2, Jan. 1961, pp. 10–13, 36, 38, 44.

Active Satellites—Prospects for World-Wide Communication Systems, by L. Pollack, *Wireless World*, vol. 67, no. 2, Feb. 1961, pp. 52–56.

Resonance Probe—A New Probe Method for Measuring Electron Density and Electron Temperature in the Ionosphere, by A. Miyazaki, K. Hirao, Y. Aono, K. Takayama, H. Ikegami and T. Ichimiya, *Radio Res. Labs. J., Japan*, vol. 7, no. 34, Nov. 1960, pp. 148–159.

Observations of Cosmic Radio Nose at 18 Mc/s in Hawaii, by W. R. Steiger and J. W. Warwick, *J. Geophys. Res.*, vol. 66, no. 1, Jan. 1961, pp. 57–66.

Field-Aligned Ionospheric Irregularities and the Scintillation of Satellite Radio Transmissions, by D. G. Singleton, G. J. E. Lynch and J. A. Thomas, *Nature*, vol. 189, no. 4758, Jan. 7, 1961, pp. 30–31.

A Design Approach to Communication Links for Space Vehicles, by F. Sinnott, *Control Engng.*, vol. 8, no. 3, March 1961, pp. 155–159.

Two Instruments for Measuring Distributions of Low-Energy Charged Particles in Space, by Michel Bader, Thomas B. Fryer and Fred C. Witteborn, *NASA Tech. Note* D-1035, July 1961, 42 pp.

Calibration of Pressure Gages in Dust-Laden Air Flow, by Horst W. Kriebel and A. R. Kriebel, *Stanford Res. Inst., DASA 1204, Final Rep.* (for Phase I), June 1961.

Development of High-Temperature Strain Gages, by J. W. Pitts and D. G. Moore, *National Bur. Standards, Monograph* 26, March 1961, 20 pp.

A Maser System for Radar Astronomy, by W. H. Higga, *Calif. Inst. Tech., Jet Propulsion Lab., Tech. Rep.* 32-103, June 1961, 19 pp.

An Excitation and Instrumentation System for Vibrating Plate Studies, by Charles Wesley Beck II, *Texas Univ., Defense Res. Lab.* CF-2930, March 1961, 33 pp., 26 figs. (Thesis, M.S.)

An Experimental Investigation of a Flow Modulator Using a Piezo-electric Crystal as the Driving Element, by Leon M. Wenzel, *NASA Tech. Note* D-877, July 1961, 10 pp.

Measurement of Pier Tilt with a Quartz Torsion Fiber Pendulum, by Ted G. Baxter, *Calif. Inst. Tech., Jet Propulsion Lab. Tech. Rep.* 32-44, July 1961, 33 pp.

Use of an Air Dead-Weight Tester for the Precise Control of Constant Gas Pressure in Closed Systems, by M. K. Laufer, *Atomic Energy Commission*, SCTM-339-59-47, Dec. 1959, 7 pp.

The Artificial Earth Satellite—A New Geodetic Tool, by Bruce C. Murray, ARS JOURNAL, vol. 31, no. 7, July 1961, pp. 924–931.

The State of Development of Telemetering Components, by C. R. Cearley, *Control Engng.*, vol. 8, no. 8, Aug. 1961, pp. 101–104.

The Construction and Performance of an Airborne Microwave Refractometer, by J. A. Lane, D. S. Froome and G. J. McConnell, *Institution Elect. Engrs., Proc., Part B, Electronic and Communication Engng.*, vol. 108, no. 40, July 1961, pp. 398–402.

A Self-Optimizing Non-Linear Filter (Communication), by J. K. Lubbock, *Institution Elect. Engrs., Proc., Part B, Electronic and Communication Engng.*, vol. 108, no. 40, July 1961, pp. 439–440.

An Instrument for Measuring the Intensity of Pulsed Magnetic Fields, by Yu. L. Kurkin, N. S. Kurkina and R. D. Matsonashvili, *Instruments and Experimental Techniques*, no. 6, June 1961, pp. 981–982.

Proposed Method of Measuring Thermal Diffusivity at High Temperatures, by Robert D. Cowan, *J. Appl. Phys.*, vol. 32, no. 7, July 1961, pp. 1363–1370.

Device for the Stabilization of Helium Cryostat Temperatures, by C. J. Adkins, *J. Scien. Instr.*, vol. 38, no. 7, July 1961, pp. 305–306.

Measurement of Short Times by Semiconductors and Saturated Photomultipliers, by R. Ballini and E. Pomelas, *Nuclear Instruments and Methods*, vol. 11, no. 2, May 1961, pp. 331–335. (In French.)

Optimum Resolving Power for an Ultraviolet Space Telescope, by R. J. Davis and E. A. Godfredsen, *Planetary and Space Sci.*, vol. 5, July 1961, pp. 207–212.

Optical Methods for Tracking Earth Satellites, by I. S. Shklovskii, *Planetary and Space Sci.*, vol. 5, no. 3, July 1961, pp. 233–237.

Simple Apparatus for Comparative Density Measurements, by J. Pelsmaekers and S. Amelinckx, *Rev. Scien. Instr.*, vol. 32, no. 7, July 1961, pp. 828–830.

Radio-Frequency Breakdown Controlled by Drift of Electrons in an Inhomogeneous Magnetic Field, by L. T. Shepherd and H. M. Skarsgard, *Canadian J. Phys.*, vol. 39, no. 7, July 1961, pp. 983–992.

On Measurement of Thermal Conductivity at High Temperatures, by M. J. Laubitz, *Canadian J. Phys.*, vol. 39, no. 7, July 1961, pp. 1029–1039.

Project Echo, *Bell System Tech. J.*, vol. 40, July 1961.

Participation of Bell Telephone Laboratories in Project Echo and Experimental Results, by W. C. Jakes Jr., pp. 975–1028.

System Calculations, by C. L. Ruthroff

and W. C. Jakes Jr., pp. 1029–1039.

960-mc, 10 kw Transmitter, by J. P. Schafer and R. H. Brandt, pp. 1041–1064.

Receiving System, by E. A. Ohm, pp. 1065–1094.

A Horn-Reflector Antenna for Space Communication, by A. B. Crawford, D. C. Hogg and L. E. Hung, pp. 1095–1116.

The Dual Channel 2390-mc Traveling-Wave Maser, by R. W. De Grasse, J. J. Kostelnick and H. E. D. Scovil, pp. 1117–1128.

Standby Receiver System, by L. U. Kibler, pp. 1129–1148.

FM Demodulators with Negative Feedback, by C. L. Ruthroff, pp. 1149–1156.

Satellite Tracking Radar, by O. E. De Lange, pp. 1157–1182.

961-mc Lower-Sideband Up-Converter for Satellite Tracking Radar, by M. Uenohara and H. Seidel, pp. 1183–1206.

Antenna Steering System, by R. Klahn, J. A. Norton and J. A. Githens, pp. 1207–1225.

Boresight Cameras, by K. L. Warthman, pp. 1227–1233.

An Assessment of Readout Errors Encountered in Radio Telemetry from Gun-Launched Hyper-velocity Projectiles, by M. K. Kingery and P. L. Clemens, *Arnold Engng. Dev. Center,* TN-61-58, May 1961, 43 pp.

Statistical Parameters of a Electromagnetic Wave which has Passed Through an Inhomogeneous Layer—of Magnetoactive Plasma, by N. G. Denisov, *Johns Hopkins Univ., Appl. Phys. Lab.* TG 230-T236, May 1961, 17 pp. (Transl. from *Izvestiia Vysshikh Uchebnykl Zavedenii Radiofizika,* vol. 3, no. 4, 1960, pp. 619–630.)

Some Problems of Transmission of Single Radio Signals Through Delay Systems with Nonlinear Phase Characteristics, by V. I. Tverskoi, *Johns Hopkins Univ., Appl. Phys. Lab.* TG 230-T222, March 1961, 5 pp. (Transl. from *Izvestiia Vysshikh Uchebnykh Zavedenii, Radiofizika,* vol. 3, no. 5, Sept.–Oct. 1960, pp. 1974–85.)

The Mariner Planetary Communication System Design, by Benn D. Martin, *Calif. Inst. Tech., Jet Propulsion Lab. Tech. Rep.* 32–85, (Rev. No. 1), May 1961, 62 pp.

The Effect of Accelerometer Low-Frequency Response on Transient Measurements, by M. E. Gurtin, *Experimental Mechanics,* vol. 1, no. 6, June 1961, pp. 206–209.

Noise Figure Measurements Using Celestial Sources, by Franklin G. Kelly, *Inst. Radio Engrs., Trans. on Space Electronics and Telemetry,* vol. 7, June 1961, pp. 32–33.

Low-Speed Time-Multiplexing with Magnetic Latching Relays, by John F. Meyer, *Inst. Radio Engrs., Trans. on Space Electronics and Telemetry,* vol. 7, June 1961, pp. 34–41.

Thermal-Noise Errors in Simultaneous-Lobing and Conical-Scan Angle-Tracking Systems, by Jean A. Develet Jr., *Inst. Radio Engrs., Trans. on Space Electronics and Telemetry,* vol. 7, June 1961, pp. 42–50.

Some Elementary Considerations of Satellite-Earth Communication Systems, by T. Teichmann, *Inst. Radio Engrs., Trans. on Space Electronics and Telemetry,* vol. 7, June 1961, pp. 51–54.

Threshold Improvement in an FM Subcarrier System, by J. J. Spilker Jr., *Inst. Radio Engrs., Trans. on Space Electronics and Telemetry,* vol. 7, June 1961, pp. 55–59.

Circular Aerial Arrays for Radio Astronomy, by J. P. Wild, *Royal Society, London, Proc.,* vol. A262, no. 1308, June 1961, pp. 84–99.

Atmospheric and Space Physics

The Determination of the Incident Flux of Radio-Meters, by T. R. Kaiser, *Royal Astronom. Soc., Monthly Notices,* vol. 121, no. 3, 1960, pp. 284–298.

A Note of the Cause of Sudden Ionization Anomalies in Regions Remote from High-Altitude Nuclear Bursts, by C. M. Crain and P. Tamarkin, *J. Geophys. Res.,* vol. 66, no. 1, Jan. 1961, pp. 35–39.

Proceedings (Advances in the Astronautical Sciences, U. S.), American Astronautical Society, Western National Meeting, Plenum Press, New York, 1960, 355 pp.

The Origin of the Gravitation Field, by F. E. Alzofon, pp. 309–319.

The Lunar Gravitational Potential, by Igor Alexandrov, pp. 320–324.

Lunar and Terrestrial Atmospheres, by Robert Jastrow, pp. 338–345.

Seasonal, Latitudinal and Diurnal Variations in the Upper Atmosphere, by W. G. Stroud and William Nordberg, *NASA Tech. Note* D-703, April 1961, 16 pp.

Physics of the Upper Atmosphere, J. A. Ratcliffe (ed.), Academic Press, New York, 1960, 586 pp.

The Thermosphere—the Earth's Outermost Atmosphere, by Sidney Chapman, pp. 1–16.

The Properties and Constitution of the Upper Atmosphere, by M. Nicolet, pp. 17–72, 60 refs.

The Upper Atmosphere Studied by Rockets and Satellites, by Homer E. Newell Jr., pp. 73–132, 99 refs.

The Sun's Ionizing Radiations, by Herbert Friedman, pp. 133–218, 95 refs.

The Airglow, by D. R. Bates, pp. 219–267, 221 refs.

General Character of Auroras, by D. R. Bates, pp. 269–298, 88 refs.

The Auroral Spectrum and its Interpretation, by D. R. Bates, pp. 299–353, 159 refs.

Radar Studies of the Aurora, by Henry G. Booker, pp. 355–375, 29 refs.

The Ionosphere, by J. A. Ratcliffe and K. Weeks, pp. 377–470, 318 refs.

The Upper Atmosphere and Meteors, by J. S. Greenhow and A. C. B. Lovell, pp. 513–549, 55 refs.

Advances During the IGY 1957/58, by J. S. Greenhow and A. C. B. Lovell, pp. 551–563.

Ballistic Missile and Space Technology, Vol. 3: Guidance Navigation, Tracking and Space Physics (Symposium on Ballistic Missile and Space Technology, Los Angeles, Aug. 1960) Donald P. Le Galley (ed.), Academic Press, New York, 1960, 450 pp.

Radio Propagation Experiments for Investigating the Solar Wind, by S. Rubin and S. D. Softky, pp. 393–403.

Scientific Results of the Satellite, Explorer VI, by E. J. Smith and Alan Rosen, pp. 405–443, 29 refs.

The Dynamic Stability of the Upper Atmosphere of Venus, by Jean I. F. King, pp. 445–450.

The Radio Noise Spectrum, Donald H. Menzel (ed.), Harvard Univ. Press, Cambridge, Mass., 1960, 183 pp.

Meteor Scatter, by Von R. Eshleman, pp. 49–78, 60 refs.

Electromagnetic Emission from Meteors, by Gerald S. Hawkins, pp. 79–92.

Whistler-Mode Propagation, by R. A. Helliwell, pp. 93–100.

The Radio Spectrum of Solar Activity, by A. Maxwell, G. Swarup and A. R. Thompson, pp. 101–110.

Solar Whistlers, by Thomas Gold and Donald H. Menzel, pp. 123–128.

Interstellar Hydrogen, by Thomas Gold, pp. 177–179.

The Determination of Absorption in the Ionosphere by Pulse Amplitude Observations, by Gerhard Umlauft, *Archiv für Technisches Messen,* no. 302, March 1961, pp. 53–56. (In German.)

Tiros Program Results, by Morris Tepper, ASTRONAUTICS, vol. 6, no. 5, May 1961, pp. 28–29, 63–66, 68.

Effect of Geomagnetic Disturbances on the Drift of Ionized Gas in the Upper Atmosphere, by V. P. Dokuchaev, *Johns Hopkins Univ., Appl. Phys. Lab.* TG 230-T228, April 1961, 4 pp. (Transl. from *Izvestiia Vysshikh Uchebnykh Zavedenii,* vol. 3, no. 5, Sept.–Oct. 1960, pp. 901–903.)

Thermal History of the Moon and of the

CHANGE-OF-ADDRESS NOTICE

In the event of a change of address, it is necessary to include both your old and new addresses, as well as your membership number and coding, when notifying ARS headquarters, in order to insure prompt service. If you are moving or have moved, send the following form to Membership Dept., American Rocket Society, 500 Fifth Ave., New York 36, N. Y.:

Name_____

Membership Card No._____ Coding_____

Old Address_____

_____

New Address_____

_____

Terrestrial Planets, by Kopal Zdenek, *Calif. Inst. Tech., Jet Propulsion Lab. Tech. Rep.* 32-108, May 1961, 24 pp.

Organic Matter and the Moon, by Carl Sagan, *National Res. Council, Pub.* 757, 1961, 49 pp., bibliog. pp. 45–49.

Tektites and Natural Satellites of the Earth, by John A. O'Keefe and Barbara E. Shute, *Aerospace Engng.*, vol. 20, no. 7, July 1961, pp. 26–27, 65–66.

Vertical Distribution of Sodium in the Upper Atmosphere, by W. R. Bullock and D. M. Hunten, *Canadian J. Phys.*, vol. 39, no. 7, July 1961, pp. 976–982.

Tropospheric Scatter Observations at 3480 Mc/s with Aerials of Variable Spacing, by R. W. Meadows, *Institution Elect. Engrs., Proc., Part B, Electronic and Communication Engng.*, vol. 108, no. 40, July 1961, pp. 349–360.

The Aerial Survey of Terrestrial Radioactivity, by D. Williams and H. Bisby, *Institution Elect. Engrs., Proc., Part B, Electronic and Communication Engng.*, vol. 108, no. 40, July 1961, pp. 403–412.

Atmospheric Phenomena Noted in Simultaneous Observations of 1958, by J. Aarons, H. E. Whitney, R. S. Roger, J. Thomson and others, *Planetary and Space Sci.*, vol. 5, no. 3, July 1961, pp. 169–184.

The Influence of Resonance Absorption in the Sodium Layer on Temperature and Density Measurements in the Upper Atmosphere, by T. M. Donahue, J. E. Blamont and M. L. Lory, *Planetary and Space Sci.*, vol. 5, no. 3, July 1961, pp. 185–195.

Radiation Measurements During the Flight of the Second Cosmic Rocket, by A. E. Chudakov, P. V. Vakulov, Yu. I. Logachev and A. G. Nikolaev, ARS JOURNAL, vol. 31, no. 7, July 1961, pp. 967–970.

Connection Between the Motion of Matter in the Corona and the Prominences, by M. G. Karimov and N. S. Shilova, ARS JOURNAL, vol. 31, no. 7, July 1961, pp. 970–976.

Comments on Tidal Winds in the High Atmosphere, by B. Haurwitz, *Planetary and Space Sci.*, vol. 5, no. 3, July 1961, pp. 196–201.

Atmospheric Water Vapor Measurements at 6–7 Microns from a Satellite, by F. Moller, *Planetary and Space Sci.*, vol. 5, no. 3, July 1961, pp. 202–206.

Local Electron Densities Deduced from the Faraday Fading of Satellite Transmissions Using Measurements During Two Consecutive Transits, by L. Liszka, *Planetary and Space Sci.*, vol. 5, no. 3, July 1961, pp. 213–222.

Soviet Investigations of the Ionosphere Employing Rockets and Artificial Earth Satellites, by V. I. Krasovskii, *Planetary and Space Sci.*, vol. 5, no. 3, July 1961, pp. 223–232.

Preliminary Report on Geomagnetic Measurements on the Third Soviet Artificial Earth Satellite, by S. Sh. Dolginov, L. N. Zhuzgov and N. V. Pushkov, *Planetary and Space Sci.*, vol. 5, no. 3, July 1961, pp. 244–247.

The Observation of Corpuscles by Means of the Third Artificial Earth Satellite, by V. I. Krasovskii, Yu. M. Kushner, G. A. Bordovskii and others, *Planetary and Space Sci.*, vol. 5, no. 3, July 1961, pp. 248–250.

An Annotated Bibliography on Interplanetary Dust, by Paul W. Hodge, Frances W. Wright and Dorrit Hoffleit, *Smithsonian Contributions to Astrophysics*, vol. 5, no. 8, 1961, pp. 85–111.

Estimation of Errors in the Numerical Integration of the Equations of Celestial Mechanics, by V. F. Miachin, *Johns Hopkins Univ., Appl. Phys. Lab.* TG 230-T230, April 1961, 36 pp. (Transl. from *Bull. Instituta Theoreticheskoi Astronomii*, vol. 7, no. 4 (87), 1959, pp. 257–280.)

Monthly and Annual Wind Distribution as a Function of Altitude for Patrick Air Force Base, Cape Canaveral, Florida, by J. W. Smith and W. W. Vaughan, *NASA Tech. Note* D-610, July 1961, 118 pp.

Empirical Three-Sign Wind Component Profiles, 45-Degree Missile Flight Azimuth, Atlantic Missile Range Patrick AFB (Cape Canaveral), Florida, by William W. Vaughan, *NASA Tech. Note* D-606, July 1961, 63 pp.

Results from a Rocket-Borne Langmuir Probe Experiment, by Gideon P. Serbu, *NASA Tech. Note* D-570, July 1961, 9 pp.

Sporadic-E as Observed with Rockets, by J. Carl Seddon, *NASA Tech. Note* D-1043, July 1961, 13 pp.

Range of Density Variability from Surface to 120 KM Altitude, by Orvel E. Smith and Halsey B. Chenoweth, *NASA Tech. Note* D-612, July 1961, 24 pp.

Density in a Planetary Exosphere, by Jackson Herring and Herbert L. Kyle, *NASA Tech. Note* D-1065, July 1961, 6 pp.

On the Electron Density Distribution Above the F2 Peak, by S. J. Bauer, *NASA Tech. Note* D-1042, July 1961, 5 pp.

New Theory of the Aurora Polaris, by S. I. Akasofu and S. Chapman, ARS JOURNAL, vol. 31, no. 6, June 1961, pp. 775–783.

Measurement of Air Density at 430 Km by Sodium Resonance Cloud Techniques, by J. Pressman and F. F. Marmo, ARS JOURNAL, vol. 31, no. 6, June 1961, pp. 819–821.

Irradiation of a Lunar Satellite, by W. Leon Francis, ARS JOURNAL, vol. 31, no. 6, June 1961, pp. 835–836.

Meteorological Analysis of Churchill Rocket Sounding Data, by Sidney Teweles, ARS JOURNAL, vol. 31, no. 6, June 1961, pp. 841–864.

Variable Conditions of the Terrestrial Exosphere, by H. K. Paetzold and H. Zschorner, *Astronautica Acta*, vol. 6, no. 6, 1960, pp. 373–378.

The Earth's Dust Belt, by Fred E. Whipple, *Astronaut. Sci. Rev.*, vol. 3, no. 2, April–June 1961, pp. 17–20.

A New Approach to the Measurement of Turbulent Fluxes in the Lower Atmosphere, by R. J. Taylor, *J. Fluid Mech.*, vol. 10, part 3, May 1961, pp. 449–458.

Radiation Measurements During the Flight of the Third Cosmic Rocket, by S. N. Vernov, A. E. Chudakov, P. V. Vakulov and A. G. Nikolaev, *Soviet Phys.: Doklady*, vol. 6, no. 1, July 1961, pp. 43–45.

Altitude Dependence of Extensive Air Showers, by E. V. Gedalin, *Soviet Phys.: JETP*, vol. 13, no. 1, July 1961, pp. 123–124.

The Earth Current Effects Caused by High-Altitude Atomic Explosions (Complete), by V. A. Troitskaya, *Akademiia Nauk SSSR, Izvestia, Seria Geofiz.*, no. 9, Sept. 1960, pp. 1321–1327 (Transl. in Phys. Express, vol. 3, no. 4, Dec. 1960, pp. 19–23.) (In Russian.)

Auroral Temperature Determinations from A 211 X 2Σ Bands of the N_2^+ Molecule, by W. G. Mathews and L. Wallace, *J. Atmospheric and Terrestrial Phys.*, vol. 20, Feb. 1961, pp. 1–8.

Observations on Cherenkov Radiation from the Night Sky, by J. White, N. A. Porter and C. D. Long, *J. Atmospheric and Terrestrial Phys.*, vol. 20, no. 1, Feb. 1961, pp. 40–48.

Results of Observations of Charged Particles Observed out to R = 100,000 KM, with the Aid of Charged-Particle Traps on Soviet Space Rockets, by K. I. Gringau, V. G. Kurt, V. I. Moroz and I. S. Shklovskii, *Soviet Astronomy AJ*, vol. 4, no. 4, Jan.–Feb. 1961, pp. 980–995.

Definition Elements for Comets 1905 IV (KOPFF), 1941 VIII (VAN GENT), 1946 I (TIMMERS) and 1946 VI (JONES), by G. Pels, *Astronom. Inst. of the Netherlands, Bull.*, vol. 15, no. 499, Dec. 30, 1960, pp. 127–155.

Methods for Computing the Original Orbits of Comets, by E. H. Bilo and H. C. van de Hulst, *Astronom. Inst. of the Netherlands, Bull.*, vol. 15, no. 29, Dec. 30, 1960, pp. 119–127.

The Movement of the Enkebacklund Comet for the Years 1898–1911, and a New Determination of the Mass of Mercury, by S. G. Makover and N. A. Bokhan, *Akademiia Nauk SSSR, Doklady*, vol. 134, no. 3, Sept. 1960, pp. 552–554. (In Russian.)

The Original Values of 1/a for 17 Cemetary Orbits, by E. H. Bilo and I. van Houten-Groeneveld, *Astronom. Inst. of the Netherlands, Bull.*, vol. 15, no. 499, Dec. 30, 1960, pp. 155–162.

The Original Values of 1/a for Comets 1941 VIII (VAN GENT) and 1946 VI (JONES), by H. A. Pels-Kluyver, *Astronom. Inst. of the Netherlands, Bull.*, vol. 15, no. 499, Dec. 30, 1960, p. 163.

Present Status of the Question of the Origin of Cosmic Rays, by V. L. Ginzburg and S. I. Syrovatskii, *Soviet Physics-Uspekhi*, vol. 3, no. 4, Jan.–Feb. 1961, pp. 504–541.

Asymmetry in the Recovery from a Very Deep Forbush-Type Decrease in Cosmic-Ray Intensity, by D. C. Rose and S. M. Lapointe, *Canadian J. Phys.*, vol. 39, no. 2, Feb. 1961, pp. 239–251.

Dynamical Calculations Relating to the Origin of the Solar System, by R. A. Lyttleton, *Royal Astronom. Soc., Monthly Notices*, vol. 121, no. 6, 1960, pp. 551–569.

Origin of the Solar System, by W. H. McCrea, *Ciel et Terre*, vol. 76, no. 11–12, Nov.–Dec. 1960, pp. 369–385. (In French.)

The Belt of Equatorial Spread-F, by A. J. Lyon, N. J. Skinner and R. W. H. Wright, *J. Atmospheric and Terrestrial Phys.*, vol. 19, no. 3, Dec. 1960, pp. 145–159.

Ionospheric Absorption at Times of Auroral and Magnetic Pulsations, by W. H. Campbell and H. Leinbach, *J. Geophys. Res.*, vol. 66, no. 1, Jan. 1961, pp. 25–34.

The Effective Recombination Coefficient of an Ionosphere Containing a Mixture of Ions, by S. A. Bowhill, *J. Atmospheric and Terrestrial Phys.*, vol. 20, no. 1, Feb. 1961, pp. 19–30.

Skip-Distance Ray-Focusing in the Ionosphere, by E. Golton, *Nature*, vol. 189, no. 4758, Jan. 7, 1961, pp. 48–49.

Investigation of the Ionosphere and of the Interplanetary Gas with the Aid of Artificial Satellites and Space Rockets, by Ya. L. Al'pert, *Soviet Physics-Uspekhi*, vol. 3, no. 4, Jan.–Feb. 1961, pp. 479–503.

Dipole-Field Type Magnetic Disturbances and Auroral Activities, by B. K. Bhattacharyya, *Canadian J. Phys.*, vol. 39, no. 2, Feb. 1961, pp. 350–366.

On the Relationship Between the Effect of Chromospheric Bursts and the Geomagnetic Activity (Based on Observation During 1947–1959), by O. M. Barsukov, *Akademiia Nauk SSSR, Izvestia, Seria*

Geofiz., no. 7, July 1960, pp. 977–978. (In Russian.)

The Occurrence of the Spread-F and the Geomagnetic Field, by T. Shimazaki, *Radio Res. Labs.*, J., vol. 7, no. 33, Sept. 1960, pp. 437–450.

Pulsation of the Earth's Electromagnetic Field with Periods 1 to 15 Seconds and Their Connection with Phenomena in the High Atmosphere, by V. A. Troitskaya, *J. Geophys. Res.* vol. 66, no. 1, Jan. 1961, pp. 5–18.

Apparent Steady Component of Interplanetary Magnetic Field, by V. A. Bailey, *Nature*, vol. 189, no. 4758, Jan. 7, 1961, pp. 44–45.

The Dependence of the Mean Hourly Rates of Recorded Meteors on the Parameters of Meteoroids, the Atmosphere, and the Radar System, by E. I. Fialko, *Soviet Astronomy AJ*, vol. 4, no. 4, Jan.–Feb. 1961, pp. 711–721.

A Theory of Ionization of Meteor Trails. II. The Role of Ionization Phenomena at the Surface of a Meteoroid in the Ionization of the Meteor Trail, by A. M. Furman, *Soviet Astronomy AJ*, vol. 4, no. 4, Jan.–Feb. 1961, pp. 705–710.

Isotopic Composition of Xenon from Enstatite Chrondrites, by J. H. Reynolds, *Zeitschrift für Naturforschung*, vol. 15A, no. 12, Dec. 1960, pp. 1112–1114. (In German.)

Lead and Its Isotopic Composition in Iron Meteorites, by I. E. Starik, *Akademiia Nauk SSSR, Doklady*, vol. 134, Sept. 1960, pp. 555–558. (In Russian.)

Radio Echo Measurements of the Orbits of Faint Sporadic Meteors, by J. G. Davies and J. C. Gill, *Royal Astronom. Soc., Monthly Notices*, vol. 121, no. 5, 1960, pp. 437–462.

A Southern Hemisphere Survey of the Radiants of Sporadic Meteors, by A. A. Weiss and J. W. Smith, *Royal Astronom. Soc., Monthly Notices*, vol. 121, 1960, pp. 5–16.

The Importance of Initial Trail Radius on the Apparent Height and Number Distributions of Meteor Echoes, by J. S. Greenhow and J. E. Hall, *Royal Astronom. Soc., Monthly Notices*, vol. 121, no. 2, 1960, pp. 183–196.

The Variation of Meteor Heights with Velocity and Magnitude, by J. S. Greenhow and J. E. Hall, *Royal Astronom. Soc., Monthly Notices*, vol. 121, no. 2, 1960, pp. 174–182.

Spectropolarimetry of Some Regions of the Lunar Surface, by V. G. Teifel' *Soviet Astronomy AJ*, vol. 4, no. 4, Jan.–Feb. 1961, pp. 669–673.

Enhanced Lunar Thermal Radiation During a Lunar Eclipse, by R. W. Shorthill, H. C. Borough and J. M. Conley, *Astronom. Soc. Pacific, Publ.*, vol. 72, no. 429, Dec. 1960, pp. 481–485.

Variation of Parameters for Elliptic and Near Circular Orbits, by S. Pines, *Astronom J.*, vol. 66, no. 1, Feb. 1961, pp. 5–7.

The Sizes of Habitable Planets, by Su Shu, *Astronom. Soc. Pacific, Publ.*, vol. 72, no. 429, Dec. 1960, pp. 489–493.

World Warning Agency Report July–September 30, 1960, *Natl. Acad. Sci., IGY Bull.*, no. 43, Jan. 1961, pp. 13–15.

Sources of Solar Ultraviolet Radiation, by R. G. Athay, *J. Geophys. Res.*, vol. 66, no. 2, Feb. 1961, pp. 385–390.

Solar Radio Emissions and Geophysical Disturbances During July 1959, by M. P. Hughes, *J. Geophys. Res.*, vol. 66, no. 2, Feb. 1961, pp. 651–653.

Deflection of Light in the Gravitational Field of the Sun, by N. S. Japolsky, *Nature*, vol. 189, no. 4765, Feb. 25, 1961, pp. 651–652.

The Radio Brightness of the Quiet Sun at 21 CM Wavelength Near Sunspot Maximum, by N. R. Labrum, *Australian J. Phys.*, vol. 13, no. 4, Dec. 1960, pp. 700–711.

Charged Particles in the Inner Van Allen Radiation Belt, by A. H. Armstrong, F. B. Harrison, H. H. Heckman and L. Rosen, *J. Geophys. Res.*, vol. 66, no. 2, Feb. 1961, pp. 351–357.

X-Rays From Van Allen Belt Electrons, by J. B. Cladis and A. J. Dessler, *J. Geophys. Res.*, vol. 66, no. 2, Feb. 1961, pp. 343–350.

The Planet Venus, by C. Sagan, *Science*, vol. 133, no. 3456, March 24, 1961, pp. 849–858.

Human Factors and Bio-Astronautics

Radiation Shielding for Manned Space Flight, by Lewis E. Wallner and Harold R. Kaufman, *NASA Tech. Note* D-681, July 1961, 45 pp.

Waste-Recovery Processes for a Closed Ecological System, by W. O. Pipes, *National Res. Council, Pub.* 898, 1961, 22 pp.

Gas Regeneration and Food Production in a Closed Ecological System, by Jack E. Myers and Allan H. Brown, *National Res. Council, Pub.* 893, 1961, 13 pp., 22 refs.

Proceedings, Conference on Results of the First U. S. Manned Suborbital Space Flight, Washington, D. C., June 1961, Sponsored by NASA in cooperation with Natl. Inst. of Health and Natl. Academy of Sci., Gov't. Printing Office, Washington, D. C., 1961, 76 pp.

Review of Biomedical Systems for MR-3 Flight, by Stanley C. White, Richard S. Johnston and Gerard J. Pesman, pp. 19–30.

Results of Preflight and Postflight Medical Examinations, by Carmault B. Jackson Jr., William K. Douglas and James E. Colver, pp. 31–36.

Bioinstrumentation in MR-3 Flight, by James P. Henry and Charles D. Wheelwright, pp. 37–44.

Physiological Responses of the Astronaut in the MR-3 Flight, by William S. Augerson and C. Patrick Laughlin, pp. 45–52.

Pilot Training and Preflight Preparation, by Donald K. Slayton, pp. 53–60.

Results of In-Flight Pilot Performance, by Robert B. Voas, John J. Van Bockel, Raymond G. Zedekar and Paul W. Backer, pp. 61–68.

Pilot's Flight Report, including In-Flight Films, by Alan B. Shepard Jr., pp. 69–76.

The Chimpanzee: Procurement, Standardization and Use in Biomedical Research, by James E. Cook, Jerry Fineg, Eldon D. Miksch and William E. Britz, *Air Force Missile Dev. Center, Tech. Rept.* 61-23, 1961, 4 pp. (Reprint from J. Amer. Veterinary Medical Assoc., vol. 138, no. 7, April 1, 1961, pp. 366–369.)

Psychological and Social Problems of Man in Space—A Literature Survey, by B. D. Goodman, ARS JOURNAL, vol. 31, no. 7, July 1961, pp. 863–872, 159 refs.

Response of Subjects to Some Conditions of a Simulated Orbital Flight Pattern, by E. Hendler and L. J. Santa Maria, *Aerospace Medicine*, vol. 32, no. 2, Feb. 1961, pp. 126–133.

Measurement of Higher Intellectual Functioning in the Chimpanzee. Its Relevance to the Study of Behavior in Space Environment, by F. H. Rohles, R. E. Belleville and M. E. Grunzke, *Aerospace Medicine*, vol. 32, no. 2, Feb. 1961, pp. 121–125.

Is There Life on Other Planets? by N. Horowitz, *Engng. and Sci.*, vol. 24, no. 6, March 1961, pp. 11–15.

Instrumentation of Animals for Biosatellite Research: Surgical Implantation of Radio Transmitters for Determining Viability in the Mouse, by H. A. Gorman, *Amer. Veterinary Medical Assoc. J.*, vol. 137, no. 12, Dec. 15, 1960, pp. 693–697.

On the Supply of Oxygen and Food During Long-Lasting Space Journeys, by L. Enebo, *Astronautik, Sweden*, vol. 2, no. 2, 1960, pp. 103–126.

Sanitation in Space Means Recycling, by E. Thompson, *Engng.*, vol. 190, no. 4931, Oct. 21, 1960, pp. 552–553.

Space Medicine and Astronaut Selection, by A. H. Schwichtenberg, *Minnesota Medicine*, vol. 43, no. 12, Dec. 1960, pp. 797–812.

Aviation Medicine to Space Medicine in Four Decades, by P. A. Campbell, *Medical Times*, vol. 88, no. 11, Nov. 1960, pp. 1245–1253.

Human Engineering or Engineering of the Human Being—Which? by R. S. Pogrund, *Aerospace Medicine*, vol. 32, no. 4, April 1961, pp. 300–315.

The Problem of Survival, by H. Bloom, *Space World*, vol. 1, no. 8, June 1961, pp. 32–35, 60–62.

The Human Factor, by J. Rublowsky, *Space World*, vol. 1, no. 8, June 1961, pp. 18–19, 46–48.

A Study of Animal Reflexes During Exposure to Subgravity and Weightlessness, by G. J. D. Shock, *Aerospace Medicine*, vol. 32, no. 4, April 1961, pp. 336–340.

Orientation to the Vertical During Water Immersion, by J. L. Brown, *Aerospace Medicine*, vol. 32, no. 3, March 1961, pp. 209–217.

Physiological Effects of Postural Disorientation by Tilting During Weightlessness, by B. G. King, *Aerospace Medicine*, vol. 32, no. 2, Feb. 1961, pp. 137–140.

Effects of Zero Gravity Upon the Cardiovascular System, by L. J. Stutman and R. Olson, *U.S. Armed Forces Medical J.*, vol. 11, no. 10, Oct. 1960, pp. 1162–1168.

Symptoms Resulting from Prolonged Immersion in Water: The Problem of Zero G Asthenia, by A. Graybie and B. Clark, *Aerospace Medicine*, vol. 32, no. 3, March 1961, pp. 181–196.

Some Engineering Aspects of Psycho-Motor Training, by R. L. Berry, *Kentucky Engr.*, vol. 23, no. 2, Jan. 1961, pp. 10–11, 36–43, 53.

Aspects of a Bio-astronautics Project, by B. G. Taylor, *Kentucky Engr.*, vol. 23, no. 2, Jan. 1961, pp. 12–13, 26.

A Rational Framework for Interpreting the Behavioral Effects of Atmospheric Ions, by A. H. Frey, *IRE Trans. on Bio-Medical Electronics*, vol. BME-8, no. 1, Jan. 1961, pp. 12–16.

The Moon as a Collector of Biological Material, by E. Anders, *Science*, vol. 133, no. 3459, April 14, 1961, pp. 1115–1116.

Education, Sociology, Law

Who Owns What? by W. A. Hyman, *Space World*, vol. 1, no. 8, June 1961, pp. 36–39, 59–60.